Author:
Luckham, Stephen

Title:
Kinetics and Equilibrium in Iron-Catalysed Cross-Coupling Reactions

Kinetics and Equilibrium in Iron-Catalysed Cross-Coupling Reactions

Stephen L. J. Luckham

A thesis submitted to the University of Bristol in accordance with the requirements of the degree of Doctor of Philosophy in the School of Chemistry, Faculty of Science

April 2019

Abstract

Using a range of spectroscopic techniques, insights into the iron-catalysed Kumada and Negishi cross-coupling reactions are proposed. A small study on a chromium-diphosphine complex, using EPR spectroscopy, has also been carried out.

In the case of an iron-catalysed Kumada cross-coupling of a benzyl halide and a benzyl Grignard reagent, a catalytic cycle based on an iron(I)/(II)/(III) centre is proposed. The reaction proceeds unselectively, yielding a distribution of products. From a detailed kinetic investigation, it is found that the rate-limiting step for the formation of each product involves the activation of the electrophile at the iron centre, suggestive of a slow oxidation step and the formation of heteroleptic, iron(III) 'ate' species. The results of a Hammett study and an Eyring analysis suggest that this step is likely to occur by a radical pathway, with no thermodynamic preference towards any one of the products. An auto-catalytic pathway is proposed to be operative, based on the sigmoidal nature of the concentration-time plots obtained.

Addition of an NHC ligand to the iron-catalysed Kumada coupling described above is shown, *via* NMR spectroscopy, to result in a mixed iron speciation, the ratio of which is dependent upon the concentration of the NHC ligand. This is supported by the results of a small kinetic study, which indicates that the iron-NHC complexes perform as slightly more active (though equally unselective) catalysts compared to the ligand-free species.

The transmetallation of iron by zinc-aryl species is shown to occur using both 4-tolyl and mesityl nucleophiles, in the presence and absence of a diphosphine ligand. Using the kinetically stabilised mesityl group, the diphosphine ligand was shown, in a qualitative fashion, to provide a more facile transmetallation process, resulting ultimately in the complete dissociation of the diphosphine ligand from iron, and formation of a series of hetero- and homoleptic ferrate species. Transmetallation is also possible in the absence of magnesium salts, suggesting that their necessary presence within the iron-catalysed Negishi cross-coupling is not concerned with the transmetallation step. The reverse process, whereby transmetallation occurs from iron to zinc, is also shown to be possible. In this case quantification demonstrated the process to proceed efficiently with good yields.

Using NMR and X-ray absorption spectroscopies, the diphosphine ligand within an iron-catalysed Negishi cross-coupling is found to not coordinate to iron during catalytic turnover, residing instead on the zinc centre. Using XAS, a rapid burst-phase at the start of the reaction

is shown to yield metallic iron, following which the iron takes the form of homo- or heteroleptic organo-iron complexes throughout the bulk of turnover. Using ^{31}P NMR spectroscopy, the diphosphine ligand is quantifiably assigned to exist coordinated to zinc throughout the bulk of turnover.

A chromium(I) mono-diphosphine complex is shown to undergo a photochemical transformation, under action of UV irradiation, to yield a Cr(I)-bis-diphosphine complex. An intermediate in the photochemical transformation is identified as a bimetallic complex, featuring a bridging diphosphine ligand between the two chromium(I) centres.

Acknowledgements

I am very grateful that over the previous few years I have been able to work alongside some excellent chemists who have helped me with all the challenges that working in a lab brings.

I must first thank Robin, as without him this project would not have been possible. He has been a fantastic supervisor, providing me with ideas, genuine enthusiasm and support when each was needed, and I have learnt a lot from him. Although I am sure he has not learnt nearly as much from me (bad grammar aside), I hope he has enjoyed working together as much as I have. Damien in Cardiff has also been a great help whenever I have asked, in spite of his workload, and I regret not working with him more throughout my Ph.D.

Thanks to Sanita, who after all this time working together still laughs at my jokes that last too long and occur too frequently; Mattia, who never succeeded in making me automate my calibration spreadsheet but did help me improve my awful Italian; Wilko, whose quick-wit made him a great person to work alongside (at the cost of his music); and Ben, who added some much-needed sports chat to the group (at the cost of his music). Thanks also to Harry, particularly for helping me to settle into the group when I first arrived; Soneela, whose company I was glad to have in library whilst writing up in the evenings; Antonis, whose methodical and logical approach to work I have come to greatly appreciate over the last year and a half; Pablo, with whom it was a pleasure to help enjoy his brief stay in Bristol; and Emma and Andrea, for always patiently taking the time to help me whenever I was over in Cardiff. Thanks also to Paul Lawrence, David, Oscar, Carolina, Hubert, Matt, Charlotte, Jack, Alex, Gavin and Hao.

Seb, Nim, Ash and Brazier were fantastic students to supervise (though I use the term lightly as they all helped me at least as much as I helped them) and I thoroughly enjoyed working with each of them.

I am particularly indebted to Mattia, Antonis, Sanita, Wilko and Damien who read some very rough drafts of this thesis, and to Robin and Bene, who helped me put it all together at the end…the errors within this work are not the fault of the proofreaders!

Finally, thanks again to Bene, who (in addition to the above) helped me more than she will ever know, in so many different ways.

Declaration

I declare that the work in this thesis was carried out in accordance with the regulations of the University of Bristol and no part of this thesis has been submitted for any other academic award. The work is original, except where indicated by reference in the text and any work done in collaboration with, or with the assistance of others, is indicated as such. Any views expressed are those of the author.

Stephen LJ Luckham

University of Bristol

April 2019

Abbreviations

acac	Acetylacetone	Me	Methyl
μ_B	Bohr-Magneton	Mes	Mesityl
Ar	Aryl	mM	Millimolar
ATRP	Atom transfer radical polymerisation	MO	Molecular orbital
Bn	Benzyl	Nap	Naphthyl
Cp	Cyclopentadienyl	NMP	*N*-methyl-2-pyrrolidone
Cp*	Pentamethylcyclodienyl	NMR	Nuclear magnetic resonance
CW-EPR	Continuous-wave EPR	NZT	Nuclear Zeeman term
Cy	Cyclohexyl	O.A.	Oxidative addition
DFT	Density functional theory	pin	Pinacol
dipp	2,6-Diisopropylaniline	ppm	Parts per million
dmbz	1,2-Bis(dimethylphosphino)phosphine	QEXAFS	Quick-EXAFS
DMF	Dimethylformamide	R.E.	Reductive elimination
dpbz	1,2-Bis(diphenylphosphino)benzene	r.t.	Room temperature
dppe	1,2-Bis(diphenylphosphino)ethane	RDS	Rate determining step
dppp	1,2-Bis(diphenylphosphino)propane	s	Second(s)
EPR	Electron paramagnetic resonance	SIPr	1,3-Bis(2,6-di*iso*propylphenyl)imidaolidin-2-ylidene
eq.	Equivalents	SOMO	Singly occupied molecular orbital
Et	Ethyl	t	Time
EXAFS	Extended X-ray absorption fine structure	T	Temperature
EZT	Electronic Zeeman term	^{t}Bu	Tertiary-butyl
GC	Gas chromatography	THF	Tetrahydrofuran
GC-MS	Gas chromatography mass spectrometry	TM	Transmetallation
h	Hour(s)	TMEDA	Tetramethylethylenediamine
HFC	Hyperfine interaction	TMS	Trimethylsilyl
HOMO	Highest occupied molecular orbital	UV / Vis	Ultraviolet / visible spectroscopy
^{i}Pr	*Iso*-propyl	XANES	X-ray absorption near edge structure
IR	Infrared spectroscopy	XAS	X-ray absorption spectroscopy
k	Rate constant	ΔG	Gibbs free energy
L	Ligand	ΔS	Entropy
LUMO	Lowest unoccupied molecular orbital	ΔV	Molar volume of activation

Contents

Chapter 1 *Introduction*

1.1 Cross-coupling reactions

Transition-metal catalysis has developed into a near indispensable tool for the modern synthetic chemist, whether in an industrial or academic setting. Whilst heterogeneously catalysed reactions benefit from more facile catalyst separation and recyclability, the well-defined nature of molecular homogeneous catalysts allows for exquisite catalyst design to be carried out, due to the ease with which the steric and electronic properties of the catalyst can be altered. It is therefore not surprising that there exists an almost innumerable quantity of publications and patents based upon homogeneously-catalysed systems, from well-established industrial processes such as the oxidation of hydrocarbons and the hydroformylation of alkenes (processes carried out on the mega-tonne scale)[1] to the development of intricate catalytic molecular motors.[2] One of the most-ubiquitous classes of transition-metal catalysed processes is that of cross-coupling reactions, whereby an organic electrophile is coupled with an organometallic nucleophile (Figure 1.1, *i*). Since their initial discovery, the scope and functional group tolerance of these reactions have expanded to cover almost all classes of organic substrate, and as such, the catalytic formation of C-O, C-N and C-S bonds (amongst others) is now possible.[3] However, most commonly, cross-coupling reactions are used for the formation of new carbon-carbon bonds (Figure 1.1, *ii*).

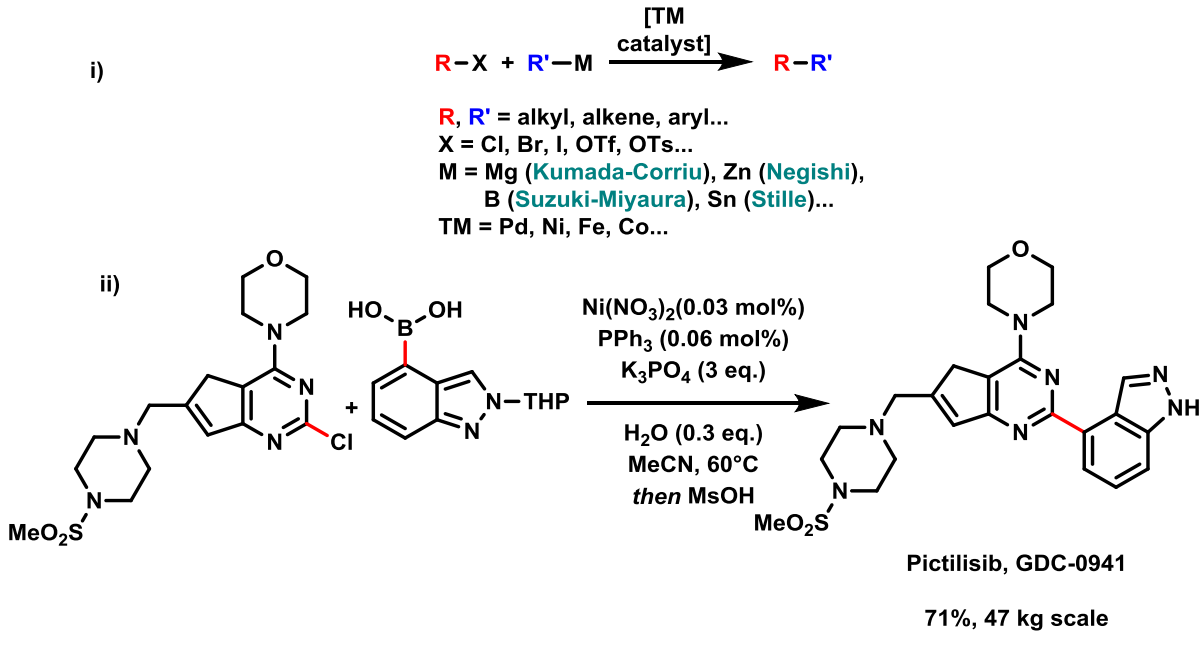

Figure 1.1: *i*: General representation of a transition metal catalysed cross-coupling reaction to form a new carbon-carbon bond. *ii*: A nickel catalysed Suzuki cross-coupling reaction (using a boron nucleophile), developed by Genentech for the synthesis of pictilisib, a potential anti-cancer agent.[4, 5]

1.2 Palladium-catalysed cross-coupling reactions

Currently, most cross-coupling reactions are carried out using palladium catalysts,[6] due to the broad substrate scope they tolerate, in addition to their well-studied mechanisms. Together, this allows for the benefits associated with homogeneous catalysis to be realised, resulting in good control of selectivity and excellent yields, with catalyst loadings below 0.001 mol% possible.[7] Once optimised, the efficacy of palladium-catalysed cross-coupling reactions can allow significant time and money savings to be made within an industrial setting. For example, in the synthesis of ledipasvir, one of two active ingredients in the anti-hepatitis-C drug Harvoni (Gilead), a one-pot borylation / Suzuki-Miyaura step is carried out using the same palladium catalyst, allowing for two transformations to be carried out with only one purification (Figure 1.2).[8]

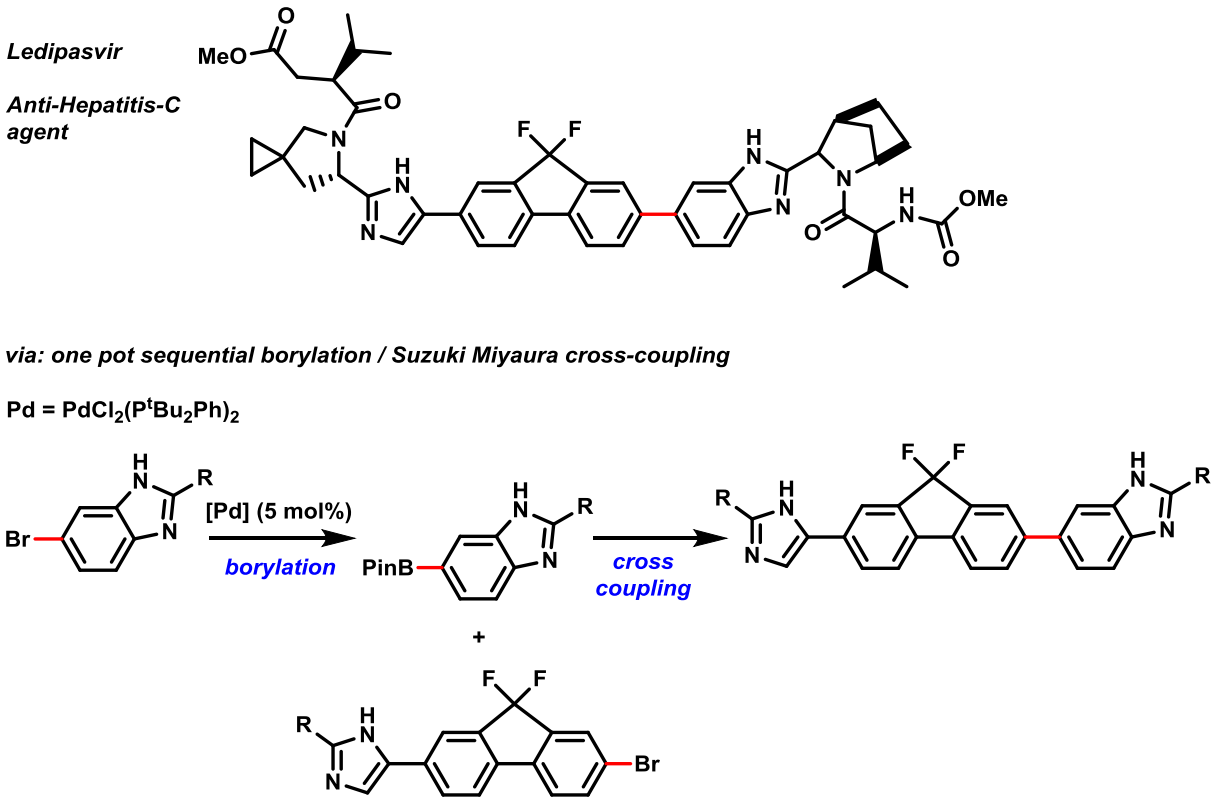

Figure 1.2: A sequential borylation / Suzuki-Miyaura cross-coupling, allowing for the synthesis of an intermediate in the production of Ledipasvir, one component of the commercial drug Harvoni.

Despite earlier reports of iron,[9] cobalt[9] and nickel[10, 11] catalysed cross-couplings, the superior performance of the corresponding palladium-catalysed systems meant that its use as the metal of choice for these reactions surpassed those of the other metals. Due to their now-widespread use and importance to industry, much time has been spent understanding palladium

catalysed cross-couplings, allowing for ever-more refined processes to be developed. Therefore, a significant body of literature regarding the mechanisms by which these processes operate has been developed since their initial discovery in the 1970s.[12–15] As generalised in Figure 1.3, the mechanism of these reactions is understood to occur *via* the sequential oxidative addition of the electrophile to a palladium(0) centre, transmetallation with the organometallic nucleophile and a final reductive elimination from the palladium(II) centre, regenerating the palladium(0) species.

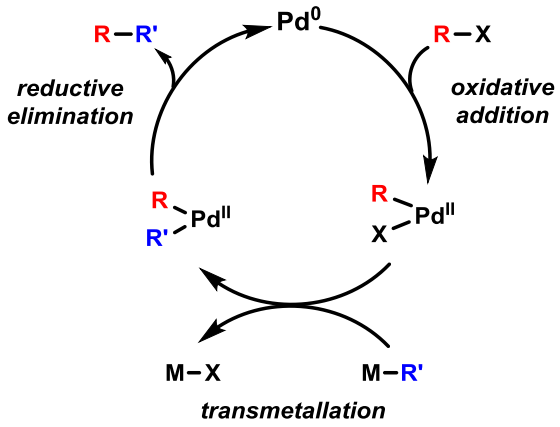

Figure 1.3: General cycle for a palladium-catalysed cross-coupling reaction.

The oxidative addition step to the Pd(0) centre generally occurs through concerted, two-electron pathways; either *via* an S_N2 pathway (in the case of alkyl halides)[16] or a three centred transition state (in the case of aryl halides and sulfonates).[17] The reductive elimination step also occurs *via* a concerted, two-electron pathway, from a cis-coordination geometry.[18] Whilst the transmetallation event remains the somewhat less studied step of the cycle, there exists a growing understanding of how it takes place, depending on the organometallic partner used. [19, 20]

1.2.1 Drawbacks of a palladium based chemical-economy

Despite the significant advances made using palladium catalysed systems, there remain drawbacks associated with its use. These issues do not concern the chemical reactivity of palladium (which currently far out-performs any other metal within the context of cross-coupling reactions), but with its use before and after the reaction has taken place. For the most part, these issues are due to the limited reserves of palladium available within Earth's crust.[21] As a result of this scarcity, the cost of palladium fluctuates, whilst always remaining high (the cost per troy ounce has nearly doubled over the previous 5 years).[22] Whilst the recovery of

palladium from waste streams is a well-established process, the widespread use of palladium in other high-value industries means that there will always be pressure on the market for further extraction.[23] These processes are highly deleterious to the environment; the extraction of 1 kg of palladium has been estimated to have an associated global warming potential of approximately 3880 kg of CO_2, due to issues with terrestrial acidification and freshwater eutrophication.[24] Aside from the issues regarding scarcity, there are tight specifications towards the amount of palladium (10 ppm) allowed within pharmaceutical agents, resulting in further purification steps to ensure its removal from products intended for human consumption.[25]

Whilst these issues do not prevent the use and further development of palladium catalysed reactions (indeed, they may drive the development of ever more efficient procedures), as we move through the 21st century there is a growing consensus that the need for more sustainable processes, from a cost and environmental perspective, is growing. This is reflected by the ongoing replacement of precious metals (which collectively share many of the drawbacks associated with palladium) with more Earth-abundant derivatives in other fields of catalysis.[26]

1.3 The benefits of using iron-catalysts

In contrast to palladium and other precious group metals, iron does not present many of the drawbacks described above. It is highly abundant in Earth's crust,[21] leading to a stable and low price,[27] and its extraction carries a global warming potential three orders of magnitude lower than that of palladium, per kg extracted.[24] Furthermore, iron is currently permitted within pharmaceutical agents to a level of over 1000 ppm.[i] These factors mean that iron has the potential to function as a cheaper and more environmentally sustainable alternative to palladium in cross-coupling reactions.

In addition to these admirable ambitions for more sustainable technologies, towards the ultimate goal of ever more benign chemical transformations, one further advantage is that the chemistry of iron, and other first-row metals, can differ significantly from that of the platinum group. This can lead to novel and interesting reactive pathways, away from those that have traditionally been taught and investigated over the previous decades, with the potential to utilise

[i] This is not to say that iron should be described as 'non-toxic'; the toxicity of a given element has been shown to be strongly dependent upon both oxidation state and coordination environment.[210, 211]

new chemical-space.[28] Selected recent examples demonstrating this novel reactivity are displayed in Figure 1.4. The Lewis-acidic behaviour of an iron(III) catalyst was shown by Schindler to be significantly increased due to the *in situ* formation of a homo-bimetallic iron(III) dimer, with the increased electrophilicity allowing for the development of a carbonyl-olefin metathesis reaction in the absence of an added ligand (Figure 1.4, *i*).[29] Chirik has demonstrated that the oxidative addition to a Co(I) centre operates *via* different pathways, depending upon the electrophile used. In the case of hydrogen, a concerted pathway was observed, resulting in a Co(III) product. However the di-boron reagent B_2Pin_2 underwent a bimetallic oxidative addition, resulting in two-Co(II) centres (Figure 1.4, *ii*).[30] Recently, the first example of a terminal binding fluoroborylene (BF) ligand was reported by Figueroa, who used bulky, anionic ligands to stabilise the resulting iron centre (Figure 1.4, *iii*).[31]

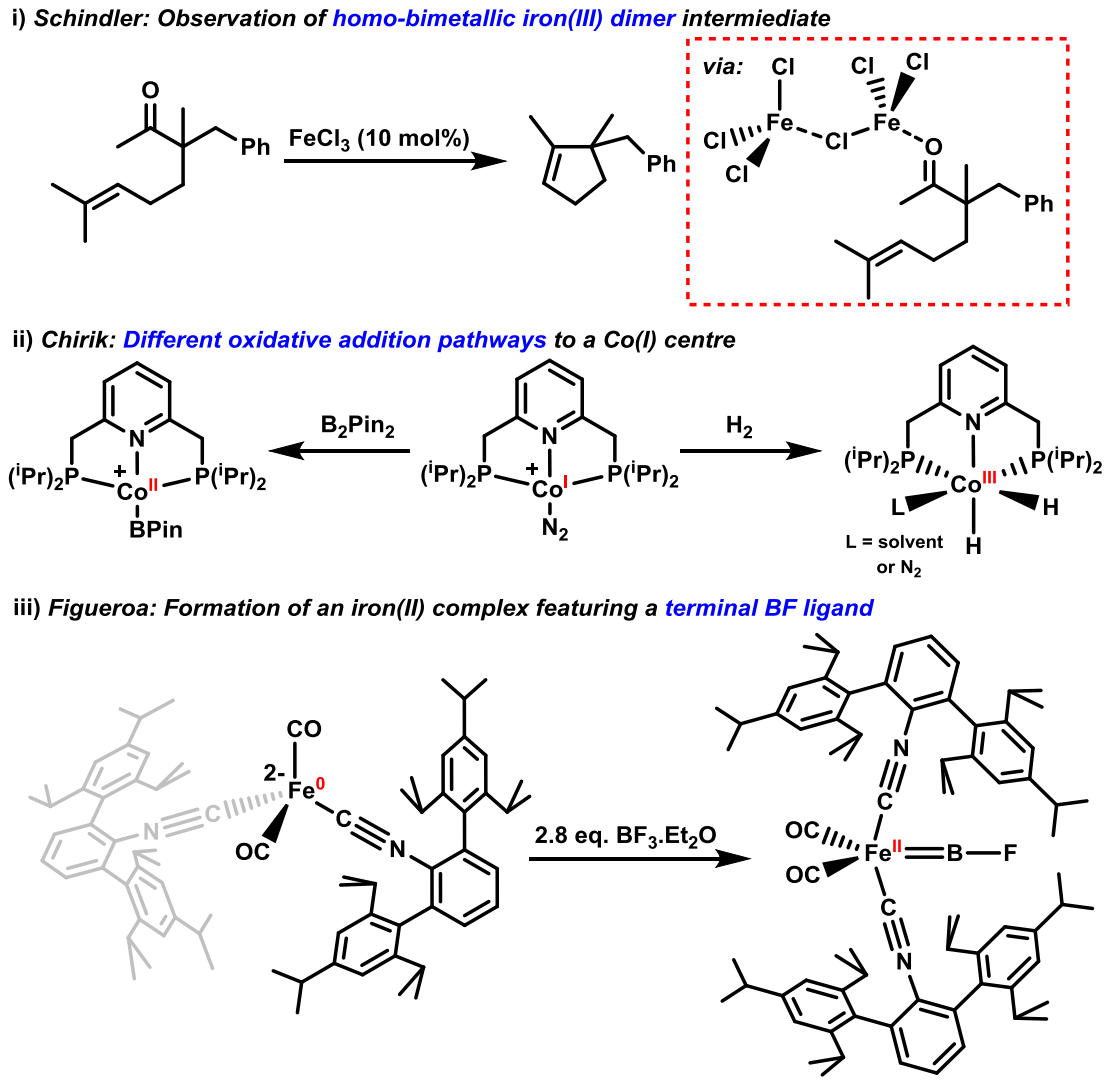

Figure 1.4: Selected examples demonstrating the novel reactivity of first row metals compared to that of palladium and other precious group metals.

1.4 Iron-catalysed cross-coupling reactions

Despite the potential benefits of using iron as a catalyst, and although iron is already well established as the metal of choice in several areas of catalysis (most notably in the heterogeneous Haber-Bosch process),[32] the predominance of palladium catalysed cross-coupling reactions over the latter part of the 20th century resulted in a somewhat under-developed field of iron-catalysed cross-coupling reactions. However, over the last two decades many significant breakthroughs within the field have been achieved, some of which are highlighted below (Figure 1.5).[9, 33–41]

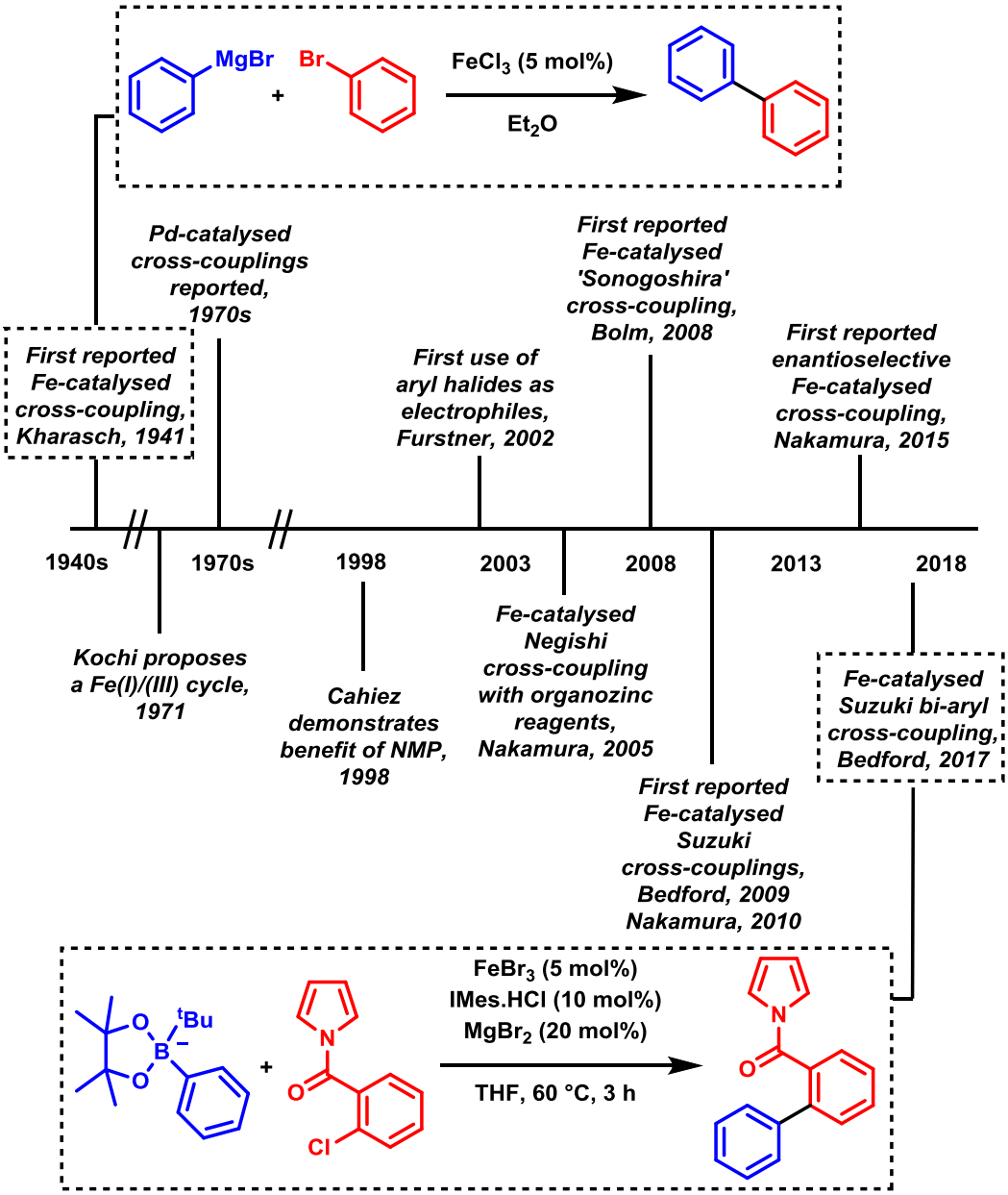

Figure 1.5: A timeline demonstrating notable breakthroughs within the field of iron-catalysed cross-coupling reactions.

1.4.1 Current limitations of iron-catalysed cross-coupling reactions

As shown in Figure 1.5, the synthetic development of iron-catalysed cross-coupling reactions has been impressive. However, there remains a lack of mechanistic understanding as to how these reactions operate. Questions regarding the oxidation state of the iron centre within the reaction, in addition to whether oxidative and reductive processes occur *via* mono- or-bi-nuclear pathways, are among those yet to be conclusively answered (Figure 1.6).

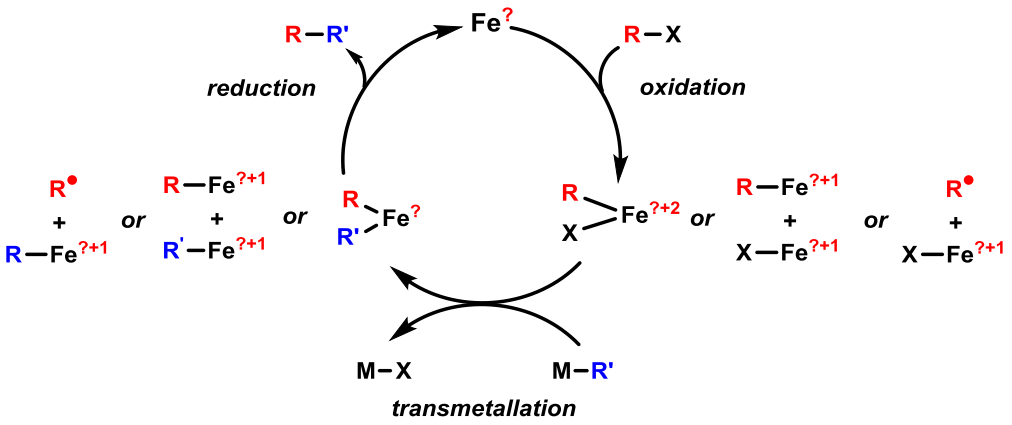

Figure 1.6: Catalytic cycle for an iron-catalysed cross-coupling reaction, highlighting the issues regarding the oxidation state of the iron centre, and its mode of interaction with the electrophilic and nucleophilic components of the reaction.

This is frustrating not only within the direct context of cross-coupling reactions (preventing the development of iron-catalysts able to out-perform existing palladium-catalysed processes) but also more generally, as a thorough mechanistic underpinning of these reactions could then be used to elucidate new iron-catalysed pathways within other areas of chemistry, which other metals are unable to carry out (*cf.* Figure 1.4).

There are reasons for the lack of mechanistic insight into how iron-catalysed cross-couplings take place. The air and thermal sensitivity of many organoiron intermediates makes their isolation difficult, whilst the resulting species are often paramagnetic, meaning that multiple non-routine techniques (for example, Mössbauer, EPR and paramagnetic NMR spectroscopies) are often required in combination for a definitive characterisation of the product. Further, the ability of iron to exist within, and change seamlessly between, numerous oxidation states means that there may be multiple pathways occurring at any given time within a reaction, further complicating the assignment of an intermediate's importance within a cycle.[42] In spite of the difficulties associated with the analysis of iron-catalysed cross-coupling reactions, efforts have been made towards elucidating the mechanisms by which they operate.

These mechanistic proposals can generally be split into those using a ligand (either in the form of a well-defined iron pre-catalyst, or the separate addition of iron salt and ligand into reaction mixtures) and those in the absence of a ligand.[ii]

1.4.2 Proposed mechanisms in ligand-free iron-catalysed cross-couplings

Although iron-catalysed cross-couplings are possible in the absence of an added ligand, it should be noted that to date, only those involving Grignard reagents (a Kumada cross-coupling) have been reported under such conditions. Until recently, many of the mechanistic proposals surrounding ligand-free iron catalysed cross-coupling reactions have been taken directly from one of the earliest reports upon the subject from Kochi in the 1970's, who, following on from Kharasch,[9] found that iron(III) chloride was able to effect an iron-catalysed cross-coupling reaction using Grignard reagents in moderate yields.[33] An EPR analysis of the reaction led to the observation of an S = ½ iron signal, based on which it was proposed that reduction to Fe(I) was taking place, with concomitant formation of ethane (Figure 1.7).

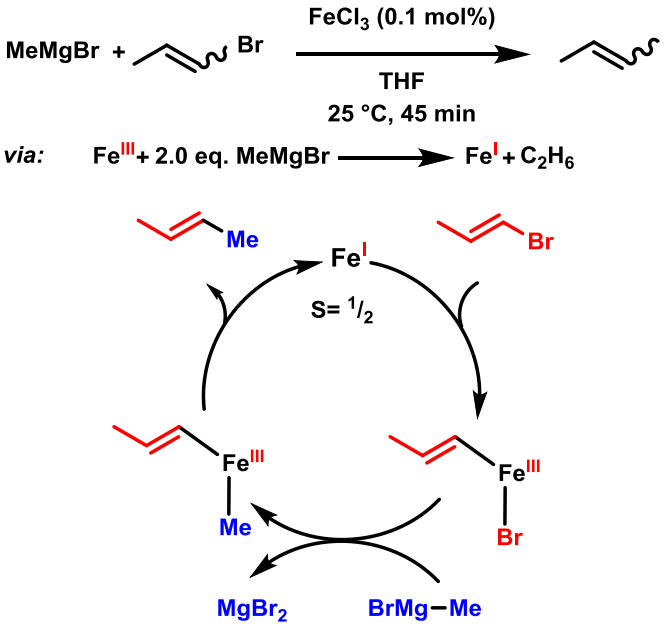

Figure 1.7: Proposed catalytic cycle from Kochi for the iron-catalysed cross-coupling of MeMgBr with haloalkenes, *via* an iron(I)/(III) couple. This elusive S = ½ species was later termed the 'Kochi complex'.

[ii] It is acknowledged that in fact any component of a reaction (including the solvent) can act as a ligand, especially the nucleophile. The term ligand is here applied to a component added to the reaction at a molar loading comparable to that of iron.

Following an oxidative addition of the haloalkene to give an Fe(III) centre, reductive elimination was proposed to occur, yielding the product and regenerating the iron(I) species. The moderate yields resulting from this reaction were addressed in 1998, when Cahiez reported that through the addition of a polar co-solvent (amongst others, NMP), improved selectivity and activity towards the desired product was achievable in ligand-free iron-catalysed cross-coupling reactions.[34] No rationale was provided towards the role played by NMP in the reaction, and in later years its role was vaguely described as that of a co-solvent. However, it should be noted that around this time several groups successfully reported iron-catalysed cross-couplings in the absence of NMP when different Grignard reagents were used,[43] and in some cases found NMP to have a deleterious effect upon the reaction.[44, 45] In what was still a developing field, little new mechanistic information was forthcoming, with a greater focus upon expanding the range of electrophile substrates tolerated within reactions. A computational study from Norrby did demonstrate that oxidative addition to an iron(I) centre, and reductive elimination from an iron(III) centre, were feasible, under the assumption that the mechanism was operating *via* a mononuclear pathway.[46]

An alternative to the Fe(I)/(III) cycle originally proposed by Kochi came from Fürstner and Bogdanovic, who suggested an iron(-II)/(0) couple to be in operation within ligand-free cross-coupling reactions, on the basis that the formation of inorganic Grignard reagents[47] may be occurring (Figure 1.8). [35, 48]

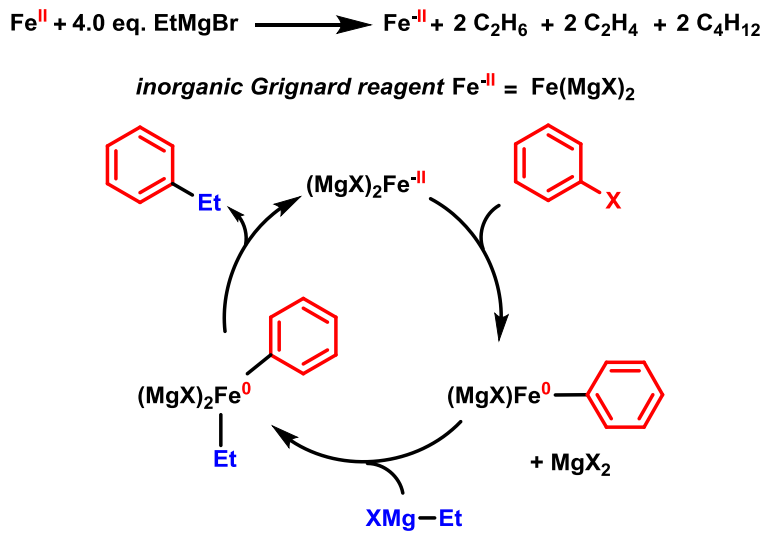

Figure 1.8: Proposed catalytic cycle from Fürstner for the iron-catalysed cross-coupling of alkyl Grignard reagents (possessing β-hydrogens) with aryl halides, *via* an iron(-II)/(0) couple.

This was proposed to occur *via* the reaction of the iron(II) halide with an excess of the Grignard reagent (possessing β-hydrogens), yielding alkene and alkane products in addition to a reduced iron centre. Furthermore, a previously reported iron(-II) complex[49] functioned as an active pre-catalyst within a cross-coupling reaction.[50] Fürstner later reported that this Fe(-II) complex out-performed several other iron pre-catalysts in oxidation states of (0) to (+III) in a representative cross-coupling reaction.[51] However, there are several contentious points regarding the mechanism displayed in Figure 1.8; perhaps most importantly, in the original paper hypothesising their formation, the presence of Mg(0) within the reaction was reasoned to allow for the reduction to iron(-II),[47] which is absent from the cross-coupling reactions reported by Fürstner. Furthermore, when drawing conclusions regarding the activity of iron pre-catalysts in different oxidation states, notable differences within the structures of each, which may have affected the outcome of the investigation, were overlooked; all of the complexes, except that in oxidation state (-II), had a Cp ring bound, which is likely to have provided a substantial stabilising effect to those in higher oxidation states. The high barrier to a reductive elimination step to yield an iron(-II) centre was demonstrated computationally by Norrby to be thermodynamically unfeasible,[46] providing further evidence towards an iron(-II)/(0) cycle as being unlikely. Due to these doubts, and the lack of recent literature supporting an iron(-II)/(0) cycle (and the literature actively disproving it),[52, 53] it is disregarded from the following discussion.

Since Kochi's initial report suggesting an active S = ½ iron centre, efforts were made towards the elucidation of the 'Kochi complex', assumed to be a key intermediate within ligand-free cross-coupling reactions operating within an Fe(I)/(III) cycle.[54] However, when this was achieved recently by Neidig, it was found that the long-sought S = ½ Kochi complex was not an Fe(I) species, rather the organoiron cluster $[Fe_8Me_{12}]^-$, **1**, which possesses a mixed Fe(I)/(II) centre within an overall S = ½ system, as confirmed by a range of physical-inorganic techniques. However, **1** does not function as an active intermediate, representing instead a catalytic resting state that reacts poorly with electrophiles (Figure 1.9, *i*).[55] Interestingly, Neidig was also able to elucidate the role played by NMP towards generating an active catalytic system using methyl Grignard reagents (first realised by Cahiez),[34] which functions to prevent formation of the Kochi complex, with preferential formation instead of a trimethyliron(II) 'ate' complex, $[FeMe_3]^-$, **2**. In the solid state this crystallised as $[FeMe_3]_2[Mg(NMP)_6]$), with coordination of NMP to magnesium rather than iron (Figure 1.9, *ii*).[56]

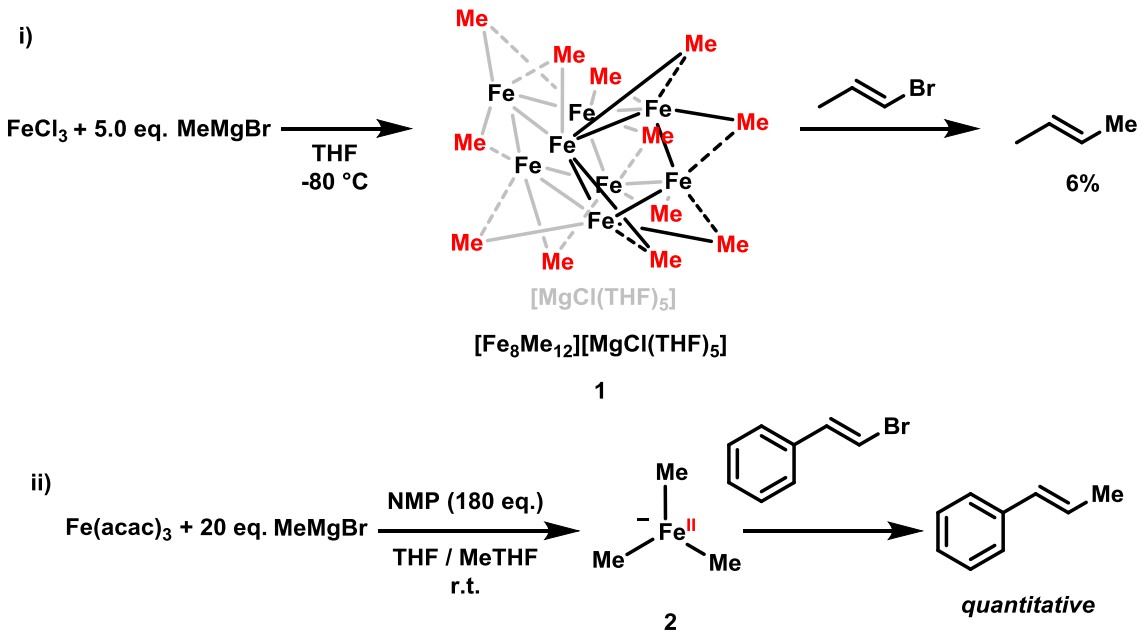

Figure 1.9: *i*) Formation of the S = ½ Kochi complex **1** and its poor reactivity towards an electrophile.[55] *ii*) Elucidation of the role played by NMP towards furnishing an active catalytic system, yielding a trimethyliron(II) 'ate' species **2** which was found to be reactive towards electrophiles to give cross-coupled product.[56]

Taken together, these results suggest that the active reduced iron species within ligand-free cross-coupling reactions are in the form of iron(II) 'ate' complexes, rather than the Fe(I) intermediate originally proposed by Kochi.[33] Importantly, the observation of ferrate species within catalytic mixtures using nucleophiles other than methyl has also been reported, with Bedford demonstrating that the formation of iron(II) 'ate' complexes takes place within catalytically representative mixtures of iron(II) or (III) salts with mesityl and benzyl Grignard reagents.[57]

It would however be remiss to completely rule out the possibility of Fe(I) pathways, as evidence supporting the formation of iron species in oxidation states below that of Fe(II) has been found when less bulky Grignard reagents (benzyl, albeit slowly,[58] phenyl[59] and tolyl[59]) have been used in cross-couplings. This suggests that following the formation of iron(II) or (III) 'ate' complexes a reductive elimination step or disproportionation is possible, if the nucleophile bound to iron is not sufficiently bulky to prevent this process. A serendipitous confirmation of this reactivity was demonstrated by Hu, who isolated a monometallic iron(I) 'ate' complex, **3**, in which η-6 coordination to a biphenyl molecule was observed, suggested to form as a result of a reductive elimination from a higher oxidation state ferrate complex

(Figure 1.10).[60] However the reaction of **3** with an electrophile results in low conversion to cross-coupled product, suggesting that it does not function as an active catalytic species.

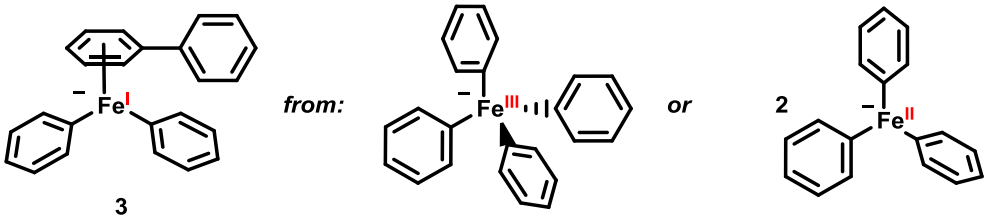

Figure 1.10: Formation of a monometallic iron(I) ferrate complex **3**, reasoned to result following a reductive elimination step from a higher oxidation state iron-ferrate complex.

In summary, it would appear that in the absence of added ligands, the iron speciation within cross-coupling reactions is dependent upon the bulk of the nucleophile used. In the case of mesityl Grignard reagents, the formation of iron(II) 'ate' species is observed, with no further reduction to Fe(I). However, in the case of less bulky nucleophiles a reduction to Fe(I) is possible. While the iron(I) intermediates isolated to date do not display catalytic competency, it is possible that the true iron(I) intermediates (for example, complexes featuring σ-only coordination) remain elusive.[61] In the case of methyl nucleophiles, the beneficial role played by NMP in cross-couplings is due to the resulting preferential formation of iron(II) 'ate' species, preventing the formation of the Kochi complex, **1**. However, the identity of the oxidised iron-intermediates within any of these reactions is yet to be ascertained, meaning that a truly representative cycle remains elusive (Figure 1.11).

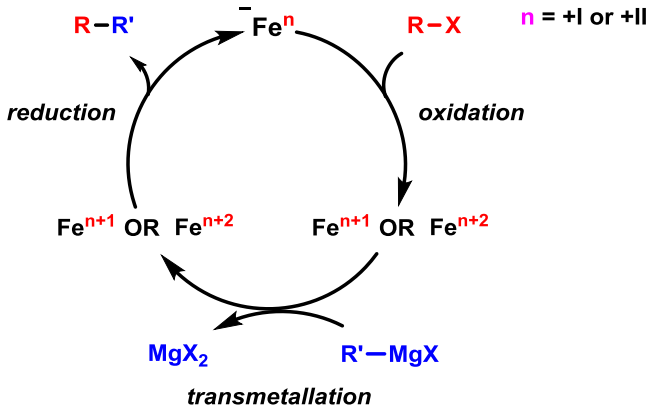

Figure 1.11: Proposed catalytic cycle of a ligand-free iron catalysed cross-coupling, based on the reduced iron species taking the form of either an iron(I) or iron(II) 'ate' species, depending upon the steric bulk of the nucleophile used.

1.4.3 Proposed mechanisms in iron-catalysed cross-couplings with an added ligand

Following on from the work of Cahiez demonstrating the positive role played by a large excess of NMP within some iron-catalysed cross-couplings,[34] it was realised that sub-stoichiometric amounts of ligands could also be used in these reactions to good effect, allowing for nucleophiles other than Grignard reagents to be used as coupling partners. Initially, di-amine ligands such as TMEDA were used,[62] but it has since been realised that the formation of ligand-free ferrate species is likely to occur within their presence, suggesting that their role may lie away from iron within the primary catalytic cycle.[58] Furthermore, over the previous 10 years diphosphine and, to a lesser extent, NHC ligands have superseded diamines as the ligands of choice.

1.4.3.1 Reactions using diphosphine ligands

Most cycles proposed based on iron-diphosphine systems suggest iron(II) as being the lowest oxidation state accessible within catalysis. However, an iron(I) bis-diphosphine intermediate (diphosphine = dpbz), **4**, was isolated and characterised from mixtures representative of an iron-catalysed Negishi cross-coupling by Bedford, leading to the suggestion that reduction to iron(I) is possible within catalysis.[63] Furthermore, an iron(0) mono-diphosphine complex (diphosphine = SciOPP), featuring an η-6 coordinated biphenyl (*cf.* Figure 1.10), **5**, was isolated from mixtures representative of a Suzuki cross-coupling reaction by Neidig (Figure 1.12).[64] Both were suggested to form as a result of a reductive elimination (**4** *via* a bimolecular pathway, from two iron(II) aryl-species, **5** from a single iron(II) species) and functioned as competent pre-catalysts within their respective reactions.

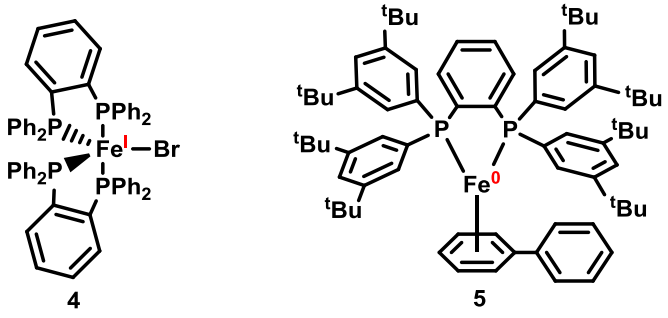

Figure 1.12: Iron-diphosphine complexes **4** and **5**, isolated from catalytically relevant mixtures and shown to function as pre-catalysts within cross-couplings, from Bedford[63] and Neidig.[64]

However, due to the poor performance of **5** compared to a range of iron(II)-diphosphine complexes in a series of stoichiometric reactions, it was proposed to be an off-cycle intermediate, with an iron(II)/(III) cycle proposed for the Suzuki cross-coupling (Figure 1.13).[64]

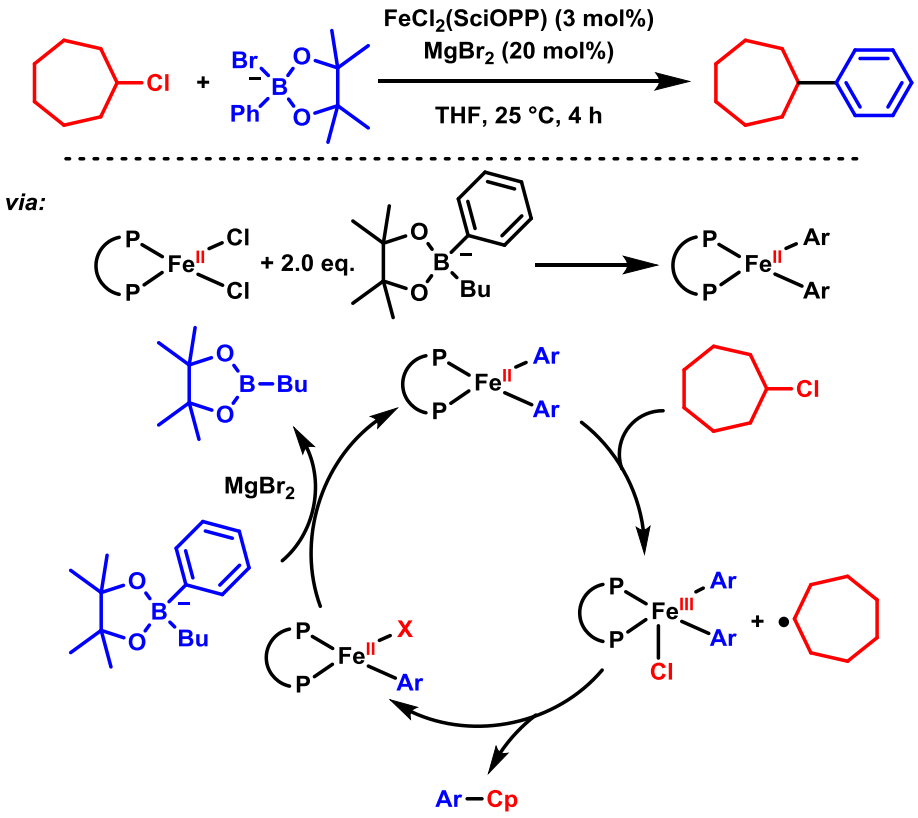

Figure 1.13: Proposed catalytic cycle for an iron-catalysed Suzuki cross-coupling reaction, operating *via* an Fe(II)/(III) couple, from Nakamura[39] and Neidig.[64]

A similar cycle to that displayed in Figure 1.13 was also proposed by Nakamura and Neidig in the case of an iron-catalysed Kumada cross-coupling, using alkynyl Grignard reagents (Figure 1.14).[65, 66] Upon the addition of one equivalent of the Grignard reagent to the pre-catalyst $FeCl_2$(SciOPP), the ferrate species, **6**, was observed, suggestive of rapid ligand scrambling. However, **6** was ascribed as an off-cycle intermediate, the formation of which was detrimental to the generation of cross-coupled product (upon mixing with electrophile no product was observed). Conversely, slow-addition of the Grignard reagent resulted in the observation of the neutral iron(II) species, **7** and **8**, postulated to be the active species within catalysis (both reacted with electrophile to yield cross-coupled product at similar rates). This result is consistent with the initial literature report, in which the slow addition of the Grignard reagent was necessary for good product yields to be observed.[66]

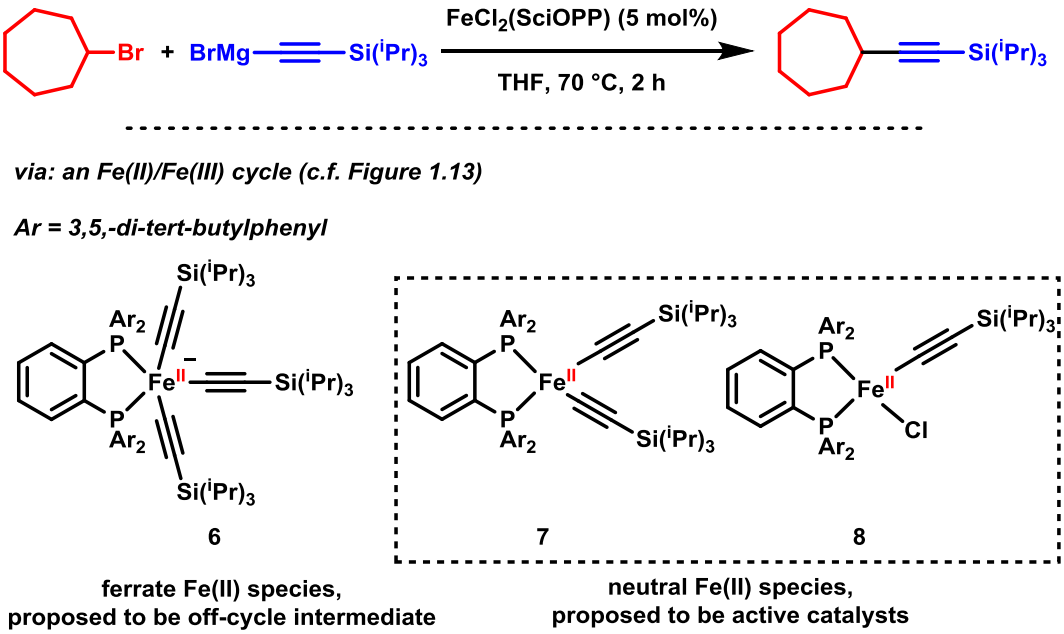

Figure 1.14: Observed iron(II)-diphosphine species from an iron-catalysed Kumada cross-coupling reaction, using alkynyl Grignard reagents.

It is pertinent to consider the steric bulk of the diphosphine ligand used within the reactions discussed above. As demonstrated in Figure 1.12, when the less bulky diphosphine ligand dpbz is used in cross-coupling reactions, a reduction to iron(I) appears feasible, as has been reported in the case of iron-catalysed Suzuki and borylation reactions featuring the same ligand.[67–69] However, the increased bulk present within the diphosphine ligand SciOPP, together with the slow addition of the nucleophile often required within cross-coupling procedures, suggests that iron(II) complexes are often present as the active catalytic species within reactions employing a ligand.

1.4.3.1 Reactions using NHC ligands

Although there are many reports detailing the use of NHC ligands within iron-catalysed cross-couplings,[70–73] there have been only limited insights into the mechanisms they may induce. However, as with diphosphine ligands, it is suggested that their presence within the catalytic manifold serves to prevent reduction of the iron centre below iron(II), although there are a number of well-defined iron(I)-NHC complexes within the literature.[74–76]

A reduction to iron(I), as part of a stepwise iron(I)/(II)/(III) cycle, was proposed by Cárdenas to be occurring within an iron-catalysed Kumada cross-coupling reaction using alkyl Grignard reagents (containing a dioxane functional group), and the ligand IMes.HCl.[72] This was on the basis of an observed S = ½ iron signal, suggested to be due to an iron(I) species,

from an EPR analysis of the reaction. However later work by Neidig (using Mössbauer and EPR spectroscopies) demonstrated that the S = ½ species (which could not be identified) comprised less than 0.5% of total iron-speciation within the reaction.[77] Neidig went on to suggest an iron(II)/(III) cycle, due to the isolation of a dialkyl iron(II)-NHC complex, **9**, which was shown to function as an active pre-catalyst for the reaction, in addition to yielding cross-coupled product in stoichiometric reactions with an electrophile (Figure 1.15). A similar cycle had been proposed earlier by Tonzetich for an iron-catalysed Kumada cross-coupling of aryl Grignard reagents, in combination with NHC ligands.[78]

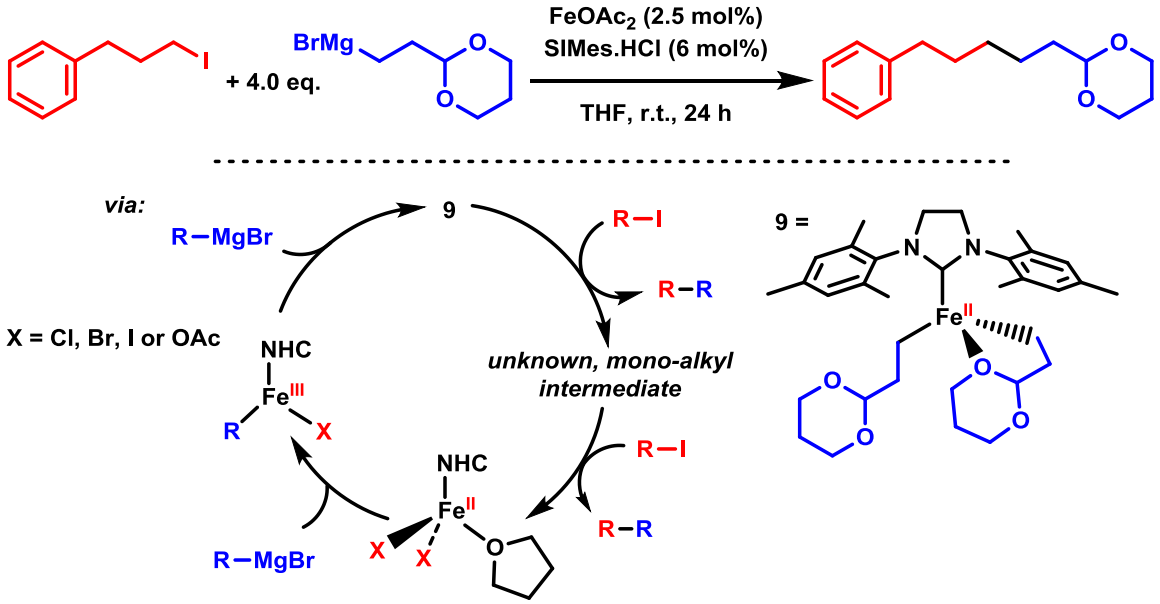

Figure 1.15: Proposed iron(II)/(III) cycle from Neidig, for an iron-catalysed Kumada cross-coupling reaction using an NHC ligand.

It would therefore appear that much like diphosphine ligands, a reduction to iron(I) is possible when NHC ligands are used in catalysis; however whether they function as active catalysts remains unknown (none of the reported iron(I)-NHC complexes are accompanied by a discussion on their reactivity towards electrophiles).

In a series of reports using iron(III) fluoride as a pre-catalyst within Kumada cross-coupling reactions, Nakamura proposed an Fe(II)/(IV) cycle to be operative (Figure 1.16).[73, 79] Following reduction of the iron(III) centre (in the presence of SIPr) to give a difluoroiron(II)-NHC intermediate, **10**, transmetallation with the Grignard reagent was suggested to yield the organoferrate species **11**. Subsequent coordination of the electrophile to the tethered, cationic magnesium centre, followed by a two-electron oxidative addition was proposed to yield an iron(IV) centre, reductive elimination from which generated the cross-coupled product.

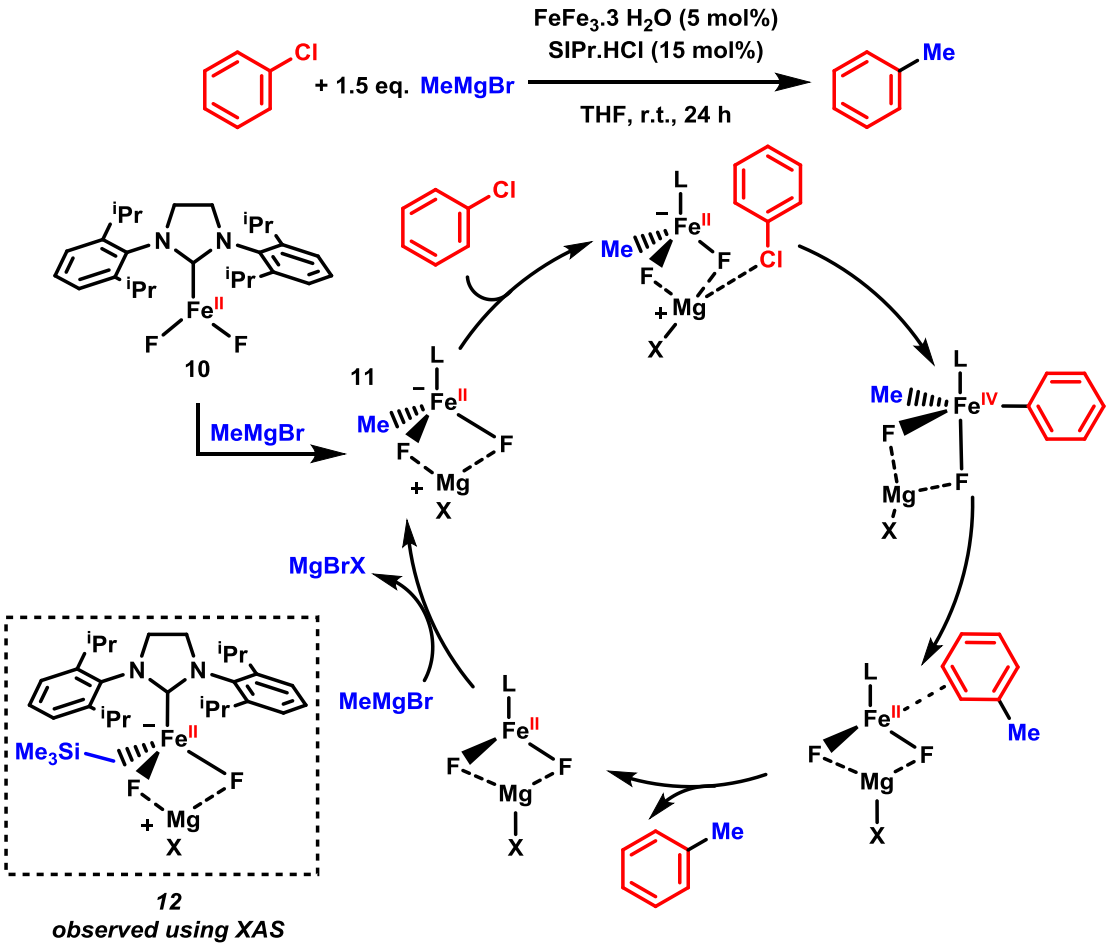

Figure 1.16: Proposed iron(II)/(IV) cycle from Nakamura, for an iron-catalysed Kumada cross-coupling reaction using an NHC ligand. L = SIPr.

Due to the instability of iron-aryl complexes, a series of stoichiometric reactions were carried out using a bulkier, silylated Grignard reagent. Using XAS, a silylated derivative of **11**, **12**, was found to provide a good fit with the experimental data from the reaction of iron(III) fluoride, SIPr and the silylated Grignard reagent. Upon reaction with electrophile, **12** was shown to selectively form cross-coupled product. The proposed mechanism was also supported by DFT calculations, which suggested a strong fluoride effect to be present within the reaction, as highlighted by the lack of reactivity when no source of fluoride was added to the reaction (pre-mixing of iron(III) chloride with KF restored activity). Using the same conditions, Nakamura has also suggested a similar mechanism, based on an iron(II)/(IV) cycle, to be operative when aryl Grignard reagents are used for cross-couplings in the presence of an NHC ligand.[80] Taken together, these results suggest that in combination with the fluoride ligand (which is less easily displaced from the iron centre than a chloride or bromide ligand),[80] the iron-NHC complexes formed *in situ* are prevented from reducing to oxidation states below

iron(II). However, whilst the use of iron fluoride as a pre-catalyst is able to furnish highly active systems, the mechanistic insights into reactions in which it is present cannot be applied more generally to iron-catalysed cross-couplings, due to the non-innocence of the fluoride ligand compared to that of other halides / pseudo-halides.[iii]

In conclusion, the use of ligands within cross-coupling reactions appears to stabilise the iron-centre to which they are bound with respect to reductive pathways. Whilst well-defined iron-complexes, bearing either a diphosphine or NHC ligand, in oxidation states 0 and I have been isolated, and in some cases observed within catalytic reactions, it would appear that most generally, reduction below iron(II) is not widely observed within most reports involving ligands. This is especially the case when the bulky diphosphine ligand SciOPP is used. There remains little understanding regarding the active oxidised iron-species within cross-couplings, in the presence or absence of a ligand, with suggestions of both iron(III) and iron(IV) intermediates.

As was the case with palladium-catalysed cross-couplings (from which bulky, mono-dentate phosphines and phosphites emerged as superior ligand classes), there is significant scope for improved reaction efficiency through ligand design. This has started to be applied to iron-catalysed cross-couplings, with reports offering explanations into the dramatic changes in reaction yields observed with a slight change in the NHC or diphosphine ligand used.[81–84]

1.5 Current mechanistic perspective

Summarising the above discussion, it can be said that whilst there is now a not-insignificant body of literature discussing the mechanisms by which iron-catalysed cross-couplings operate, there remain gaps within this understanding. This is perhaps best demonstrated by the discussion available regarding the active oxidation state within these reactions: in contrast to the reductive pathways that may be operative, which have been the focus of several highly detailed kinetic and physical-inorganic investigations,[42, 61] little is known upon the oxidative pathways that may be taking place. If the benefits of iron-catalysed reactions are to be fully realised and applied within a general context, then the oxidative manifold within them (*i.e*. the interaction of the iron centre with the electrophilic component

[iii] Nakamura has also noted that reactions using an iron(III) fluoride pre-catalyst remain dark brown, whilst those using iron(III) chloride, bromide or iodide rapidly turn black, suggestive of different catalytic pathways being operative.

of the reaction) must be addressed. Whilst challenging, the success in this regard within other iron-catalysed processes (perhaps most notably, high valent iron-systems are a feature of bio-inorganic chemistry)[85] suggests that this is attainable.

Chapter 2 *On the intermediacy of heteroleptic species in the iron-catalysed Kumada cross-coupling*

2.1 Introduction

2.1.1 Homoleptic species relevant to iron-catalysed Kumada cross-coupling reactions

Due to the often-increased stability and improved reactivity observed, ligands (such as diphosphines and NHCs) are used in many iron-catalysed cross-coupling reactions. However these reactions are also possible in the absence of added ligands, dating back to the earliest reports from Kharasch,[9] and later Kochi,[33] who reported the coupling of methylmagnesium bromide with alkenyl bromides (Figure 2.1, *i*). In these ligand-free reactions, the active iron intermediates observed are often homoleptic, resulting from the reaction between a metal salt and the nucleophilic component of the reaction; in the case of Kumada cross-coupling reactions, this takes the form of a Grignard reagent. The high sensitivity towards air, moisture and temperature of such complexes makes their isolation and characterisation difficult. This is highlighted by the isolation only very recently of an intermediate first reported by Kochi in the 1970s,[33] the so-termed Kochi complex, $[Fe_8Me_{12}]^-$, **1**, by Neidig (Figure 2.1, *ii*).[55]

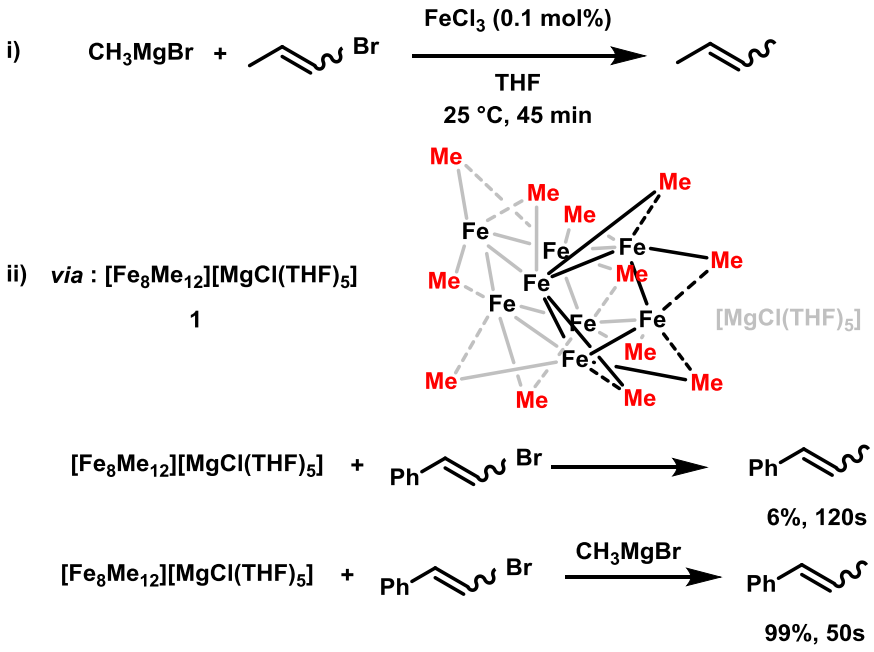

Figure 2.1 An early report of a ligand-free iron catalysed cross-coupling reaction from Kochi, which was shown by Neidig to go *via* the iron cluster species **1**.

However, perhaps surprisingly due to its extreme sensitivity, the iron-methyl cluster compound **1** was shown not to be catalytically competent and does not react with an electrophile at a rate representative of the catalytic reaction. The formation of multinuclear iron species was also observed by Neidig in the reaction between iron salts and phenylmagnesium

bromide, yielding $[FePh_2(\mu\text{-}Ph)]_2^{2-}$, **13**. However as with the Kochi complex, **13** was found to be unreactive towards electrophiles. In this case the authors were able to isolate the more reduced, tetra-iron species $Fe_4(\mu\text{-}Ph)_6(THF)_4$, **14**, which did undergo reaction with an electrophile at a rate representative of the catalytic reaction (Figure 2.2).[59]

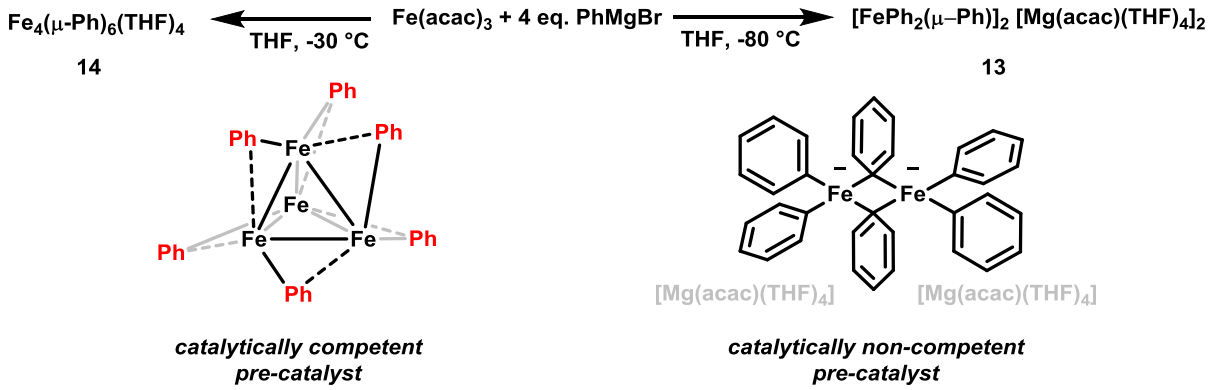

Figure 2.2: Synthesis of the multinuclear iron-phenyl species **13** and **14**.

Aside from the complexes **1**, **13** and **14**, the majority of isolated homoleptic complexes with relevance to iron catalysed cross-couplings are mono-nuclear species. As with the multinuclear complexes discussed, the organometallic reagents used generally do not possess hydrogen atoms capable of undergoing β-hydride elimination, due to the kinetic lability of metal-alkyl bonds, particularly so with iron(II) and iron(III) complexes.[86] Additionally, steric bulk is often incorporated into the organometallic nucleophile, so as to retard the rate of reductive elimination, with selected examples represented by **15**, **16** and **17** (Figure 2.3).[87–89] An exception to this is provided by Fürstner,[53] who reported the remarkable iron(IV) complex, $FeCy_4$, **18** which is possible through stabilisation by both electronic and steric factors.

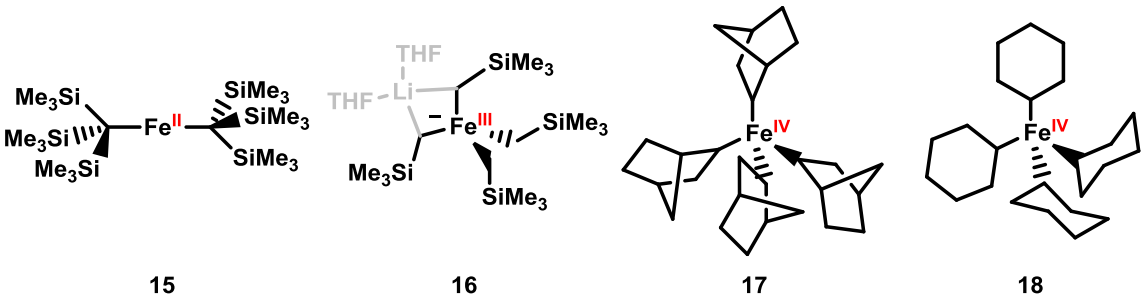

Figure 2.3 Examples of structurally characterised homoleptic iron complexes **15 - 18**, in oxidation states II, III and IV:.[53,87–89]

The respective reactivities of the complexes displayed in Figure 2.3 are either not discussed,[88, 89] or are poor.[87, 53] However, discussions regarding homoleptic iron complexes

bearing benzyl,[58] mesityl[58, 90] and naphthyl ligands are more readily available. In the case of homoleptic iron-mesityl complexes, and reactions using mesityl nucleophiles in general,[62] little or no catalytic reactivity is observed after extended reaction times,[58] due to the kinetic protection afforded by the *ortho*-methyl groups resulting in slow rates of reaction. However the less bulky and more generally representative benzyl nucleophile affords reaction mixtures that display catalytic competency on more relevant timescales when mixed with iron halide precursors (Figure 2.3, *i*).[91, 92] Homoleptic iron-benzyl ferrate complexes have been shown to form preferentially over the corresponding iron-amine complexes,[57] and have been isolated in oxidation states II, **19**, and III, **20**, from mixtures representative of catalytic conditions (Figure 2.4, *ii*).[92]

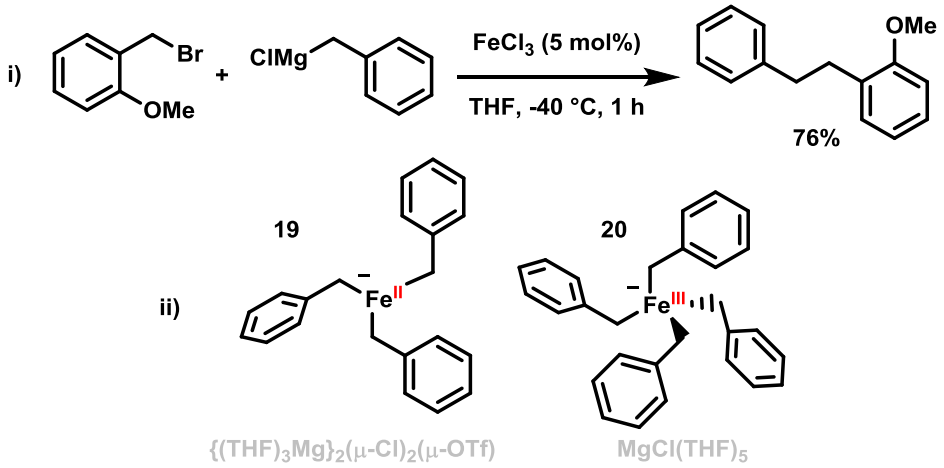

Figure 2.4: *i*: Iron catalysed Kumada cross-coupling reaction using benzyl nucleophiles and electrophiles. *ii*) Iron-benzyl ferrate intermediates **19** and **20**, isolated from mixtures of iron halides with benzyl Grignard reagents.

2.1.2 Iron-naphthyl complexes as systems for model heteroleptic reactivity

Whilst homoleptic iron species in a range of oxidation states are readily accessible and can often be observed or isolated from catalytically relevant mixtures of reagents, it is remiss to assume that they constitute the active catalytic species within reaction mixtures. This is demonstrated by reactions concerned with the cross-coupling of naphthyl Grignard reagents with alkyl halides. A four coordinate, homoleptic iron(II)-naphthyl complex**,** **21**, has been known in the literature for over 30 years.[93] However more recent preliminary work from within the Bedford group has demonstrated that in addition to the three coordinate homoleptic ferrate complex **22**, the heteroleptic complexes **23** and **24**, bearing both naphthyl and bromide ligands,

can also be accessed (Figure 2.5, *i*). Interestingly, it was found that the heteroleptic complexes reacted faster with electrophiles in model reaction studies (Figure 2.5, *ii*).

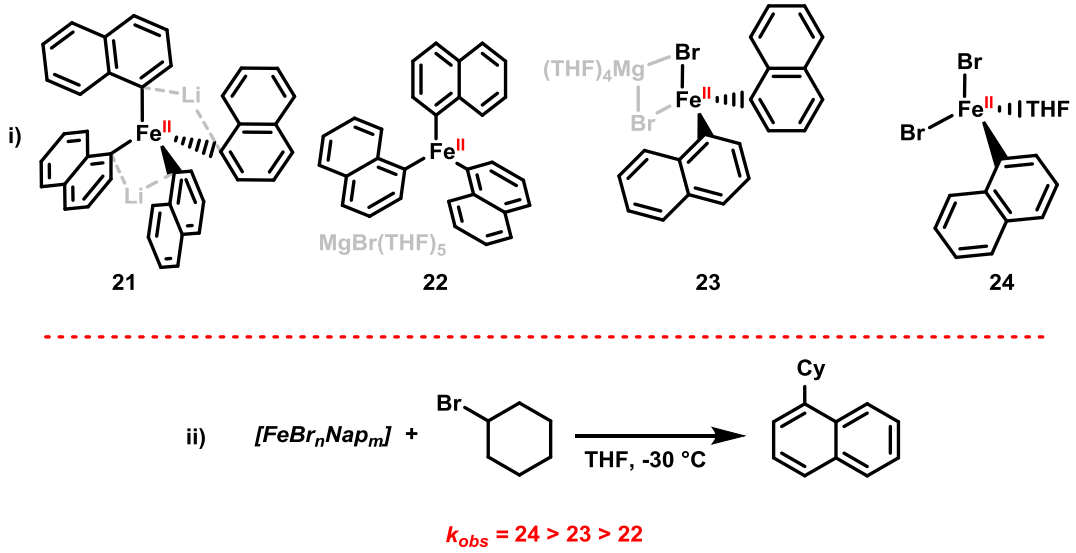

Figure 2.5: *i*: Previously reported homoleptic (**21**)[93] and unreported homo- and heteroleptic iron-naphthyl complexes (**22 – 24**). *ii*) The comparative model reactivity of homo- and heteroleptic iron-naphthyl complexes with a representative electrophile.

Due the extreme thermal sensitivity of the complexes displayed in Figure 2.5, the model reactions were carried out at a temperature of -30 °C, using only stoichiometric loadings of each complex with respect to electrophile, and in the absence of added Grignard reagent. However, the observed reactivity suggests that, whilst homoleptic iron complexes are more straightforward to synthesise and have previously been observed during catalytic turnover,[58] the active iron species within such reactions may be heteroleptic, incorporating both halide and carbon-based ligands, such as those displayed in Figure 2.5 *i*.

Whilst heteroleptic ligand-free species are commonly proposed as intermediates within mechanistic cycles,[57] they are often considered as intermediate species to be transmetallated to the active, homoleptic species, from which carbon-carbon bond formation occurs (Figure 2.6).[92] Further, whilst there is little direct evidence for them forming from *in situ* reaction mixtures, this is most likely due to the vast majority of mechanistic studies within the field of ligand-free iron-catalysed cross-coupling reactions focussing on reactions between iron salts and organometallic nucleophiles in the absence of electrophiles.[56,60,94]

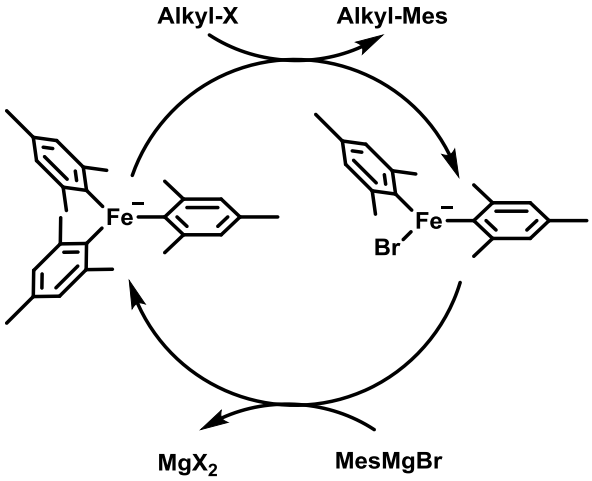

Figure 2.6: A simplified version of a previously proposed catalytic cycle regarding the role of homo- and heteroleptic iron complexes within cross-coupling reactions.[57]

It is therefore not surprising that a lack of such intermediates have been reported and characterised. However, if heteroleptic iron-species were to be present even in small amounts (with respect to the amount of homoleptic iron-species present at the same time) the Curtin-Hammett principle[95] dictates that such species could be the active catalytic component of the reaction.[61] Kinetic investigations have previously been used to comment on the mechanism of iron-catalysed cross-coupling reactions,[96, 97] and compared to the isolation and characterisation of organometallic complexes, can provide information more relevant to the reaction as a whole,[98] rather than the reactivity of a complex in isolation.

2.1.3 General considerations

In an attempt to provide information on the role played by heteroleptic iron-intermediates within cross-coupling reactions, a more robust system than the iron-naphthyl one discussed in Section 2.1.2 was chosen, allowing for mechanistic insights on the reaction manifold to be obtained through a kinetic investigation. Accordingly, the work in this chapter details a kinetic investigation into an iron-catalysed Kumada cross-coupling reaction of benzyl Grignard reagents with benzyl electrophiles.

2.2 Model reaction

Preliminary results on the comparative reactivity of a range of iron naphthyl / halide complexes of general formula $[FeBr_n(Nap)_m]^-$ (where $0 \leq n$, m 3) with an alkyl halide suggest that the presence of a halide on the iron centre increases the rate of cross-coupled product formation. In order to elucidate further the role that such heteroleptic intermediates may have within iron-catalysed cross-couplings in general, a more robust model was sought. To this end, the cross-coupling of benzyl Grignard reagents with alkyl electrophiles presents a feasible solution. Iron-benzyl species have been isolated and characterised previously,[58] and their reactivity towards benzyl electrophiles is known.[91, 92] So as to minimise potential bias in any intermediates or transition states that form during the course of a reaction, the chosen model system is the coupling of two benzyl derivatives, each substituted in the *para*- position by substituents that are essentially sterically and electronically similar, whilst being chemically different, and therefore spectroscopically distinguishable. Accordingly, methyl and ethyl groups were chosen as the substituents, due to the small steric difference between the two, and the same Hammett values being reported for each.[99] To ensure complete conversion of the electrophile starting material, 1.5 equivalents of the Grignard reagent with respect to electrophile were used in the standard reaction.

2.2.1 Comparison of catalysed and non-catalysed reaction

Before proceeding further, it must first be acknowledged that in the absence of a catalyst, reactions between a benzyl halide and a benzyl Grignard reagent (in this case 4-ethylbenzyl chloride, **25**, and 4-methylbenzyl magnesium chloride, **26**, respectively) proceed at ambient temperature to quantitatively yield the desired product (in this case, 1-ethyl-4-(4-methylphenethyl)benzene, **27**), *via* a nucleophilic substitution mechanism (Figure 2.7). A full kinetic profile of this reaction is displayed in Chapter 7.

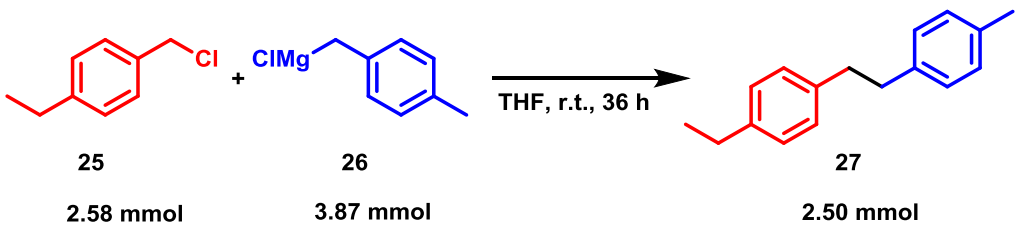

Figure 2.7: Non-catalysed reaction of a benzyl Grignard reagent with a benzyl halide.

The reaction proceeds slowly at room temperature with a pale-yellow colour and no side product formation. However, upon the introduction of a catalytic loading of an iron salt pre-

catalyst to the reaction, a deep red solution is observed, and a much-increased rate of reaction is recorded, in addition to a loss of selectivity. A distribution of products is obtained, in which the formation of homo-coupled electrophile, **28**, homo-coupled Grignard reagent, **29**, and hydro-dehalogenated electrophile, **30**, occurs, in addition to **27** (Table 2.1). The profile of the catalysed reaction over time is displayed in Figure 2.8. For the purpose of clarity, hydro-dehalogenated products are omitted from all concentration time plots and will not be discussed in the context of catalytic turnover (it is also possible that they will be formed as a result of the quench employed when sampling).

Table 2.1: Iron-catalysed Kumada cross-coupling of a benzyl halide with a benzyl Grignard reagent, to give a distribution of products.

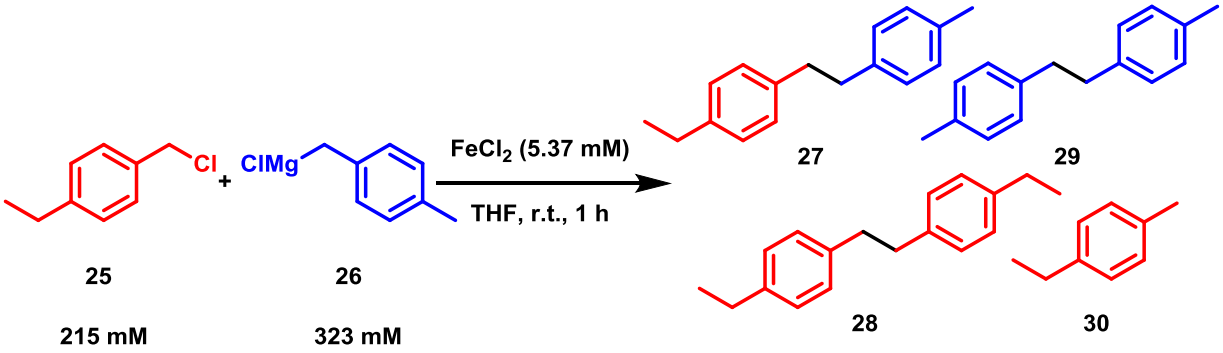

Entry	**27** (mmol)	**28** (mmol)	**29** (mmol)
1[a]	1.21	0.38	0.80
2[b]	1.19	0.41	0.78
3[c]	1.25	0.36	0.80
4[d]	1.22	0.37	0.74

Conditions: *a*: **25** (2.58 mmol), **26** (3.87 mmol), $FeCl_2$ (0.064 mmol), THF, room temperature, 1 h; *b*: as for conditions *a* but **26** added over the course of 2 h; *c*: as for conditions *a* but **25** added over the course of 2 h; *d*: as for conditions *a* but carried out at -40 °C over the course of 72 h.

As demonstrated in Figure 2.8, the increased rate of reaction observed upon the addition of a catalyst renders the catalyst-free pathway insignificant (after 1 hour, the non-catalysed reaction undergoes approximately 10% conversion to **27**, Figure 2.8, ▲), meaning that any observed reactivity is due to catalytic processes.

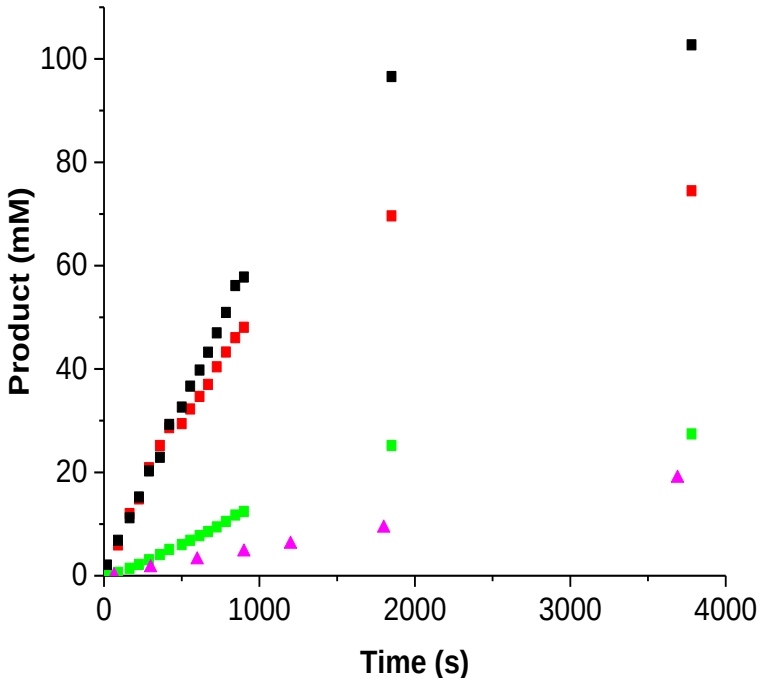

Figure 2.8: Reaction profile for the iron-catalysed cross-coupling reaction displayed in Table 2.1. ■ = **27**, ■ = **28**, ■ = **29**, ▲ = **27** in the absence of catalyst.

Upon the completion of the reaction (as measured by product formation), the major product formed is **27**, corresponding to approximately 50% of the electrophile starting material. The remaining electrophile mass balance is composed of **28** and **30**. The amount of Grignard reagent remaining at any point in the reaction cannot be commented on due to the method of analysis being *via* GC (for which a quench is necessary, destroying organometallic compounds); however, the mass balance for the nucleophilic and electrophilic components at the end of the reaction is good. The yields of iron-catalysed cross-couplings have been improved previously through the use of low temperatures and the slow addition of reagents,[100] however, changing these variable had no effect upon the distribution of products observed (Table 2.1, entries 2 – 4).

2.2.2 Product inhibition experiment

One of the biggest problems affecting catalytic systems as reactions progress is a loss of catalyst selectivity / catalyst deactivation, due to the formation of reaction products (or side-products) that provide competing reaction pathways, through competitive-binding to the catalyst centre. Termed product inhibition, this can lead to enzyme deactivation within biological systems[101] and reduce the activity of molecular homogeneous catalysts.[102] Whilst this is unlikely to be happening for the bi-benzyl products of the reaction between **25** and **26**,

it is possible that the magnesium chloride formed following any transmetallation process may coordinate to the iron centre,[103] affecting catalyst activity and causing the poor selectivity observed. In order to investigate whether catalyst deactivation may be occurring as a result of the formation of magnesium salts, a product inhibition experiment was performed, in which a known amount (55 mol%) of $MgCl_2$ was added before initiation of the reaction (Figure 2.9).

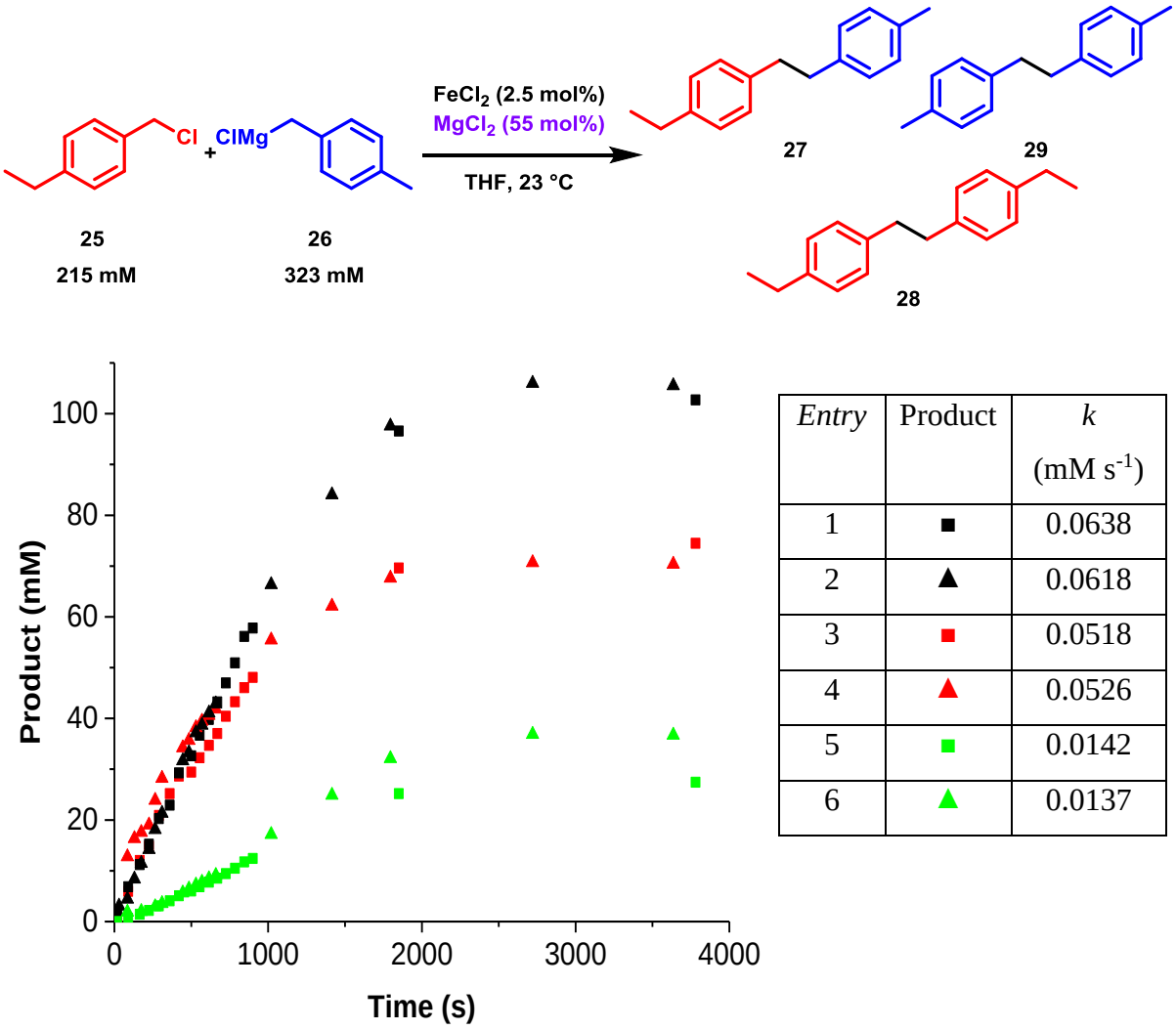

Entry	Product	*k* (mM s^{-1})
1	■	0.0638
2	▲	0.0618
3	■	0.0518
4	▲	0.0526
5	■	0.0142
6	▲	0.0137

Figure 2.9: Top: Product inhibition experiment performed through the addition of a known amount of $MgCl_2$ before the start of the reaction between **25** and **26**, using a $FeCl_2$ pre-catalyst. Bottom: Concentration-time plots and the corresponding initial rate of each reaction, resulting from the product inhibition experiment. ■ = 0 mol% $MgCl_2$, ▲ = 55 mol% $MgCl_2$; Black = **27**, green = **28**. red = **29.**

If catalyst deactivation, as a result of product inhibition, were to be taking place, an overlay of the resulting concentration-time plot with the standard reaction would result in a poor fit of the two data sets. However, as displayed in Figure 2.9 the resulting plots overlap well with one another, suggesting that catalyst deactivation processes are not occurring due to the formation of magnesium chloride during the course of the reaction, and that the lack of

selectivity observed is not due to the presence of magnesium salts. This is perhaps surprising, as magnesium salts have been postulated to play a prominent role in other iron-catalysed cross-coupling reactions.[41]

2.2.3 Isolation and characterisation of homoleptic iron-benzyl complexes

As discussed in section 2.1, homoleptic iron-benzyl complexes have been previously isolated from mixtures of iron salts and benzyl Grignard reagents.[58] Accordingly, following the addition of Grignard reagent, **26**, to iron(II) chloride in THF, ^{1}H NMR analysis of the resulting deep red solution indicates the formation of the homoleptic iron(II) 'ate' complex, [Fe(4-MeBn)$_3$]$^-$, **31**. Each of the resulting proton environments are visible in the corresponding ^{1}H NMR spectrum, with the characteristic peaks most notably defined by the benzylic signal, shifted to δ 945.4 ppm (Figure 2.10).

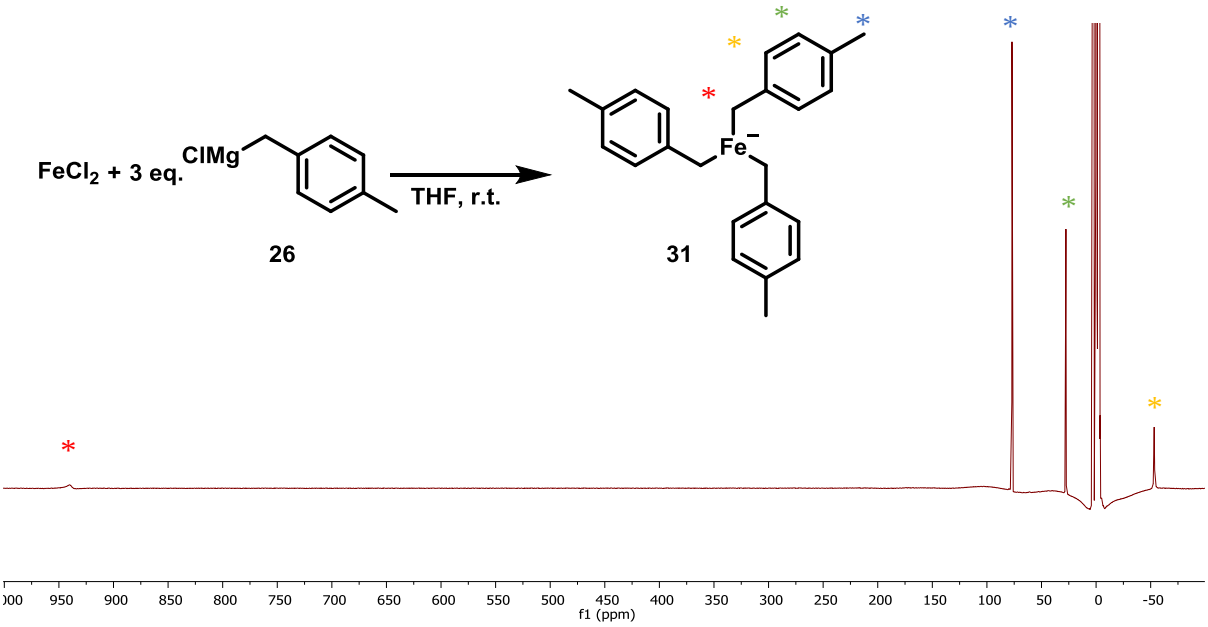

Figure 2.10: Reaction of $FeCl_2$ with **26** to give the homoleptic, iron(II) ferrate complex **31** and the resulting paramagnetic ^{1}H NMR spectrum, from -100 to 1000 ppm.

A sample of **31** suitable for X-ray diffraction was prepared by storing the THF solution resulting from a mixture of $FeCl_2$ with **26**, as per Figure 2.10, at -30 °C for 48 h, yielding dark-red air-sensitive crystals, analysis of which confirmed the structure to be [**31**][MgCl(THF)$_5$] (Figure 2.11).

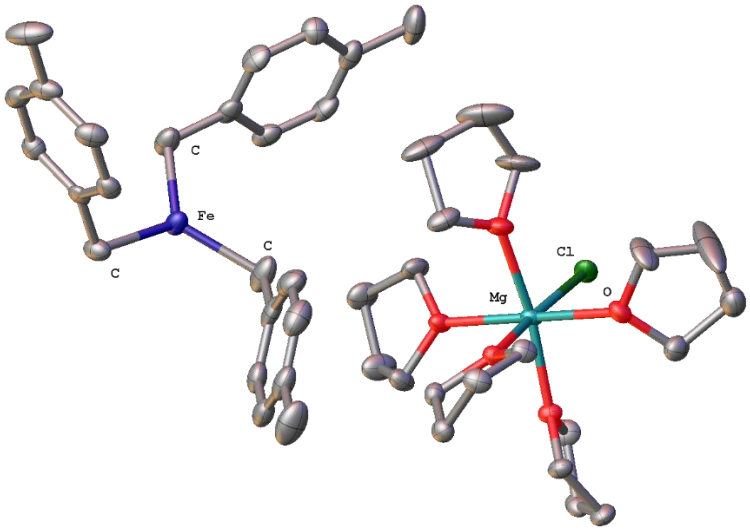

Figure 2.11: X-ray crystal structure of **[31]**[MgCl(THF)$_5$)] with hydrogen atoms omitted for clarity.

The Fe-C bond lengths in **31** are between 2.071(4) to 2.075(3) Å, and are in good agreement with the previously reported complex homoleptic iron-benzyl complex [FeBn$_3$]$^-$, **19**, (2.088(5) to 2.115(6) Å).[58] The C-Fe-C angles in **31** are in the range 117.4 – 122.3°, with an average of 120°, consistent with an ideal trigonal planar geometry. Three-coordinate, homoleptic iron(II)-benzyl complexes have been previously reported to undergo a suspected disproportionation reaction to yield the corresponding four-coordinate, homoleptic iron(III) ate complex;[58] accordingly, after leaving solutions from which crystals of **31** were grown for an extended period (up to 7 days) at -30 °C, crystals of [Fe(4-MeBn)$_4$]$^-$, **[32]**[MgCl(THF)$_5$], were grown (Figure 2.12).

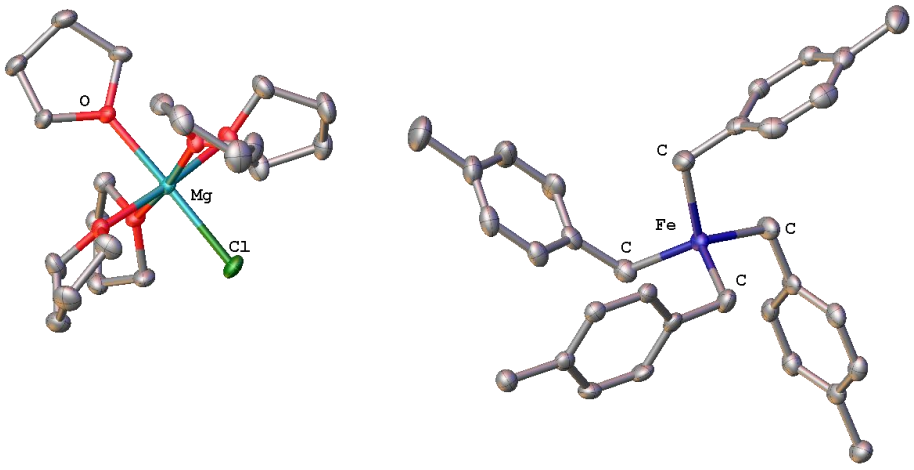

Figure 2.12: X-ray crystal structure of **[32]**[MgCl(THF)$_5$] with hydrogen atoms omitted for clarity.

The Fe-C bond lengths in **32** range from 2.079(2) to 2.092(3) Å, which is in good agreement with the previously reported iron(III) homoleptic complexes $[Fe(CH_2Si(CH_3)_3)_4][Li(THF)_2]$, **16**, ()[88] and $[FeBn_4][MgCl(THF)_5]$, **20**, (2.081(2) to 2.101(2) Å).[58] The C-Fe-C angles in **32** are in the range 107.1 – 112.3°, with an average of 108.9°, consistent with a geometry about the metal centre of a slightly distorted tetrahedral structure (in which the average bond angle is 109.5°). No further experimental data is available for **32**, due to the failure to separate it from **31**.

2.2.4 Attempted synthesis of heteroleptic iron-benzyl complexes

As discussed in Section 2.1, heteroleptic iron-ferrate complexes, bearing naphthyl ligands have been isolated and characterised previously within the Bedford group, from the reaction of iron(II) halide salts with the corresponding Grignard reagent. However, there are no reports of heteroleptic iron-benzyl complexes in the absence of a stabilising ligand, within the literature. Their attempted synthesis here was unsuccessful; mixtures of iron(II) chloride with less than 3 equivalents of **26** results in turbid mixtures, analysis of which by paramagnetic ^{1}H NMR spectroscopy gives rise to signals corresponding to **31** only (Figure 2.13). The same result is observed if iron(II) chloride is added to a pre-formed solution of **31**.

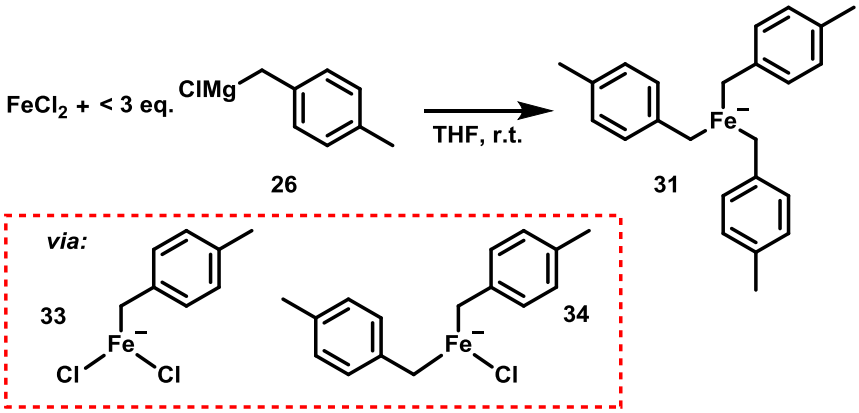

Figure 2.13: Reaction of iron(II) chloride with less than three equivalents of **26**, resulting in the formation of **31**.

The formation of **31** when less than three equivalents of **26** are added with respect to iron suggests that the homoleptic complex **31** provides a thermodynamic sink, preventing the observance and isolation of heteroleptic complexes of the type $[FeCl_2Bn]^-$, **33**, and $[FeClBn_2]^-$, **34**. Although they must form as intermediates before **31**, it would appear that, in contrast to the naphthyl analogues, heteroleptic iron halide / benzyl complexes are not synthetically isolable.

2.3 Preliminary reactivity studies

*2.3.1 Reactivity of homoleptic iron complex **31***

Complexes **31** and **32** demonstrate that upon the initial mixing of iron(II) chloride and the benzyl Grignard reagent **26**, the formation of homoleptic iron(II) 'ate' species occurs; however, their role within the cross-coupling reaction is unclear. Complex **32** was always formed only after extended periods of storage at -30 °C and can therefore be assumed to be initially absent within reaction mixtures. In order to further elucidate the reactivity of the three-coordinate homoleptic complex **31**, a series of reactions between it and substrates present within a catalytic reaction were investigated.

*2.3.1.1 Reactivity of **31** towards excess Grignard reagent*

It is possible that homoleptic iron species are present within catalytic reaction mixtures as a reversibly formed, off-cycle reservoir,[102] as has been previously postulated for iron-nanoparticles formed during the course of other iron-catalysed Kumada cross-coupling reactions.[104] If this were the case, an oxidative or reductive event at the metal centre could result in the subsequent 'activation' of the homoleptic complex. Within the catalytic reaction investigated here, the most likely reductant is the benzyl Grignard reagent, **26**. However the reaction of iron(II) chloride with an excess of **26** (at a ratio of 1: 60, representative of a catalytic reaction but without the electrophile) does not result in a change in iron speciation beyond that of **31**, as evidenced by ^{1}H NMR spectroscopy. Further, the amount of the homo-coupled Grignard reagent, **29**, formed over time does not increase when monitored by GC analysis (Figure 2.14).[iv] This suggests that upon the reaction of $FeCl_2$ with a large excess of **26**, the formation of **31** occurs, which is stable towards both further reaction with **26** and reductive elimination.

[iv] Whilst a small amount of **29** is formed (0.36 mol per mol of iron), suggestive of a reductive homocoupling at iron, Neidig has demonstrated for iron-aryl[64] and -alkyl[77] complexes that chemical quenching of iron(II) species can result in the formation of homo-coupled nucleophile. It would therefore be remiss to ascribe the **26** formed here to a non-quench induced process.

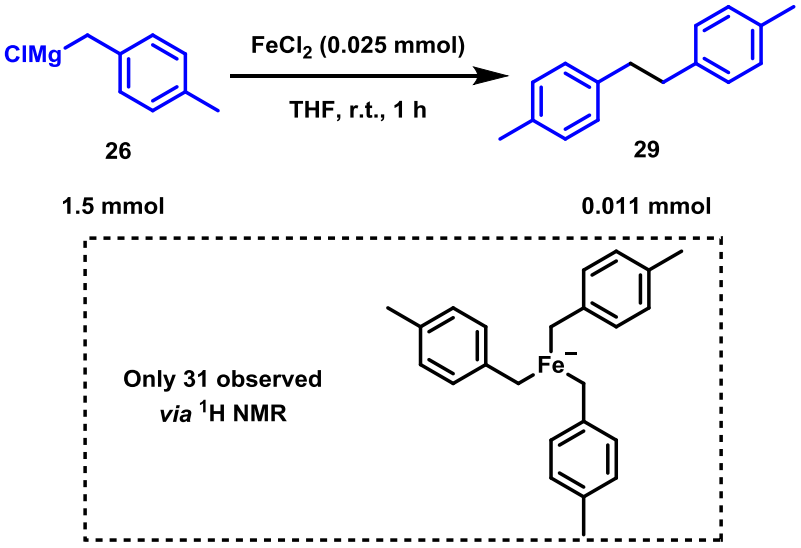

Figure 2.14: Reaction of iron(II) chloride with an excess of the Grignard reagent **26**.

*2.3.1.2 Reactivity of **31** in the presence of the oxidant DCE*

The absence of carbon-carbon bond forming activity for mixtures of iron(II) chloride with Grignard reagent alone suggests that the presence of an oxidative species is required to invoke reactivity within the cross-coupling reaction investigated here. 1,2-Dichloroethane (DCE) has been used previously as an oxidant in the iron-catalysed homo-coupling of aryl-Grignard reagents using iron(III) chloride.[105] Upon the addition of DCE to a mixture of **26** and iron(II) chloride, the homo-coupled product **29** was observed in good yield (Figure 2.15).

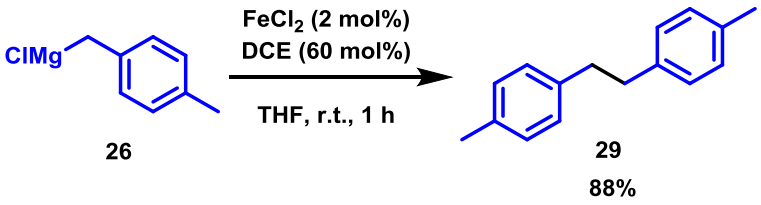

Figure 2.15: Iron-catalysed homocoupling of the benzyl Grignard reagent **26** to give **29**.

Taken together with the lack of homo-coupling in the oxidant's absence, the data is suggestive of the iron centre (in oxidation state II following the initial reaction with the Grignard reagent), having to undergo oxidation before catalytic activity takes place. ^{1}H NMR analysis of reaction mixtures resulted in blank spectra, suggesting that NMR silent species are present (the formation of diamagnetic intermediates is unlikely) during the reaction. However, this result strongly suggests that following an oxidation of **31**, the formation of an iron(III) or iron(IV) species is occurring before reductive elimination can take place (Figure 2.16).

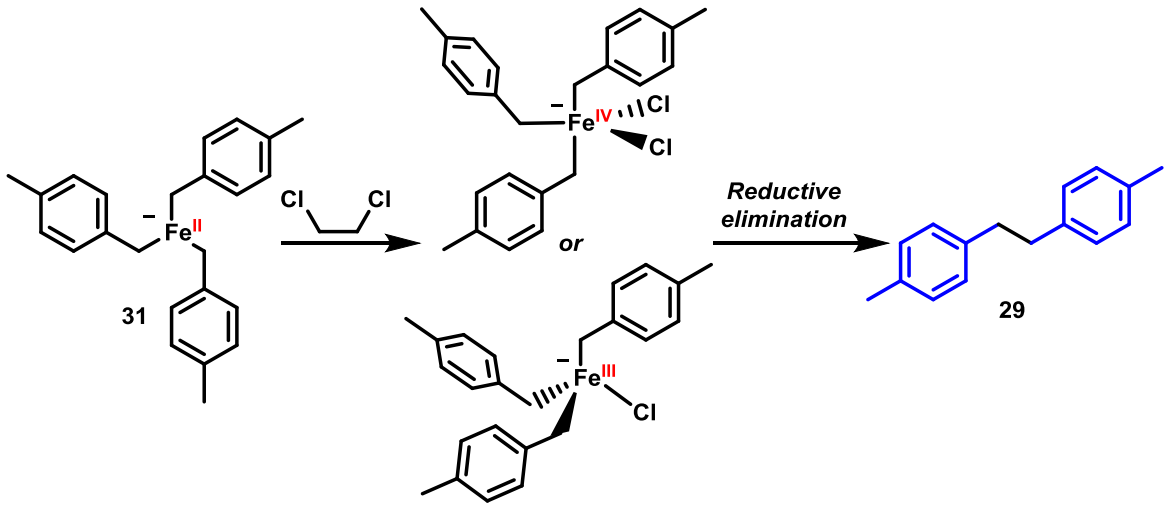

Figure 2.16: Proposed oxidation of **31** to a heteroleptic Fe(III) or Fe(IV) intermediate, followed by subsequent reductive-elimination and formation of the homo-coupled product **29**.

*2.3.1.3 Reactivity of **31** with a benzyl halide electrophile*

Due to the failure to synthesise the desired heteroleptic iron-benzyl / halide complexes (*cf.* those described in Figure 2.13), a direct comparison of the reactivity of homoleptic and heteroleptic complexes towards DCE, and the subsequent rate of Grignard homo-coupling, is not possible. Further, the lack of characterisation regarding iron speciation following the likely oxidation of **31** upon reaction with DCE means that it cannot be said with any certainty that heteroleptic iron-species are present within reaction mixtures at all. However, whilst the preparative aspect of the heteroleptic complexes of interest is likely to remain challenging, a demonstration of their reactive competency is indirectly possible. To this end, a series of reactions between the homoleptic complex **31** and varying amounts of the electrophile **25** were carried out (1 to 10 equivalents with respect to iron); in each case, a product distribution was observed (Table 2.2).

Table 2.2: Reaction of the homoleptic, iron(II) benzyl complex **31** with increasing amounts of the benzyl halide electrophile **25**.

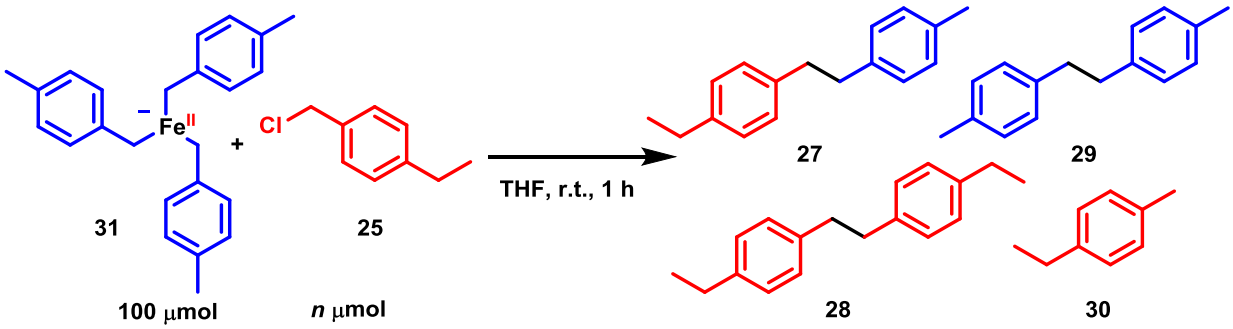

Entry	*n*	**27**, μmol	**28**, μmol	**29**, μmol[a]	**30**, μmol	**Σ products** μmol
1	0	0	0	44	0	44
2	50	21	7	76	13	117
3	100	54	13	85	22	174
4	200	92	47	85	10	234
5	300	125	77	106	6	314
6[b]	400	128	84	100	1	313
7[c]	500	112	74	87	1	274
8[d]	1000	107	68	81	1	257

Reaction quenched through the addition of 0.1 M HCl, followed by extraction into DCM and analysis using GC-FID (dodecane internal standard). [a] Values calculated accounting for the amount of **29** already present within a solution of the Grignard reagent **26**; [b] 80 μmol **25** remaining; [c] 200 μmol **25** remaining; [d] 620 μmol **25** remaining.

Entry 1 is in effect a control run, demonstrating approximately how much of the homo-coupled product **29** is formed from a quench of **31**. Entries 2-8 therefore demonstrate bond-forming reactivity as a result of the reaction of **31** with **25**, less the 44 μmol of **29** formed as a result of the quenching process. Although this does not represent a catalytic reaction for any one of the products formed (as an approximation, there is at most one turnover per iron centre per product), the sum total of μmol formed for each entry demonstrates the competency of species other than **31** towards carbon-carbon bond forming processes.

This assertion can be made on the basis that if **31** alone were responsible for the observed reactivity, then after the formation of 100 μmol of **27** (equivalent to 1 total turnover per iron centre, and transfer of one 4-MeBn group from iron) no further carbon-carbon bond forming

processes would take place, due to the iron : benzyl ratio being below 1:2 (Figure 2.17, path A). However, this is not the case, with approximately 300 µmol of total products being formed (equivalent to 3 turnovers per iron centre) when an increased amount of electrophile with respect to iron is added (Table 2.2, entries 4-7). To account for this reactivity, it would appear possible that the formation, and subsequent reactivity towards **25**, of heteroleptic iron benzyl / halide species, could be occurring (Figure 2.17, path B).[v]

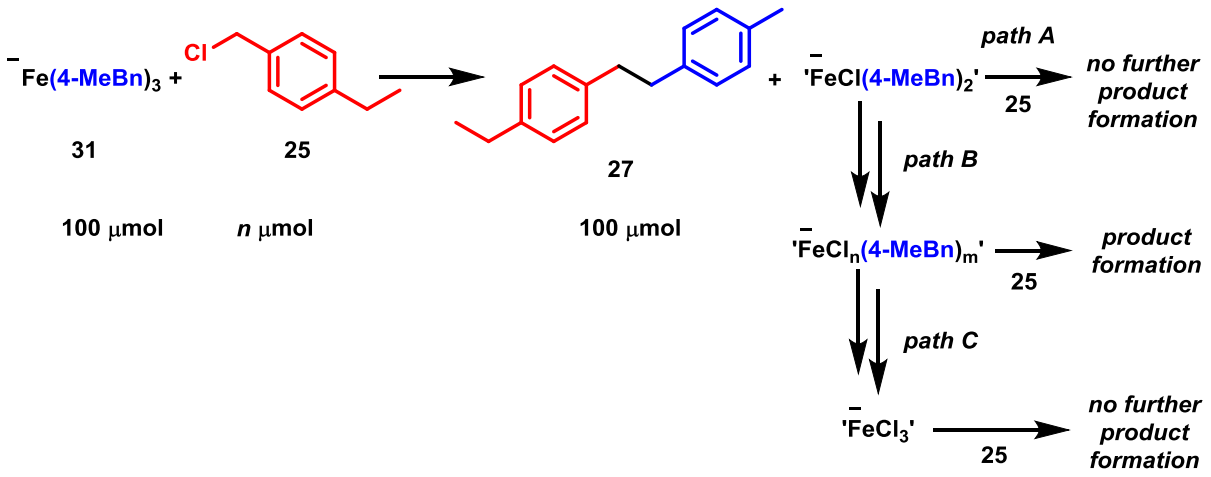

Figure 2.17: Expected lack of carbon-carbon bond forming activity following product formation should **31** be the sole species responsible for bond forming processes, in contrast to the observed reactivity, suggesting that heteroleptic iron complexes are forming. *n* and *m* are between 0 and 3.

As can be seen in entries 5-8, increasing the amount of **25** added beyond 300 µmol does not result in an increase in the amounts of products formed. This suggests that product formation does not take place in the presence of homoleptic chloro-ferrate species (Figure 2.17, path C), which would be expected to form after the transfer of all the benzyl groups originally on the iron centre (equal to 300 µmol).[103]

Whilst the data presented in Table 2.2 are suggestive of the formation and competency of heteroleptic iron-benzyl / halide species, the reaction conditions are not representative of those used in a catalytic reaction. Furthermore, there is no information on the comparative rates

[v] It should be noted that it is also possible that upon the loss of (4-MeBn) from iron to form **27** or **29**, equilibration between the remaining iron species could occur, meaning that there could always be a proportion of **31** present within the reaction mixture, which is responsible for all carbon-carbon bond forming activity. However, if this were the case such a large product distribution would not necessarily be expected, in contrast to the results presented here.

of product formation, or the distribution of the reaction as a function of time. Accordingly, in an attempt to answer these (and other) questions, a kinetic investigation of the catalytic reaction was undertaken.

2.4 Kinetic investigation

Due to the unselective distribution of products formed, any study of the reaction must consider the effect of a change upon each of the products in turn. The results gained should allow for insights into three reactions at once: the heterocoupling reaction (formation of **27**), the homocoupling of the electrophilic species **25** (formation of **28**) and the homocoupling of the nucleophilic species **26** (formation of **29**).

The rate of a chemical reaction is defined as the change in concentration of reactants or products with respect to time; because the concentration of reactants and products changes as a reaction progresses, so, therefore, does the rate of reaction.[106] The dependence on concentration of the reaction rate is expressed as a proportionality constant, *k*. This term, along with the concentrations of each reactant, constitutes a reaction rate law. However, the extent to which the concentration of each individual reactant influences the rate may be different, therefore the concentration of each reagent within the rate law has an exponent, expressing the order of reaction for that reactant (Figure 2.18).[106]

$$A + B \rightarrow C$$

$$rate = -\frac{d[A]}{dt} = k[A]^x[B]^y$$

$$rate = \frac{d[C]}{dt} = k[A]^x[B]^y$$

Figure 2.18: Rate equations for the rate of consumption of a reagent, *A*, and the rate of formation of a product, *C* for a given chemical reaction. *k* = the rate constant; *x* and *y* are the orders of reaction with respect to the reactants *A* and *B*. It should also be noted that the order of a reaction with respect to a catalyst can be recorded.

Traditionally, this data is collected using the method of initial rates, whereby a change is made to the concentration of one of the reagents and the reaction is sampled / monitored until the conversion reaches around 10%. In cases where the initial phase of the reaction does not represent the greatest rate, it is also possible, as an approximation, to use data from the part of the reaction in which the gradient is steepest.[106] More recently, the use of Reaction Progress

Kinetic Analysis (RPKA)[107] and the closely related Variable Time Normalisation Analysis (VTNA)[108] have emerged as methods of interpreting kinetic data. In addition to the orders of reaction, these modern methods of analysis can provide a more accurate interpretation of the recorded data, if analysis *via* the method of initial rates is not possible to a sufficient degree of accuracy (for example, where sigmoidal reaction profiles are observed). In such cases, the simplicity of VTNA (the technique is carried out by overlaying entire data plots) allows for non-ideal data sets of kinetic data to be compared quickly, with less ambiguity as to which part of the reaction should be monitored. However in the case of VTNA it is important that a reaction is analysed in isolation, as the method does not account for side product formation.[108]

In the following section, the method of initial rates is primarily used, supported in places by VTNA. All of the following data was recorded *via* manual sampling of the reaction at regular intervals, followed by quenching and analysis using GC-FID. Due to the complexity of the system, with 3 reactions occurring and being monitored simultaneously, the results will be disclosed for each product in turn, rather than by reagent.

2.4.1 Orders of reaction for the heterocoupled product, ***27***

2.4.1.1 Order in iron

The reaction between **25** and **26** was first monitored whilst varying the concentration of the iron salt pre-catalyst, $FeCl_2$. From the resulting concentration-time profiles, displayed in Figure 2.19, the maximum rate of reaction for each loading of $FeCl_2$ was calculated using the method of initial rates.

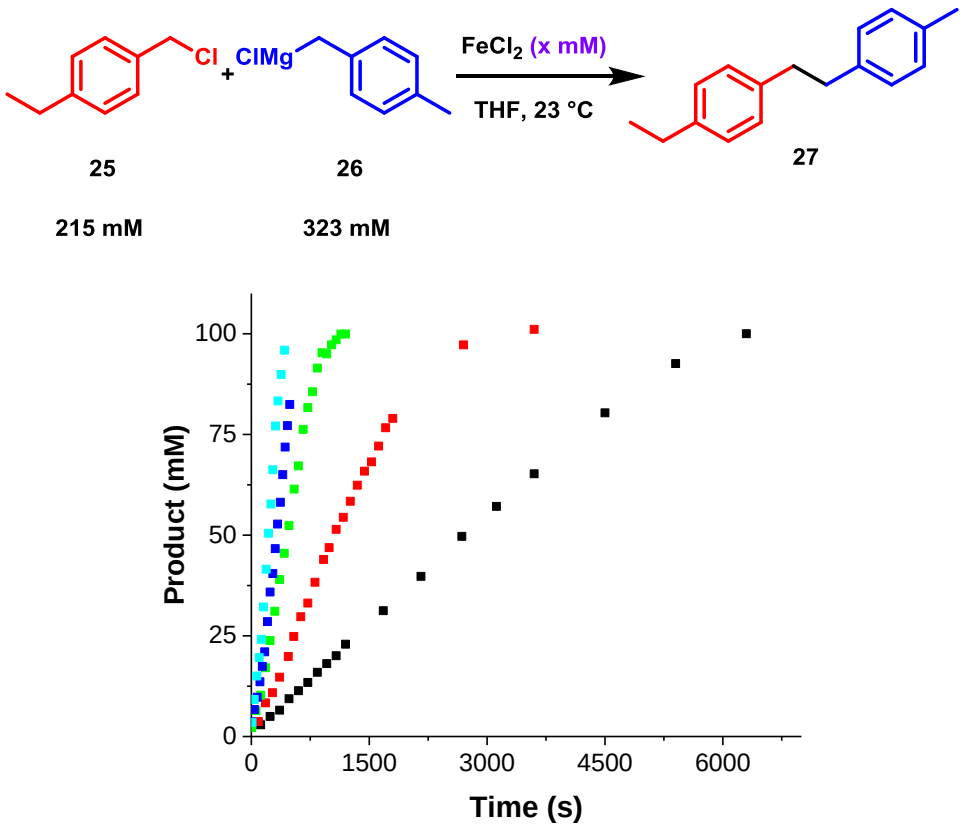

Figure 2.19: Concentration-time plots for the reaction of **25** with **26** to produce **27**, using a varying concentration of $FeCl_2$ pre-catalyst. ■ [Fe] = 2.15 mM, ■ [Fe] = 5.37 mM, ■ [Fe] = 10.8 mM, ■ [Fe] = 16.1 mM, ■ [Fe] = 21.2 mM.

Using the method of initial rates, the rate of reaction for each loading of $FeCl_2$ was calculated. When the logarithm of each recorded initial rate is plotted against the logarithm of the concentration in $FeCl_2$, the gradient of the line obtained yields the reaction order in $FeCl_2$ for the production of **27** (Figure 2.20).

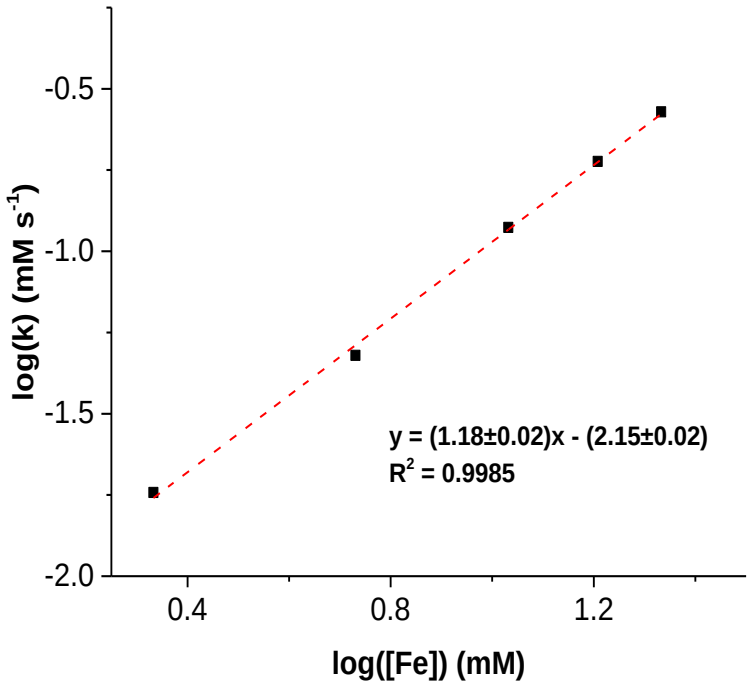

Entry	$FeCl_2$ (mM)	k_{max} (mM s^{-1})
1	2.15	0.0181
2	5.37	0.0478
3	10.75	0.1184
4	16.13	0.1889
5	21.51	0.2684

Figure 2.20: Approximate initial rates measured from the concentration-time profiles displayed in Figure 2.19, and the corresponding logarithm plot.

As displayed in Figure 2.20, the plot yields a gradient of 1.18, suggesting that the reaction to produce **27** is approximately first order in iron. In this case the data is of sufficient quality to allow for the confident use of the method of initial rates, meaning that analysis using VTNA is not necessary. However, this provides a good opportunity to use the VTNA method as a means of validating whether it is applicable for this reaction; if so, a similar value for the order of reaction with respect to iron should be obtained using both methods. As can be seen in Figure 2.21, the time normalised reaction profiles at different iron loadings overlay well for an order in iron between 1.1 and 1.2, which is in excellent agreement with the value of 1.18 obtained when using the method of initial rates. Therefore, in cases where the method of initial rates is not possible, VTNA can be expected to give a reasonable value for the formation of **27**.

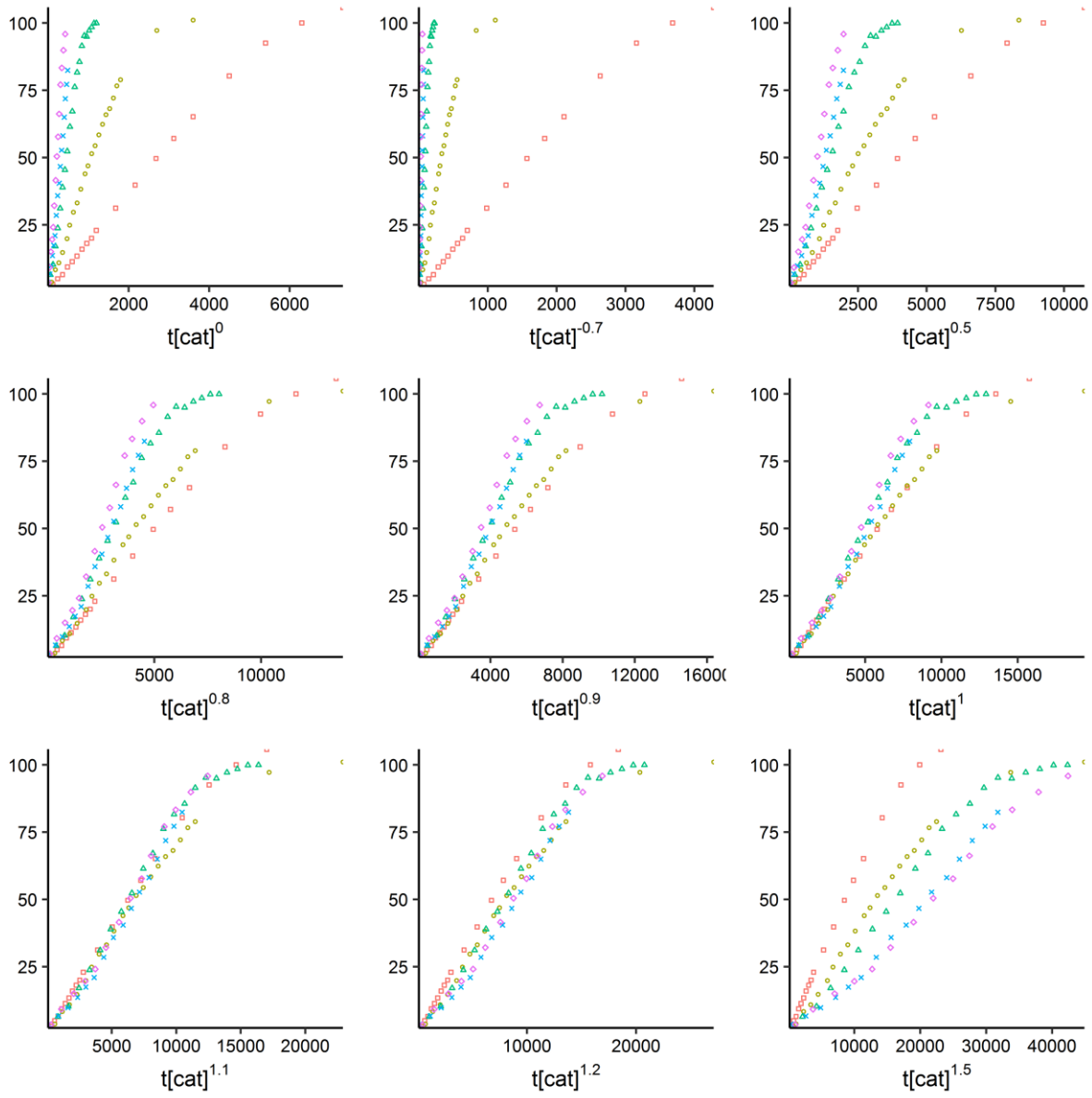

Figure 2.21: Variable time normalisation analysis (VTNA) for the reaction between **25** and **26** catalysed by various concentrations of $FeCl_2$, for the determination of the order in Fe with respect to **27**. *y* axis in all cases = concentration (mM). All graphs composed by Dr. Antonis Messinis.

*2.4.1.2 Order in electrophile **25***

The order of reaction with respect to the electrophile **25**, for the production of **27**, was next obtained using the method of initial rates. The resulting concentration-time profiles are displayed in Figure 2.22.

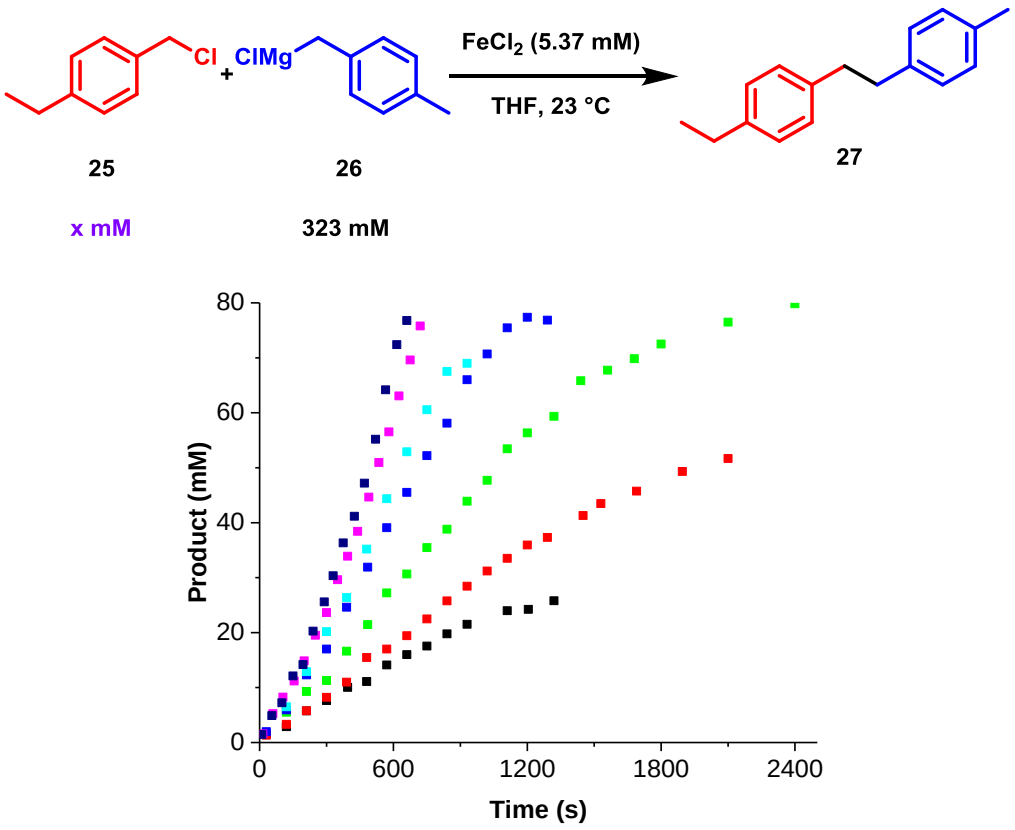

Figure 2.22: Concentration-time plots for the reaction of **25** and **26**, using an $FeCl_2$ pre-catalyst, using a varying concentration of the electrophile **25**. ■ [**25**] = 71 mM, ■ [**25**] = 107 mM, ■ [**25**] = 142 mM, ■ [**25**] = 215 mM, ■ [**25**] = 322 mM, ■ [**25**] = 538 mM, ■ [**25**] = 646 mM.

Taking the steepest gradient along each curve, an estimate of the initial rate was made for each concentration of the electrophile **25**; the results are displayed in Figure 2.23.

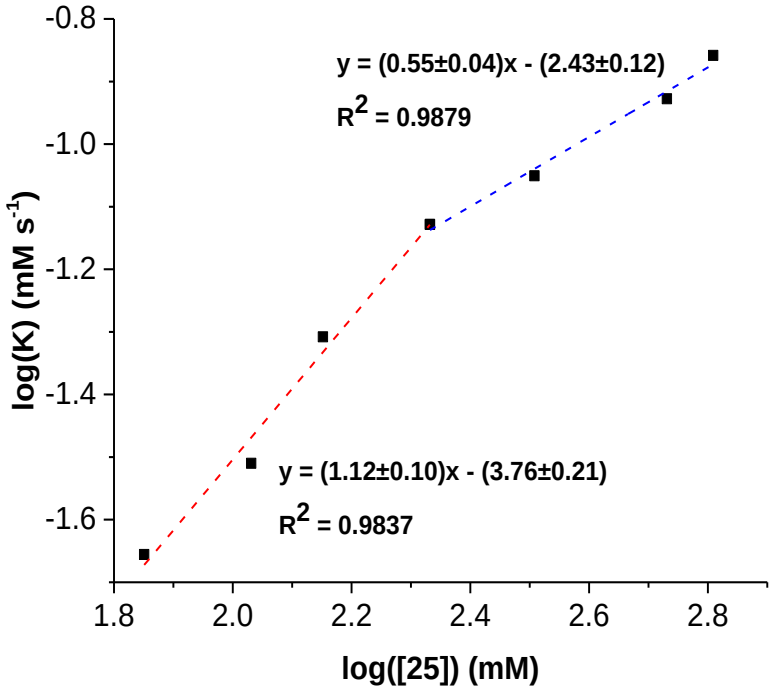

Entry	**25** (mM)	k_{max} (mM s^{-1})
1	71	0.022
2	107	0.031
3	142	0.049
4	215	0.074
5	322	0.089
6	537	0.118
7	645	0.136

Figure 2.23: Approximate initial rates measured from the concentration-time profiles displayed in Figure 2.22, and the corresponding logarithm plot.

From the resulting logarithm plot, it appears that the positive effect upon the rate of production of **27** through increasing the concentration of **25** appears to saturate for the reactions employing a high concentration of **25**. It is therefore perhaps more appropriate to consider logarithm plot as two separate sets of data.[vi] Taking the data which correspond to reactions in which an excess of the Grignard reagent, **26**, is present with respect to **25** (Figure 2.23, entries 1 - 4), a value of 1.12 is obtained, suggesting the reaction to produce **27** is approximately first order in **25**. However, where **25** is present in excess compared to **26** (Figure 2.23, entries 5 – 8), the value obtained is 0.55, demonstrating a less pronounced effect of **25** upon the rate of production of **27**.

*2.4.1.3 Order in the Grignard reagent **26***

The order of reaction with respect to the Grignard reagent **26** for the production of **27** was next investigated. In contrast to the variation in concentration of the iron catalyst and electrophile **25**, the resultant concentration-time plots displayed little variation upon a change in the concentration of **26** (Figure 2.24).

[vi] Considering the plot in Figure 2.23 as a single set of data yields a value of 0.81 for the order of reaction with respect to **25** for the production of **27**, with $R^2 = 0.966$

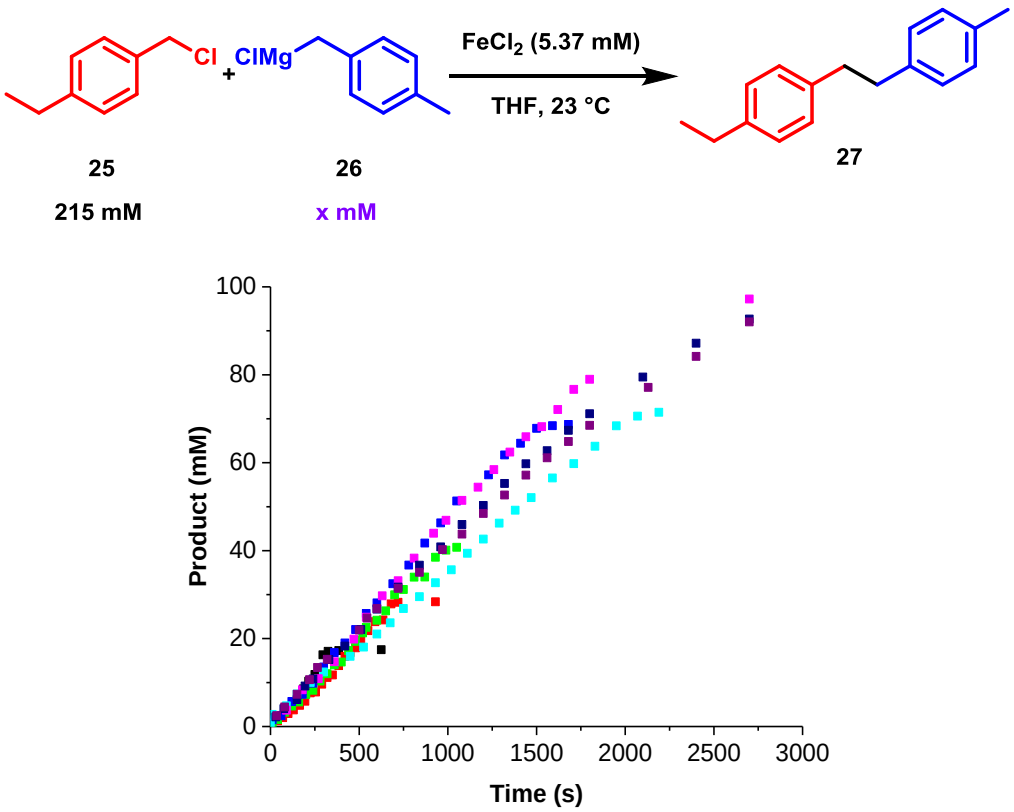

Figure 2.24: Concentration-time plots for the reaction of **25** and **26**, with an $FeCl_2$ pre-catalyst, using a varying concentration of the Grignard reagent **26**. ■ [**26**] = 71 mM, ■ [**26**] = 108 mM, ■ [**26**] = 142 mM, ■ [**26**] = 215 mM, ■ [**26**] = 269 mM, ■ [**26**] = 322 mM, ■ [**26**] = 430 mM, ■ [**26**] = 538 mM.

Taking the steepest gradient along each curve, an estimate of the initial rate was made for each concentration of the Grignard reagent **26**; the results are displayed in Figure 2.25.

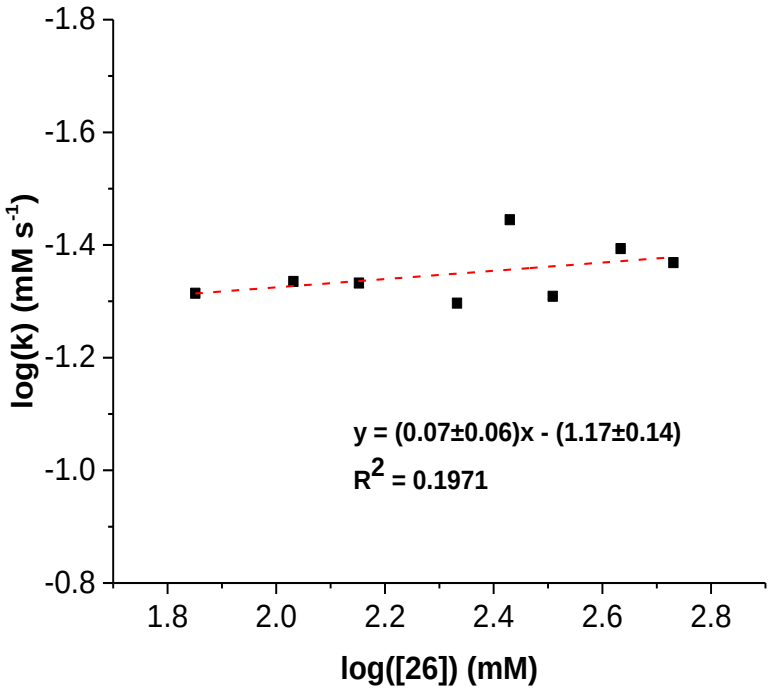

Entry	**26** (mM)	k_{max} (mM s^{-1})
1	71	0.048
2	108	0.046
3	142	0.046
4	215	0.051
5	269	0.036
6	322	0.049
7	430	0.040
8	538	0.043

Figure 2.25: Approximate initial rates measured from the concentration-time profiles displayed in Figure 2.24, and the corresponding logarithm plot.

The value obtained of 0.07 from the logarithm plot displayed in Figure 2.25 confirms that the reaction for the production of **31** is best described as 0 order with respect to the Grignard reagent **26**.

*2.4.2 Orders of reaction for the homo-coupled electrophile product, **28***

2.4.2.1 Order in iron

The orders of reaction with respect to $FeCl_2$, **25** and **26** were next calculated for the production of the homo-coupled electrophile, **28**. The concentration-time plots resulting from varying the concentration of $FeCl_2$ are displayed in Figure 2.26.

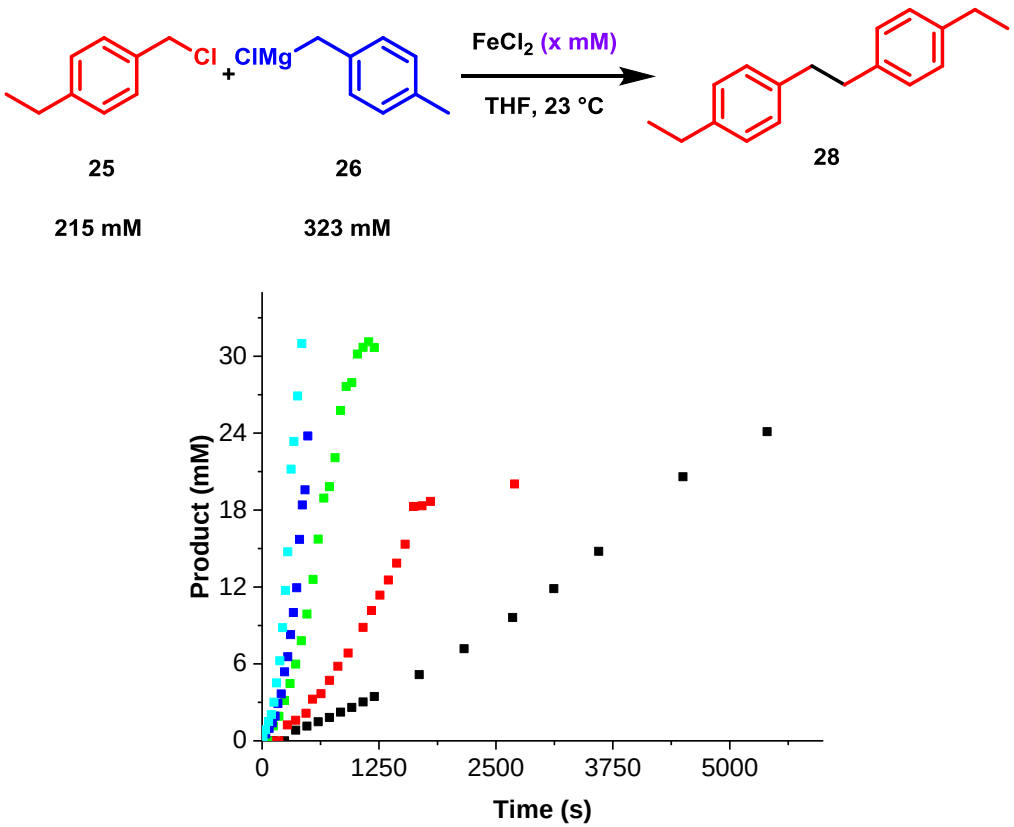

Figure 2.26: Concentration-time plots for the reaction of **25** and **26**, using a varying concentration of the $FeCl_2$ pre-catalyst. ■ [Fe] = 2.15 mM, ■ [Fe] = 5.37 mM, ■ [Fe] = 10.8 mM, ■ [Fe] = 16.1 mM, ■ [Fe] = 21.2 mM.

Due to the sigmoidal nature of the resulting plots, VTNA was initially used to elucidate the order of reaction. However, a poor overlap was observed at all order values, most likely as the reaction is not being viewed in isolation (other products containing the electrophile are being formed simultaneously) and **28** representing only a fraction of these products. This is a drawback of the method (see section 8.2 for VTNA plots and a small discussion).[109] Taking the steepest gradient along each curve, an estimate was made for the rate of reaction at each concentration of iron; the results are plotted in Figure 2.27.

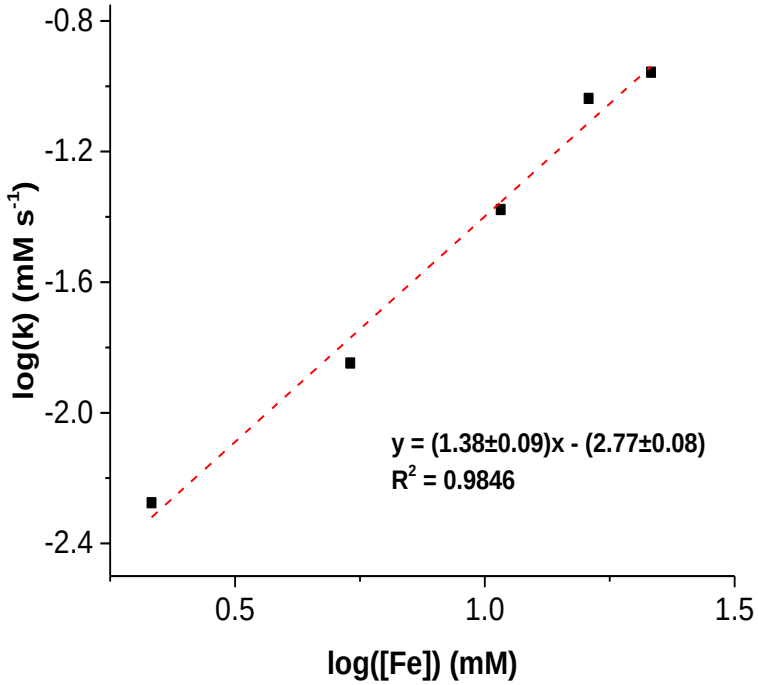

Entry	$FeCl_2$ (mM)	k_{max} (mM s^{-1})
1	2.15	0.0053
2	5.37	0.0142
3	10.75	0.0419
4	16.13	0.0918
5	21.51	0.1104

Figure 2.27: Approximate initial rates measured from the concentration-time profiles displayed in Figure 2.26, and the corresponding logarithm plot.

The corresponding logarithm plot yields an order in iron for the production of **28** of 1.38, suggestive of a near first order process.

*2.4.2.2 Order in electrophile, **25***

The order of reaction with respect to the electrophile **25** for the production of the homo-coupled electrophile product **28** was next investigated; the resultant concentration-time profiles are displayed in Figure 2.28.

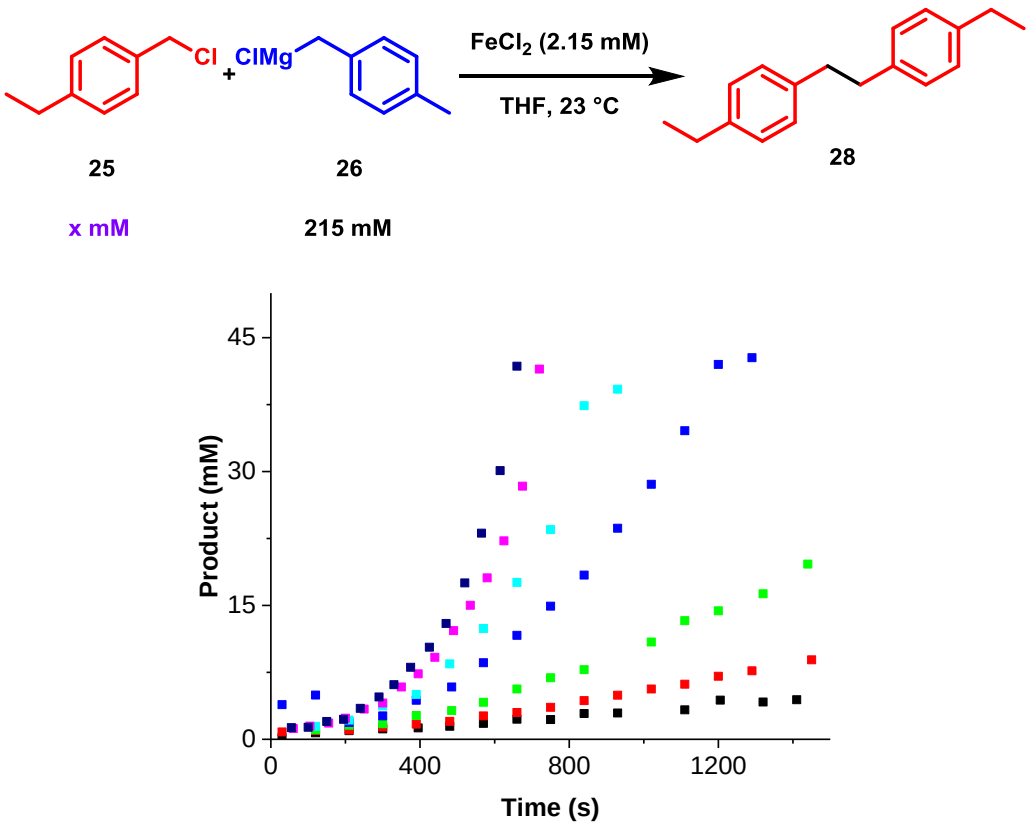

Figure 2.28: Concentration-time plots for the reaction of **25** and **26**, using a $FeCl_2$ pre-catalyst, using a varying concentration of the electrophile **25**. ■ [**25**] = 71 mM, ■ [**25**] = 107 mM, ■ [**25**] = 142 mM, ■ [**25**] = 215 mM, ■ [**25**] = 322 mM, ■ [**25**] = 538 mM, ■ [**25**] = 646 mM.

Taking the steepest gradient along each curve, the maximum rate of reaction was estimated using the method of initial rates; the results are displayed in Figure 2.29.

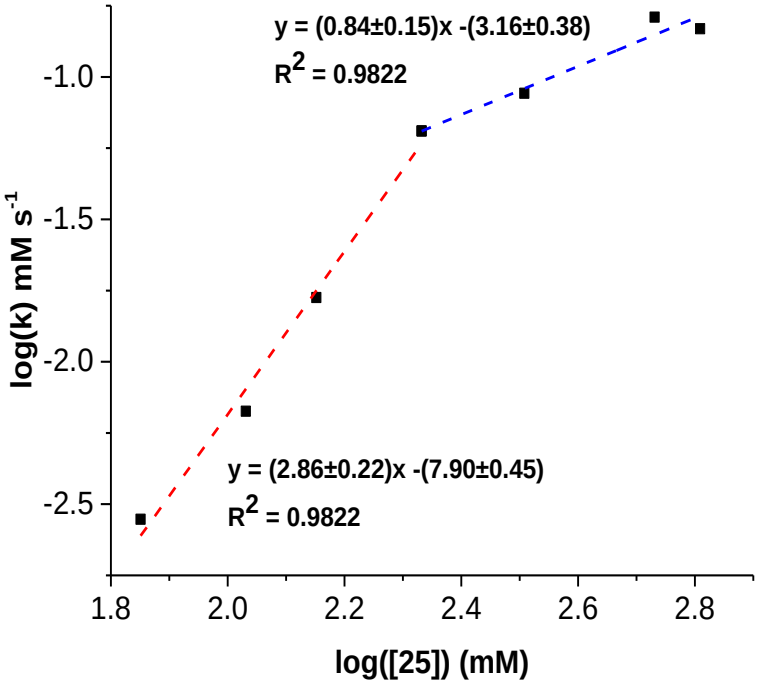

Entry	**25** (mM)	k_{max} (mM s^{-1})
1	71	0.0028
2	107	0.0067
3	142	0.0168
4	215	0.0646
5	322	0.0876
6	537	0.1621
7	645	0.1475

Figure 2.29: Approximate initial rates measured from the concentration-time profiles displayed in Figure 2.28, and the corresponding logarithm plot.

As in the case of the product **27**, from the logarithm plot above it appears that the positive effect upon the rate of production of **28** through increasing the concentration of **25** saturates for reactions employing a high concentration of **25**. Considering the plot as two separate sets of data,[vii] a value of 2.86 is initially obtained (entries 1-4) when the Grignard reagent **26** is present in excess, however when the concentration of **25** becomes greater than that of **26**, this value drops to 0.84, demonstrating a less pronounced effect of **25** upon the rate of production of **28**.

*2.4.2.3 Order in the Grignard reagent, **26***

The order with respect to the Grignard reagent **26** for the reaction to produce **28** was next calculated. As with the production of **27**, the resultant concentration-time profiles display little variation upon changing the concentration of **26** (Figure 2.30).

[vii] Considering the plot in Figure 2.29 as a single set of data yields a value of 1.86 for the order of reaction with respect to **25** for the production of **28**, with with $R^2 = 0.931$

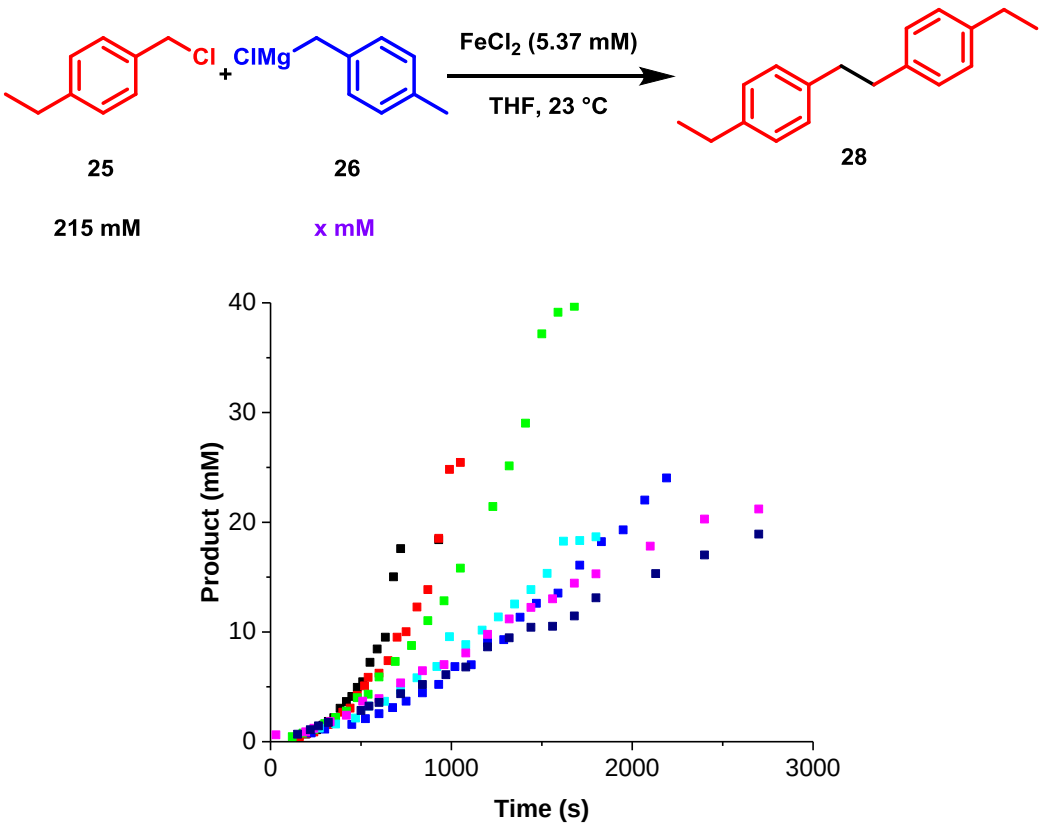

Figure 2.30: Concentration-time plots for the reaction of **25** and **26**, using a $FeCl_2$ pre-catalyst, with varying concentrations of the Grignard reagent **26**. ■ [**26**] = 71 mM, ■ [**26**] = 108 mM, ■ [**26**] = 142 mM, ■ [**26**] = 215 mM, ■ [**26**] = 269 mM, ■ [**26**] = 322 mM, ■ [**26**] = 430 mM, ■ [**26**] = 538 mM.

The method of initial rates was employed in order to ascertain the order of reaction with respect to **26**. In doing so, the acceleration in the rate of production of **28** at low concentrations of **26** ([**26**] < 322 mM) later on in the reaction profiles is ignored. The initial rates of reaction for each concentration of **26** and the corresponding logarithm plot are displayed in Figure 2.31.

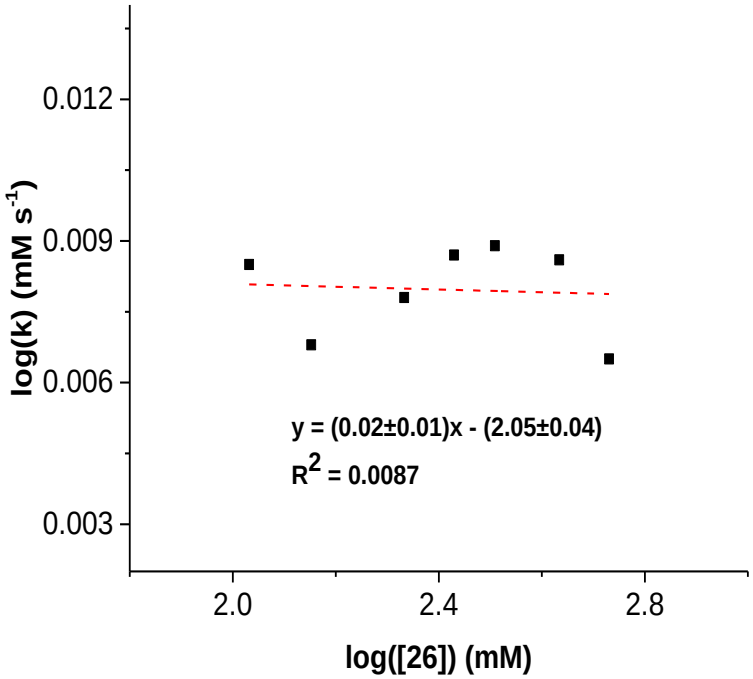

Entry	**26** (mM)	k_{max} (mM s^{-1})
1	108	0.0085
2	142	0.0068
3	215	0.0078
4	269	0.0087
5	322	0.0089
6	430	0.0086
7	538	0.0065

Figure 2.31: Approximate initial rates measured from the concentration-time profiles displayed in Figure 2.30, and the corresponding logarithm plot.

The corresponding logarithm plot yields a value of 0.02, corresponding to an order in **26** for the production of **28** of 0.

*2.4.3 Orders of reaction for the homo-coupled nucleophile product, **29***

2.4.3.1 Order in iron

The orders of reaction with respect to $FeCl_2$, **25** and **26** were next calculated for the production of the homo-coupled nucleophile product, **29**. The concentration-time plots resulting from varying the concentration of $FeCl_2$ are displayed in Figure 2.32.

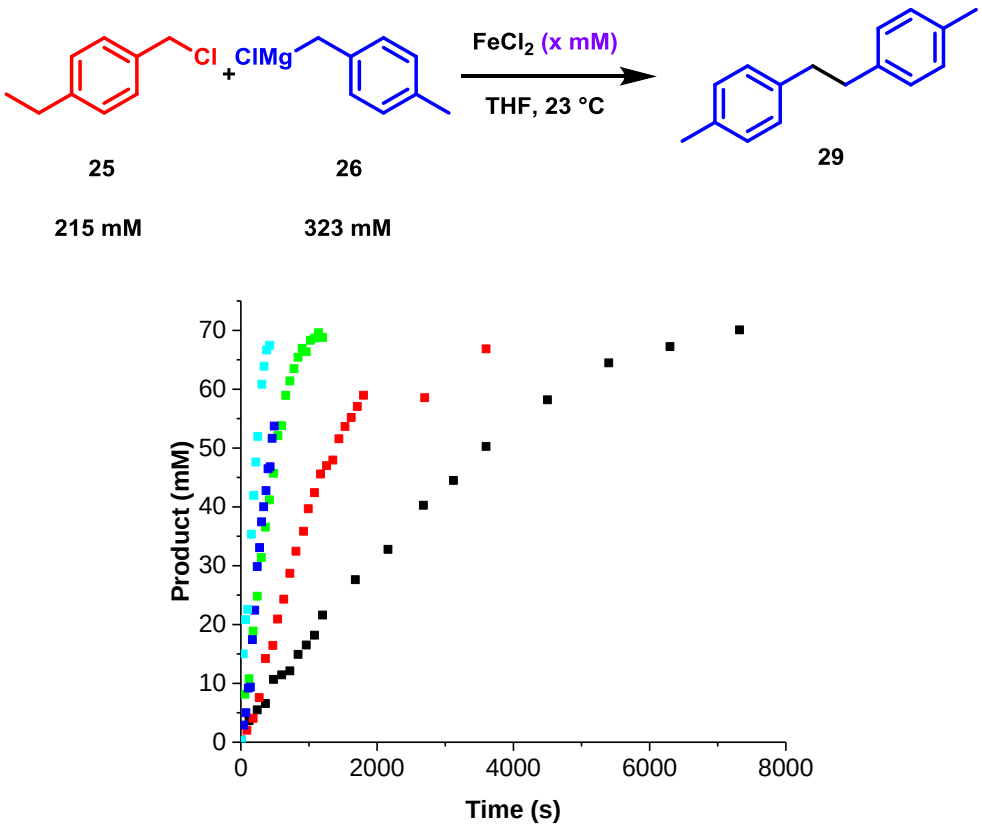

Figure 2.32: Concentration-time plots for the reaction of **25** and **26**, using a varying concentration of the $FeCl_2$ pre-catalyst. ■ [Fe] = 2.15 mM, ■ [Fe] = 5.37 mM, ■ [Fe] = 10.8 mM, ■ [Fe] = 16.1 mM, ■ [Fe] = 21.2 mM.

Using the method of initial rates, the steepest gradient of each plot was used to provide an approximate value for the maximum rate of reaction; the results are displayed in Figure 2.33.

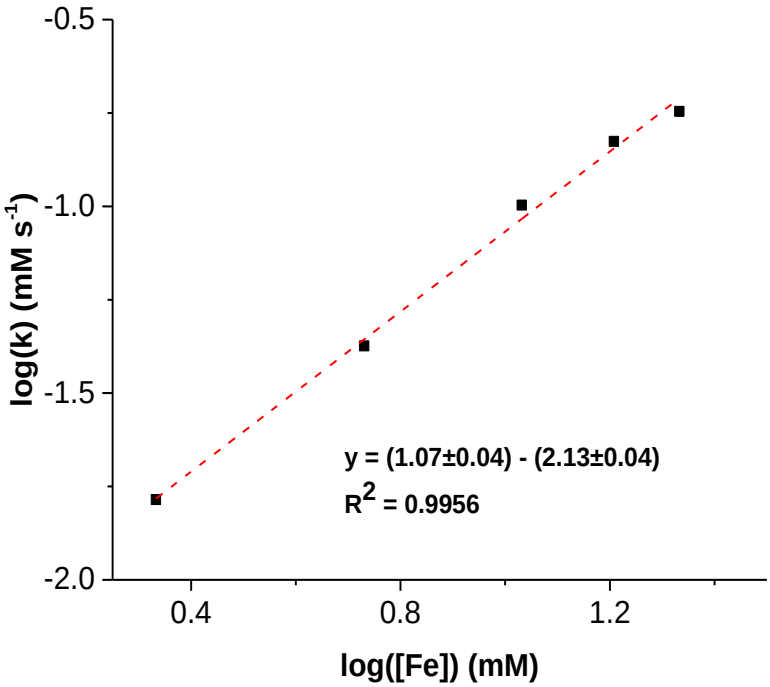

Entry	$FeCl_2$ (mM)	k_{max} (mM s^{-1})
1	2.15	0.0164
2	5.37	0.0423
3	10.75	0.1008
4	16.13	0.1492
5	21.51	0.1795

Figure 2.33: Approximate initial rates measured from the concentration-time profiles displayed in Figure 2.32, and the corresponding logarithm plot.

The value obtained from the logarithm plot of 1.07 suggests that the reaction is first order in iron for the production of **29**.

*2.4.3.2 Order in the electrophile, **25***

The order of reaction with respect to the electrophile **25** for the production of the homo-coupled nucleophile product **29** was next investigated; the resultant concentration-time profiles are displayed in Figure 2.34.

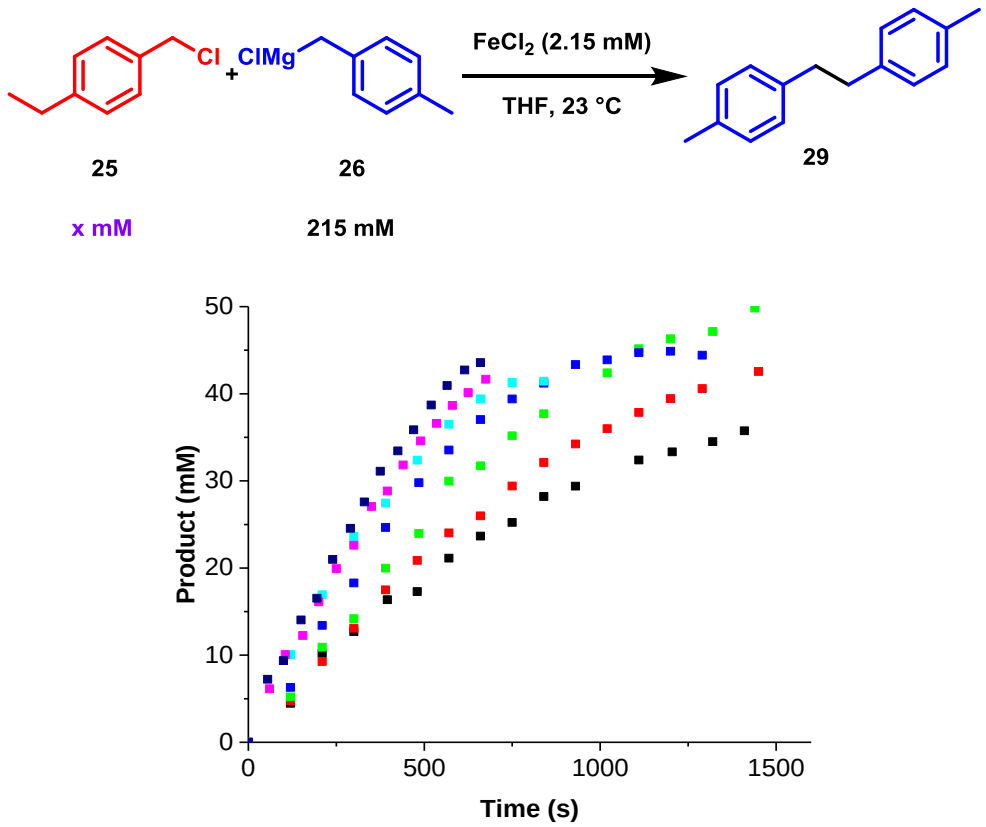

Figure 2.34: Concentration-time plots for the reaction of **25** and **26**, using a $FeCl_2$ pre-catalyst, using a varying concentration of the electrophile **25**. ■ [**25**] = 71 mM, ■ [**25**] = 107 mM, ■ [**25**] = 142 mM, ■ [**25**] = 215 mM, ■ [**25**] = 322 mM, ■ [**25**] = 538 mM, ■ [**25**] = 646 mM.

Using the method of initial rates, the steepest gradient of each plot was used to provide an approximate value for the maximum rate of reaction; the results are displayed in Figure 2.35.

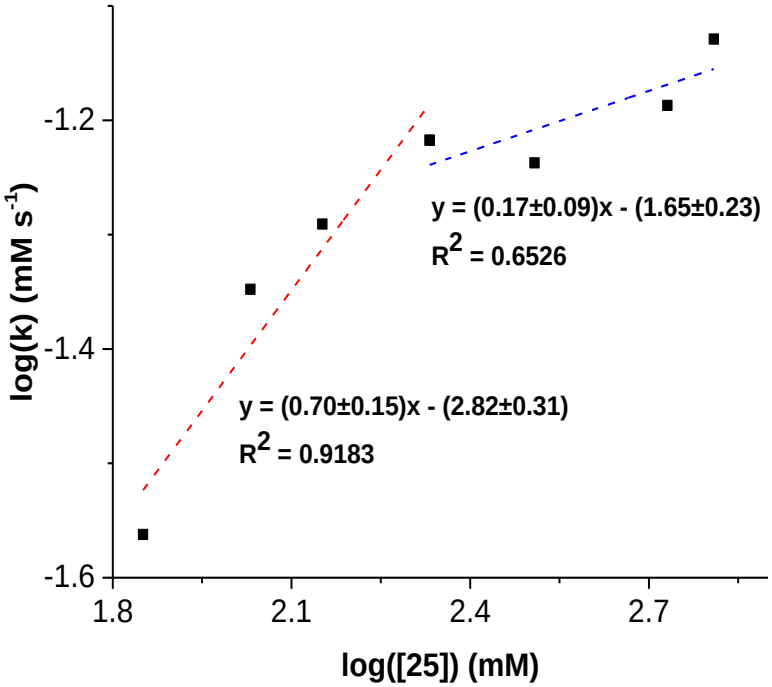

Entry	**25** (mM)	k_{max} (mM s^{-1})
1	71	0.0274
2	107	0.0449
3	142	0.0512
4	215	0.0606
5	322	0.0579
6	537	0.065
7	645	0.0743

Figure 2.35: Approximate initial rates measured from the concentration-time profiles displayed in Figure 2.34, and the corresponding logarithm plot.

Considering the logarithm plot in Figure 2.35 as a two separate sets of data,[viii] a value of 0.70 is obtained when the Grignard reagent, **26**, is present in excess with respect to the electrophile (Figure 2.35, entries 1 – 4). Whilst this does not correspond to an exactly first order process, it is most certainly non-zero order, which suggests that the presence of the electrophile accelerates the reaction to produce the homo-coupled nucleophile. Where the electrophile **25** is present in excess compared to **26** (Figure 2.35, entries 5 – 8), the value obtained is 0.17, demonstrating a less pronounced effect of **25** upon the rate of production of **29**.

*2.4.3.3 Order in the Grignard reagent, **26***

The order with respect to the Grignard reagent **26** for the reaction to produce **29** was next calculated. As with the production of **27** and **28**, the resultant concentration-time profiles display little variation upon changing the concentration of **26** (Figure 2.36).

[viii] Considering the plot as a single set of data yields a value of 0.35 for the order of reaction with respect to **25** for the production of **29**, with R^2 of 0.801

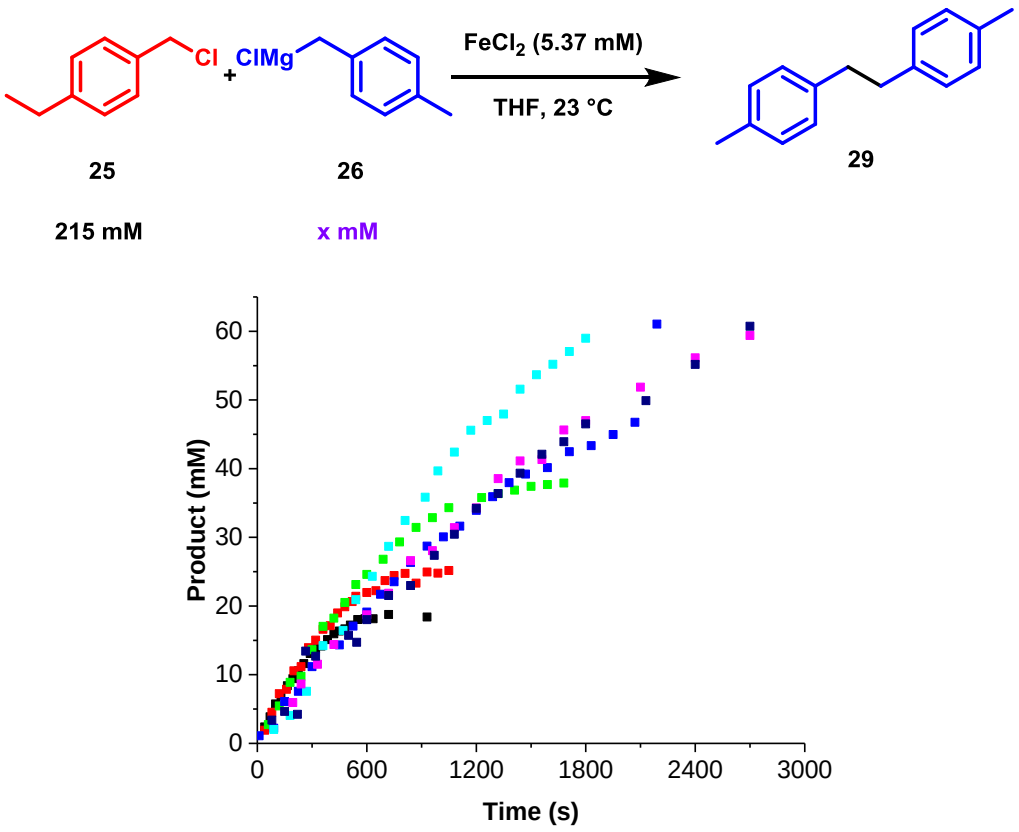

Figure 2.36: Concentration-time plots for the reaction of **25** and **26**, using a $FeCl_2$ pre-catalyst, with varying concentrations of the Grignard reagent **26**. ■ [**26**] = 71 mM, ■ [**26**] = 108 mM, ■ [**26**] = 142 mM, ■ [**26**] = 215 mM, ■ [**26**] = 269 mM, ■ [**26**] = 322 mM, ■ [**26**] = 430 mM, ■ [**26**] = 538 mM.

Taking the steepest gradient along each curve, an estimate of the initial rate was made for each concentration of the **26**; the results are displayed in Figure 2.37.

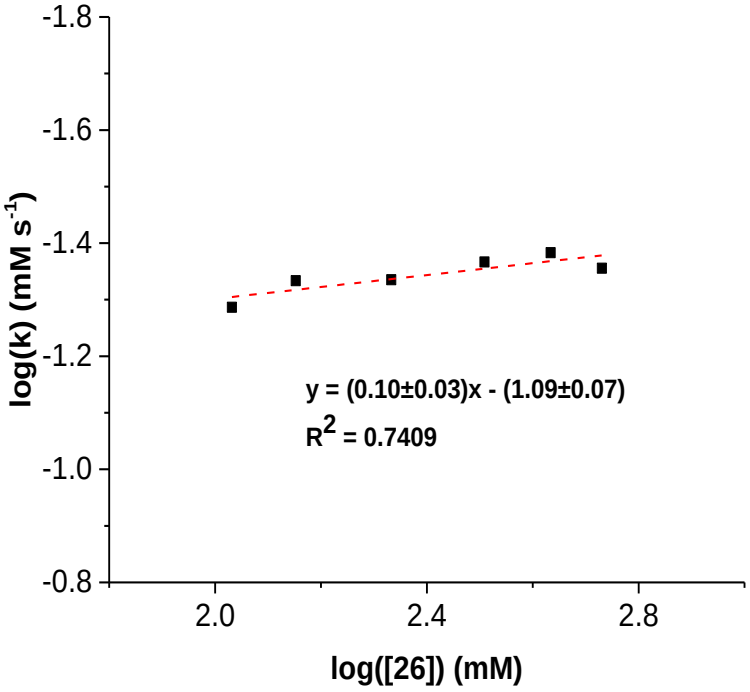

Entry	**26** (mM)	k_{max} (mM s^{-1})
1	107	0.0517
2	142	0.0464
3	215	0.0462
4	322	0.0430
5	430	0.0414
6	537	0.0441

Figure 2.37: Approximate initial rates measured from the concentration-time profiles displayed in Figure 2.36, and the corresponding logarithm plot.

The value obtained from the logarithm plot of 0.105 suggests that the reaction to produce **29** is zero order with respect to the Grignard reagent **26**. This is surprising, as **29** is formed directly from two equivalents of **26**.

2.4.4 Oxidation as the rate-limiting step

In order to appreciate the data resulting from the investigation performed, the calculated rate-laws for each product are presented below (Figure 2.38). The fractional orders obtained suggest that there are complex kinetic pathways occurring, which is expected due to multiple reactions occurring simultaneously.[110] From the derived data, it can be said that each product is formed from a single metal centre, as each product is best described as being first order with respect to iron. The lack of dependence on the concentration of the Grignard reagent, **26**, upon the rate of formation of each product suggests that the transmetallation steps taking place within the reactions are comparatively fast (with respect to the other reaction steps). Whilst these results are not particularly striking for any of the reactions taking place, the non-zero order dependence with respect to the electrophile, **25**, for each product, is. This suggests that for each of the products formed, the oxidation of iron is involved in the rate-limiting step of the cycle.

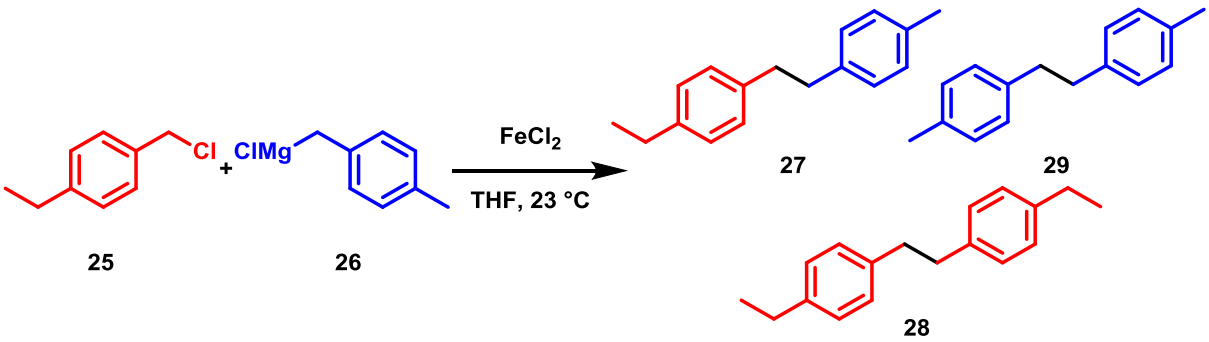

$$rate = \frac{d[\mathbf{27}]}{dt} = k[FeCl_2]^{1.2}[\mathbf{25}]^{1.1}[\mathbf{26}]^0$$

$$rate = \frac{d[\mathbf{28}]}{dt} = k[FeCl_2]^{1.4}[\mathbf{25}]^{2.8}[\mathbf{26}]^0$$

$$rate = \frac{d[\mathbf{29}]}{dt} = k[FeCl_2]^{1.1}\mathbf{25}^{0.7}[\mathbf{26}]^0$$

Figure 2.38: Experimentally obtained rate laws, with respect to iron, the electrophile **25** and the Grignard reagent **26**, for the production of **27**, **28** and **29**.

The calculated orders of reaction with respect to iron and **25** for the production of **28** are interesting, and suggest that a departure from steady state kinetics (that is, for an intermediate within a chemical reaction, the assumption that its concentration is low and varies slowly) may be occurring; [111, 112] this will be discussed further in section 2.5. One further reason as to why a large order effect is observed may be due the scrambling of benzyl ligands, which has been reported previously by Tonzetich on an iron(II) centre in the presence of benzyl Grignard reagents (Figure 2.39).[78]

Figure 2.39: Previously observed scrambling of benzyl moieties at an iron(II) centre; at a high concentration of Grignard reagent, the equilibrium would be expected to lie very much on the right-hand side.

It is therefore not unfeasible to suggest that at low concentrations of electrophile (and comparatively high concentrations of Grignard reagent), a more pronounced effect upon the rate would be observed due to perturbation of the equilibrium displayed in Figure 2.39, as is the case here.

It is also interesting to note that for each product, the positive effect induced by increasing the concentration of **25** appears to saturate once the concentration of **25** exceeds that of the Grignard reagent **26**. This suggests that the rate-limiting step within each reaction is changing, to one less dependent upon the electrophile. However, this cannot be transmetallation, or any step involving the Grignard reagent, as at no concentration is an order dependence observed with respect to **26**.

So as to comment on the nature of the oxidative process occurring at the iron-centre with the benzyl halide **25**, a Hammett study was undertaken, in which the substituent at the *para* position of the electrophile was varied.

2.4.5 Hammett study

The changing of a substituent within a substrate has both a steric and electronic effect. By altering the position *para* to the benzylic centre, steric effects are minimised, and the electronic factors of changing a substituent can be investigated in isolation.[106] Each substituent has a corresponding substituent parameter, σ_X, originally derived empirically by Hammett.[113] In the decades following Hammett's original report, several other substituent scales were developed, with varying rationales.[99] However in all cases, hydrogen acts as the absolute reference, and has a value $\sigma_H = 0$.[114] When investigating a new reaction, it is not always clear which σ scale must be used, and fitting the data obtained to several different parameters may be necessary. However the experiments required are the same in every case, whereby the reaction is carried out using a range of electronically diverse substrates, and the rate of each reaction (k_x) is recorded; $\log(\frac{k_x}{k_H})$ against σ_X is then plotted. The gradient of the plot yields a value (ρ) from which information on the sensitivity of the reaction towards substituent effects can be determined. The screen of *para*-substituted derivatives of benzyl chloride used in this study are displayed in Figure 2.40.

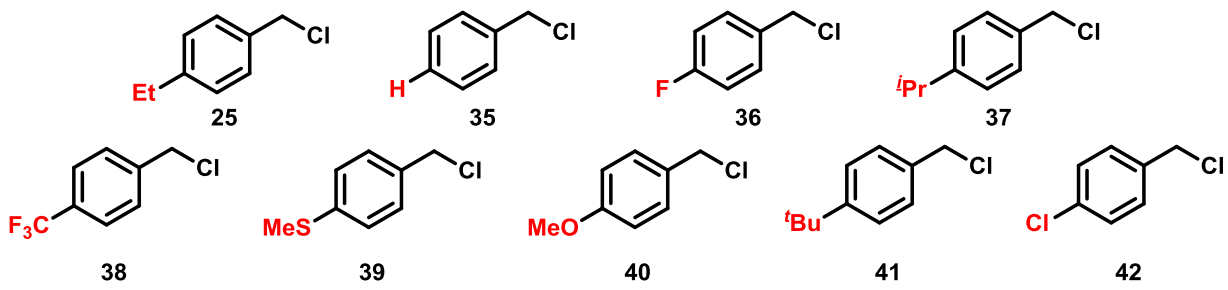

Figure 2.40: Screen of para-substituted benzyl chloride electrophiles (**25** and **35** – **42**) used in the iron-catalysed Kumada cross-coupling reaction as part of a Hammett study.

The corresponding concentration-time plots for the formation of each hetero-coupled product are displayed in Figure 2.41. As can be seen, a variation in the initial rates of reaction, calculated in each case *via* the method of initial rates, is observed upon changing the *para*-substituent of the electrophile.

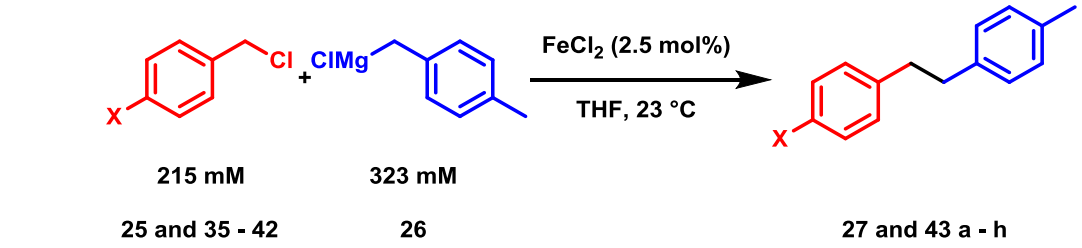

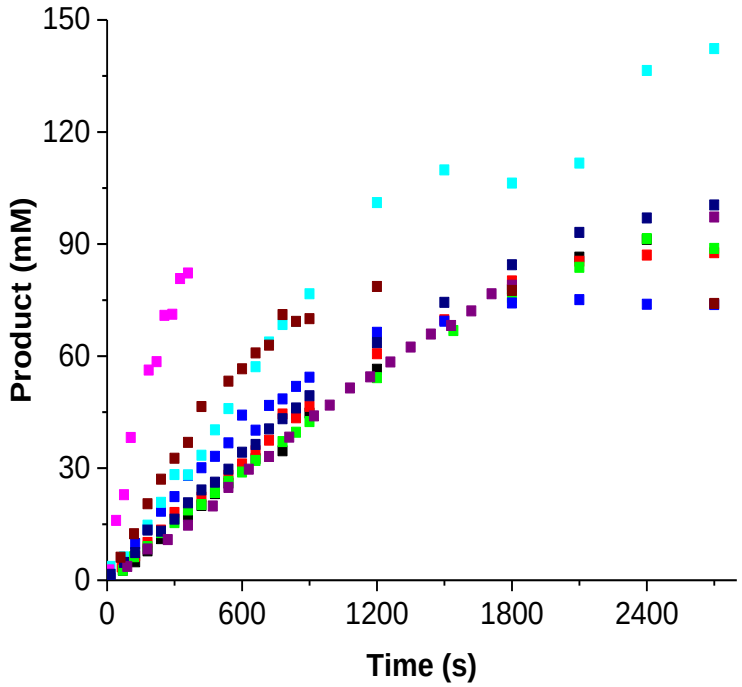

Entry	**X**	k_{max} (mM s^{-1})
1	H	0.0503
2	^{i}Pr	0.052
3	F	0.0468
4	Cl	0.076
5	OMe	0.0806
6	CF_3	0.3038
7	^{t}Bu	0.0539
8	Et	0.0491
9	SMe	0.1007

Figure 2.41: Concentration-time plots for the reaction of **26** with the substituted benzyl-chloride derivatives displayed in Figure 2.40, and the corresponding rates of reaction. ■ X = H, ■ X = ^{i}Pr, ■ X = F, ■ X = Cl, ■ X = OMe, ■ X = CF_3, ■ X = ^{t}Bu, ■ X = Et, ■ X = SMe

Using the data displayed in Figure 2.41, the ratio of $\log(\frac{k_x}{k_H})$ can be calculated and plotted against a desired scale of σ. For this reaction, a reasonable fit was not obtained using classical Hammett values, or with the σ^+ and σ^- scales (used in the case of a positive or negative charge build up, respectively, stabilised *via* resonance delocalisation by the substituent), suggesting that there is not a significant build-up of charge within the rate-limiting step of the reaction.[97] However, a good fit was obtained by using a scale devised by Creary, based on the rearrangement of methylene cyclopropanes in non-polar media, which serves as a measure of

the stabilisation provided by the substituent *X* on the benzylic radical suggested to form in the proposed transition state of the rearrangement (Figure 2.42).[115]

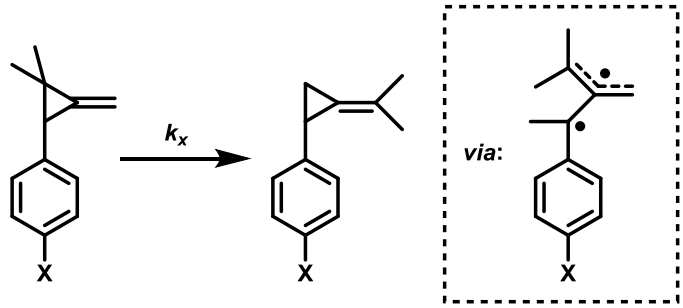

Figure 2.42: Rearrangement of a substituted methylene cyclopropane, used by Creary to develop the corresponding Creary scale.[115]

The corresponding σ_{Creary} values are displayed in Table 2.3; the corresponding Hammett plot is displayed in Figure 2.43 (no data is available for *X* = ^{i}Pr). Upon removal of the data corresponding to X = CF_3 (which has been suggested previously to induce a different mechanism within iron-catalysed cross-couplings),[96] a good fit is observed (Figure 2.43, red line, R^2 = 0.883), suggesting that the Creary parameter is valid for the reaction, with a value of +0.69 obtained for ρ. However the Creary scale is best applied to reactions with very low polar character; the mixing of the σ_{Creary} scale with the standard $\sigma_{Hammett}$ scale has been previously used by Norrby in order to account for polar influences within reactions.[97] Doing so here resulted in a slightly better fit compared to that for the σ_{Creary} parameter alone (Figure 2.43, black line, R^2 = 0.933), with a value for ρ of +0.97.

Table 2.3: σ_{Creary} values for the electrophiles used in the Hammett study, in addition to the $\sigma_{80/20}$ values obtained by mixing of the Creary and Hammett σ values in a 4:1 ratio.[115, 116]

Entry	**X**	σ_{Creary}	$\sigma_{80/20}$
1	H	0.0	0.0
2	F	-0.08	-0.034
3	Cl	0.12	0.144
4	OMe	0.24	0.138
5	^{t}Bu	0.13	0.064
6	Et	0.11	0.058
7	SMe	0.43	0.344

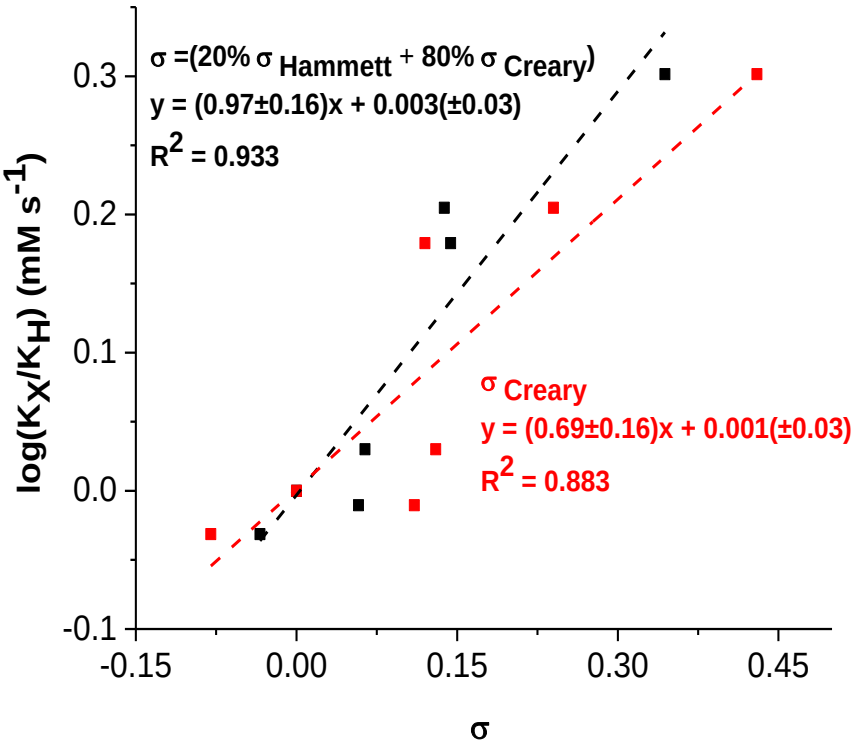

Figure 2.43: Hammett plot based on the data obtained from 2.41, and the values in Table 2.3.

The ρ value obtained suggests that the formation of a benzylic based radical could be occurring within the reaction, with some build-up of negative charge. This is most likely to occur *via* an inner-sphere process involving chloride abstraction from the benzyl halide, and formation of a caged radical pair, as the value obtained for ρ is not high enough to correspond to discrete radical species (Figure 2.44, *i*).[117] This process is consistent with the first step in an atom transfer radical polymerisation (ATRP) mechanism (Figure 2.44, *ii*).[118] ATRP systems using benzyl halide derivatives are known, and have been shown to proceed with an equilibrium constant of the magnitude 10^{-7}, suggesting a particularly disfavoured abstraction step, consistent with the rate-limiting data obtained here.[119]

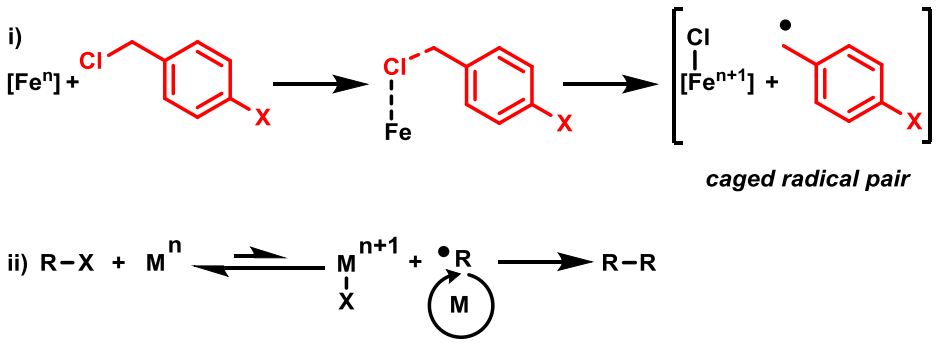

Figure 2.44: *i*: Proposed one-electron oxidation of iron by the benzyl halide electrophile, to form an iron-halide species. *ii*: The first step in an atom transfer radical polymerisation reaction, in which halide abstraction is proposed to take place.

2.4.6 Determination of activation parameters

In order to determine the activation parameters of the reaction, thus allowing for information regarding the transition state of the rate-limiting step of the reaction to be obtained, the rate constant for the production of the hetero-coupled product **27** was determined at varying reaction temperatures; the resulting concentration-time profiles are displayed in Figure 2.45.

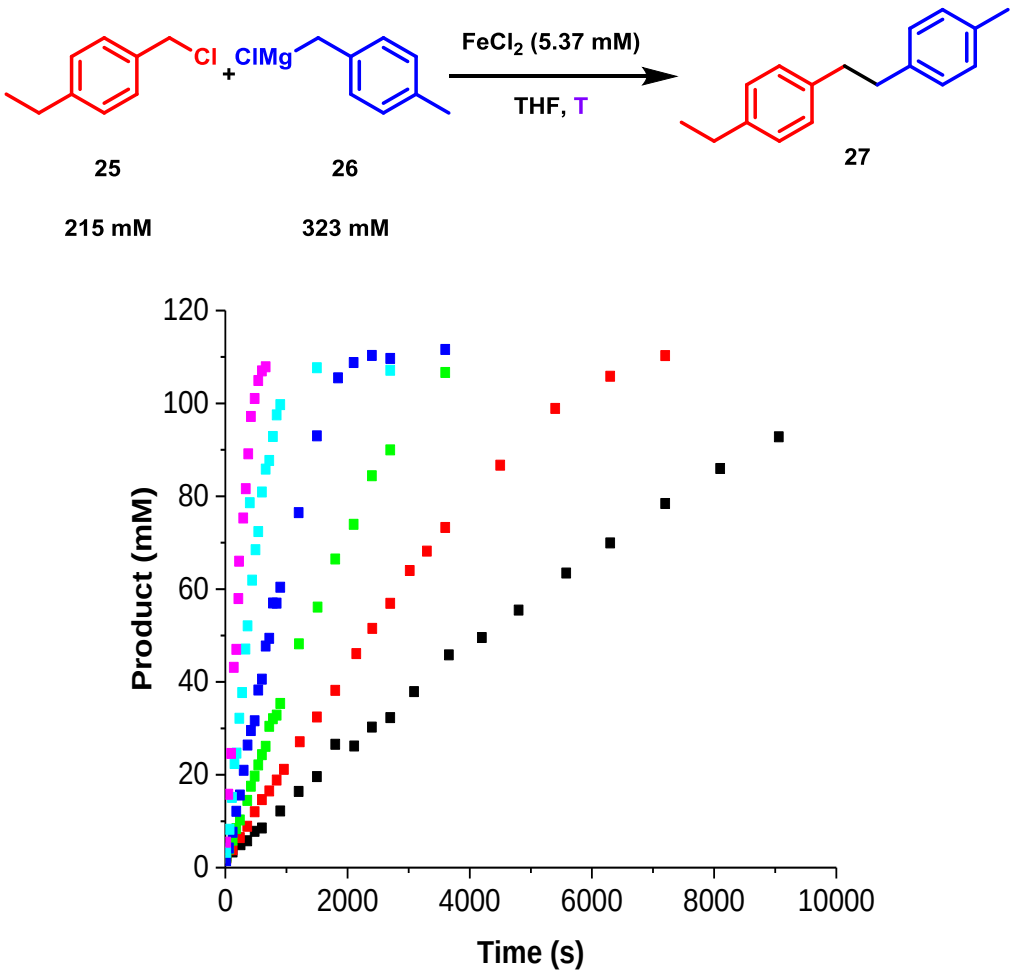

Figure 2.45: Concentration-time profiles for the reaction between **25** and **26**, using a $FeCl_2$ pre-catalyst, to give the hetero-coupled product **27**, at varying reaction temperatures. ■ T = 283 K, ■ T = 288 K, ■ T = 293 K, ■ T = 398 K, ■ T = 303 K, ■ T = 308 K

As displayed in Figure 2.45, there is a significant change in the rate of product formation upon varying the reaction temperature. The initial rate of reaction was recorded at each temperature using the method of initial rates, and using the linearised version of the Eyring equation, a plot of $(ln\frac{k}{T})$ against $\frac{1}{T}$ was carried out, from which $\Delta H^{\ddagger}$ and $\Delta S^{\ddagger}$ (from the gradient and intercept, respectively) can be obtained (Figure 2.46).

$$ln\frac{k}{T} = -\frac{\Delta H^{\ddagger}}{RT} + \frac{\Delta S^{\ddagger}}{R} + \ln\frac{k_B}{h}$$

$$\Delta G^{\ddagger} = \Delta H^{\ddagger} - T\Delta S^{\ddagger}$$

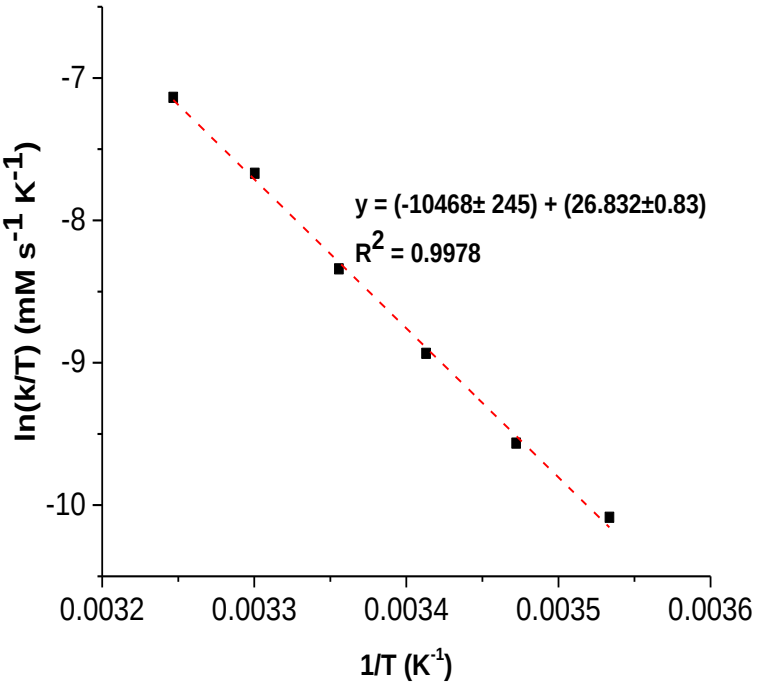

Entry	***T*** (K)	*k* (mM s^{-1})
1	283	0.0118
2	288	0.0202
3	293	0.0386
4	298	0.0711
5	303	0.1415
6	308	0.2452

Figure 2.46: Linearised version of the Eyring equation, in addition to the equation to find the free energy of activation and the corresponding plot of $(ln\frac{k}{T})$ against $\frac{1}{T}$, from which the values of enthalpy and entropy of activation can be found. *k* = rate constant; T = absolute temperature; $\Delta H^{\ddagger}$ = enthalpy of activation; R = the gas constant' $\Delta S^{\ddagger}$ = entropy of activation k_B = Boltzmann constant; *h* = Planck's constant.

An excellent fit is observed for the plot displayed in Figure 2.46. The calculated values of the enthalpy and entropy of activation and the corresponding free energy of activation for the reaction are displayed in Table 2.4, along with the values for the two homo-coupled products, **28** and **29**, which were derived using the same method.

Table 2.4: Experimentally calculated parameters for the reaction of **25** with **26**, using a $FeCl_2$ pre-catalyst, to give the bi-benzyl product **27**, **28** and **29**.

Entry	Activation parameter	**27**	**28**	**29**
1	$\Delta H^{\ddagger}$ (kJ mol^{-1})	+87.0 (±2.04)	+90.9 (±6.04)	+86.0 (±3.76)
2	$\Delta S^{\ddagger}$ (J mol^{-1} K^{-1})	+25.5 (±0.59)	+25.9 (±1.72)	+21.4 (±0.94)
3	$\Delta G_{298}{}^{\ddagger}$ (kJ mol^{-1})	+79.4 (±1.86)	+83.2 (±5.53)	+79.6 (±3.48)

The positive values obtained for the experimentally derived enthalpy of activation and free energy of activation are expected, as the data obtained correspond to the rate-determining step of the reaction. The positive value obtained for the entropy term reveals that the transition state of the rate-limiting step involves an increase in entropy, suggestive of a dissociative mechanism, in which ligand dissociation from the metal centre occurs before substrate coordination.[120] However it should be noted that associative and dissociative mechanisms represent extreme ends of what is a mechanistic continuum;[121] accordingly the data is perhaps best explained as a dissociative interchange step, I_D, in which the transition state is comprised mostly of a bond breaking process, with some bond forming character in an encounter complex, as displayed in Figure 2.47.

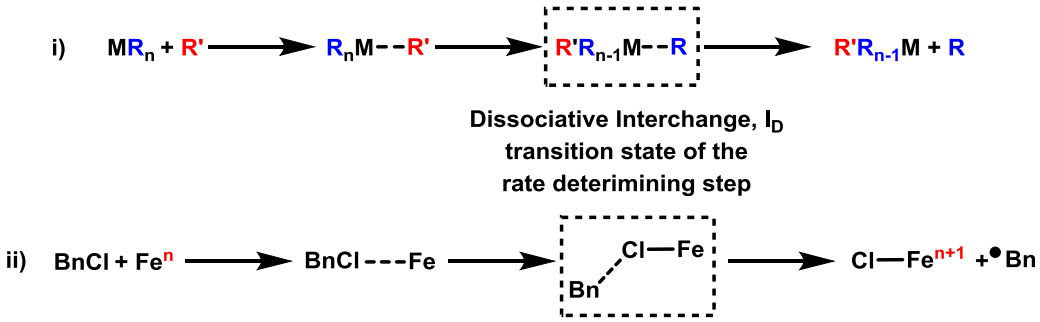

Figure 2.47: *i*: Representation of a dissociative interchange (I_D) transition state. *ii*: Proposed I_D transition state for the reaction between an iron species and benzyl halide electrophile.

2.5 Mechanistic considerations

The fact that the activation parameter values are similar for each of the products formed (within error) suggests that there is no thermodynamic preference for the formation of one bi-benzyl product over the other. This is expected, due to the electronic and steric similarities of the *para*-methyl and *para*-ethyl substituents, which were deliberately chosen so as to minimise any bias towards one product or the other in such a scenario. In effect, once bonded to iron, the *para* substituent on each benzyl fragment becomes indistinguishable from the perspective of reactivity, whilst still allowing for product identification. Therefore, for an iron centre on which there are two or more benzyl fragments bound, there will be no steric or electronic favourability towards the formation of one of the products **27**, **28** or **29**. From this point onwards in the discussion, the benzyl groups on an iron centre will be referred to simply as 'Bn', rather than differentiating between the *para*-methyl or -ethyl derivative.

As the iron present within solution is initially in the (+II) oxidation state following the reaction of iron(II) chloride with **26** (yielding **31**), it is suggested that an oxidation to iron(III)

takes place, with formation of an iron-halide species and a benzyl radical within a caged intermediate, **44**. This step is proposed to be rate-limiting and represents the first step within an ATRP mechanism.[122] Displayed in Figure 2.48 are two pathways that can be reasonably suggested to be taking place following the formation of **44**, representing a further oxidation (path A) or a reductive elimination (path B).

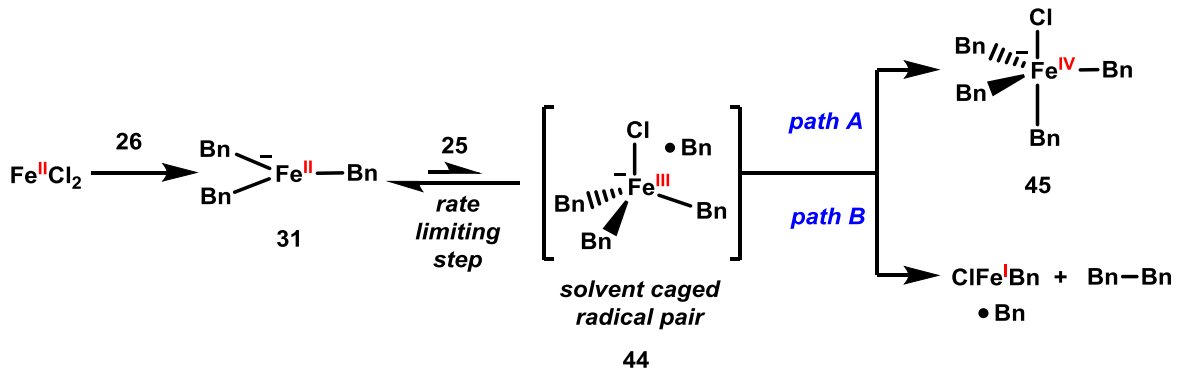

Figure 2.48: Proposed pathways for the complex **31** to follow, involving collapse of the solvent cage to yield an iron(IV) intermediate **45** (path A), or a reductive elimination to yield an iron(I) intermediate (path B).

The first path involves collapse of the caged radical pair to afford an iron(IV) intermediate, **45** (Figure 2.48, path A). However, within an ATRP mechanism further oxidation of the metal centre (to M^{n+2}) does not occur, most likely due to the stabilisation provided by the solvent cage.[122] It is therefore suggested that oxidation to iron(IV) is unlikely to occur here, and that a reductive elimination from **44** takes place, yielding an iron(I) species and formation of a bi-benzyl product, with the caged radical pair still intact (Figure 2.48, path B). Reductive elimination from iron(III) to iron(I) has been previously proposed by Norrby, who found the process to be thermodynamically feasible using DFT within an atom transfer manifold.[46 97]

2.5.1 Proposed catalytic cycle

Taking all of the preceding data together, there are several points to be drawn together, from which suggestions toward the reaction mechanism can be made:

i) The reaction of simple iron salts and a large excess of benzyl Grignard reagent, **26**, results in the homoleptic iron species **31**, which alone does not afford homo-coupled product. However, in the presence of an oxidant (DCE or a benzyl halide, **25**) coupling takes place.

ii) Heteroleptic iron-benzyl / halide species are not isolable, but their reactivity towards the electrophile **25** was confirmed through a series of stoichiometric experiments.

iii) Kinetic studies indicate that the reactions to produce **27**, **28** and **29** all operate *via* a monometallic iron centre, with a zero-order dependence on the Grignard reagent **26**, suggesting that transmetallation occurs quickly within the reaction timeframe. However, the rate of formation of each product is non-zero with respect to the electrophile **25**, suggesting that oxidation of iron is rate-limiting in each case.

iv) However, when the electrophile is present in excess this rate enhancement is less pronounced.

v) A Hammett analysis of the reaction to produce the hetero-coupled products **26** and **43a-h** suggests that the formation of a benzylic radical occurs within the reaction, consistent with the first step in an ATRP mechanism.

vi) An Eyring investigation suggests that the transition states of the reactions to produce **27**, **28** and **29** occur *via* dissociative interchange processes, in which the transition state of the rate-limiting step of the reaction has some bond forming character but is mainly composed of a bond-breaking encounter complex.

Considering the above summation, the catalytic cycle displayed in Figure 2.49 is suggested, based on an iron(I)/(II)/(III) pathway. All of the iron intermediates are proposed to exist as anionic ferrate species. The cycle is based upon a series of mono-metallic iron species, consistent with the first order dependence upon iron for each of the products formed. Transmetallation steps within the cycle are proposed to be fast, accounting for the zero-order dependence upon **26** observed in each case. It is important to note that within the cycle displayed in Figure 2.49, the benzyl groups bound to iron can refer to either the 4-methyl and 4-ethyl moieties.

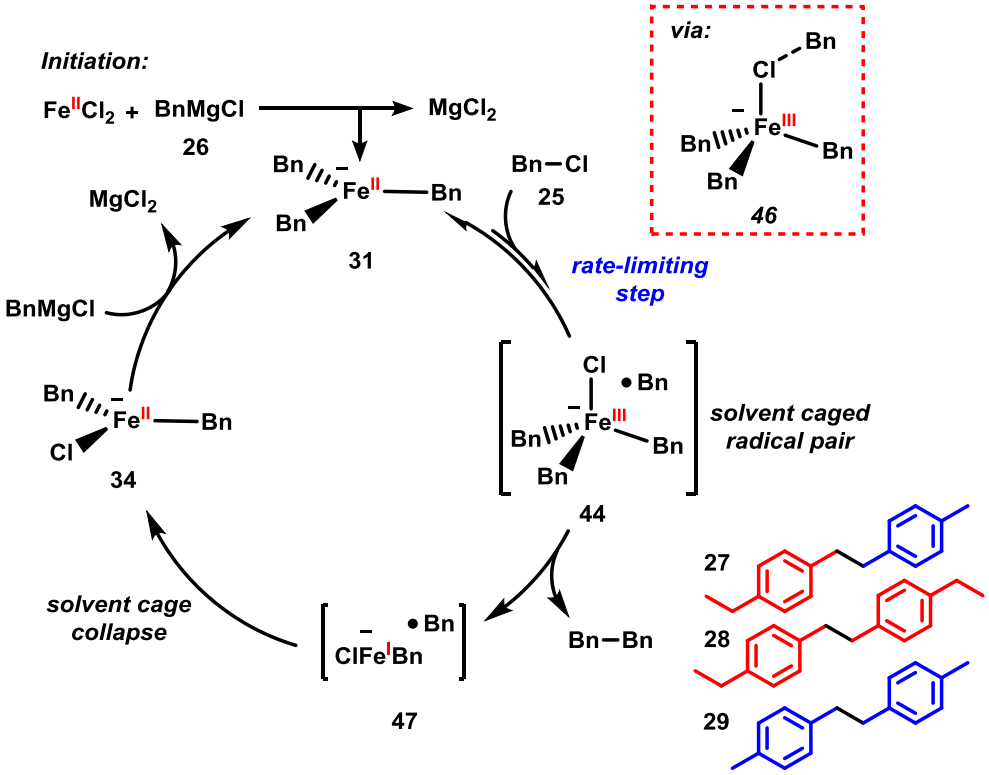

Figure 2.49: Proposed catalytic cycle for the reaction between **25** and **26**, using an iron(II) chloride pre-catalyst, based upon the data described above.

Following the formation of **31** from the reaction of iron(II) chloride with **26** (as demonstrated by ^{1}H NMR studies), the rate-limiting step of the cycle is proposed to be the reversible oxidation of iron(II) to iron(III), as observed within ATRP chemistry. This is consistent with the positive order dependence upon **25** for each product formed, and the Hammett studies, which indicate the formation of a benzylic radical is taking place. The transition state of this rate-limiting step is suggested to go *via* the formation of the interchange complex **46**, consistent with the positive entropy value obtained from the Eyring analysis of the reaction. Upon formation of the solvent caged radical pair **44**, a direct reductive elimination to an iron(I) species is proposed, with formation of a bi-benzyl product (**27**, **28** or **29**). As discussed in section 1.4, iron(I) has been demonstrated to be the lowest kinetically relevant oxidation state accessible within catalysis for several systems,[61, 123] suggesting that further reduction is unfeasible. The iron(I) intermediate **47** is likely to be much more susceptible towards oxidation than **44**, and it is suggested that solvent cage collapse, yielding an iron(II) species **34**, now takes place. A final transmetallation (consistent with the results in Figure 2.13) regenerates **31** and restarts the cycle. Thus, any one of the three bi-benzyl products can be formed from the cycle, which together with the similar reaction parameters obtained for each product, is suggested as the reason as to why the system behaves so unselectively.

2.5.2 Autocatalytic manifold

To account for the decreased order dependence upon **25** observed when the electrophile is present in high concentrations, it is suggested that an autocatalytic process, rather than a change in the rate-determining step of the reaction, is taking place.[124] In this scenario, one of the products formed acts as a starting material or catalyst for the overall reaction, resulting in a deviation from the steady-state approximation (Figure 2.50, *i*). [111, 112] Due to the first step of the proposed mechanistic cycle (the formation of **44**) being reversible and rate-limiting , this equilibrium is likely to saturate at a high ratio of **25** : Fe.

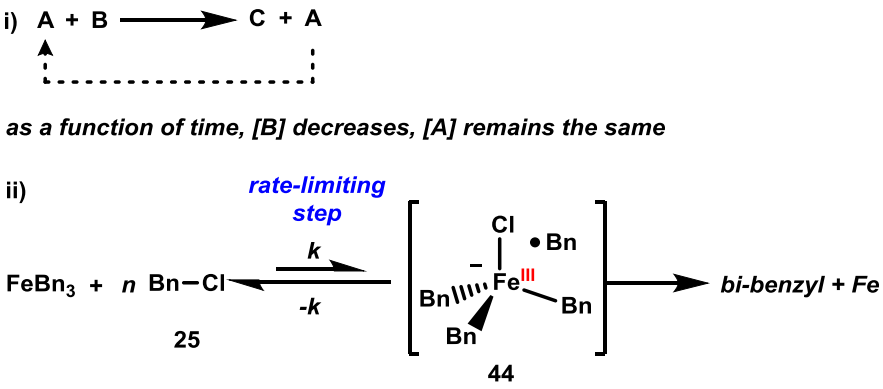

Figure 2.50: *i*: Representation of an auto-catalytic reaction. *ii*: The proposed equilibrium for the reversible abstraction of chloride from **25**.

Therefore, if one measures the initial rate of reaction as a function of increasing BnCl concentration (as carried out in this work, where the method of initial rates was employed as a kinetic probe), a positive effect with respect to the rate of product formation will be observed (where *n* > Fe in Figure 2.50, *ii*), followed by a plateauing (where *n* >> Fe in Figure 2.50, *ii*).

This behaviour is observed for the formation of each of the bi-benzyl products **27**, **28** and **29** when the concentration of **25** is varied (in each case a decrease in the order dependence with respect to electrophile was recorded). However, it is demonstrated most clearly for the production of the homo-coupled electrophile product **28**, the data for which is re-plotted in Figure 2.51. As can be seen, the logarithm plot demonstrates a pronounced kink in the gradient, demonstrating the effect clearly. The saturation appears to occur once the **25** : Fe ratio reaches 100:1.

However, this kink alone does not rule out the possibility of a change in the rate determining step of cycle, to a step less dependent upon **25**. The confirmation that an auto-catalytic process, rather than a change in rate determining step, is taking place is demonstrated

by the subsequent increase in the rate of product formation as time progresses within the reactions employing a high concentration of **25**. This is clearly visible due to the inflection point within the concentration-time plots for reactions where [**25**] > 215 mM (■, ■ and ■, Figure 2.51). This increased rate of reaction, following a brief induction period, is due to the ratio of **25** : Fe decreasing as time progresses, due to the consumption of **25** (to form bi-benzyl products) and the continuous regeneration of the iron catalyst. Therefore, the equilibrium within the rate-limiting step is no-longer saturated, and the concentration of **25** will positively influence the rate of product formation (*n* > Fe in Figure 2.50, *ii*).

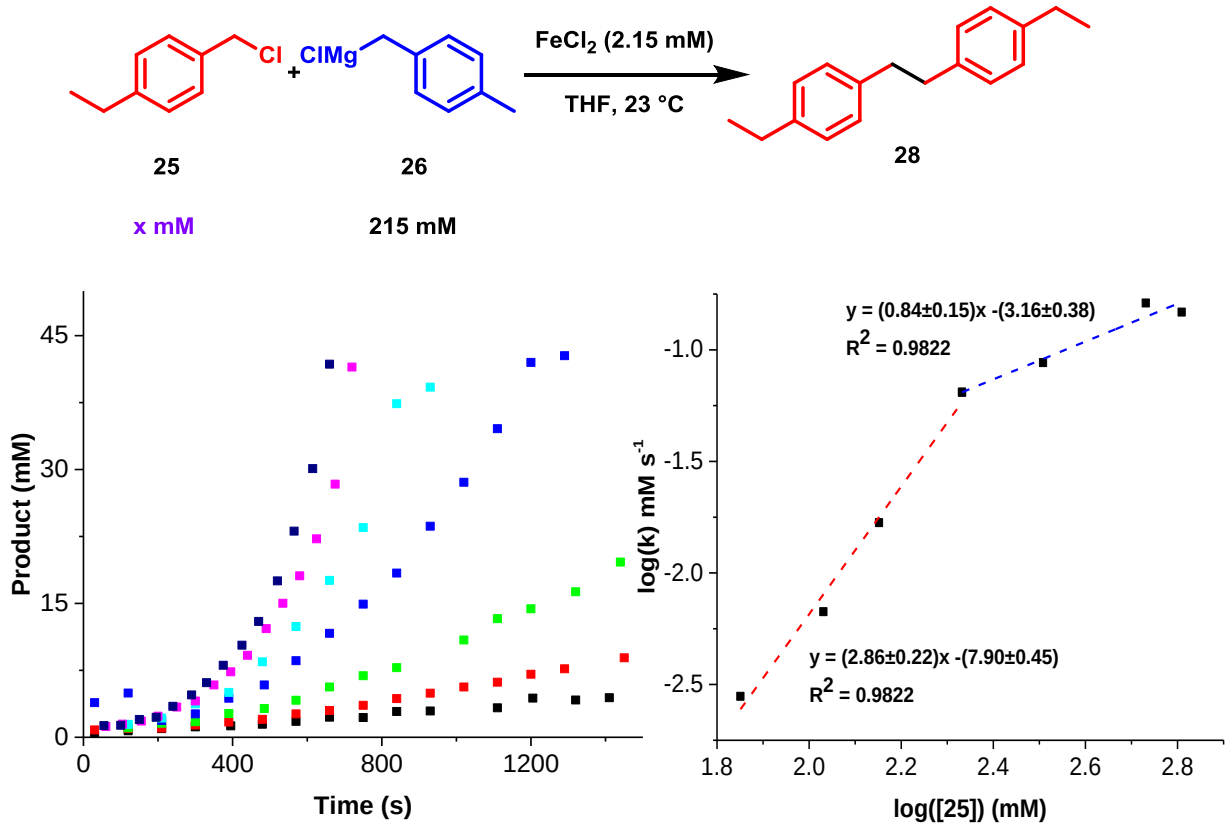

Figure 2.51: Demonstration of the auto-catalytic behaviour of the reaction between **25** and **26** using an $FeCl_2$ pre-catalyst. Concentration-time plots for the reaction of **25** and **26**, using a $FeCl_2$ pre-catalyst, using a varying concentration of the electrophile **25**. ■ [**25**] = 71 mM, ■ [**25**] = 107 mM, ■ [**25**] = 142 mM, ■ [**25**] = 215 mM, ■ [**25**] = 322 mM, ■ [**25**] = 538 mM, ■ [**25**] = 646 mM; in addition to the resulting logarithm plot.

Thus, the sigmoidal behaviour observed within the concentration-time plots when the concentration of **25** is varied can be ascribed to an autocatalytic regime, further supporting the rate-limiting step of the cycle as being the reversible transfer of chloride from **25** to iron. Therefore, the unusually large order of reaction obtained (2.86) can be thought of as more of an amplification effect as a result of the steady state approximation not being valid, rather than

the traditionally collected order of reaction value obtained when operating within a system at steady state[111, 124].

On the basis that the proposed rate-limiting step of the reaction involves iron and **25**, one would expect to see the same behaviour (that is, evidence of an auto-catalytic manifold) within the concentration time plots resulting from the variation in iron concentration for the production of **28** (the data for which is re-plotted in Figure 2.52). However, a linear logarithm plot is obtained, with no kink, suggesting that saturation does not occur.

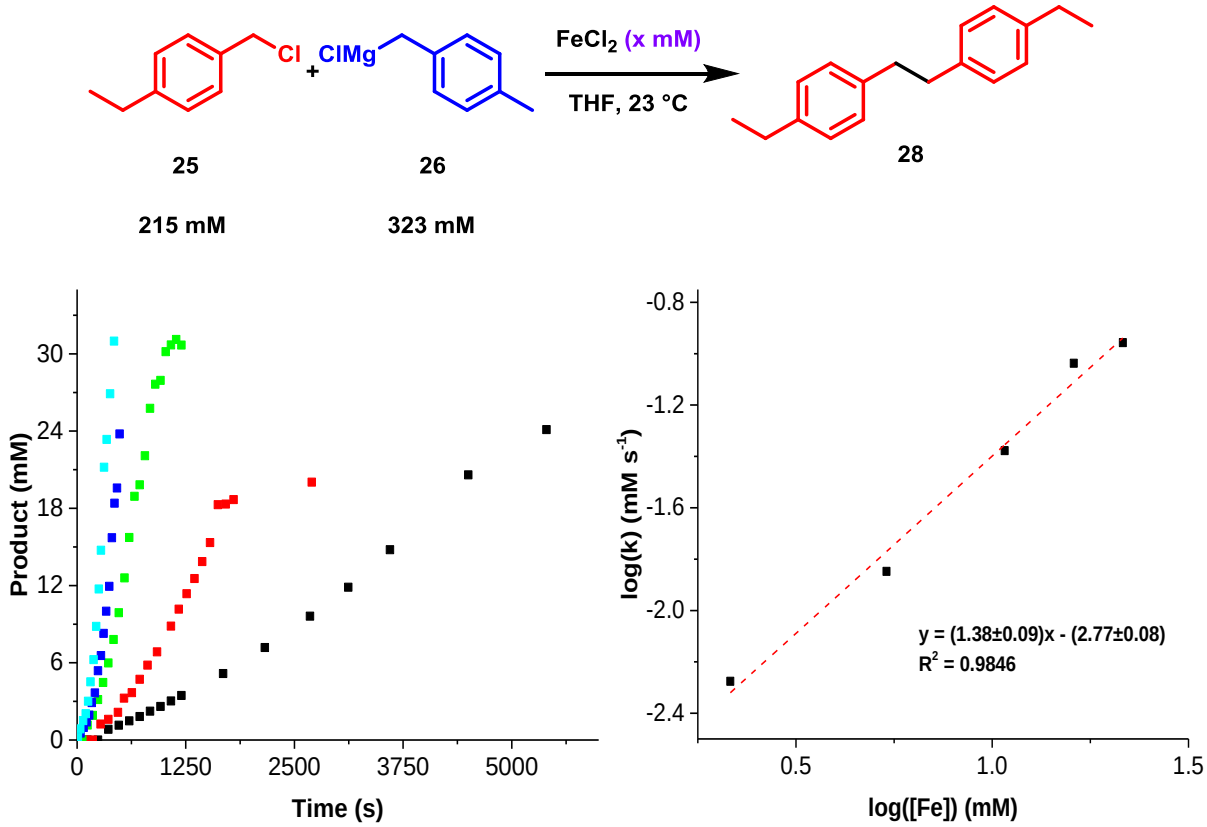

Figure 2.52: Concentration-time plots for the reaction of **25** and **26**, using a varying concentration of the $FeCl_2$ pre-catalyst. ■ [Fe] = 2.15 mM, ■ [Fe] = 5.37 mM, ■ [Fe] = 10.8 mM, ■ [Fe] = 16.1 mM, ■ [Fe] = 21.2 mM; in addition to the resulting logarithm plot.

However, a closer inspection of the reaction concentrations at which this data was recorded suggests that the saturation effect may have already ended. The lowest concentration of iron for which rate data was obtained corresponds to a ratio of **25** : iron of 100:1 the ratio at which the inflexion point of the saturation is observed in Figure 2.51. All other rate data was recorded at a higher concentration of iron (*i.e.* a ratio of **25** : iron of below 100:1, within the saturated regime). One would therefore expect a greater order of reaction to be observed at a concentration of iron below 2.15 mM, which is unfortunately not currently available.

2.6 Conclusions and future work

A thorough investigation into the iron-catalysed reaction between a benzyl halide, **25**, and a benzyl Grignard reagent, **26** has been carried out, revealing several significant points towards elucidation of a proposed reaction mechanism, some of which may be relevant in the more general context of iron-catalysed cross-coupling reactions. In the presence of an iron(II) chloride pre-catalyst, the reaction proceeds rapidly and unselectively to give the products **26** **27** and **28**. No improvement in the selectivity of the reaction was observed through alteration of the reaction temperature, or the period of time over which the reagents were added.

Although the homoleptic, iron(II) 'ate' complex **31** was isolated, it is stable for an extended period of time and does not afford the homo-coupled bi-benzyl product, **28**. However, upon the addition of an oxidant, homo-coupling occurs rapidly, suggesting that an oxidation of the iron centre is necessary before product formation. This was proposed to occur from a heteroleptic ferrate species; although none were successfully isolated here, their competency towards carbon-carbon bond formation was demonstrated through a series of stoichiometric reactions with the electrophile **25**.

The results of a detailed kinetic profiling of the reaction, from which the rate laws for the production of each bi-benzyl product were derived, suggest that each of the products are formed from a single iron centre, ruling out any bimetallic bond-forming pathways. Further, the oxidation of the active iron species within the reaction was found to be rate-limiting for each of the products **27**, **28** and **29**, suggesting that prior to the formation of each product, oxidation of the iron-centre by the electrophile within the reaction, **25**, occurs. A Hammett profile of the reaction, using a range of electronically diverse *para*-substituted benzyl chloride derivatives, suggested that the formation of a benzylic radical was occurring within the reaction. This is consistent with an atom-transfer step and the formation of a caged radical intermediate, **44**.

An Eyring analysis allowed for the derivation of the activation parameters $\Delta H^{\ddagger}$, $\Delta S^{\ddagger}$ and $\Delta G^{\ddagger}$ for the formation of each of the products **27**, **28** and **29**. The similarity between the obtained values for each parameter suggests that there is no thermodynamic preference for the formation of any one of the products over the others. The positive value of the derived entropic terms is suggestive of a dissociative interchange mechanism, with the transition state of the rate-limiting step mainly composed of a bond-breaking process.

The proposed catalytic cycle is based upon an iron(I)/(II)/(III) regime, in which the rate-limiting step is the oxidation of iron(II) to iron(III), suggested to occur *via* a chloride abstraction from **25**. This is in agreement with the rate-law data obtained for each product, in addition to the Hammett and Eyring studies. The transition state of this rate-limiting step is proposed to be composed of an encounter complex, with mostly bond breaking character. On the basis of the increased rate of product formation observed as a function of time when the electrophile **25** is present at high concentrations, an auto-catalytic regime was suggested to be taking place.

The use of DCE as an oxidant was shown to allow the iron-catalysed homo-coupling of the Grignard reagent to occur. However, it is not clear if DCE acts as a one or two-electron oxidant. If using electrochemistry, the oxidation from iron(II) to iron(III) was found to be reversible or to lead to decomposition without further oxidation to iron(IV), a reductive step from iron(III), as proposed, would appear likely.

A brief attempt was made to probe the reaction discussed in this Chapter using EPR spectroscopy, but no EPR signals were observed from aliquots taken from reaction mixtures. A more thorough examination of the reaction would still be worthwhile and could be used to provide support for the formation of an iron(I) intermediate. Importantly spin-quantified spectra should be obtained, so as to be able to comment upon the proportion of total iron speciation that any observed species may constitute.

Ongoing work within the Bedford group is probing the mechanism of the reaction *via* DFT and encouraging results have so far been obtained in support of the halide abstraction step between **31** and **25**, to yield an iron(III) species such as **44**. If the theoretically derived reaction parameters correspond well to the experimentally obtained values, then strong support in favour of the proposed cycle would be obtained.

The data obtained here demonstrate that oxidation of iron is likely to constitute the rate-limiting step of the reaction. As mentioned in Chapter 1, there is currently a disparity between the knowledge regarding reduced and oxidised iron species within cross-coupling reactions. If the oxidation of iron is found to be rate-limiting across a representative body of iron-catalysed processes, then catalyst design in future studies should be amended accordingly.

If, as proposed, a radical mediated mechanism is taking place within the reaction a racemisation of any stereochemistry present at the benzylic carbon would be expected within the product, due to the formation of a benzylic-based radical. If therefore instead of benzyl chloride a chiral-benzyl derivative was used, one would expect a racemised product to be

formed (Figure 2.53, *i*). However, if a retention (Figure 2.53, *ii*) or inversion (Figure 2.53, *iii*) of stereochemistry was observed, then this would be suggestive of a concerted, two-electron oxidative addition or a S_N2 step to be occurring.

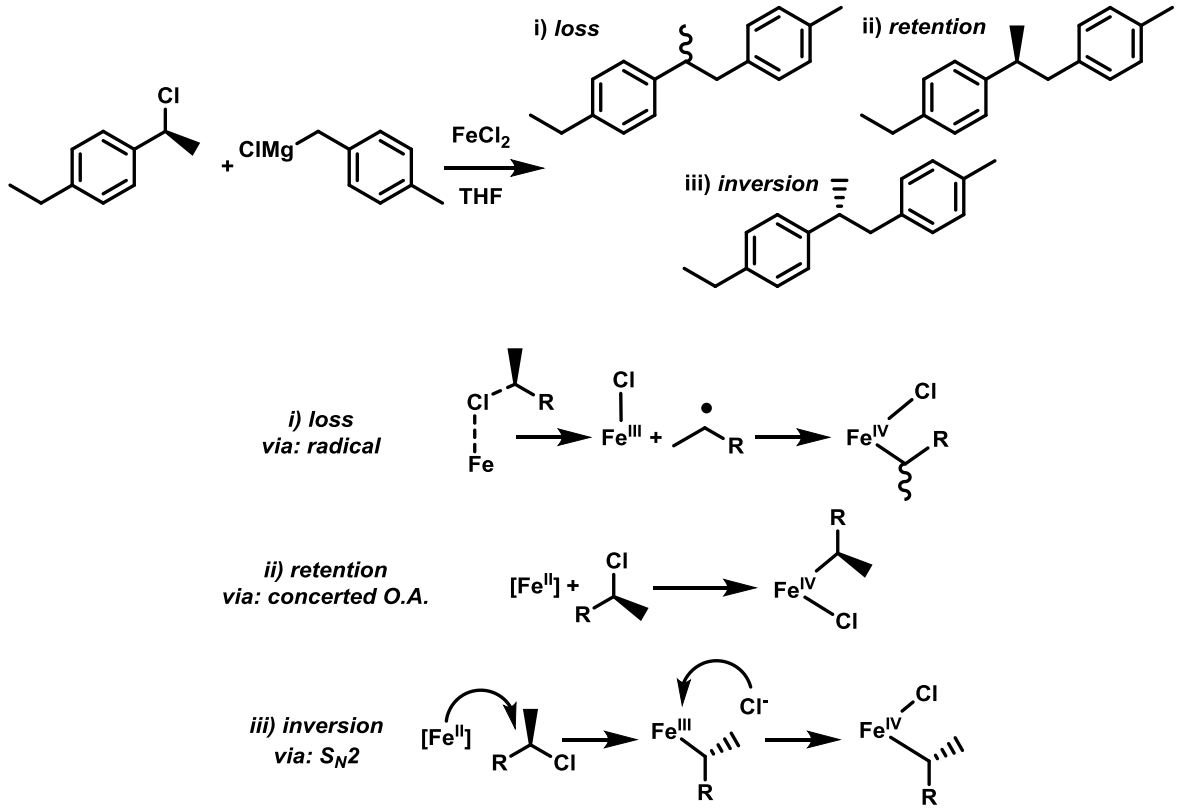

Figure 2.53: Proposed use of an enantiopure benzyl chloride derivative, and the resultant stereochemistry expected should one of the mechanisms above be taking place within the reaction.

Chapter 3 *Equilibria resulting from the addition of an NHC ligand to an iron-catalysed cross-coupling*

3.1 Introduction

In the previous Chapter, the Kumada cross-coupling reaction of the benzyl halide **25** with the benzyl Grignard reagent **26** using an iron(II) chloride pre-catalyst was investigated. The reaction produces the cross-coupled product **27**, in addition to the homo-coupled products **28** (from the electrophile) and **29** (from the Grignard reagent). A kinetic profiling led to the suggestion that the oxidation of an iron(II) to iron(III) was rate-limiting for each product (Figure 3.1).

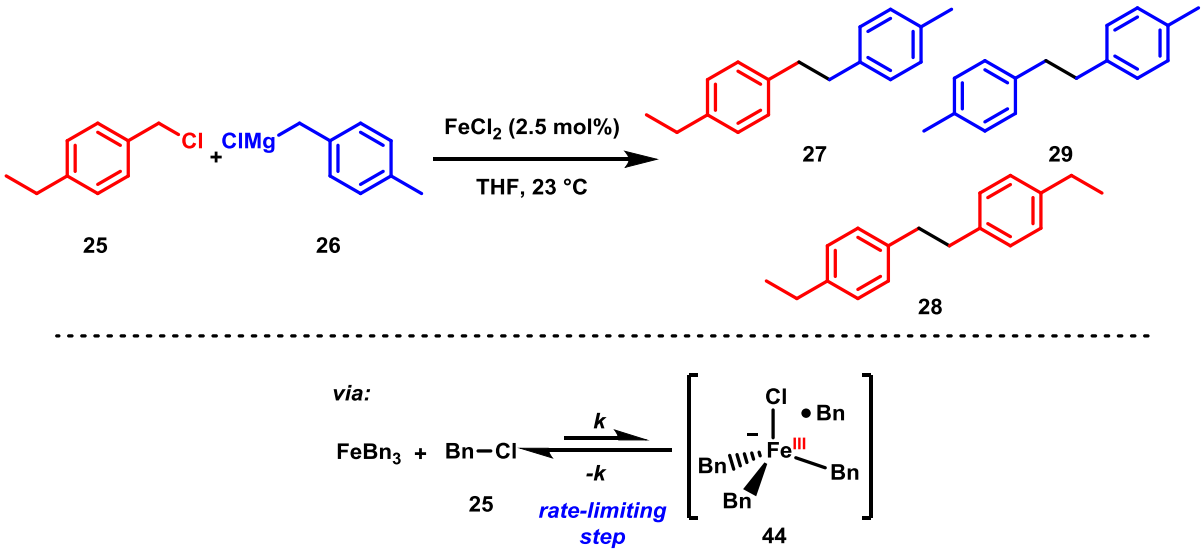

Figure 3.1: The iron-catalysed Kumada cross-coupling investigated in the previous Chapter, proposed to go *via* a reversible and rate-limiting oxidation of iron(II) to iron(III).

The selectivity of the reaction was shown to be insensitive to both the rate at which the reagents were added and the temperature of the reaction (the same distribution of products was observed in all cases). However, the effect of ligands upon the reaction was not discussed.

3.1.1 NHC ligands in iron-catalysed Kumada cross-coupling reactions

Due to their ease of synthesis and structural diversity, N-heterocyclic carbene (NHC) ligands have been used extensively within iron-catalysed Kumada cross-coupling reactions.[84] Subtle changes to the structure of the NHC used within a catalytic reaction can alter the resulting steric and electronic properties of the metal centre, which in turn has been shown to have a profound effect upon the activity of the resulting system.[82] The first report of an iron-NHC system within iron-catalysed cross-coupling reactions was from Bedford, who found that an NHC ligand bearing *tert*-butyl groups, in combination with an iron(III) chloride, delivered excellent yields in the coupling of an alkyl halide with an aryl Grignard reagent (Figure 3.2,

i).[70] A bulkier NHC, SIPr, was used by Nakamura in combination with an iron(III) fluoride pre-catalyst to afford excellent selectivity in a bi-aryl coupling reaction (Figure 3.2, *ii*),[71] while the closely related SIMes was employed by Cárdenas[72] to successfully effect an alkyl-alkyl coupling (Figure 3.2, *iii*).

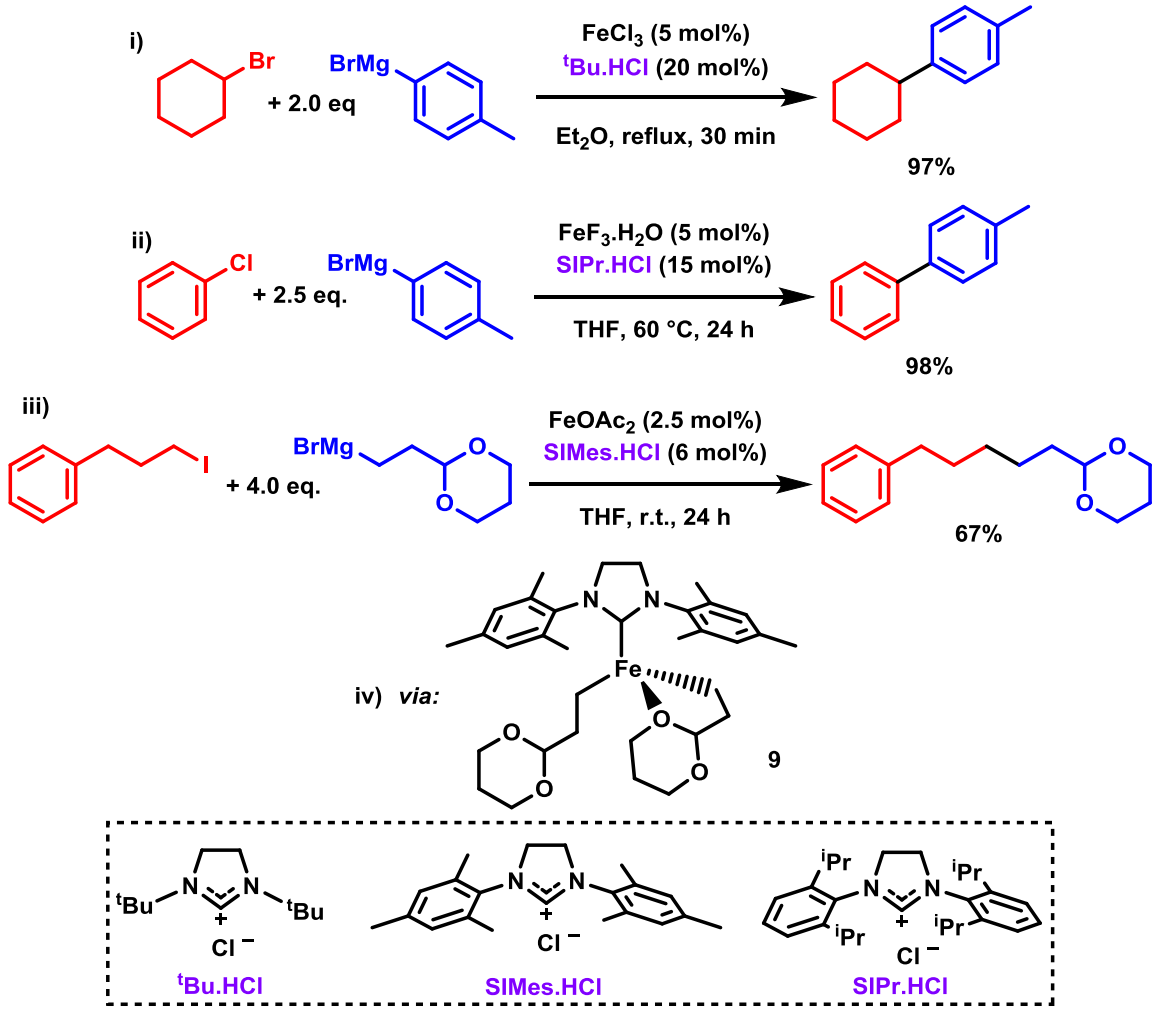

Figure 3.2: Examples of iron-catalysed Kumada cross-coupling reactions employing a NHC-ligand from Bedford,[70] Nakamura[71] and Cárdenas[72] / Neidig.[77]

More recently, Neidig[77] has demonstrated that the bulk of the iron speciation within the system reported by Cárdenas exists as an iron(II) NHC complex, demonstrating the effectiveness of the NHC ligand towards preventing the formation of homoleptic ferrate complexes (Figure 3.2, *iv*). It can therefore be reasonably hypothesised that the use of an NHC ligand within the iron-catalysed reaction of **25** and **26**, as reported in Chapter 2, should result in different iron speciation when compared to the ligand-free reaction, which in turn may impart a more selective catalytic reaction.

3.1.2 General considerations

The work in this Chapter is concerned with trying to address the lack of selectivity observed in the ligand-free reaction between **25** and **26** using simple iron salts, through the use of a ligand. For each of the three well-defined iron pre-catalysts used, no improvement in reaction selectivity was recorded. An investigation into why this may be the case was carried out, focussing on the iron-speciation observed from mixtures of $FeCl_2$, the NHC ligand SIPr and **26**.

3.2 Kumada cross-coupling in the presence of ligands

*3.2.1 Synthesis, and performance as pre-catalysts, of the complexes **48**, **49** and **50·THF***

Though the reaction investigated in Chapter 2 was deliberately chosen as it could be performed in the absence of an added ligand, it would be remiss not to investigate whether an added ligand could have an influence upon the reaction rates and product distributions of the reaction. Accordingly, a range of well-defined iron-(II) complexes were prepared, each bearing a different class of well-known ligand: a monodentate phosphine, to give complex **48**, a bidentate phosphine, to give complex **49** and an NHC ligand, to give complex **50·THF** (Figure 3.3).

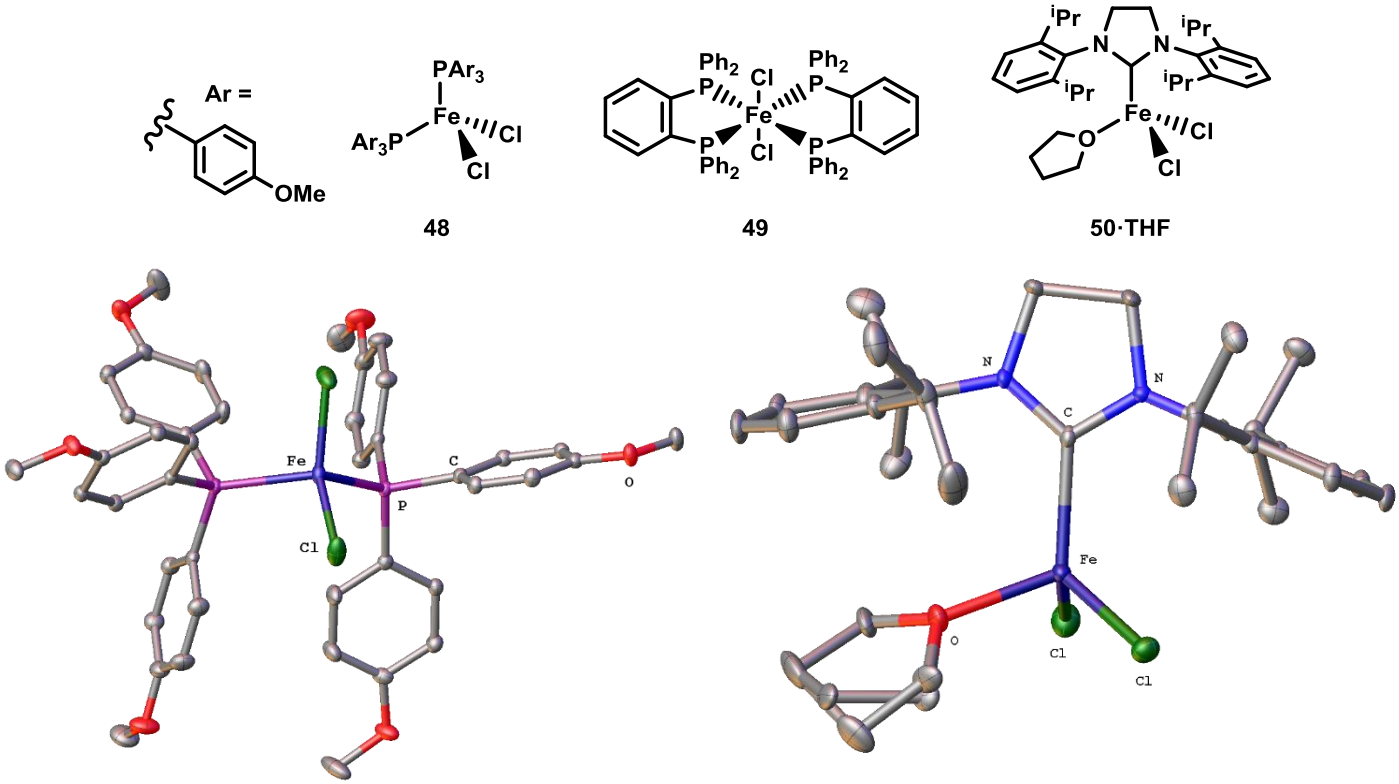

Figure 3.3: Iron(II) complexes **48**, **49** and **50·THF** synthesised for use as pre-catalysts in the cross-coupling reaction between **25** and **26**, and the corresponding X-ray crystal structures of **48** (bottom left) and **50·THF** (bottom right).

The complexes **48** – **50** were characterised *via* X-ray crystallography and, in the case of **50**, paramagnetic ^{1}H NMR spectroscopy. Each was then used separately as a pre-catalyst for the reaction between **25** and **26**, with the resulting product distributions displayed in Table 3.1, along with the result when $FeCl_2$ alone is used as the pre-catalyst.

Table 3.1: Iron catalysed Kumada cross-coupling of **25** with **26**, to give a distribution of products, using iron pre-catalysts **48**, **49** and **50·THF**.

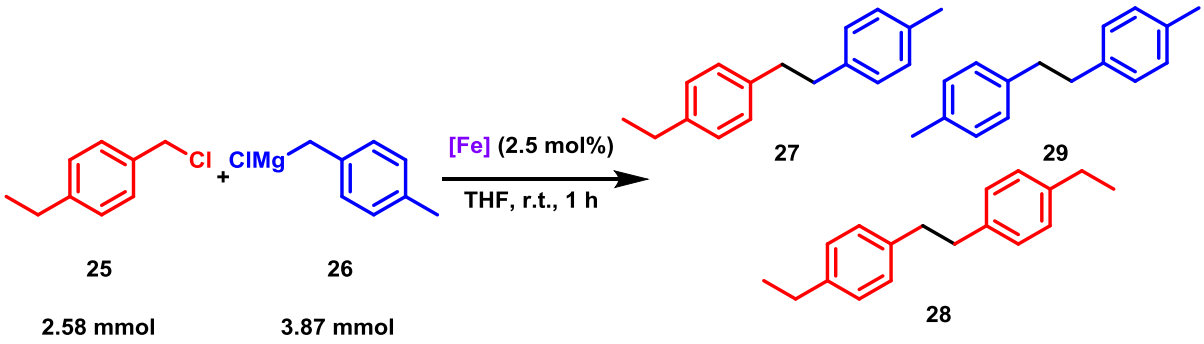

Entry	*Fe*	**27**, mmol	**28**, mmol	**29**, mmol
1[a]	$FeCl_2$	1.21	0.38	0.80
2[b]	**48**	1.24	0.36	0.82
3[c]	**49**	1.33	0.41	0.85
4[d]	**50·THF**	1.28	0.45	1.02

As demonstrated in Table 3.1, the resulting product distributions for the reaction between **25** and **26** are similar to the reaction using the simple $FeCl_2$ pre-catalyst. Furthermore, the resulting concentration-time plots indicate that the reactions using pre-catalysts **48** - **50** occur at the same rate as the reaction using $FeCl_2$, suggesting that the same catalytic manifold is in operation in each case, despite the different pre-catalysts used.

It is possible that the performances of the pre-catalysts tested are so similar to that of $FeCl_2$ alone due to the displacement of the ligands by the Grignard reagent, **26**. This reactivity has been previously demonstrated in iron-catalysed cross-coupling reactions utilising diamine ligands.[57] However, the ligands employed here are of stronger field,[125] and would therefore be expected to form stronger bonds to iron, increasing the likelihood of the ligand remaining bound to the iron centre.[126] This is particularly the case for the iron-NHC complex **50·THF**, as this class of ligand has been previously demonstrated to have a profound effect upon iron-catalysed Kumada cross-coupling reactions.[71, 77] A series of NMR investigations were therefore performed between the iron-NHC complex **50·THF** and **26**, with the aim of elucidating the resultant iron speciation, as a means of clarifying whether or not the NHC ligand remains bound to the iron centre in the presence of the Grignard reagent.

3.3 NMR investigations

*3.3.1 Preparation of the iron(II) bis-benzyl NHC complex **51***

So as to better help characterise intermediates resulting from the addition of **26** to **50**, the synthesis and isolation of an iron benzyl NHC complex, likely to form from the reaction of **26** with **50**, was undertaken. Iron bis-benzyl complexes bearing a NHC ligand have been reported previously by Danopoulos.[127] The reported procedure was used here to synthesise the iron(II) bis-benzyl SIPr complex, **51** (Figure 3.4).

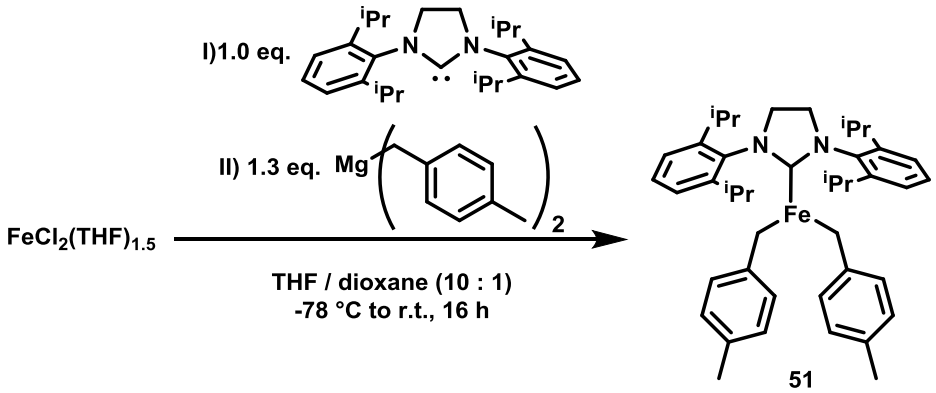

Figure 3.4: Synthesis of the iron(II) bis-benzyl NHC complex **51**.

The resulting solid was analysed by paramagnetic ^{1}H NMR spectroscopy; the resulting spectrum is similar to those of previously reported iron(II) bis-benzyl complexes,[127, 78] and is displayed in Figure 3.5. The starred peak at approximately 75 ppm corresponds to the *para*-methyl protons, which act as an excellent handle within ^{1}H NMR spectra in which this group features.[ix]

[ix] The ^{1}H NMR signals for the *para*-methyl protons are significantly shifted from the other signals observed, both in diamagnetic and paramagnetic spectra.

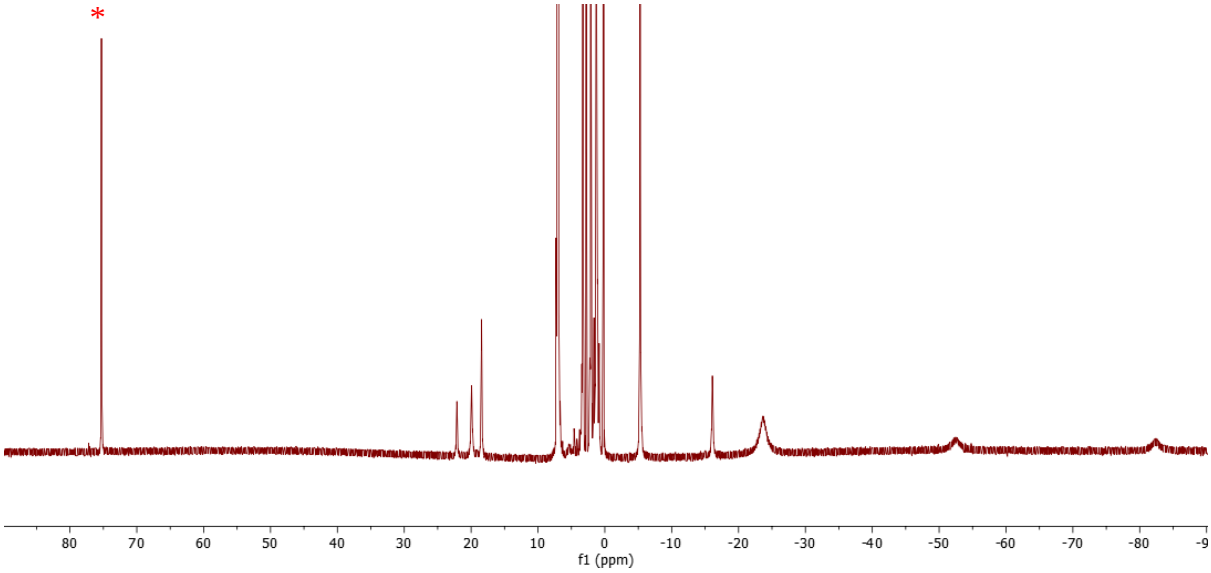

Figure 3.5: ^{1}H NMR spectrum of the iron(II) bis-benzyl NHC complex **51.** * corresponds to the *para*-methyl signal.

Dark orange crystals of **51** were grown from a toluene solution layered with hexane, and subsequently analysed by X-ray crystallography, confirming the NMR assignment (Figure 3.6). Unfortunately, although the atomic assignment and connectivity could be confirmed, a comprehensive assignment was not possible, due to twinning and disorder within the system; the same problem was found from multiple crystals grown by different methods.

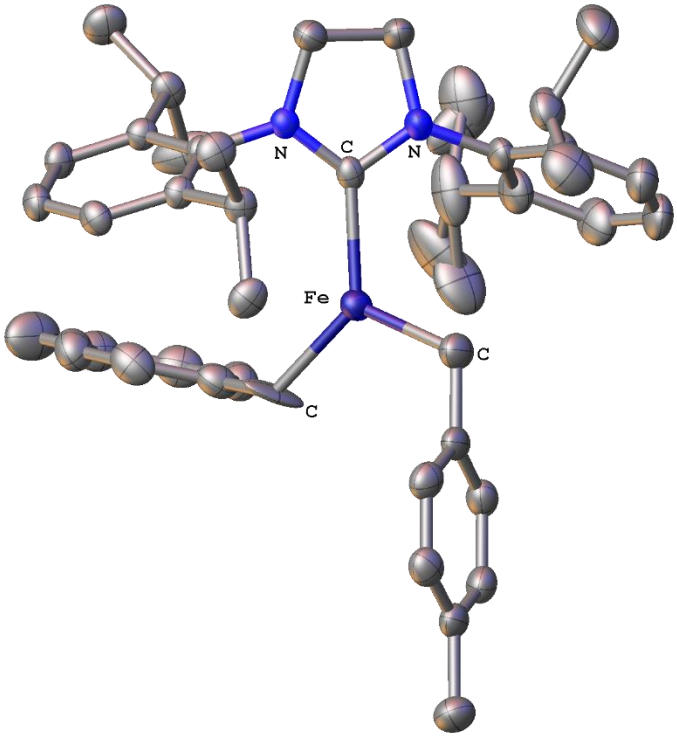

Figure 3.6: X-ray crystal structure of **51**, with hydrogen atoms omitted for clarity.

Attempts were next made to synthesise the iron(II) benzyl-chloride NHC complex, Fe(SIPr)Cl(Benzyl), **52**. A slightly shifted set of signals, suggestive of formation of **52**, was observed when the reaction was carried out on a small scale in an NMR tube. However following work-up of larger scale reaction mixtures, signals corresponding to **51** only were consistently observed, suggesting scrambling of the halide and benzyl ligands is facile (Figure 3.7).

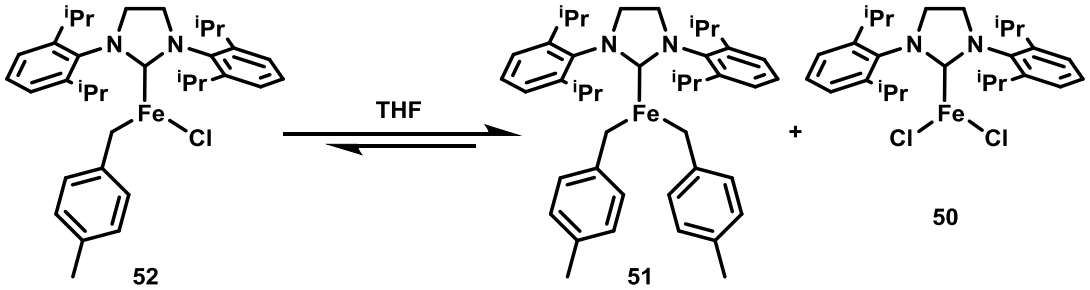

Figure 3.7: Proposed scrambling of the mono-chloride, mono-benzyl iron NHC complex **52** to give **51** and **50**.

No other iron-NHC complexes bearing benzyl groups were prepared (or observed *via* ^{1}H NMR spectroscopy). Whilst this does not preclude the formation of iron-NHC complexes with more than two bound benzyl groups within a catalytic reaction, for the purpose of the following NMR study, they can be discounted.

*3.3.2 Reaction of **50·THF** with **26***

The direct reaction of **50·THF** with an increasing amount of **26** was then examined by ^{1}H NMR spectroscopy. Following each addition, integration of the signals corresponding to the *para*-methyl hydrogens within the benzyl groups of each iron complex allowed for quantification of the relative ratios of the iron products formed. The resulting spectra are shown below, in addition to the ratio of the iron speciation observed in each case (Table 3.2 and Figure 3.8).

Table 3.2: Reaction ratios of **50·THF** with respect to **26** and the proposed resulting iron speciation observed *via* ^{1}H NMR spectroscopy.

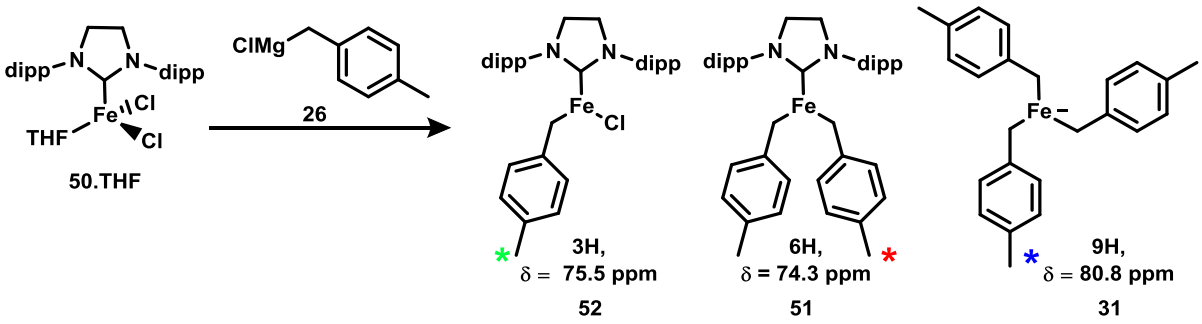

Entry	*Grignard : Fe*	**52** *	**51** *	**31** *
a	0.5	1	0	0
b	1	1	0.36	0
c	2	0	1	0.13
d	5	0	1	0.66
e	10	0	0.65	1
f	15	0	0.36	1
g	30	0	0.20	1

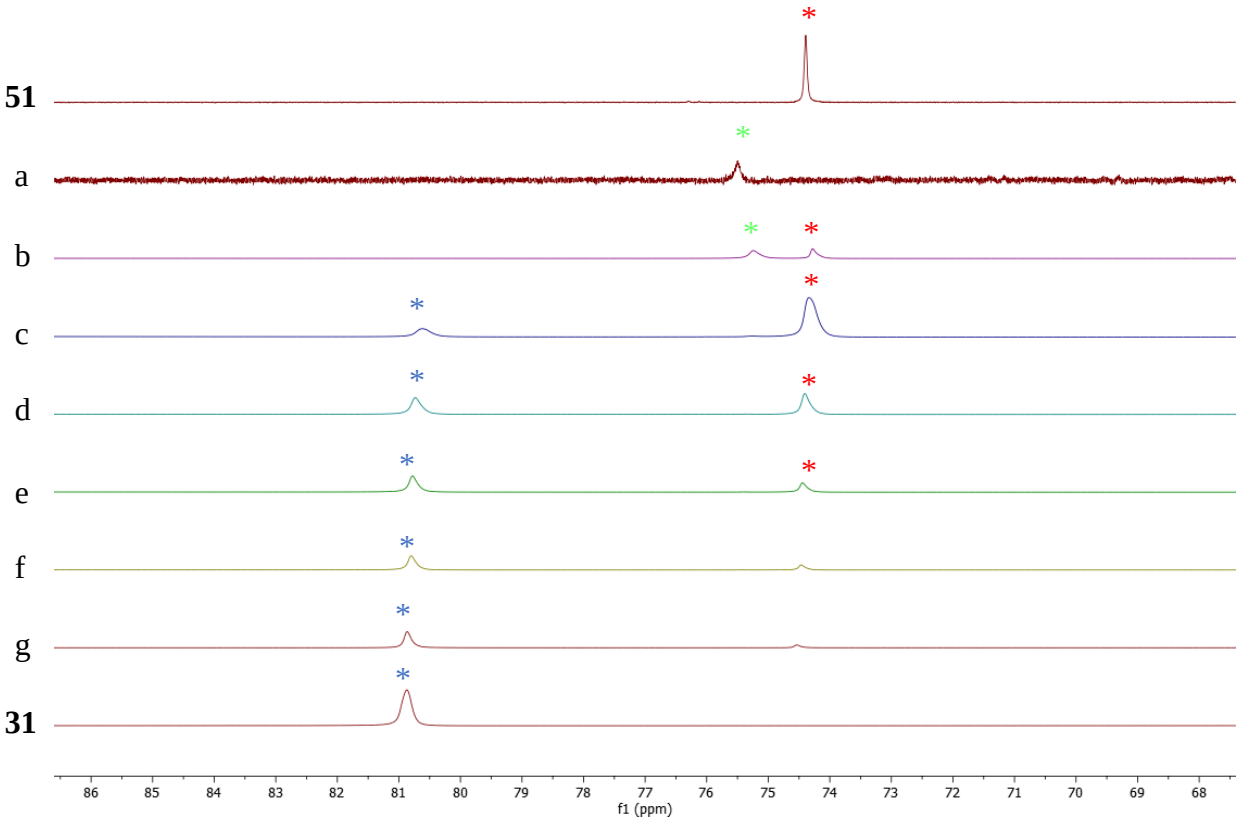

Figure 3.8: Expanded, stacked ^{1}H NMR spectra, from 67 to 87 ppm. The spectra corresponding to **51** and **31** are shown for clarity.

As displayed in Figure 3.8, the iron speciation can be seen to change as the amount of **26** added is increased. Addition of a sub-stoichiometric amount of **26** with respect to **50·THF** results in the formation of the mono-chloride, mono-benzyl iron NHC product Fe(SIPr)Cl(Bn), **52**, as the sole iron product (Figure 3.8, a). However, the facile scrambling of the halide and benzyl ligands is demonstrated by the formation of the bis-benzyl iron NHC product $Fe(SIPr)Bn_2$, **51**, in addition to **52**, when **26** and **50·THF** are mixed in an equimolar ratio (Figure 3.8, b). Further increasing the ratio of Grignard reagent to iron results in the complete disappearance of peaks corresponding to **52**, and in the appearance of peaks corresponding to both **51** and the homoleptic iron-benzyl complex **31** only (Figure 3.8, c – g). As the amount of **26** added is increased, so is the proportion of the homoleptic product **31** formed with respect to **51**, confirming that dissociation of the NHC ligand from the iron centre occurs in the presence of excess Grignard reagent. Upon the addition of 30 equivalents of **26** with respect to **50·THF**, the amount of **31** present is approximately five times greater than that of **52** (Figure 3.8, g).

*3.3.3 NMR investigation into the equilibrium between **51** and **31***

It is therefore not surprising that the iron NHC complex **50·THF** performs so similarly to simple $FeCl_2$ when used as a pre-catalyst for the reaction of **25** with **26**; upon the addition of a large excess of **26** (as would be the case in a catalytic reaction) the disassociation of the NHC ligand, and subsequent formation of **31** would appear to happen to the bulk of the iron present, resulting in a catalytic system that closely resembles that of the ligand-free system. However, when even a large excess of **26** is added, the complete formation of **31** is not observed, suggesting that an equilibrium between **31** and **51** may be present, perhaps due to the concomitant build-up of free NHC ligand (Figure 3.9).

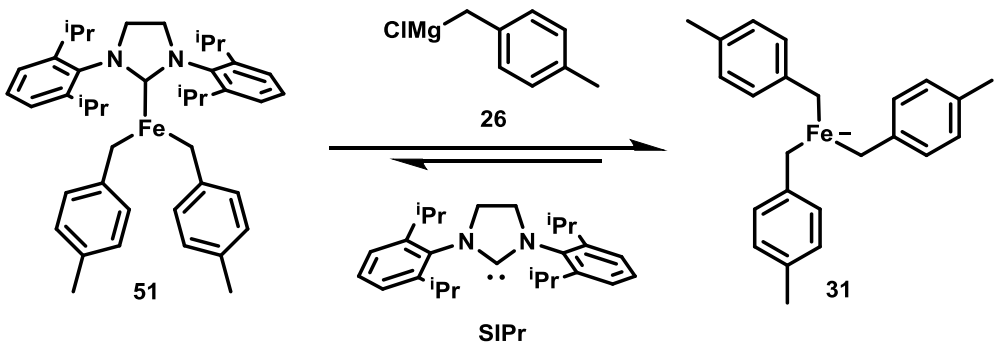

Figure 3.9: Observed equilibrium between the bis-benzyl iron-NHC complex **51** and the homoleptic tris-benzyl ferrate complex **31**.

If this were the case, then the addition of NHC ligand to reaction mixtures should result in a perturbation of this equilibrium, resulting in the preferential formation of iron-NHC species, such as **51**, rather than the homoleptic iron species **31**. In order to elucidate whether such an equilibrium may be in operation, a second NMR investigation was undertaken, in which increasing amounts of the NHC ligand SIPr were added to a pre-formed solution of **31**, in the presence of a large excess of **26**, representative of a catalytic mixture (Figure 3.10).

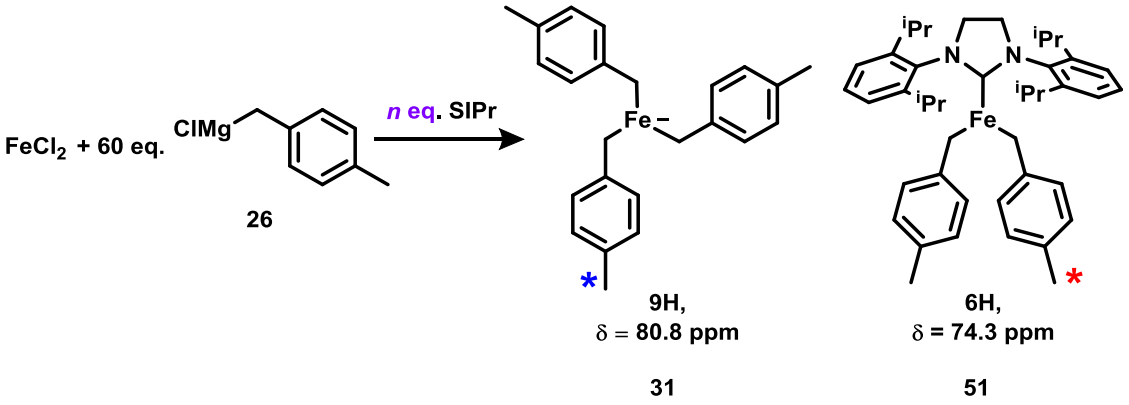

Figure 3.10: Reaction of $FeCl_2$ with 60 eq. of **26** (as per a catalytic reaction) followed by the addition of an increasing amount of the NHC ligand, SIPr, to give a mixture of the homoleptic product **31** and the iron NHC product **51**.

The stoichiometries added, and the resulting ^1H NMR spectra are displayed below (Table 3.3 and Figure 3.11). As with the previous NMR experiment, the relative ratio of the products formed was monitored *via* integration of the *para*-methyl proton signal for each of the products; the resulting ratio of the products formed, in addition to the ratio of iron, **26** and SIPr present within each reaction is displayed below.

Table 3.3: Ratio of iron, **26** and SIPr present within each experiment

Entry	*Fe: Grignard: SIPr*	**51** *	**31** *
a	1: 60: 1	1	0.28
b	1: 60: 2	1	0.54
c	1: 60: 3	1	0.85
d	1: 60: 4	0.91	1
e	1: 60: 5	0.72	1
f	1: 60: 10	0.34	1

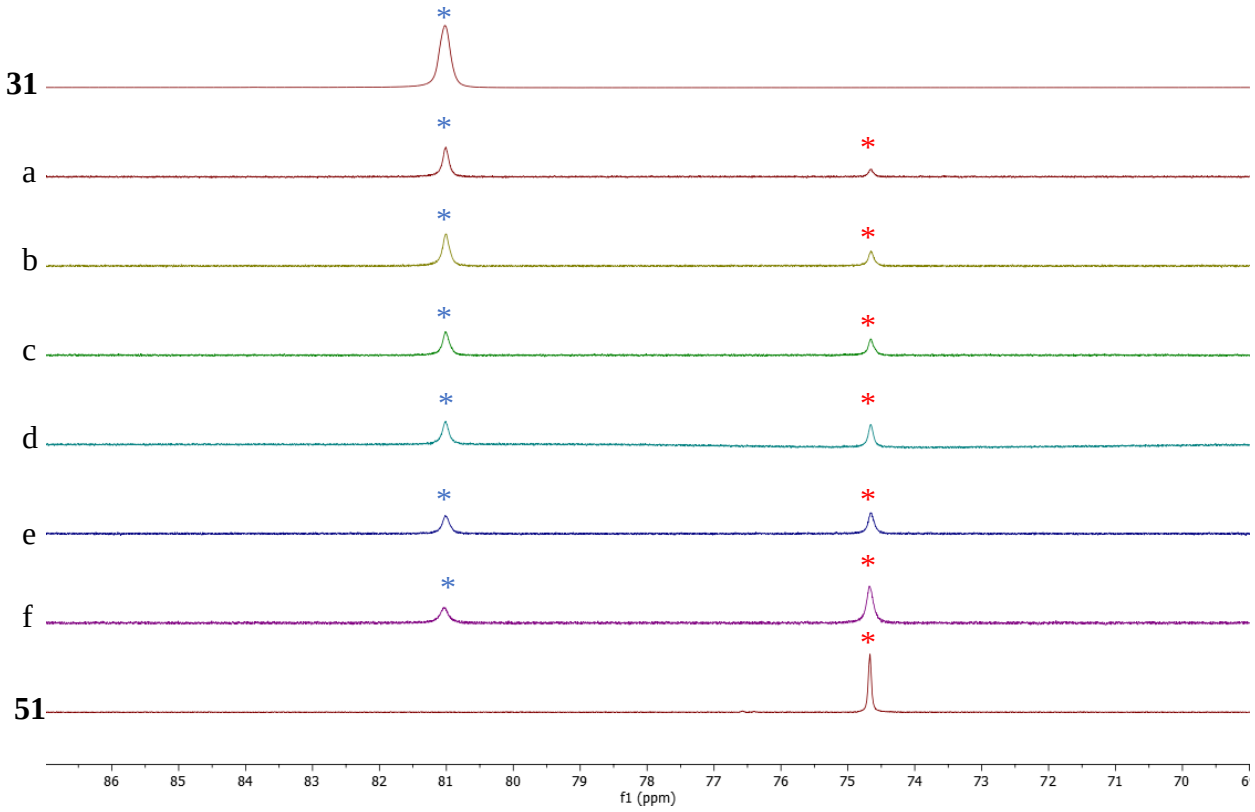

Figure 3.11: Expanded stacked ^{1}H NMR spectra, from 69 to 87 ppm, as per Table 3.3. The spectra of **31** and **51** are also shown for clarity. No signals corresponding to species other than **31** and **51** were observed.

The results in Figure 3.11 demonstrate that the equilibrium between **31** and **51** can be manipulated through the addition of SIPr. Upon the addition of up to three equivalents of SIPr with respect to iron, the homoleptic ferrate complex **31** remains the predominant iron species within solution (Figure 3.11, a – c). However, further increasing the amount of SIPr added results in the preferential formation of **51** (Figure 3.11, d – f). Upon the addition of 10 equivalents of SIPr, the iron NHC complex **51** is present in a 3:1 ratio compared to the homoleptic species **31** (Figure 3.11, f).

*3.4 Kinetic investigation into the equilibrium between **31** and **51***

Whilst the preceding NMR studies describe the position of equilibrium between the homoleptic species **31** and the iron NHC complex **51** from a thermodynamic perspective, they do not provide any information on the kinetic implications of the equilibrium. In the context of a catalytic reaction, the demonstrated change in iron speciation resulting from the addition of the NHC ligand SIPr to a catalytically representative mixture of $FeCl_2$ and **26** can be taken to represent the proportion of iron pre-catalysts within the reaction, prior to the addition of the

electrophile **25**. Accordingly, by taking the order of reaction with respect to SIPr added, the kinetic effect of the equilibrium described by the NMR experiments should be observable. The concentration against time plots for the reaction of **25** with **26**, using a $FeCl_2$ pre-catalyst and a varying concentration of SIPr, are displayed in Figure 3.12.

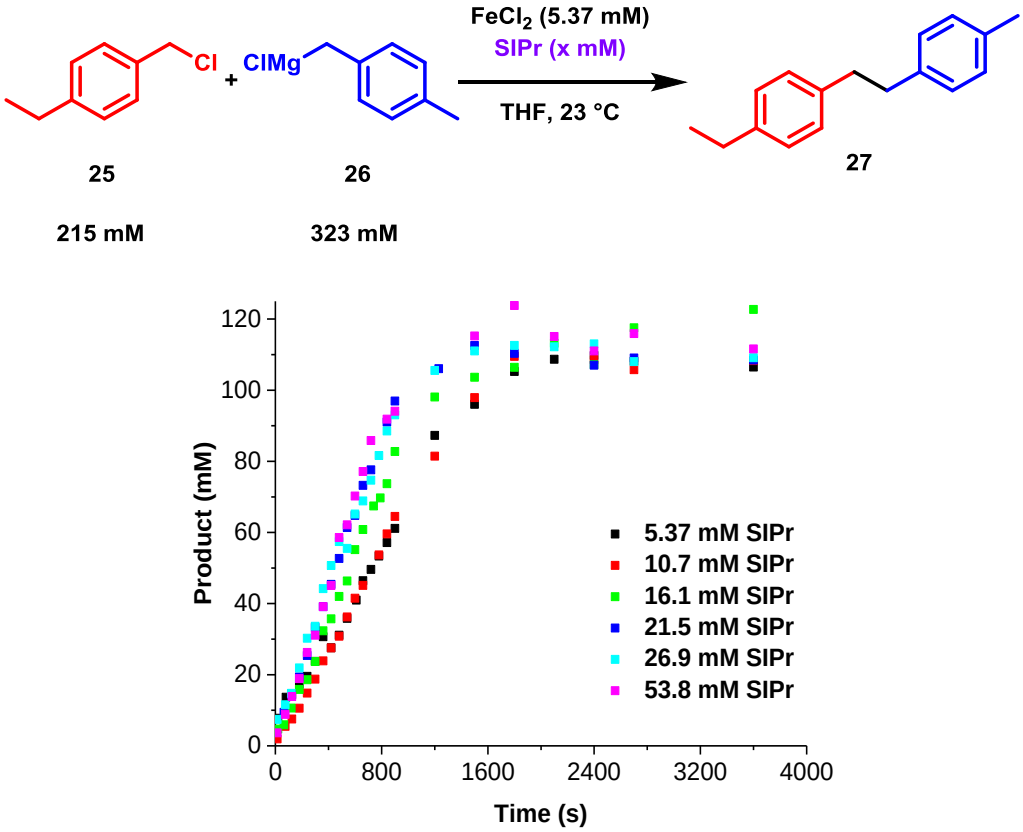

Figure 3.12: Concentration-time profiles for the reaction of **25** with **26** using a $FeCl_2$ pre-catalyst, and a varying concentration of the NHC ligand SIPr, to give the heterocoupled product **27**.

The resultant plots demonstrate a positive effect upon the rate of production of **27** as the concentration of SIPr within the reaction is increased. Using the method of initial rates, the order of reaction with respect to SIPr was estimated (Figure 3.13).

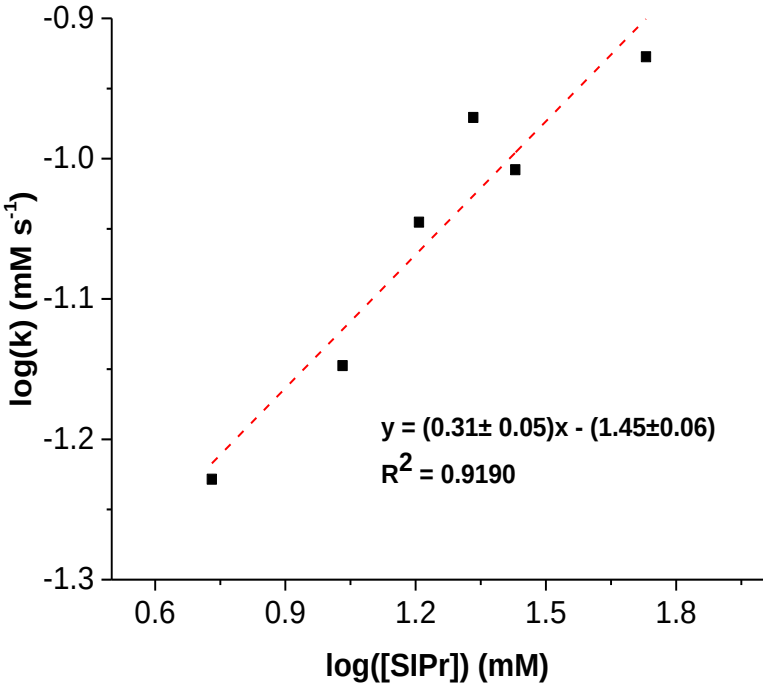

Entry	SIPr (mM)	k_{max} (mM s^{-1})
1	5.37	0.0591
2	10.7	0.0712
3	16.1	0.0901
4	21.5	0.107
5	26.9	0.0982
6	53.8	0.1182

Figure 3.13: Approximate initial rates measured from the concentration-time profiles displayed in Figure 3.12, and the corresponding logarithm plot.

The value obtained of approximately 0.3 suggests that whilst the rate of product formation is accelerated with respect to SIPr, it is by no means a first order dependence. Taken together with the NMR studies from Section 3.3, this provides good agreement with the suggestion that there is a mixture of iron speciation, composed of both heteroleptic, NHC-free species, in the form of ferrates (such as those discussed in Chapter 2) and iron species with an NHC ligand bound. From the data obtained, it is suggested that the iron-NHC species present react at a faster rate than the non-NHC iron species.

Due to the similarity of the product distributions obtained in the presence or absence of added NHC ligand, the iron-NHC intermediates formed within the reaction are likely to be electronically similar to the NHC-free iron species (Figure 3.14). If this were not the case, then the substantial electronic difference between the different iron species present would most likely result in a different product distribution being obtained.

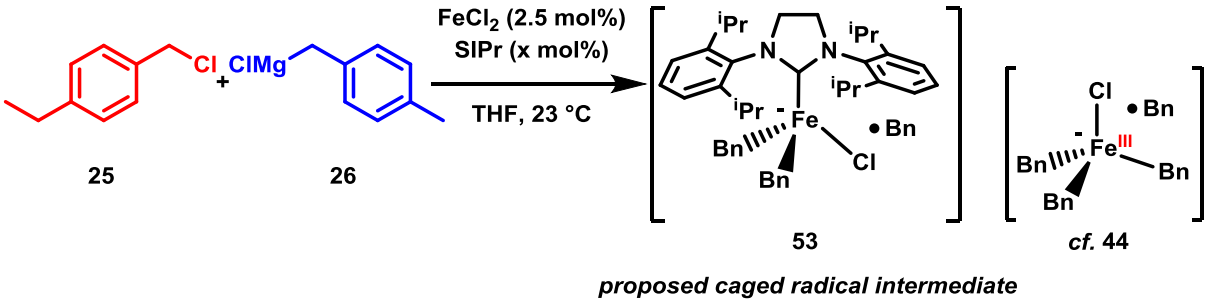

Figure 3.14: Proposed iron-NHC caged radical intermediate, **53**, suggested to form within the iron-catalysed Kumada cross-coupling reaction in the presence of the NHC ligand SIPr.

3.5 Conclusions and future work

When used as pre-catalysts for the iron-catalysed Kumada cross-coupling reaction between **25** and **26**, three well-defined iron(II) complexes (each featuring a separate class of ligand: a mono-dentate phosphine, a bidentate phosphine and an NHC) were shown to function in much the same manner, with respect to rate of reaction and resultant product distribution, as iron(II) chloride alone.

Using ^{1}H NMR spectroscopy, an investigation into the reactivity of the iron-NHC complex **50·THF** with the Grignard reagent **26**, at varying molar ratios, was undertaken, with the aim of elucidating whether the NHC ligand, SIPr, remains bound to the iron-centre in the presence of **26**. The NMR studies suggested that following the addition of **26**, there exists an equilibrium between several iron species, some containing an iron-NHC bond and some not, and that as the ratio of **26**: **50·THF** is increased, the formation of the NHC-free species becomes more favoured. The observed iron-NHC species were assigned as FeCl(4-MeBn)SIPr, **52** and Fe(4-MeBn)$_2$SIPr, **51**, while the NHC-free iron speciation was assigned as the homoleptic ferrate complex [Fe(4-MeBn)$_3$]$^-$ **31**. When the ratio of **26**: **50·THF** approaches a ratio representative of a catalytic reaction, the homoleptic ferrate complex **31** is present in a 5: 1 ratio with respect to the iron-NHC species **51**, with no **52** present, suggesting that in a catalytic reaction, the bulk of the iron-speciation would not have an NHC ligand attached.

The equilibrium between **31** and **51** was exploited further and could be shown to be pushed towards the formation of **51** through the addition of the NHC ligand, even in the presence of a large excess of **26** (representative of a catalytic reaction). At a ratio of 1 Fe: 60 **26**: 10 SIPr, the iron-NHC complex **51** was present in a 3: 1 ratio compared to the ferrate species **31**.

For the iron-catalysed reaction between **25** and **26**, a small, positive dependence (0.3) upon the rate of product formation was observed with respect to amount of SIPr added, suggesting that iron-NHC species are forming within the catalytic reaction, and that they perform catalysis at a faster rate than the NHC-free species discussed in Chapter 2. Due to the similarity of the product distributions obtained, it is suggested that the reaction proceeds *via* the same mechanism in the presence of NHC ligands as in their absence (*i.e.* that shown in Figure 2.49), with the formation of a caged radical intermediate **53**, similar to previously proposed **44**.

Stoichiometric reactions between the iron-NHC complexes (**50·THF**, **51** and **52**) and the electrophile **25** would be of interest in order to ascertain if the cross-coupled product is selectively produced. Carrying out the addition of the Grignard reagent **26** over an extended period of time, or at lower temperatures, would also be useful, in order to compare the product distributions obtained from the standard reaction conditions. Preliminary work from within the Bedford group has demonstrated that the dissociation of silylenes (silicon derivatives of carbenes) from iron centres also occurs within iron-catalysed Kumada cross-coupling reactions, despite the presence of a silicon-iron bond that is expected to be stronger than that of carbon-iron. It is therefore not unreasonable to suggest that, for catalytic reactions in which it is possible to form stable complexes between transition metal and nucleophile (or electrophile), disassociation of the ligand from the metal centre may be readily occurring, rendering the added ligand either superfluous, or functioning in a manner that may not initially be expected of it.

Chapter 4 *Transmetallation between catalytically relevant zinc and iron species*

4.1 Introduction

Within the context of cross-coupling reactions, a transmetallation refers to the replacement of a transition metal halide (or pseudohalide) bond with the nucleophilic organic group of a non-transition metal reagent, most commonly one of magnesium, zinc, tin, boron or silicon.[125] In contrast to the other steps within a classical cross-coupling reaction (oxidative addition,[128] reductive elimination[120] and migratory insertion[129]), fewer mechanistic details are available regarding transmetallation, especially in the case of magnesium and zinc-based reagents.[117]

4.1.1 Iron catalysed Negishi cross-coupling

Early work on the iron-catalysed Negishi cross-coupling reaction (in which organozinc nucleophiles are used)[x] from both Nakamura[36] and Bedford[130] required magnesium dihalide for the reaction to proceed in a synthetically useful manner (Figure 4.1, *i*, *ii*). Since these early reports, the use of diphosphine ligands, such as dpbz (Figure 4.1, *ii*), have superseded their amine counterparts; however there is little discussion available on the role the ligand and salt required may have to play within the reaction.[63]

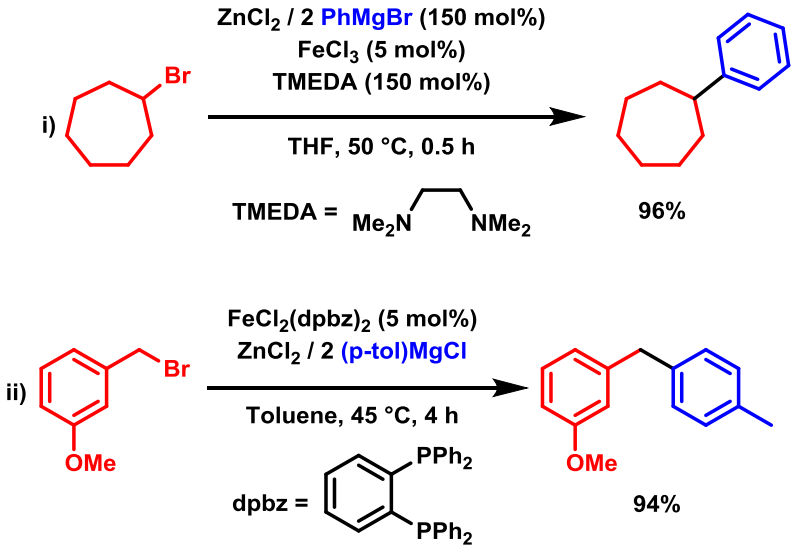

Figure 4.1: Early examples of iron-catalysed Negishi cross-coupling reactions, from (*i*) Nakamura (using an amine ligand) and (*ii*) Bedford (using a diphosphine ligand). Both require the use of magnesium dihalide.

[x] The first iron-catalysed cross-coupling using zinc reagents was from Fürstner who used successfully used *in situ* generated zincate species as nuclephiles.[48]

In addition to the requirement for magnesium salts and a diphosphine ligand within reaction mixtures, diarylzinc reagents are necessary due to the arylzinc halide counterparts resulting in poor yields.[36, 130] Their synthesis from aryllithium compounds resulted in little catalytic activity, regardless of whether or not the concomitantly formed lithium bromide was removed from reaction mixtures (Figure 4.2, *i*). This necessitates their preparation from reaction of zinc halide with two equivalents of the corresponding Grignard reagent;[xi] with the resultant magnesium bromide present in solution, robust catalytic performance is observed (Figure 4.2, *ii*, *iii*).[130] More recent work has ruled out the possibility of the triarylzincates being the active zinc species in catalysis, as while their use in reaction mixtures leads to much increased rates, the formation of homo-coupled bi-aryl product out performs that of the desired cross-coupling (Figure 4.2, *iv*).[103]

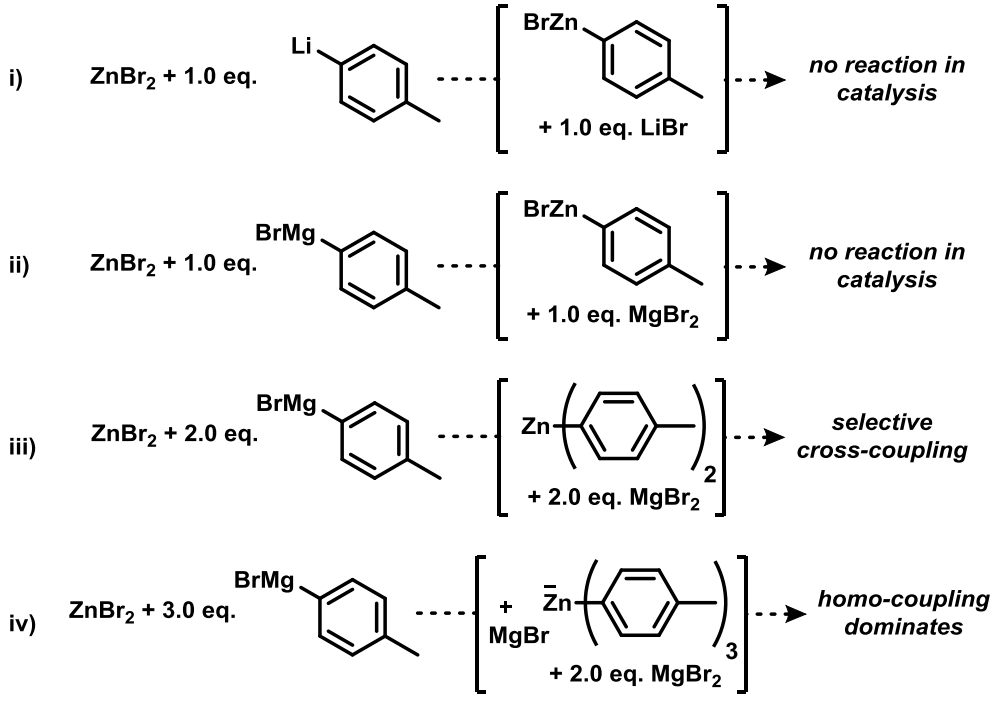

Figure 4.2: The resultant reactivity observed in a model iron-catalysed Negishi cross-coupling reaction depending on the method of synthesis of the zinc nucleophile.

4.1.2 The role of salt additives in reactions using organozinc reagents

The role of magnesium and lithium salts present in catalytic reactions has been commented upon in reactions catalysed by other transition metals. Fu reported upon the need for magnesium and lithium free diarylzinc mixtures for use in an asymmetric-nickel catalysed

[xi] As a result, the correct representation of the diarylzinc reagent is $ZnAr_2$ / 2 MgX_2.

cross-coupling reaction, with synthesis from the corresponding boronic acid necessary.[131] Whilst this was most likely associated with a loss of resultant selectivity rather than reactivity,[132] the wider implication is the non-innocent behaviour of salts present in solution. This was further highlighted by Organ in a report on a palladium-catalysed Negishi cross-coupling, whereby the removal of magnesium or lithium salts resulted in a complete loss of reactivity towards cross-coupling (Figure 4.3).[133]

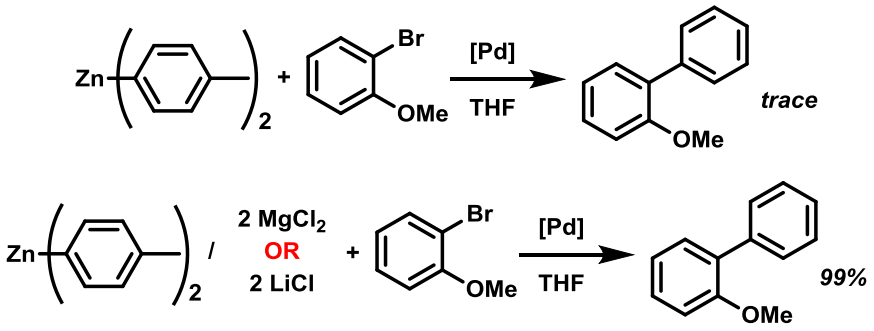

Figure 4.3: Palladium-catalysed Negishi cross-coupling of diarylzinc reagents in the presence of lithium or magnesium halide salts.[133]

It is clear therefore that metal salts in solution are not always innocent spectators in cross-coupling reactions, and the extent of their effect upon catalytic systems is often overlooked. However, less clear is the role that they may impart. Most frequently, this is assigned to an increased propensity towards transmetallation from the zinc reagent to the transition metal centre, as was eloquently displayed by Marder and Lei in the case of a nickel-catalysed cross-coupling using arylzinc halide reagents. Here a first-order dependence on zinc was observed in the presence of lithium bromide, taken to mean a slow transmetallation step was taking place (Figure 4.4, *i*). However, a zero-order reaction was observed with respect to zinc in the presence of magnesium bromide, indicating transmetallation occurred quickly (Figure 4.4, *ii*).

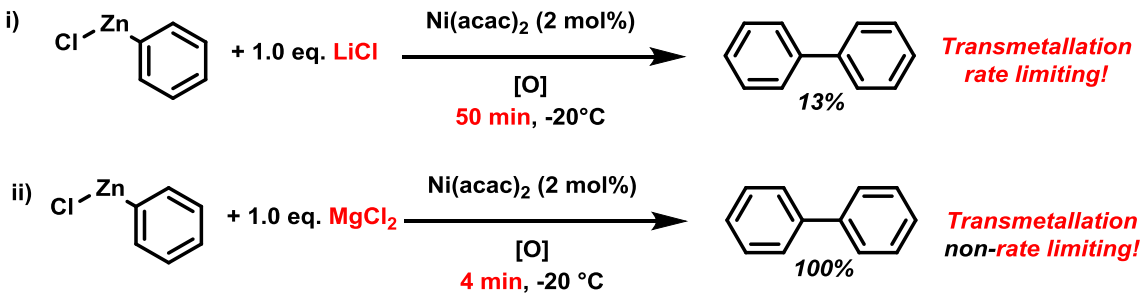

Figure 4.4: Differing rates of reaction observed in a nickel-catalysed homo-coupling reaction, dependent on the choice of salt present.

Whilst caution should be taken when drawing conclusions from reactions involving different metals, it is not unreasonable to suggest that the magnesium salts necessary in the iron-catalysed Negishi cross-coupling may be playing a similar role to that proposed using other transition metal catalysts in combination with organozinc reagents.

4.1.3 General considerations

The following chapter addresses the transmetallation from diarylzinc reagents to iron centres, which is contextualised with reference to the iron-catalysed Negishi cross-coupling reaction. Specifically, the role of magnesium salts and diphosphine ligands necessary for catalysis to proceed was investigated, with respect to transmetallation. Parts of this work were carried out by other researchers, who are credited where appropriate within the text. Portions of this work have been published.[103]

*4.2 Reaction between $FeBr_2$ and **54** in the absence of diphosphine ligand*

*4.2.1 Reaction of $FeBr_2$ with pure **54***

As discussed in section 4.1, the iron-catalysed Negishi cross-coupling reaction requires the presence of both a diphosphine ligand and magnesium salts. However, there is a poor understanding as to why these additives are required. One possible reason is that they aid in the transmetallation step within the reaction, as has been proposed in the case of reactions using other transition metals in combination with organozinc reagents (*cf.* Figure 4.4). Accordingly, the reaction between the organozinc reagent **54** and the benzyl halide **55**, yielding the cross-coupled product **56** was investigated (Figure 4.5).

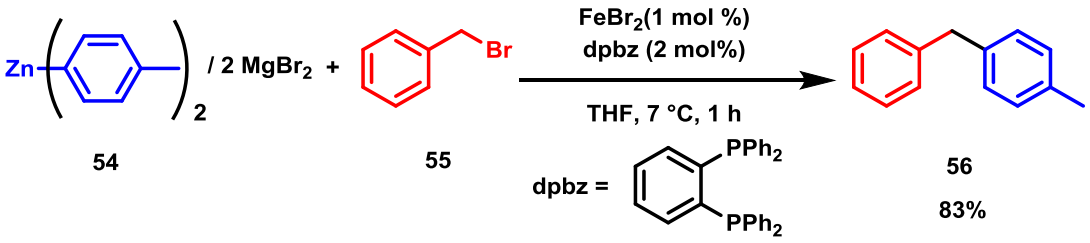

Figure 4.5: The model iron-catalysed Negishi cross-coupling reaction on which subsequent studies will be based.

In order to obtain a thorough understanding of potential transmetallation pathways, the effect of additives on reaction mixtures and resultant products formed, the following investigation was conducted in a bottom up manner. By starting from the simplest combinations of reagents and monitoring subsequent changes in reactivity with each added component, a comprehensive overview of transmetallation was sought to ultimately be applied in a catalytically relevant framing. Accordingly, the reaction of $FeBr_2$ with pure $Zn(4\text{-tolyl})_2$ **54** in a 1: 1 ratio, in the absence of any additive, was first carried out. **54** was synthesised from the lithiated derivative, allowing for removal of salt side-products.

After initial formation of a yellow solution, a rapid darkening was observed to give a heterogeneous mixture containing a black solid and colourless liquid. Monitoring of the reaction over a 12 h period demonstrated near quantitative conversion to the homo-coupled product **57.** Following magnetic separation, analysis of the black solid *via* TEM analysis confirmed the presence of iron nanoparticles, with a typical diameter of 100 – 600 nm. Previous reports from within the Bedford group have commented on the formation of iron nanoparticles as a product of reductive elimination.[104] Taken together, it can be concluded that in the absence

of any additive, transmetallation to iron, followed by reductive elimination to yield iron nanoparticles and homo-coupled nucleophile, occur readily (Figure 4.6).

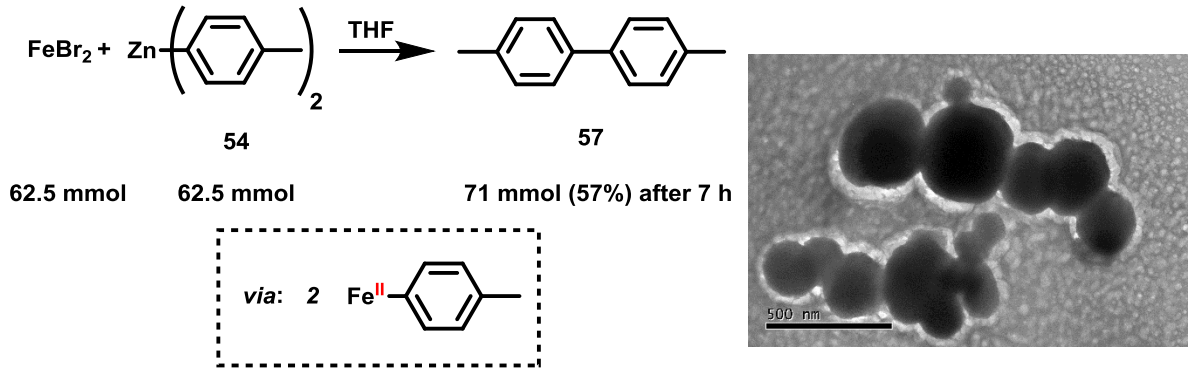

Figure 4.6: Reaction of $FeBr_2$ with one equivalent of **54**, in the absence of any additive, to give biaryl **57** and iron nanoparticle formation, as displayed in the TEM image on the right. Reaction carried out by Harry O'Brien, TEM analysis by Dr. Sean Davies.

*4.2.2 Reaction of $FeBr_2$ with **54** in the presence of magnesium salt*

The reaction displayed in Figure 4.6 provides evidence of transmetallation to iron; however, when a representative electrophile was added in pursuit of catalysis, no cross-coupled product is observed. This suggests that in the absence of additives, the rate of reductive processes from iron is greater than that of any subsequent cross-coupling. As discussed in Section 4.1, iron-catalysed Negishi cross-coupling reactions require both magnesium salts and a diphosphine ligand in order to effect turnover. As their presence can be facilitated in straightforward fashion by synthesis of the diarylzinc from the corresponding Grignard reagent (Figure 4.7), the effect of magnesium salts was first investigated.

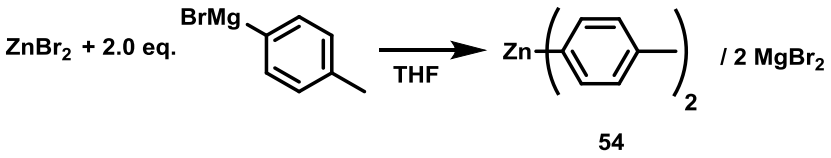

Figure 4.7: Reaction of $ZnBr_2$ with two equivalents of 4-tolylmagnesium bromide to give the diarylzinc reagent **54**, with two equivalents of magnesium dihalide.

In contrast to the magnesium-free reaction, upon mixing in THF of $FeBr_2$ with **54** / 2 $MgBr_2$ a white precipitate is observed, which remains stable with respect to decomposition for over 24 h. Upon separation, ^{1}H NMR analysis of the liquid fraction reveals almost quantitative recovery of the diarylzinc reagent, **54.** Recrystallisation of the solid was found to yield two different bromoferrate complexes, dependent on the solvent of crystallisation used. In the case

of THF, the complex $[FeBr_3]^-$ **58** is obtained, whilst when 2-MeTHF is used the bimetallic complex $[Fe_2Br_6]^{2-}$ **59** is formed (Figure 4.8).

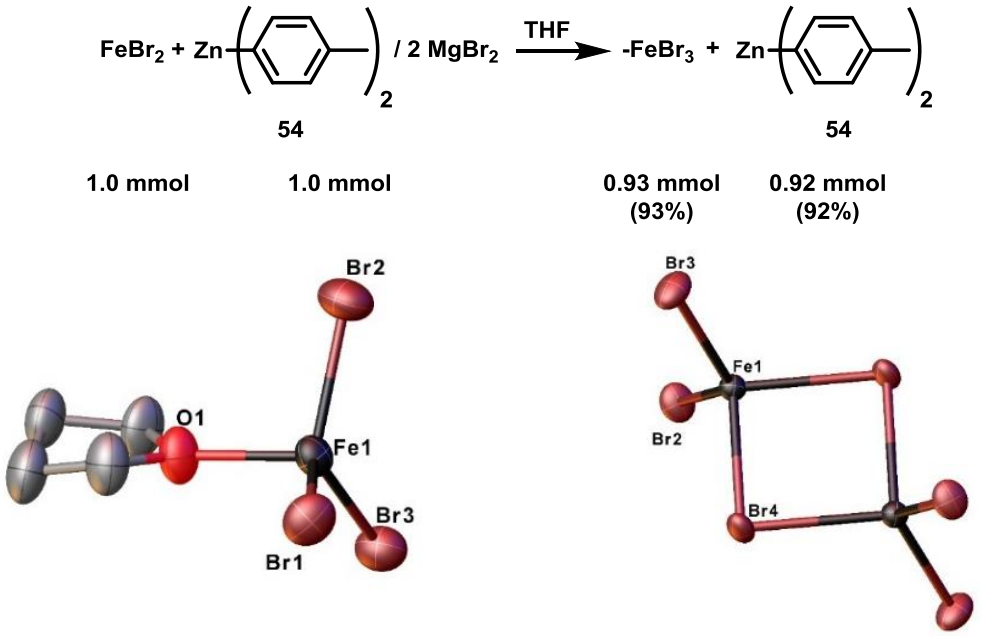

Figure 4.8: Reaction of $FeBr_2$ with one equivalent of **54** / 2 $MgBr_2$, to give quantitatively the bromoferrate complexes **58** and **59**, and recovery of the diarylzinc reagent. **58** (bottom left) was recrystallised from THF, **59** (bottom right) from 2-MeTHF. All reactions and analysis carried out by Dr. Antonis Messinis.

While it should be noted that heating the reaction displayed in Figure 4.8 at reflux leads to decomposition, akin to the salt-free mixture, these results suggest that magnesium salts in fact hinder transmetallation to iron at a stoichiometric ratio of zinc to iron.

*4.2.3 Reaction of $FeBr_2$ with **54** in the presence of zinc salt*

As the iron-catalysed Negishi cross-coupling progresses, the diarylzinc starting material **54** will be converted to a mono-arylzinc halide species, formed as a product of transmetallation. The effect of the zinc halide salts formed upon transmetallation is therefore a pertinent consideration. As with the addition of magnesium bromide, the corresponding reaction using zinc bromide yields stable, non-transmetallated iron complexes at stoichiometric ratios of iron to zinc. Analysis of crystals grown from the homogeneous yellow solution obtained reveals formation of two neutral bimetallic species: the iron bromide / zinc bromide adduct, **60**, in addition to the iron bromide / arylzinc adduct, **61** (Figure 4.9)**.**

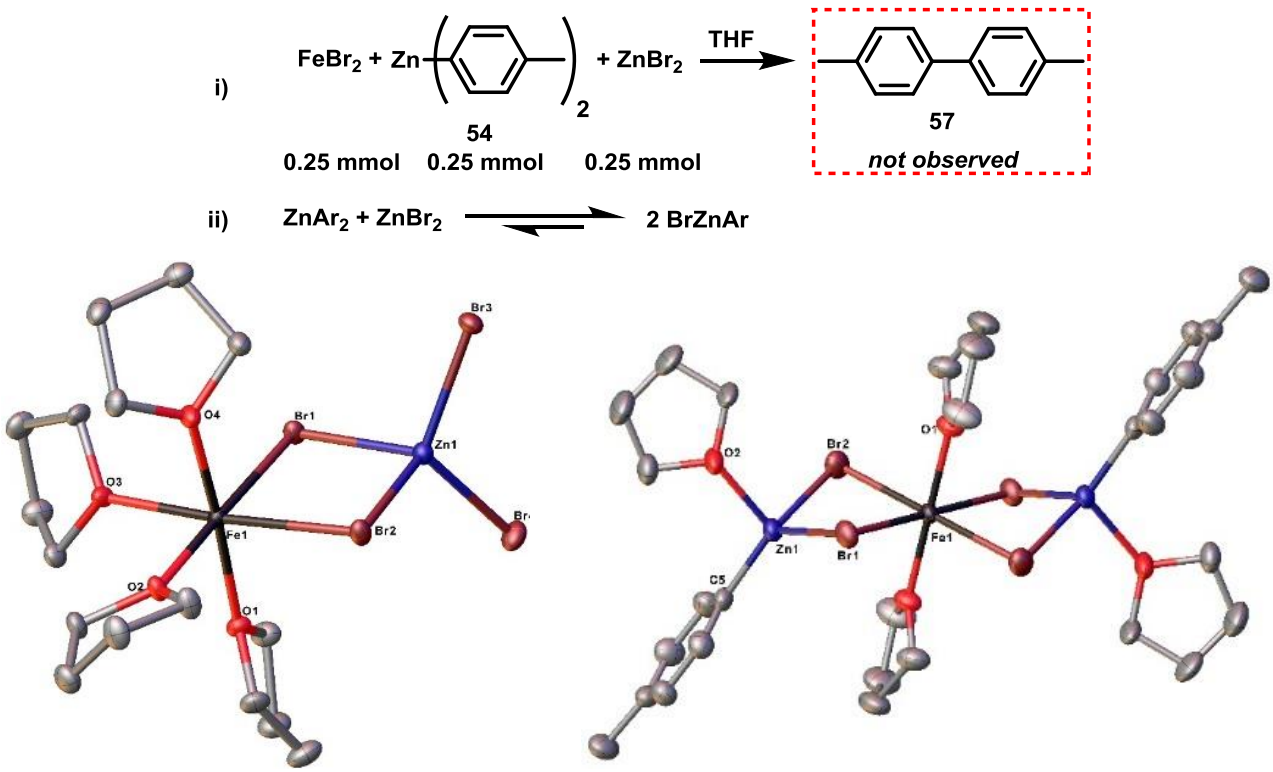

Figure 4.9: Reaction of $FeBr_2$ with one equivalent of **54** and one equivalent of $ZnBr_2$, to give iron-zinc adducts **60** (bottom, left) and **61** (bottom, right)**,** with no homocoupled product **57** observed. All reactions and analysis carried out by Dr. Antonis Messinis

The results displayed above demonstrate that the presence of magnesium and zinc salts retard considerably the rate of transmetallation from zinc to iron. This is perhaps less surprising in the case of zinc bromide, the presence of which would likely involve a Schlenk type equilibrium with the diarylzinc reagent to produce a monoarylzinc species (Figure 4.9, *ii*), which have previously been demonstrated to be ineffective in catalysis.[36] However, the behaviour of magnesium bromide containing mixtures is rather counter-intuitive. The implication is somewhat limited however, as upon increasing the zinc to iron ratio to a more catalytically relevant loading of 100:1 in the presence of magnesium bromide, decomposition is observed, indicating that the barrier to transmetallation in the presence of magnesium salts can be overcome (Figure 4.10).

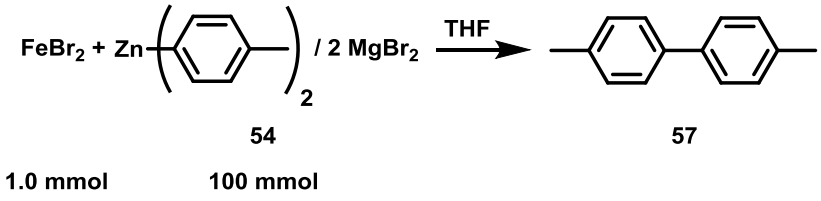

Figure 4.10: Reaction of $FeBr_2$ with a catalytic loading of diarylzinc reagent **54**, in the presence of magnesium bromide, to give transmetallation and decomposition, with formation of **57.**

Despite efforts to isolate iron-aryl intermediates, the absence of steric bulk within the 4-tolyl nucleophile results in rapid decomposition of iron-aryl intermediates above -40 °C, rendering characterisation non-trivial.[59] In an attempt to elucidate information on potential transmetallated iron intermediates, switched our attention to the bulkier mesityl substituent.

4.3 Transmetallation study using a bulky diarylzinc reagent

Due to the imposing steric bulk provided by the two ortho-methyl substituents on the aryl rings, the use of mesityl derivatives within iron-catalysed cross-coupling reactions has proved challenging and frequently returns poor yields, regardless of the coupling partner employed, rendering it a poor model for catalytic studies.[61] However, homoleptic iron-mesityl complexes were synthesised over 30 years ago, and have been characterised crystallographically in complexes that display both bridging 3-centre 2-electron (Fe_2Mes_4, **62**) and terminal ($[FeMes_3]^-$, **63**) bonding modes.[90] This suggests that a failure to transmetallate to the iron centre is not the cause of any subsequent lack of observed reactivity in catalysis when using mesityl nucleophiles. Given that the isolated species **62** and **63** display characteristic peaks in their respective ^{1}H NMR spectra, the relative thermal stability of iron-mesityl complexes and their lack of further reactivity indicate that the kinetic protection afforded by the mesityl fragment with respect to reductive processes may afford a potentially excellent model for further fundamental reactivity studies with regards to transmetallation. To this end, the transmetallation of iron by dimesitylzinc, **64**, was probed, specifically in an attempt to elucidate the position of equilibrium for transmetallation processes from zinc to iron.

*4.3.1 Reaction of $FeBr_2$ with pure **64***

Upon mixing a 1: 1 ratio of $FeBr_2$ with pure **64** in THF, an insoluble white precipitate was formed, which remains stable under an inert atmosphere for an extended period of time. Dissolving the solid in boiling THF and allowing the solution to cool led to precipitation of a gummy solid, further analysis of which was hindered due to its poor solubility in a range of solvents. However, the formation of a stable product is validation of the use of mesityl nucleophiles towards yielding more accessible intermediates. Subsequent increasing of the ratio of zinc to iron results in extremely air-sensitive homogeneous solutions, the ^{1}H NMR spectra for which (in addition to the ratio of zinc : iron present in each case), are displayed in Figure 4.11. Although the reaction with two equivalents of zinc does produce a solution, the ^{1}H NMR spectrum yielded no paramagnetically shifted peaks.

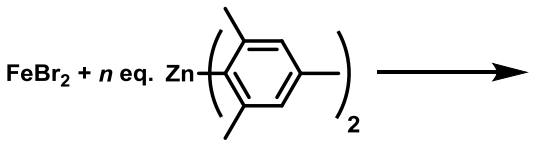

64

Spectrum	*Zn: Fe*	*signal in ^1H*
-	1: 1	insoluble white ppt
-	2: 1	no signals
a	3: 1	unknown species
b	4: 1	unknown species
c	5: 1	unknown species
d	6: 1	unknown species
e	10: 1	unknown species

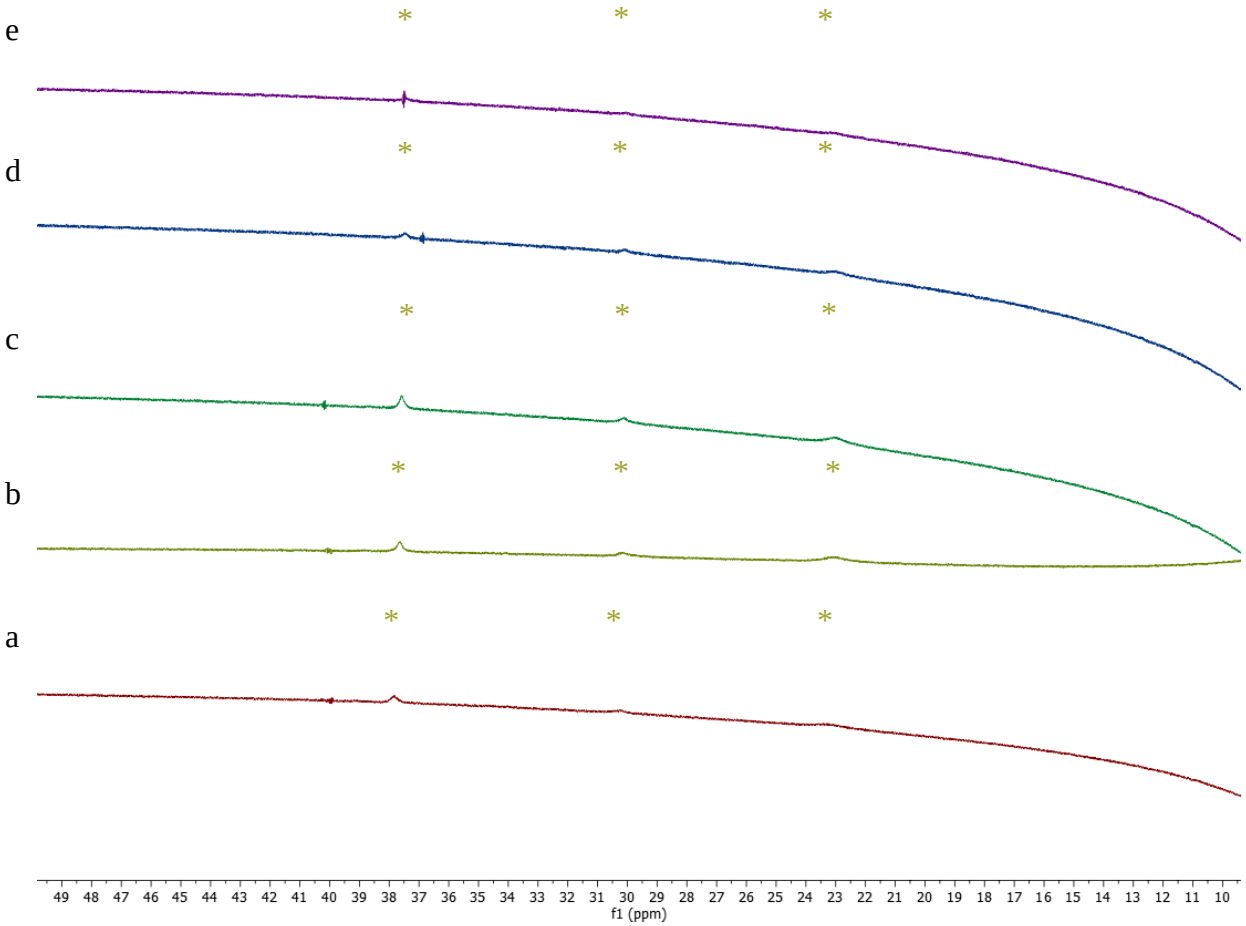

Figure 4.11: Expanded stacked ^1H NMR spectra, from 10 to 50 ppm, corresponding to the addition of increasing amounts of pure **64** to $FeBr_2$ in THF, and the relative ratio present in each spectrum.

As shown in Figure 4.11, the resultant ^1H NMR spectra all display a single set of broad, paramagnetically shifted signals (δ = 23, 30 and 37 ppm, *) indicating that coordination of the

mesityl groups to an iron centre has taken place. As will be discussed in the course of this chapter, the signals are most likely not far enough downfield to correspond to a discrete iron-aryl complex. It is therefore possible that they correspond to a bimetallic iron-zinc complex, with mesityl groups positioned in a bridging mode between zinc and iron (Figure 4.12, *i*). Alternatively, the bimetallic zinc-iron species may instead be bridged by bromide ligands, with the mesityl groups remaining completely bound to zinc (Figure 4.12, *ii*). Either arrangement would be expected to give a single set of ^{1}H NMR signals upfield from those observed for the di-iron species Fe_2Mes_4, **62**, (δ = 57, 83 and 109 ppm) and the homoleptic iron-species $[FeMes_3]^-$, **63**, (δ = 23, 112 and 123 ppm). However, considering also the structure displayed in Figure 4.12, *iii*, corresponding to the previously discussed complex **61** (in which the bromide ligands are clearly shown to bridge between the iron and zinc centres, with the aryl groups (Ar = 4-tolyl) remaining bound to zinc), the latter suggestion in which the bromide ligands act in a bridging fashion, is perhaps more likely.

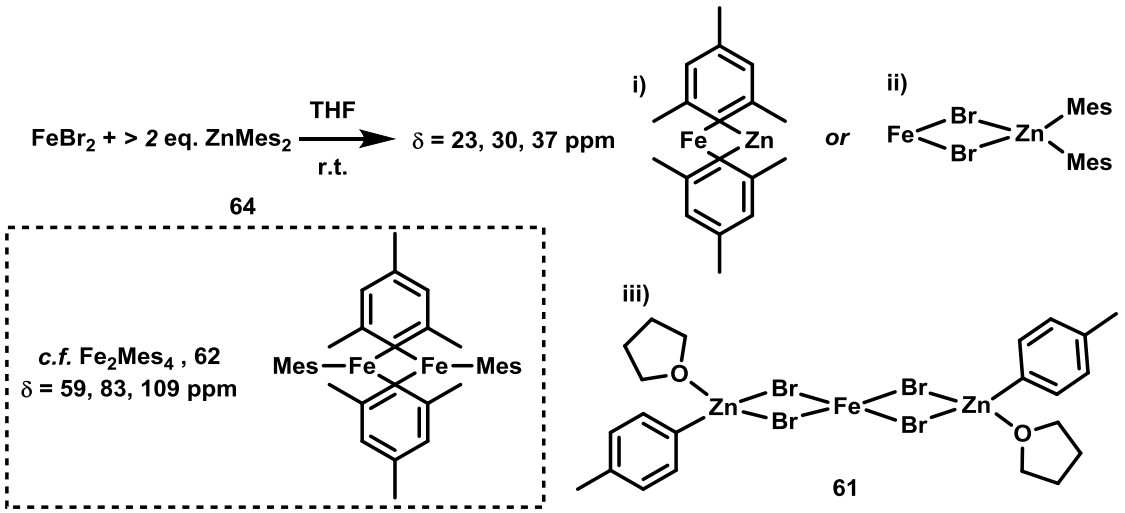

Figure 4.12: Postulated species observed from the reaction of $FeBr_2$ with pure $ZnMes_2$ in THF.

The observed stability of the resulting iron species differs significantly from the reaction of $FeBr_2$ with the less bulky 4-tolyl analogue **54**, where rapid decomposition is observed upon stoichiometric mixing with iron. In the case of **64**, upon coordination of zinc to iron, it is likely that the bulk of the mesityl groups kinetically stabilises the resulting intermediate, providing a thermodynamic sink and preventing further reactivity towards complete aryl transfer to iron, effectively shutting down transmetallation from zinc to iron. Of note is the apparent stability of this intermediate with respect to further increasing the amount of zinc present, as even the addition of a large excess with respect to iron (Zn: Fe = 25: 1) does not result in the disappearance of signals at δ = 23, 30 and 37 ppm.

In spite of the steric differences between **54** and **64**, it can be reasoned that the two nucleophiles would initially react *via* the same pathway, and as such the signals within the spectra displayed in Figure 4.11, tentatively assigned as a bimetallic iron-zinc species, represent spectroscopic evidence of a kinetically stabilised intermediate to transmetallation for diarylzinc / iron systems (Figure 4.13).

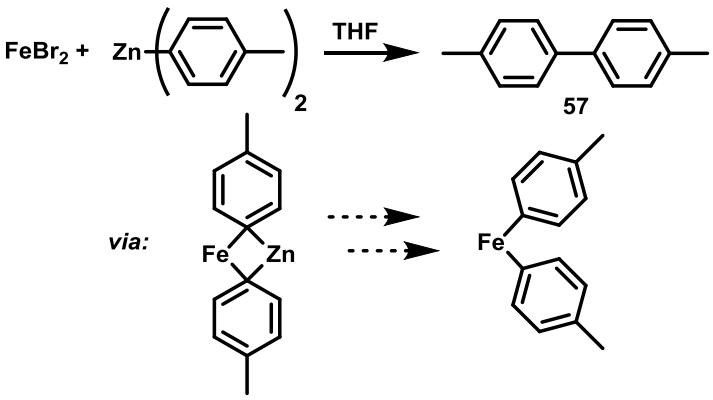

Figure 4.13: Postulated intermediate to transmetallation, featuring a bimetallic iron-zinc species formed as a result of an initial interaction between an organozinc species and an iron salt.

*4.3.2 Reaction of $FeBr_2$ with **64** in the presence of a magnesium salt*

The effect of magnesium salts on the transmetallation of $FeBr_2$ using **64** was next investigated. As with the less bulky diarylzinc reagent **54**, the separate addition of 1, 2 and 3 equivalents of **64** / 2 $MgBr_2$ to $FeBr_2$ in THF gives rise to no transmetallated product. The resultant poorly soluble off-white precipitate is most likely to be the bromoferrate complex **58** (Figure 4.14).

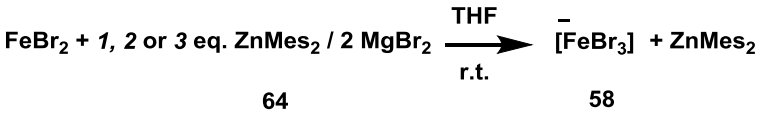

Figure 4.14: Lack of transmetallation from $ZnMes_2$ to $FeBr_2$ at low zinc to iron ratios, with suspected formation instead of the bromoferrate species **58**, mirroring the observed reactivity when the less bulky diarylzinc reagent **54** is used.

However, when the ratio is increased to 4 equivalents of zinc per iron, a pale-yellow, homogeneous solution is obtained, with no precipitate present. Analysis of the resulting solution *via* ^{1}H NMR spectroscopy reveals the presence of six peaks in the paramagnetic region (Table 4.1, *a*), though not ones corresponding to any previously reported iron-mesityl species (such as **62** and **63**), or the proposed bimetallic intermediate described in Section 4.3.1. Due to

each mesityl fragment providing three separate proton environments, the presence of six peaks could reasonably be suggested to be either: two separate iron species in equilibrium, in which the mesityl fragments exist in the same environment; or one iron centre possessing two different mesityl environments, as has been demonstrated recently by Lefevre[94] and Hu.[60]

Analysis of the ^{1}H NMR spectrum obtained from the reaction of 5 equivalents of **64** with $FeBr_2$ (Figure 4.15, *b*) indicates that it is the former case, whereby two iron-mesityl species exist in equilibrium. As can be seen, three of the peaks (δ = 62, 93 and 118 ppm, *) are significantly reduced in intensity and are only weakly visible, whilst the other three (δ 31, 105 and 131 ppm, *) remain clearly present. This suggests that there is an equilibrium in place between two distinct heteroleptic, iron mesityl / halide species, and that higher order transmetallation products are likely to be formed as the ratio of **64** present with respect to iron increases. Indeed, the equilibrium can be further driven by increasing the ratio of **64** to iron to 10 equivalents, leading to the complete disappearance of one of the unknown products (*) in the ^{1}H NMR spectrum (Figure 4.15, *c*), with the other unknown remaining (*). This is in addition to the simultaneous appearance of a new set of signals, corresponding to $[FeMes_3]^-$, **63**, (δ 23, 112 and 127 ppm, *). A qualitative analysis of the two sets of signals present in spectrum *c* indicates **63** is present as the major species. By the addition of 25 equivalents of zinc with respect to iron (Figure 4.15, *d*) there remains only a trace amount of the species corresponding to the second unknown signals (*), with **63** corresponding to the terminal transmetallation product.

Table 4.1: The relative ratio of zinc to iron, and the products observed, in each spectrum as displayed in Figure 4.15.

Spectrum	Zn: Fe	signal in ^{1}H
-	1: 1	insoluble white ppt
-	2: 1	insoluble white ppt
-	3: 1	insoluble white ppt
a	4: 1	$[FeBr_2Mes]^-$, $[FeMes_2Br]^-$
b	5: 1	$[FeBr_2Mes]^-$, $[FeMes_2Br]^-$
c	10: 1	$[FeMes_2Br]^-$, $[FeMes_3]^-$
d	25: 1	$[FeMes_2Br]^-$, $[FeMes_3]^-$

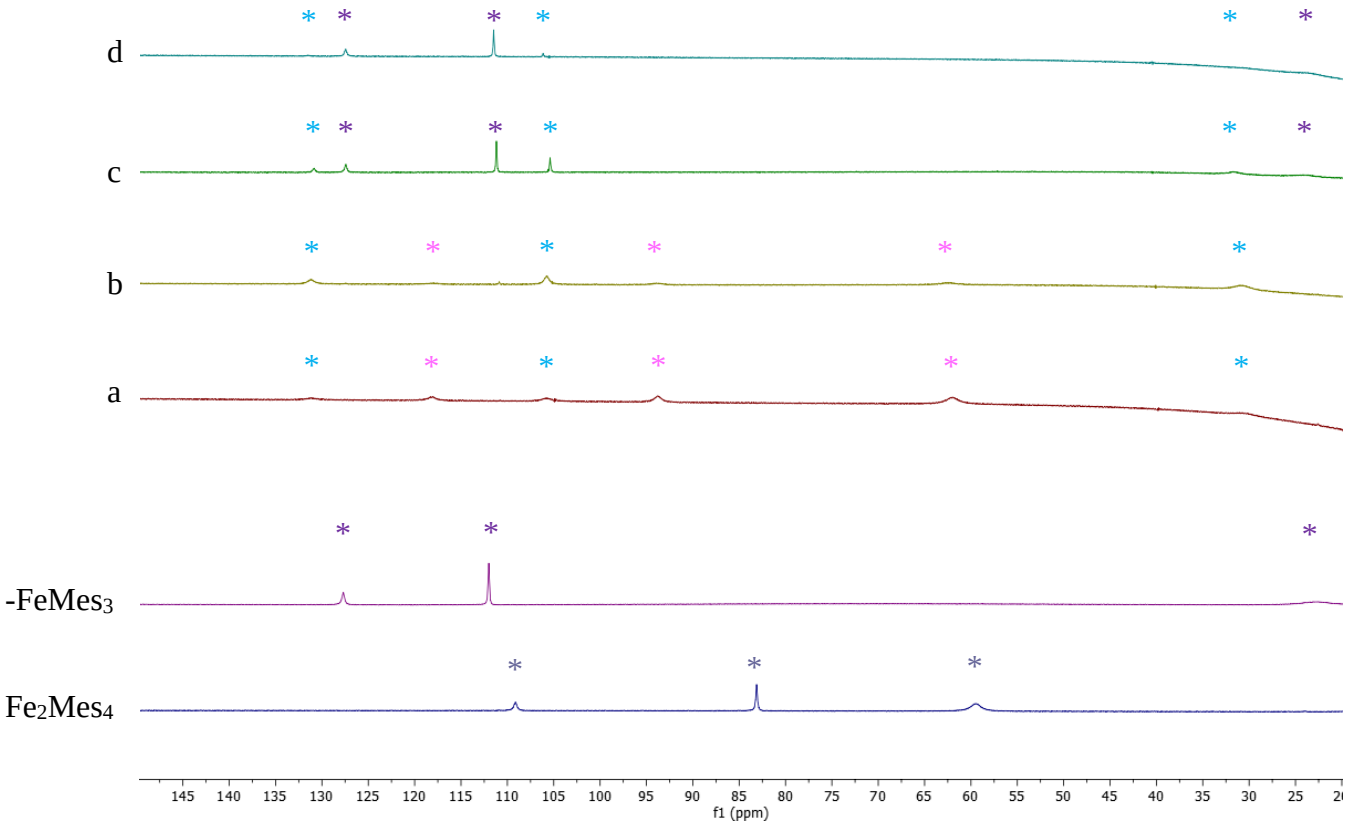

Figure 4.15: Expanded stacked ^{1}H NMR spectra, from 20 to 150 ppm, corresponding to the separate addition of 4, 5, 10 and 25 (*a*, *b*, *c* and *d* respectively) equivalents of $ZnMes_2$ / 2 $MgBr_2$ to $FeBr_2$ in THF at room temperature. The ^{1}H NMR spectra of Fe_2Mes_4, **62**, and $[FeMes_3]^-$, **63**, are also shown for clarity.

*4.3.3 Spectroscopic observation of heteroleptic ferr*ate *species*

Whilst the conversion to $[FeMes_3]^-$, **63**, is clear, and was checked against an independently prepared sample, the identity of the two intermediate species (* and *) which appear at lower zinc to iron ratios is more ambiguous. In an attempt to provide further clarity as to their structure, the equilibrium between an arylated and halogenated iron centre was manipulated by adding a bromide source to an iron centre already bearing mesityl groups, in the absence of zinc. Through removal of the organometallic diarylzinc species from the reaction mixture, the transfer of a halide ligand to iron can be observed in isolation. The previously mentioned dimeric complex Fe_2Mes_4, **62**, was prepared and reacted with $[NBu_4][Br]$, a simple and metal-free source of bromide (Figure 4.16).

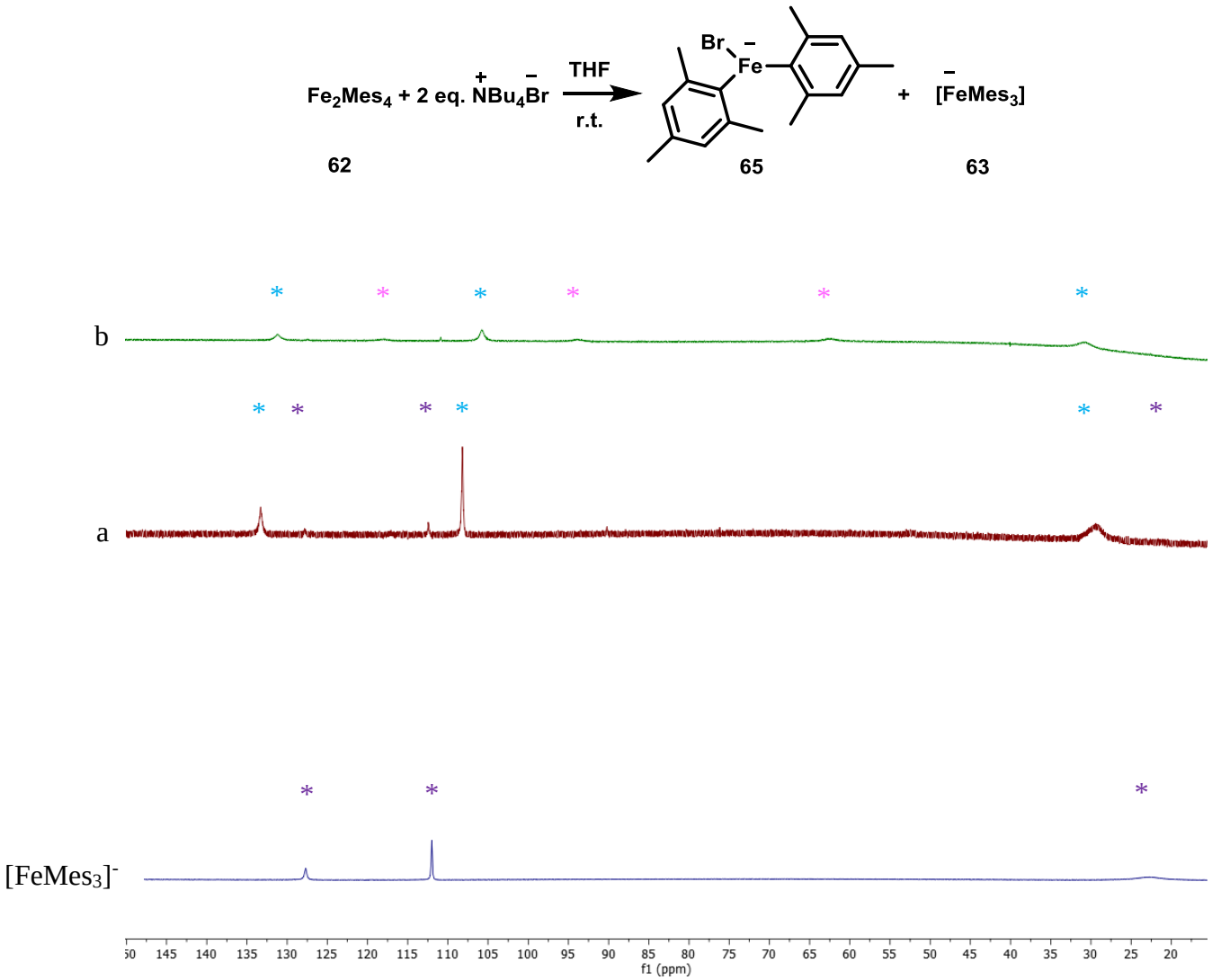

Figure 4.16: Expanded stacked ^{1}H NMR spectra, from 15 to 150 ppm, corresponding to (a) the reaction between Fe_2Mes_4, **62**, and 2 eq. of NBu_4Br; (b) $FeBr_2$ and 5 eq. of **64** / 2 $MgBr_2$. $[FeMes_3]^-$, **63**, is also shown for clarity.

The resulting ^{1}H NMR spectrum is displayed in Figure 4.16, *a*, in addition to the spectrum corresponding to the addition of 5 equivalents of **64** / 2 $MgBr_2$ to $FeBr_2$. The reaction results in the complete disappearance of signals corresponding to the starting material Fe_2Mes_4, **62**, and in the appearance of peaks corresponding to the second of the two previously unknown (*) species observed in Figure 4.15. Although the peaks are slightly shifted, most likely due to matrix effects from magnesium and zinc salts present in spectrum *b*, they are here assigned to the complex $[FeBrMes_2]^-$, **65**. This fits with the data in Figure 4.16, in which the signals assigned as **65** represent the final intermediate observed before formation of $[FeMes_3]^-$, **63**. The remaining unknown signals (*) displayed in Figure 4.15 are therefore assigned as $[FeBr_2Mes]^-$, **66**. Attempts to further drive the equilibrium towards **66** by addition of twenty equivalents of

NBu_4Br to Fe_2Mes_4, **62**, were unsuccessful, indicating that displacement of a mesityl group from iron provides a significant barrier. Interestingly, weak peaks corresponding to $[FeMes_3]^-$, **63**, are also observed from the reaction displayed in Figure 4.16. This suggests that there is likely an equilibrium between the heteroleptic ferrate species **65** and **66** and the homoleptic species **63**, even in the absence of added organometallic diarylzinc species.

These results confirm that above three equivalents of **64** added, the transmetallation of $FeBr_2$ is made possible in the presence of magnesium salts, and that an equilibrium exists between the resulting hetero- and homoleptic ferrate products. The above results are summarised in Figure 4.17.

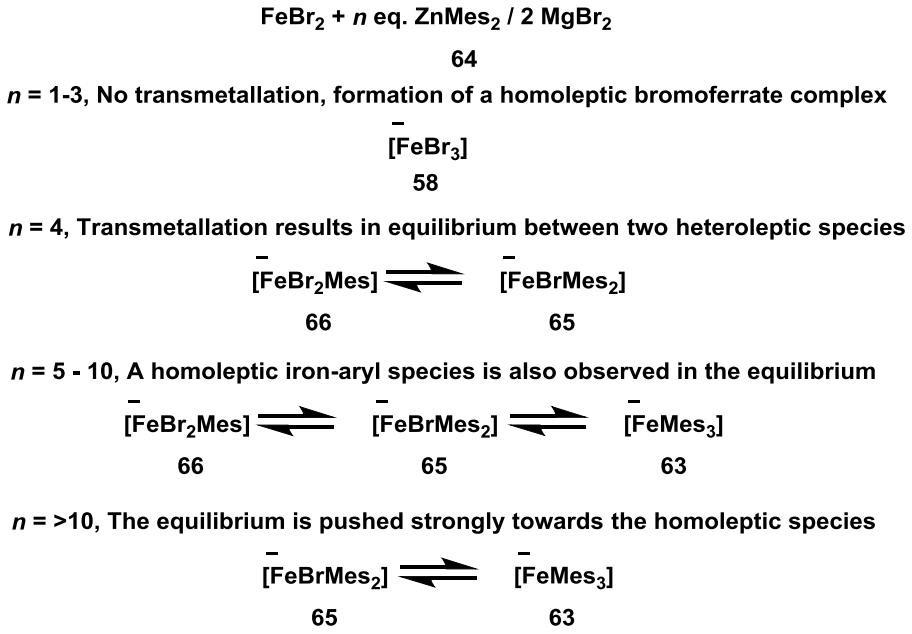

Figure 4.17: Observed reactivity of $FeBr_2$ with increasing amounts of $ZnMes_2$ / 2 $MgBr_2$, resulting in an equilibrium between hetero- and homoleptic iron species.

When the transmetallation studies of $FeBr_2$ are compared, there is a clear difference in reactivity due to the differing bulk of **54** and **64.** In the case of the less bulky nucleophile **54**, transmetallation to iron occurs readily in the absence of any additive, and despite initially being inhibited when magnesium salts are added, again occurs in a facile manner upon further increasing the amount of **54** present with respect to $FeBr_2$. However, in the case of the bulkier nucleophile **64**, transmetallation does not occur without the presence of magnesium bromide, regardless of the amount of zinc added, and instead a bimetallic zinc-iron intermediate is suggested to form. Therefore, whilst magnesium bromide appears necessary to help effect transmetallation to iron from the bulky nucleophile **64**, its poor performance in cross-coupling

reactions (Figure 4.18),[103] and the comparative success of less bulky nucleophiles towards the transmetallation of iron in the absence of magnesium salts, mean that the primary role of magnesium bromide in catalytic reactions does not appear to be the facilitation of transmetallation.

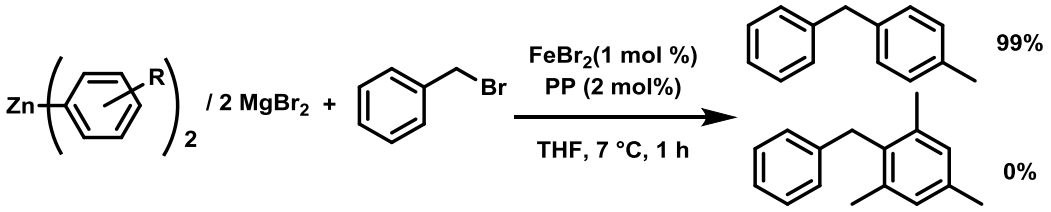

Figure 4.18: Difference in the observed catalytic reactivity in the iron-catalysed Negishi cross-coupling, depending on the diarylzinc reagent used.[103]

4.4 Transmetallation from iron to zinc

4.4.1 Zinc speciation following transmetallation

The presence of equilibrium mixtures of ferrate species (**63**, **65** and **66**) in the proceeding transmetallation reactions using the bulky diarylzinc reagent **64** is interesting, especially as the heteroleptic ferrate species **65** and **66** remain observable with more than 10 equivalents of zinc present with respect to iron.[xii] This equilibrium, in combination with the observed reactivity of Fe_2Mes_4, **62**, raises the possibility of transmetallation from iron to zinc. Whilst not directly applicable to the iron-catalysed Negishi cross-coupling, the ability of iron to transmetallate to zinc is of interest from an organometallic perspective and would also serve to demonstrate the complexity of the intermediates, and potential side-reactions, that may be occurring within reaction mixtures. Accordingly, the reaction of Fe_2Mes_4, **62** with increasing equivalents of $ZnBr_2$ was monitored by ^1H and ^{13}C NMR spectroscopy. In order to extract as much information as possible about any resulting transmetallation processes and the resultant zinc and iron species, a wide range of ratios was employed as shown in Table 4.2, with the resulting spectra in Figure 4.19.

[xii] The corresponding reaction with mesitylmagnesium bromide results in the homoleptic complex **63** with only 4 equivalents added with respect to iron.

Table 4.2: Ratios of iron and mesityl with respect to zinc, and a summary of peaks observed in the resulting ^{13}C NMR spectra, for the reaction between Fe_2Mes_4 **64** with increasing amounts of $ZnBr_2$.

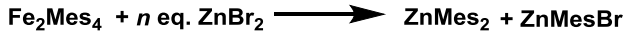

62 **64** **67**

Spectrum	Zn: Fe	Fe: Zn	Mes: Zn	signal in ^{13}C
a	0.125	8	16	$ZnMes_2$, MesH
b	0.250	4	8	$ZnMes_2$, MesH
c	0.375	2.6	5.3	$ZnMes_2$, MesH
d	0.500	2	4	$ZnMes_2$, MesH
e	0.625	1.6	3.2	$ZnMes_2$
f	1.25	0.8	1.6	$ZnMes_2$, weak
g	2.50	0.4	0.8	ZnBrMes
h	5.00	0.2	0.4	ZnBrMes
i	10.00	0.1	0.2	ZnBrMes
j	25.00	0.04	0.08	ZnBrMes

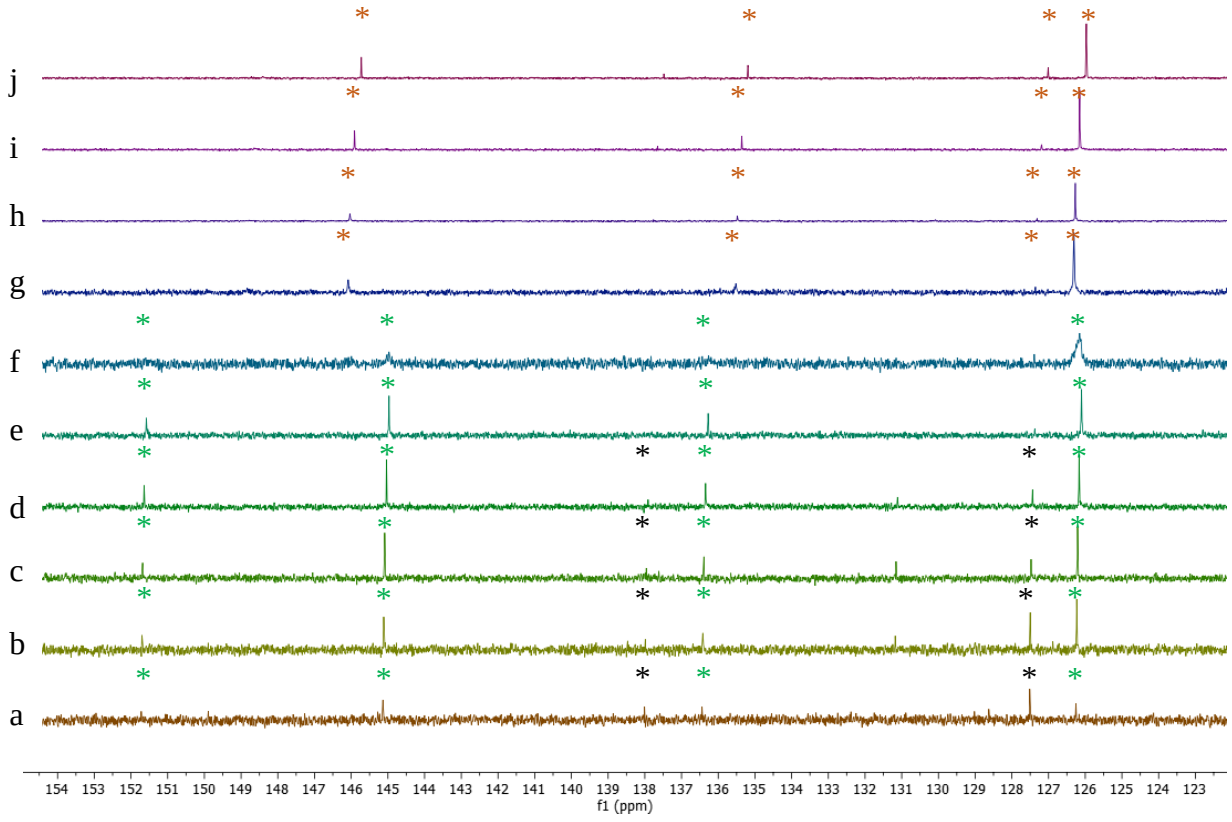

Figure 4.19: ^{13}C NMR spectra resulting from the additions of $ZnBr_2$ to Fe_2Mes_4, as per Table 4.2.

Upon the addition of 0.125 equivalents of zinc with respect to iron, signals corresponding to the diaryl zinc species $ZnMes_2$, **64**, (δ 152.0, 145.4. 136.7, 126.5 ppm, *) are observed in the aryl region of the resulting ^{13}C NMR spectrum (Figure 4.19, *a*). This immediate evidence of transmetallation is striking, but it can be rationalised by considering the ratio in the opposite manner; in effect there are 8 equivalents of nucleophile (iron) with respect to substrate (zinc).

Trace amounts of another set of signals (δ 138.0, 127.4, ppm *) corresponding to mesitylene are also present. These peaks appear as the only observable species in Figure 4.19, spectra *b*, *c* and *d*.

Spectrum *e* displays peaks corresponding solely to $ZnMes_2$ (*), with *f* also showing the same, indicating that at ratios between 3 and 1.5 mesityl groups per zinc the formation of diarylzinc product proceeds selectively, with no side product formation. Further increasing the equivalents of zinc added, so that the ratio of mesityl to zinc falls below 1 (Figure 4.19, *g*), results in signals corresponding to ZnBrMes, **67**, (δ 146.3, 136.0, 127.7, 126.6, *) being observed. Here the ratio of mesityl to zinc dictates formation of the mono-aryl zinc halide species, which remains present throughout all remaining additions (up to 25 equivalents of zinc added).

Whilst the ^{13}C NMR spectra presented are useful for a qualitative understanding of reaction products, they do not allow for a quantitative representation; as such no comment can be made as to the efficacy of the process. Accordingly, the reaction was simultaneously investigated *via* ^{1}H NMR spectroscopy using an internal standard (dodecane), allowing for quantification of *in situ* formed zinc products. The ^{1}H data matches well with the ^{13}C spectra: the immediate formation of $ZnMes_2$, **64**, (δ 6.59, *) and subsequently ZnBrMes, **67**, (δ 6.55,*) can be clearly observed, in spite of matrix effects causing slight discrepancies in their chemical shifts from the isolated products. The broad signal observed in spectrum *f* indicates that there is an equilibrium present between the two species when the ratio of zinc to mesityl is between one and two. The impurity mesitylene commented on previously is also visible in all spectra (δ 6.63, *).

Table 4.3: The ratio of Zn to Fe, and the transmetallated Zn product observed in the resulting ^{1}H NMR spectrum in each case, from the reaction of Fe_2Mes_4 with increasing amounts of $ZnBr_2$. All integral values relative to dodecane internal standard.

Spectrum	∫ 6.55	∫ 6.59	Zn: Fe	signal in ^{1}H	% yield of TM Zn product
a	0	0.76	0.11	$ZnMes_2$	76
b	0	1.68	0.22	$ZnMes_2$	84
c	0	2.43	0.34	$ZnMes_2$	81
d	0	3.21	0.45	$ZnMes_2$	80
e	0	4.11	0.57	$ZnMes_2$	82
f	0	6.24	1.14	$ZnMes_2$	72
g	6.22	0	2.29	ZnBrMes	71
h	6.12	0	4.59	ZnBrMes	70
i	5.88	0	11.48	ZnBrMes	68
j	5.50	0	22.96	ZnBrMes	63

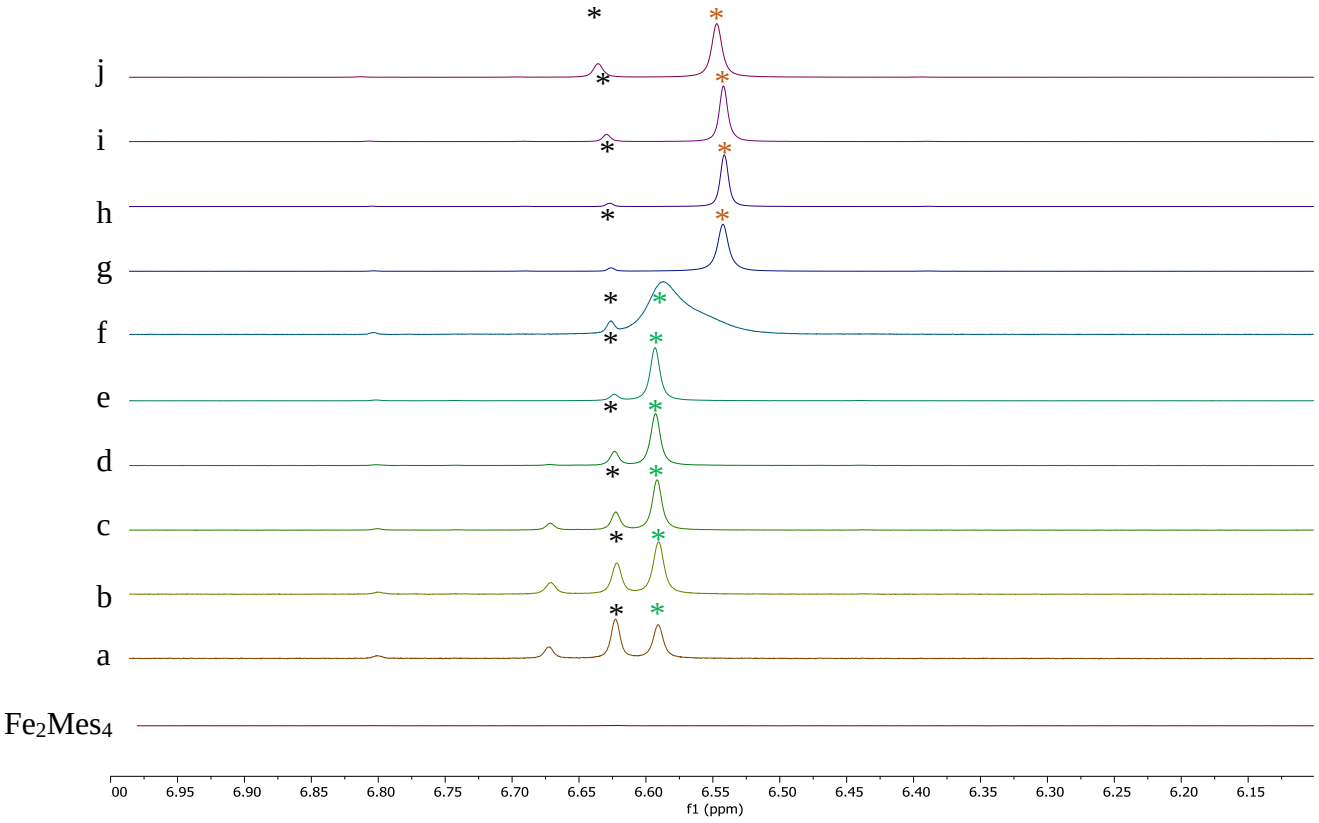

Figure 4.20: Expanded stacked ^{1}H NMR spectra, from 6.10 to 7.00 ppm, for the reaction of Fe_2Mes_4, **62**, with increasing equivalents of $ZnBr_2$, as per Table 4.3.

As displayed in Figure 4.20, transmetallation from iron to zinc proceeds in an efficacious manner, with the transmetallated zinc product being observed in yields of up to 80%, based on the limiting reagent of the given reaction.

4.4.2 Iron speciation following transmetallation

The data presented so far are concerned with the fate and quantification of zinc species following transmetallation from iron, and as the expected products are known, this process is relatively straightforward. More difficult to elucidate are the iron products formed as transmetallation occurs to the zinc centre. In order to gain information on the intermediate iron products, from Fe_2Mes_4, **62**, to $FeBr_2$ (formed following complete aryl transfer from **62**), the reaction was monitored *via* ^{1}H NMR spectroscopy, with parameters tuned so as to allow for observation of paramagnetic intermediates (Figure 4.21). Upon the addition of 0.125 equivalents of $ZnBr_2$ with respect to iron, peaks corresponding to Fe_2Mes_4, **62**, completely disappear from the ^{1}H NMR spectrum (Figure 4.21, *a*), accompanied by the appearance of as-yet unassigned peaks (δ = 38, 70 and 80 ppm, *). These peaks remain when the ratio of zinc to iron is increased to 0.25 (Figure 4.21, *b*), along with the appearance of a second as yet unassigned set of peaks (δ 70, 96 and 117 ppm, *). As more zinc is added, the first set of signals disappear (*), and the second remain until the ratio of zinc to iron exceeds 1: 1 (Figure 4.21, *f*), after which no paramagnetically shifted peaks are observed.

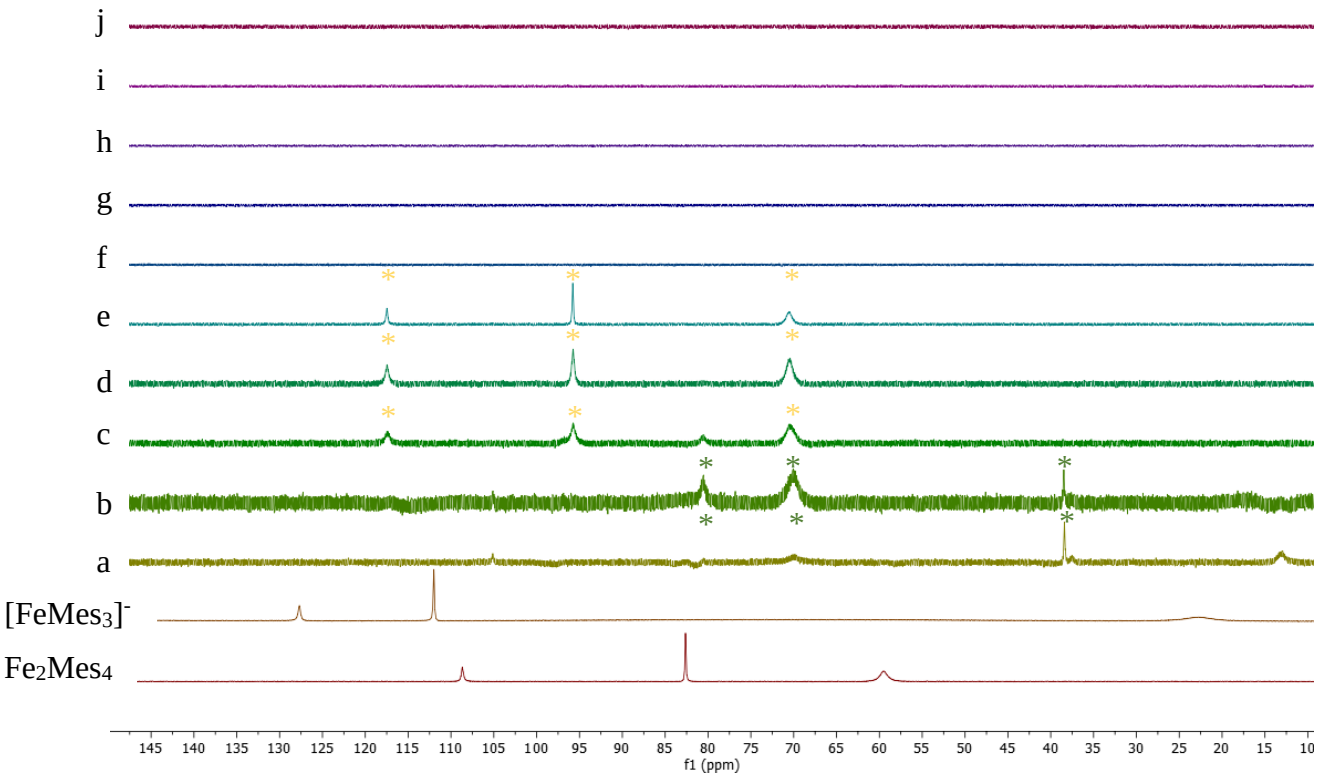

Figure 4.21: Stacked ^{1}H NMR spectra, from 10 to 150 ppm, for the reaction of Fe_2Mes_4, **62**, with increasing equivalents of $ZnBr_2$. $[FeMes_3]^-$, **63**, is also shown for clarity.

From the above data, there are several points of interest to be noted. First is the immediate disappearance of peaks corresponding to **62**, even when small ratios of zinc are present with respect to iron (0.125: 1). When taken together with the data from Figure 4.20 demonstrating the concomitant formation of $ZnMes_2$, **64**, it can be reasoned that the remaining iron and mesityl groups rapidly rearrange to give an unknown species (Figure 4.21, *a* and *b*; δ = 38, 70 and 80 ppm, *) with an iron to mesityl stoichiometry of $FeMes_{<1.75}$. This is followed by a second rearrangement to give a second unknown species (Figure 4.21, *c* – *e*; δ = 70, 96 and 117 ppm, *) when the ratio of zinc to iron is around 0.3, with a reaction stoichiometry of $FeMes_{<1.3}$. These signals remain until the zinc to iron ratio exceeds 2: 1, after which no peaks are observed in the paramagnetic region (Figure 4.21, *f* – *j*). Both these species are almost certainly multinuclear, due to the non-integer ratios of iron to mesityl. Further, the corresponding chemical shifts lie away from those typically seen for mononuclear, three co-ordinate iron-aryl complexes, such as $[FeMes_3]^-$, **63**, $[FeBr_2Mes]^-$, **66** and $[FeBrMes_2]^-$, **65**. However, the same peaks (*) were observed when Fe_2Mes_4, **62**, was reacted with both $MgBr_2$ and $FeBr_2$. Taken together, these results strongly suggest that heteroleptic, mono-metallic iron complexes (bearing both bromide and mesityl ligands) are formed as intermediate species as transmetallation from **62** (to $FeBr_2$, $MgBr_2$ or $ZnBr_2$) occurs.

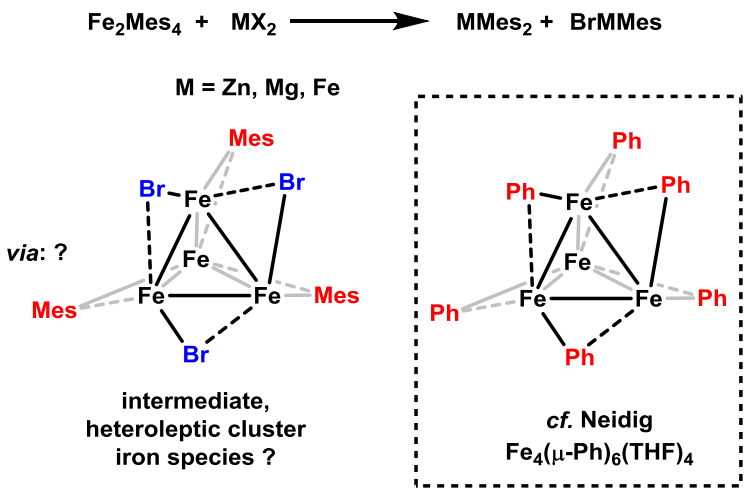

Figure 4.22: Proposed iron speciation following from transmetallation from Fe_2Mes_4 to $ZnBr_2$.

Extensive efforts were made to grow crystals from the mixtures described above, but unfortunately none were successful. Due to the extreme sensitivity of the mixtures formed, other methods of routine analysis were not available to requisite level of air and moisture sensitivity. It is therefore difficult to suggest what the intermediate iron speciation resulting from transmetallation to zinc is. However, work from Neidig on the multi-nuclear iron species

formed from mixtures of aryl Grignard reagents and simple iron salts supports the suggestion that the formation of cluster type compounds may be occurring within the reaction mixtures described here (Figure 4.22).[59]

4.5 Transmetallation in the presence of diphosphine ligand

The data so far presented demonstrate the feasibility of transmetallation from a zinc centre to iron, and from an iron centre to zinc, in the presence of magnesium salts. However, in order to obtain a more catalytically relevant model of transmetallation with regards to iron-catalysed Negishi cross-coupling reactions, the presence of a diphosphine ligand is required, as previously discussed in Section 4.1. Therefore, whilst transmetallation and catalytic turnover are discrete processes, and should be treated as such, the presence of a diphosphine ligand is necessary for any discussion on transmetallation to have relevance with respect to catalysis. Due to its proven efficacy in iron-catalysed cross-coupling reactions, dpbz was chosen as the model diphosphine ligand for these studies.

*4.5.1 Reaction of $FeBr_2$ with **54** in the presence of a magnesium salt and dpbz*

As discussed in Section 4.2, in the absence of diphosphine ligand the reaction of $FeBr_2$ with $Zn(4\text{-tol})_2$, **54**, / 2 $MgBr_2$ in a 1:1 ratio results in the formation of the insoluble bromoferrate complex $[FeBr_3]^-$, **58**, and complete recovery of the diarylzinc reagent **54**, with no transmetallation to iron. Whilst the formation of **58** is in itself intriguing, the lack of diphosphine ligand does bear consideration. Accordingly, the reaction was revisited in the presence of the ligand dpbz.

Upon the addition of two equivalents of dpbz to a suspension of **58** in THF, (freshly prepared as before, from the reaction of $FeBr_2$ with **54** / 2 $MgBr_2$**)**, dissolution occurs almost instantly with stirring to give a deep red solution. Analysis of the reaction mixture *via* UV / Vis spectroscopy indicates quantitative formation of the iron(I) complex $FeBr(dpbz)_2$, **4** (Figure 4.23), which has been previously demonstrated to form as a result of transmetallation, followed by a bimolecular reductive elimination.[63]

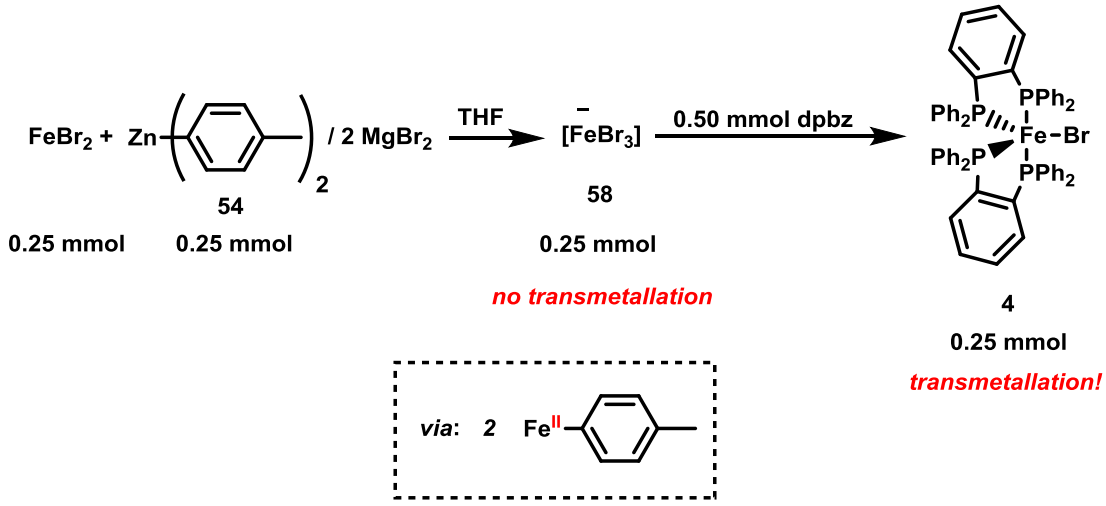

Figure 4.23: Transmetallation of **58** (formed from the reaction of $FeBr_2$ with **54** in the presence of $MgBr_2$) by $Zn(4\text{-tol})_2$ / 2 $MgBr_2$ in the presence of added diphosphine ligand.

It can therefore be reasoned that the addition of dpbz serves two purposes: it must first effect transmetallation from **54** to iron, after which it then appears to act as a trap, preventing decomposition of reduced iron species to nanoparticles, as was previously observed in its absence (*cf.* Figure 4.6). As demonstrated earlier in this chapter, by switching from the diarylzinc species using the 4-tolyl aryl fragment, **54** to the bulkier mesityl nucleophile, **64**, the instability of iron-aryl complexes was overcome to allow for intermediates in the phosphine-free transmetallation of iron to be identified. By applying the same methodology in the presence of dpbz, the identity of dpbz-adducts of iron and zinc intermediates relevant to transmetallation was sought. Accordingly, a range of potential reaction intermediates of both zinc and iron bearing dpbz and mesityl groups was first synthesised and characterised, to allow for identification in the relevant transmetallation studies.

4.5.2 Synthesis of intermediates in the reactions between $FeBr_2$, dpbz and ***64***

4.5.2.1 Iron complexes

The reaction of a 1:1 mixture of $FeBr_2$ with dpbz yields the mono-diphosphine complex $FeBr_2$(dpbz) **68**. Analysis by X-ray crystallography reveals a regular tetrahedral geometry about the metal centre (Figure 4.24). The average Fe-P bond length is 2.4271(5) Å, which is in good agreement with complex $FeBr_2$(SciOPP) from Neidig.[64] The ^{1}H NMR spectrum reveals characteristic paramagnetically shifted peaks as shown in Figure 4.28 (*), however due to the paramagnetic metal centre no signal is observed in the ^{31}P NMR spectrum. Synthesis of the bis-diphosphine complex $FeBr_2(dpbz)_2$ **69** is also possible by reaction of a 1:2 ratio of $FeBr_2$

with dpbz. The parameters obtained from a crystallographic analysis reveal a regular octahedral geometry about the metal centre (average Fe-P bond length = 2.546(5) Å), in line with those from the previously reported chloro-analogue, $FeCl_2(dpbz)_2$ from Connelly.[134]

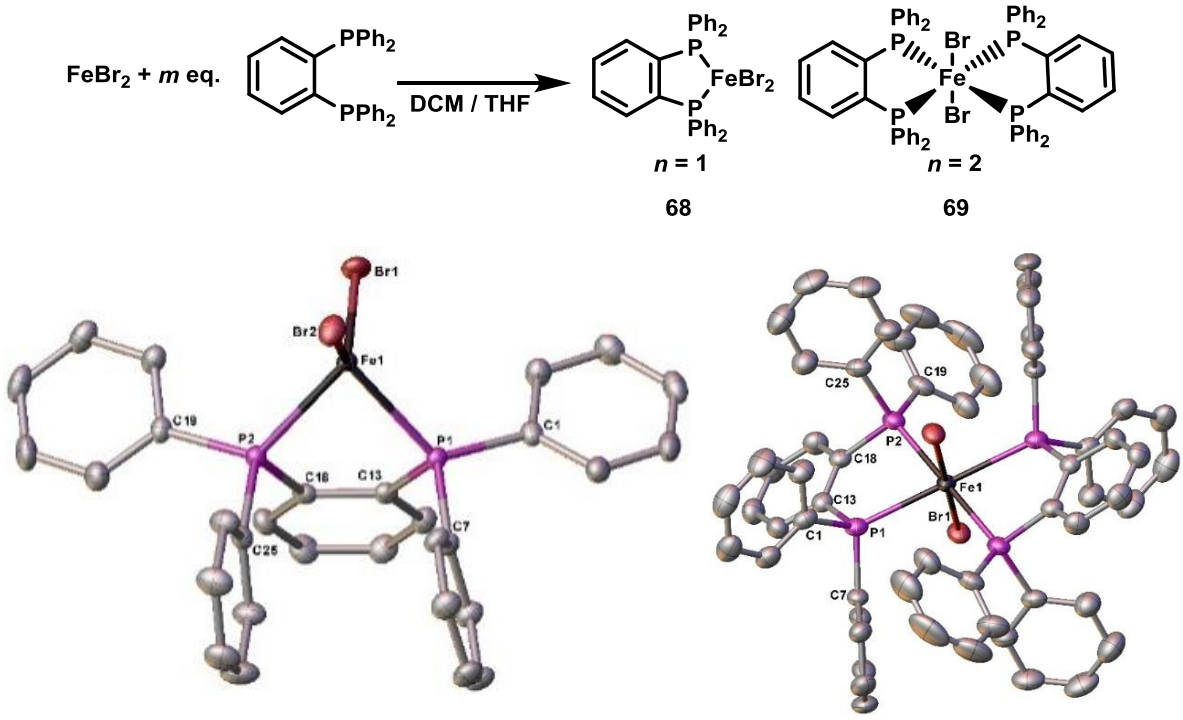

Figure 4.24: Preparation and X-ray crystal structures of $FeBr_2(dpbz)$ **68** and $FeBr_2(dpbz)_2$ **69.** Crystallographic analysis carried out by Dr. Antonis Messinis.

Interestingly, although the six-coordinate complex **69** is accessible in the solid state, analysis by XAS and NMR spectroscopy reveal an equilibrium to be present in solution between **68** and dpbz. A THF-d_8 solution of **69** yields signals corresponding to **68** in the ^1H NMR spectrum, and a single signal corresponding to free dpbz is observed in the ^{31}P NMR spectrum. Quantification of this peak against an external standard reveals one free equivalent of dpbz to be present per metal centre; taken together these data indicate that in a THF solution **68** and dpbz exist discretely (Figure 4.25).

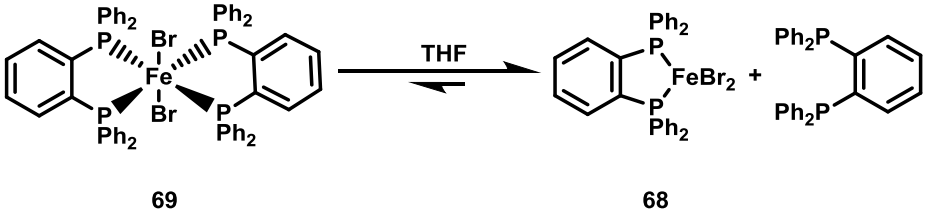

Figure 4.25: Observed equilibrium between **68** and dpbz upon dissolution in THF.

In order to access iron complexes bearing both dpbz and mesityl ligands, Fe_2Mes_4, **62** was reacted with dpbz in a 1:1 ratio of iron to phosphine. Analysis of the reaction mixture by ^{1}H NMR spectroscopy indicated complete disappearance of signals corresponding to **62**, along with the formation of several new peaks (δ = 11.6, 65.7, 75.7 and 87.0 ppm, *). Following crystallisation of the reaction mixture, dark red crystals amenable to a crystallographic analysis were grown, confirming the structure to be $FeMes_2$(dpbz), **70.** (Figure 4.26).

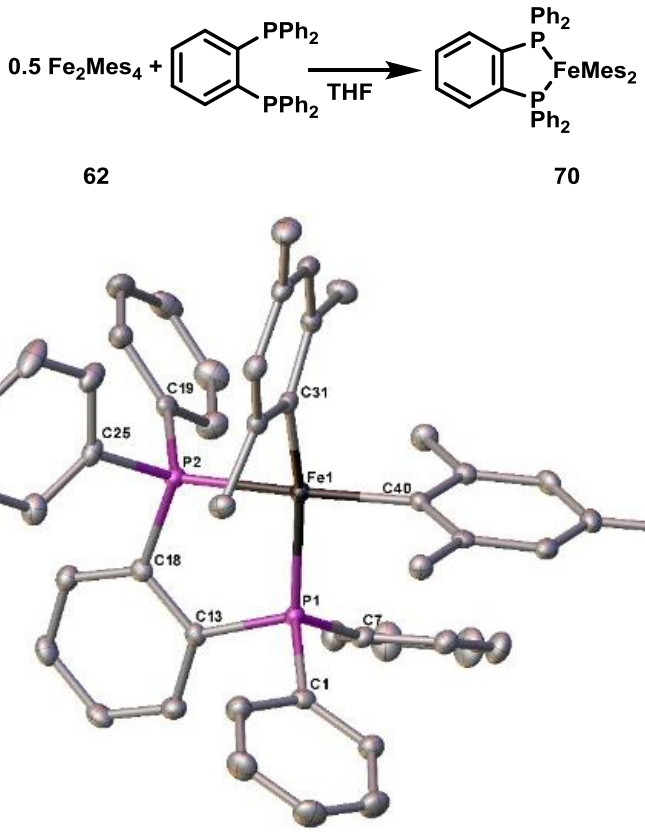

Figure 4.26: Preparation and X-ray crystal structure of $FeMes_2$(dpbz) **70.** Crystallographic analysis carried out by Dr. Hazel Sparkes.

The complex exhibits a regular tetrahedral geometry about the metal centre, with an Fe-P bond length of 2.2613(5) Å, slightly shorter than the recently characterised bulky derivative $FeMes_2$(SciOPP) from Neidig (Fe-P = 2.3225(7) Å). Attention was next turned to the synthesis and isolation of the mixed aryl-halide iron diphosphine complex, FeBrMes(dpbz). Reaction of $FeBr_2$(dpbz) with mesitylmagnesium bromide in a 1:1 ratio results in the complete disappearance of peaks corresponding to the iron starting material. However, alongside one set of predominating peaks, the resulting ^{1}H NMR spectrum indicated a mixture of products, including $FeMes_2$(dpbz), **70**, to be present. In order to induce a cleaner reaction, $FeBr_2$(dpbz) was instead reacted with mesityl lithium, allowing for the removal of excess halide from the mixture as lithium bromide (Figure 4.27). Gratifyingly, the resultant ^{1}H NMR spectrum is

much cleaner, with the predominant peaks corresponding to FeBrMes(dpbz), **71**, (δ = 12.1, 27.7, 85.9, 120.4 and 152.7 ppm, *). Despite extensive efforts, and the successful production of several different crystalline samples, none amenable to X-ray diffraction were obtained. The resulting ^{1}H NMR spectra for the iron complexes **68**, **70** and **71** are displayed in Figure 4.28.

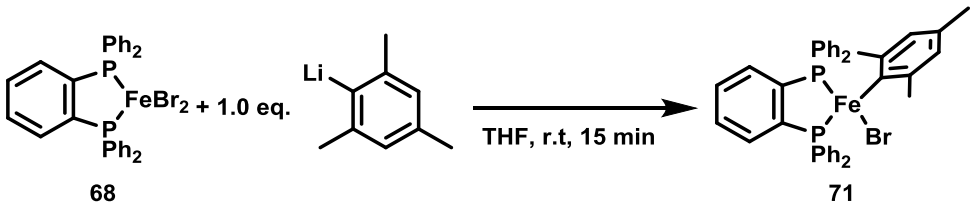

Figure 4.27: Preparation of FeBrMes(dpbz), **71.**

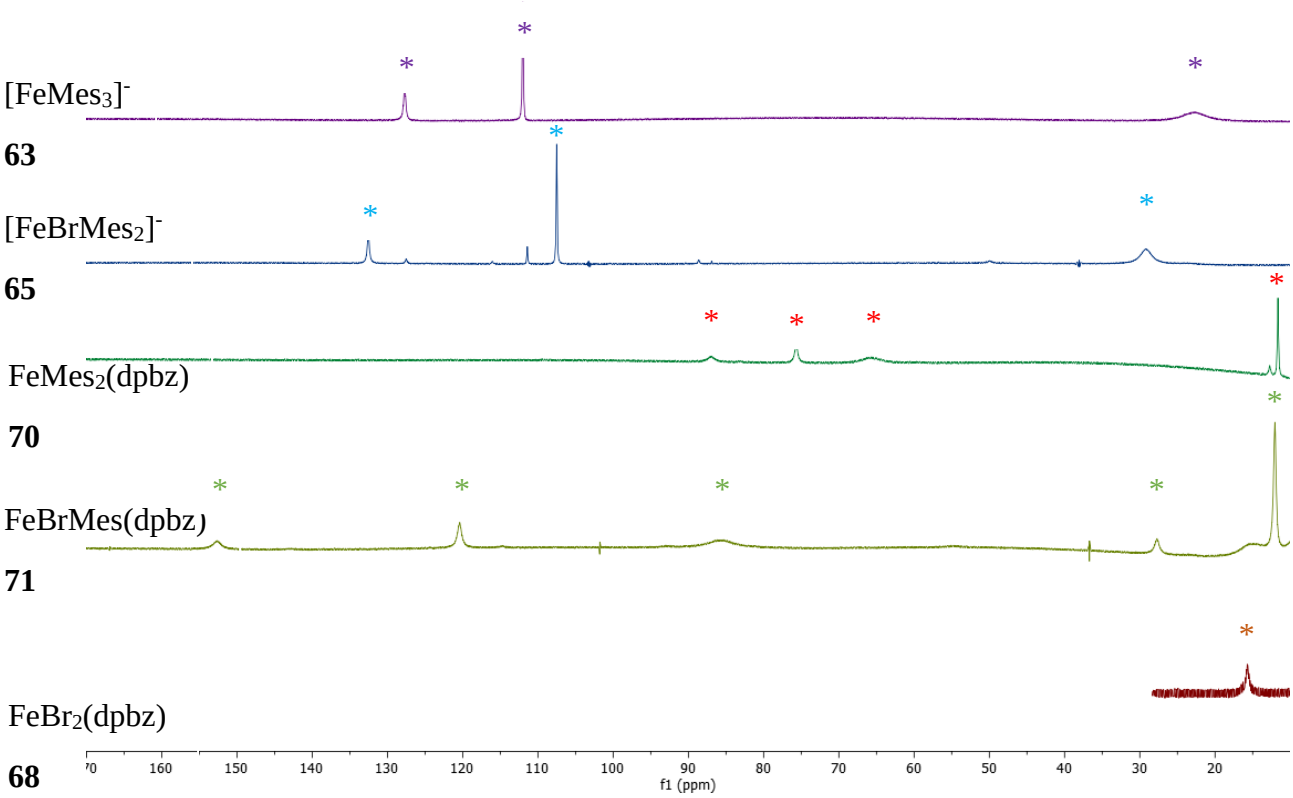

Figure 4.28: Stacked ^{1}H NMR spectra, from 10 to 170 ppm, corresponding to the iron-mesityl diphosphine complexes **68**, **71** and **70.** The ligand free heteroleptic complex **65**, and the homoleptic complex **63**, are also displayed. For clarity, peaks below 10 ppm are omitted.

4.5.2.2 Zinc complexes

Having characterised the iron species that could reasonably be expected to form as products from transmetallation reactions containing $FeBr_2$, **64** and dpbz, the corresponding zinc species were next synthesised. The reaction of a 1:1 mixture of $ZnBr_2$ and dpbz yields the

mono-diphosphine complex $ZnBr_2$(dpbz) **72.** Crystallographic analysis reveals a regular tetrahedral geometry about the metal centre (Figure 4.29).

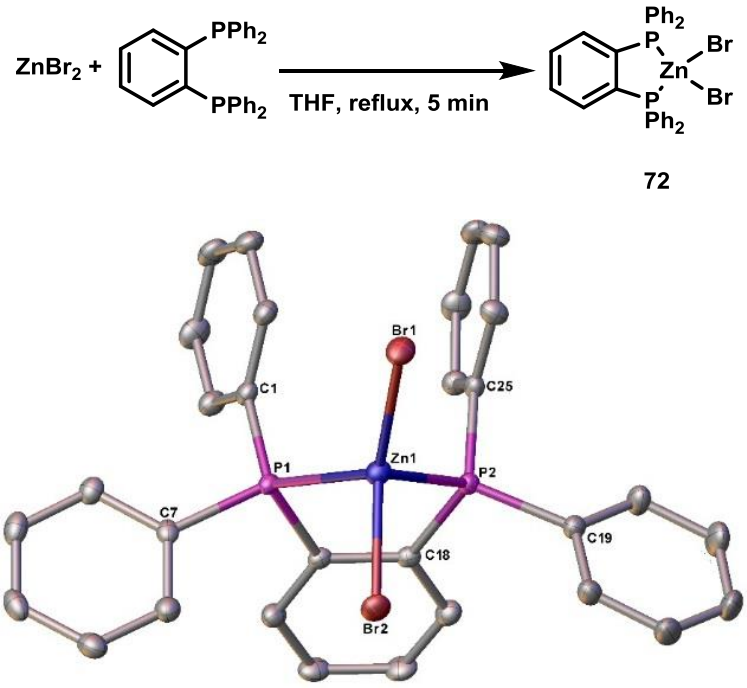

Figure 4.29: Preparation and X-ray crystal structure of $ZnBr_2$(dpbz), **72.** Crystallographic analysis carried out by Dr. Antonis Messinis.

Analysis of **72** by ^{1}H NMR spectroscopy is not instructive; although the signals do shift with respect to free dpbz and allow for characterisation in isolation, they remain in the diamagnetic aryl region, which is often convoluted in spectra resulting from *in situ* reaction mixtures. More useful is the resultant ^{31}P NMR spectrum, which displays a characteristic shift of several ppm upfield from the free ligand to δ = -22.2 ppm.

As has been previously reported in the case of other aryl groups,[135] preparation of the mono-arylzinc halide complex BrZnMes, **73**, yields a heterogeneous mixture even at concentrations below 0.1 M in THF. Gratifyingly however, upon addition of one equivalent of dpbz a homogeneous solution is formed, with analysis using ^{31}P NMR spectroscopy confirming the presence of a single broad peak at -17 ppm, assigned as ZnBrMes(dpbz), **74** (Figure 4.30). Unfortunately, despite several crystalline samples being produced from the resulting reaction mixtures, none were amenable to X-ray diffraction.

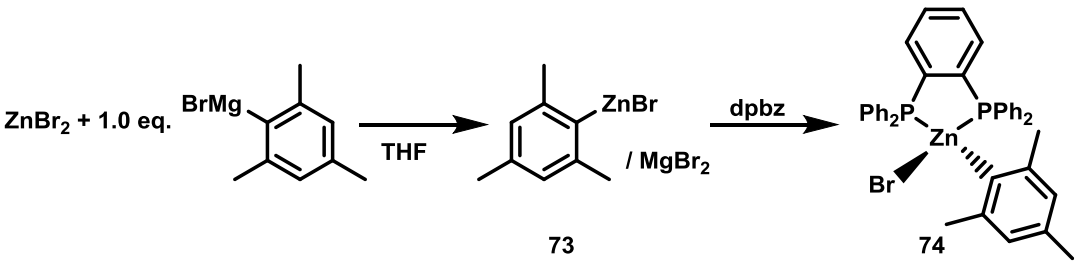

Figure 4.30: Synthesis of the arylzinc halide-diphosphine complex **74.**

Attempts to synthesise the complex $ZnMes_2$(dpbz) were unsuccessful. Reaction of $ZnMes_2$, **64**, with dpbz in a 1:1 ratio yielded no change in the resultant ^1H and ^{31}P NMR spectra compared to that of free dpbz and free $ZnMes_2$, even after 5 h heating at 70 °C. With a complete set of potential zinc and iron intermediates characterised, or otherwise accounted for, the effect of dpbz on transmetallation was investigated.

*4.5.3 Reaction of $FeBr_2$ with **64** in the presence of a magnesium salt and dpbz*

Due to the lack of reactivity of dpbz towards $ZnMes_2$, the effect of diphosphine coordination to iron with respect to transmetallation was investigated. Whilst in a catalytic reaction pre-formation of an iron-diphosphine complex is not necessary,[103] the complex $FeBr_2$(dpbz) **68** was used as the starting material to avoid ambiguity towards initial iron speciation. The reaction ratios between **68** and **64** are listed in Table 4.4; the ^1H NMR spectra resulting from each addition are displayed in Figure 4.31.

Table 4.4: Ratio of zinc to iron, and a summary of the peaks seen in the resulting ^1H NMR spectra, for the reaction between $FeBr_2$(dpbz) with increasing amounts of $ZnMes_2$ / 2 $MgBr_2$.

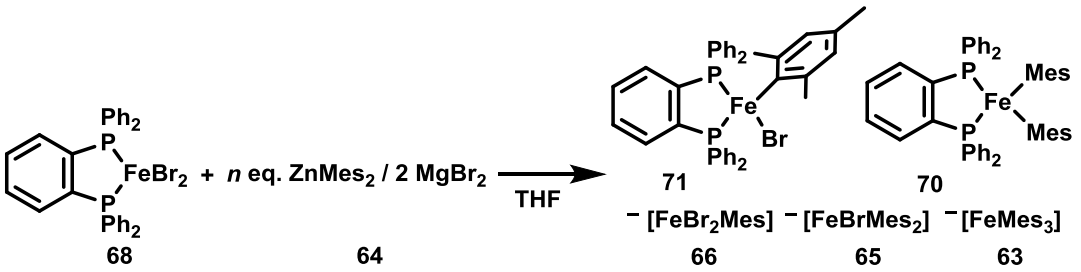

Spectrum	***68 : 64***	*Iron species observed in ^1H NMR*
a	1: 1	$FeBr_2$(dpbz), FeBrMes(dpbz)
b	1: 2	$FeBr_2$(dpbz), FeBrMes(dpbz)
c	1: 3	$FeBr_2$(dpbz), FeBrMes(dpbz)
d	1: 4	FeBrMes(dpbz), $[FeBrMes_2]^-$
e	1: 5	FeBrMes(dpbz), $FeMes_2$(dpbz), $[FeBrMes_2]^-$
f	1: 10	$FeMes_2$(dpbz), $[FeBrMes_2]^-$, $[FeMes_3]^-$
g	1: 25	$[FeMes_3]^-$

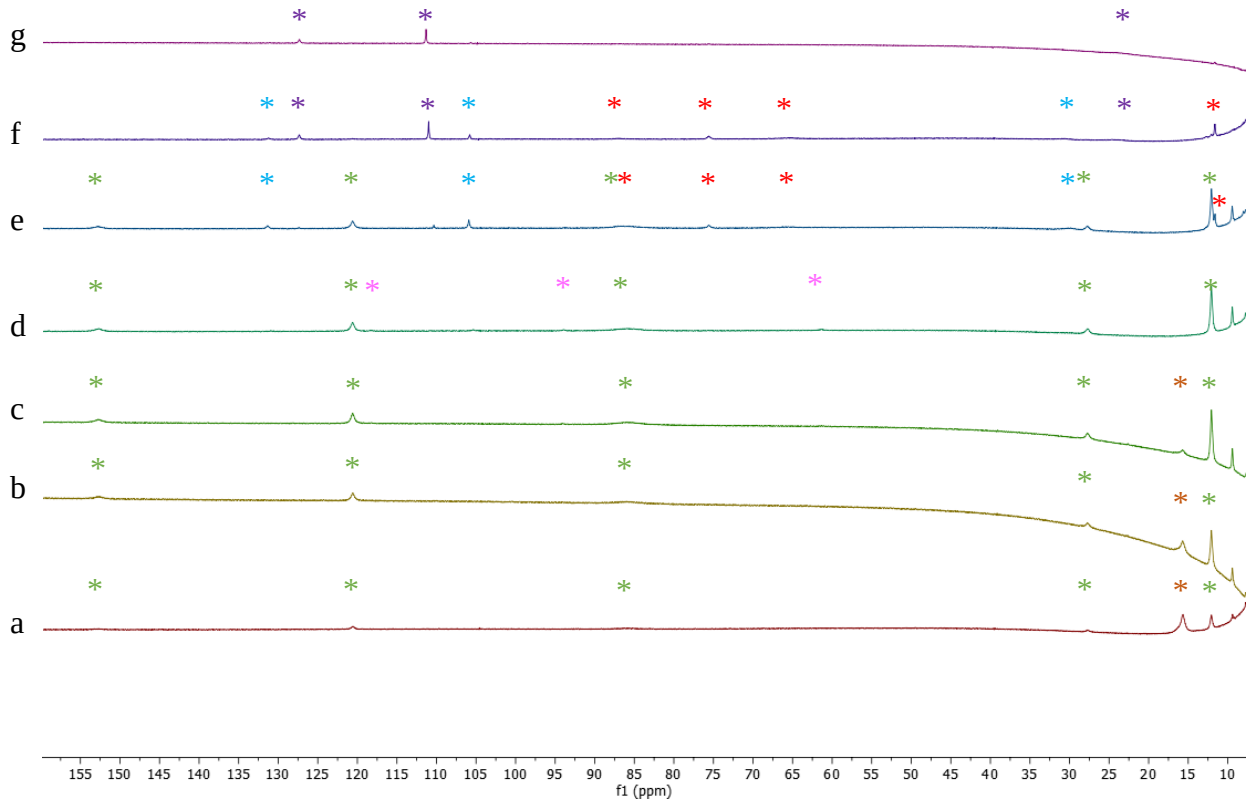

Figure 4.31: Expanded, stacked ^{1}H NMR spectra, from 10 to 160 ppm, for the reaction between **68** with increasing equivalents of **64**, as per Table 4.4.

Upon mixing of a 1:1 ratio of **64** / 2 $MgBr_2$ with **68**, a yellow solution is immediately observed. Analysis of the reaction by ^{1}H NMR spectroscopy indicates that in addition to unreacted **68** (*), the mono-transmetallated product FeBrMes(dpbz), **71**, (*) is present, albeit as a minor product (Figure 4.31, *a*). The same products are observed upon increasing the ratio of zinc to 2 and 3 equivalents with respect to iron, however the equilibrium appears to lie more in favour of the transmetallated product (Figure 4.31, *b* and *c* respectively). Further increasing the amount of zinc present to 4 equivalents results in no peaks corresponding to the starting complex **68** being observed, with peaks corresponding to FeBrMes(dpbz) (*), **71**, and the ligand free heteroleptic complex $[FeBr_2Mes]^-$, **66**, appearing weakly visible (Figure 4.31, *d* *). With 5 equivalents of zinc present further transmetallation to give both the mono- and bis-mesityl iron diphosphine complexes, **71** (*) and **70** (*) is observed, in addition to the second heteroleptic ligand free complex $[FeBrMes_2]^-$, **65**, (*) (Figure 4.31, *e*). As with transmetallation in the absence of ligand, **65** is expected to form directly from **66.** Addition of 10 equivalents of zinc with respect to iron (Figure 4.31, *f*) results in predominant formation of the homoleptic iron-aryl complex $[FeMes_3]^-$, **63**, (*), in addition to trace amounts of **65** (*) and **70** (*). In the

presence of 25 equivalents of zinc, the only observable signals correspond to **63**, (*) (Figure 4.31, *g*). The above results are summarised in Figure 4.32.

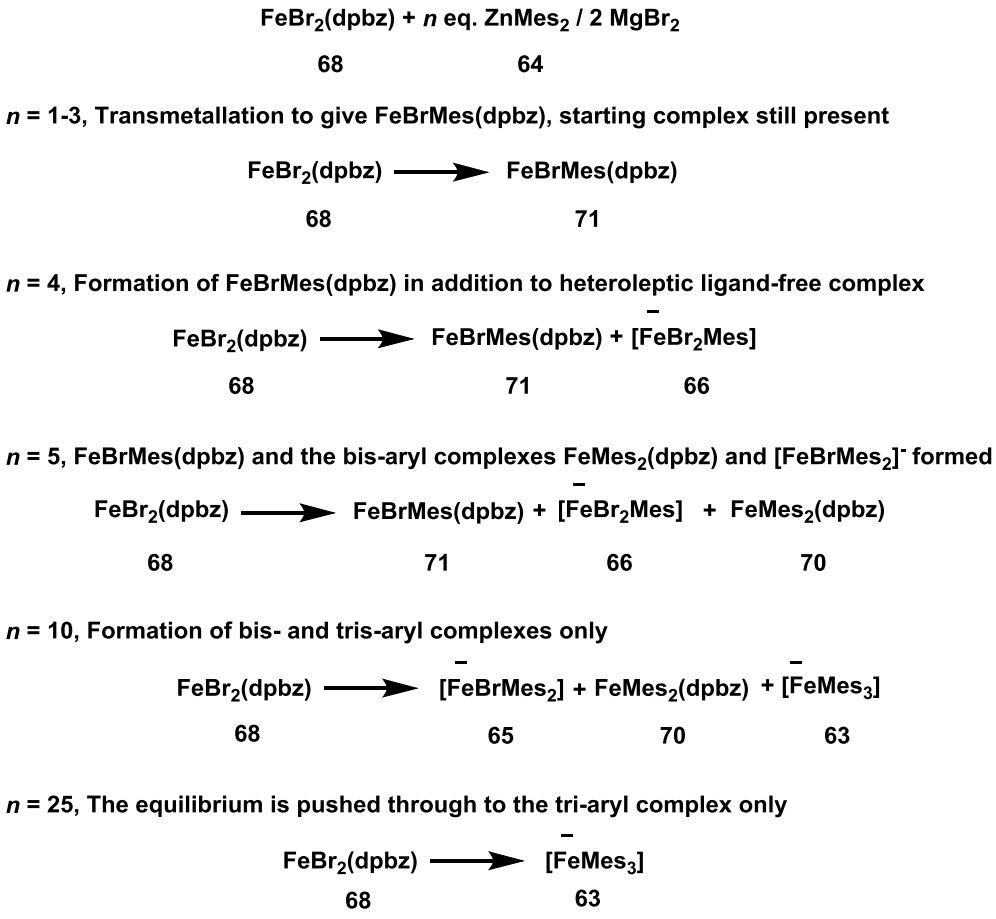

Figure 4.32: Summary of observed transmetallation products following the reaction between $FeBr_2$(dpbz), **68** and varying amounts of $ZnMes_2$, **64**, / 2 $MgBr_2$.

There are several points of interest from the summary presented in Figure 4.32. Of immediate note is the contrast with the ligand free system at low ratios of zinc to iron (*cf*. Figure 4.17). The observation of iron-aryl species **71** at below 4 equivalents of zinc added demonstrates that coordination of the diphosphine ligand to the iron centre results in a lower barrier to transmetallation as compared to the ligand free system. A qualitative comparison of the species present at 25 equivalents of zinc added confirms this: the reaction containing dpbz yields only the homoleptic complex **63**, whilst the same ratio of zinc to iron in the absence of dpbz (Figure 4.15, *d*) contains the heteroleptic complex **65.**

This decreased barrier to transmetallation may be due to a change in coordination centre about the iron centre yielding a more readily accessible iron-bromide bond, or to the presence of the ligand deterring any iron-magnesium interactions, and subsequent bromoferrate

formation. It is also possible that the bidentate phosphine dissociates, either partially or completely, from iron and coordinates to zinc, thus facilitating transmetallation (Figure 4.33). Evidence for the dissociation of dpbz from iron is presented by the formation of the heteroleptic ligand-free complexes **65** and **66.** Due to their previously noted appearance in the phosphine-ligand free transmetallation of $FeBr_2$, dictating that they must be phosphine-free iron species, and the confirmed purity of the starting material **68** used here, their presence clearly demonstrates the dissociation of dpbz from iron. Equally important is their observation at relatively low loadings of zinc, suggesting the process is a relatively facile one, and that loss of one phosphine centre from iron may be occurring reversibly at even lower ratios of zinc to iron, before complete dissociation is observed spectroscopically.

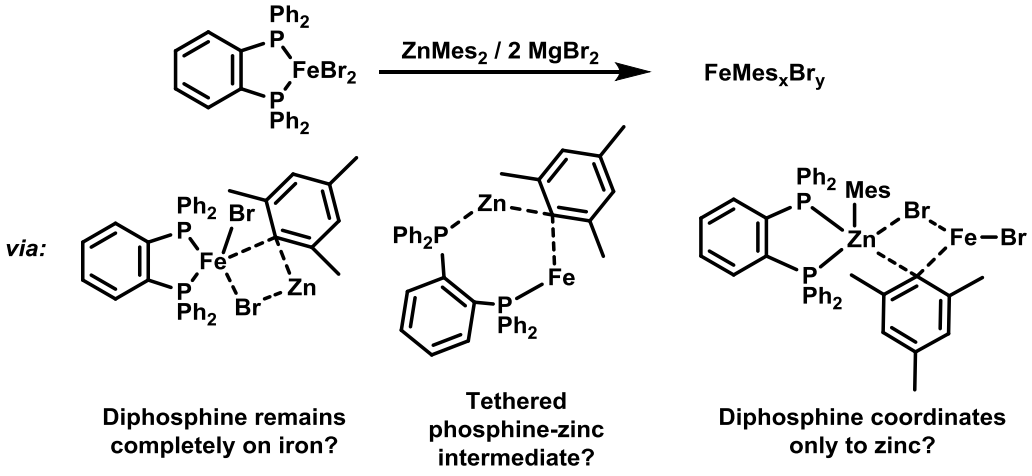

Figure 4.33: Potential intermediates in the transmetallation of iron by diarylzinc reagents in the present of a diphosphine ligand.

In order to comment upon the fate of dpbz following dissociation from iron, the reaction was also followed *via* ^{31}P NMR spectroscopy, and the resulting spectra compared to those corresponding to the iron and zinc complexes described in section 4.5.2.

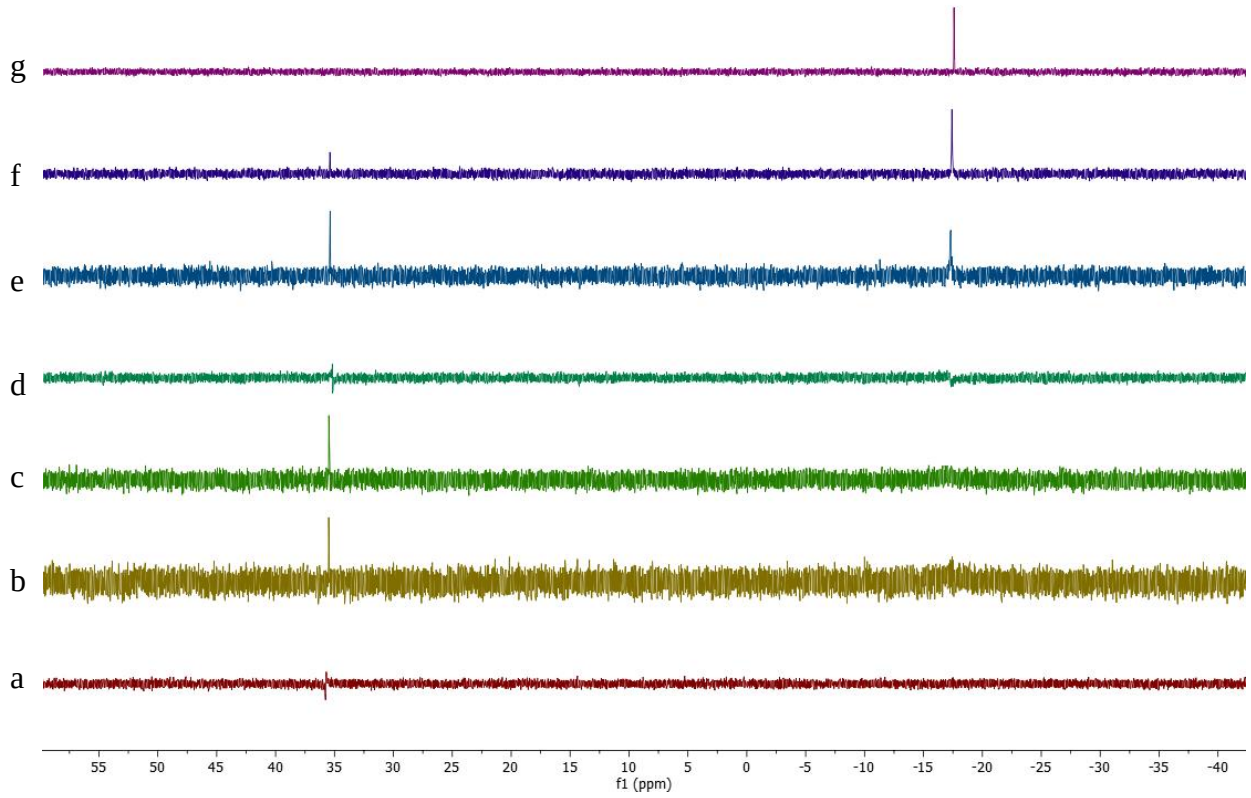

Figure 4.34: Stacked ^{31}P NMR spectra, from 10 to 160 ppm, for the reaction of $FeBr_2$(dpbz), **68** with increasing equivalents of $ZnMes_2$ (**64)** / 2 $MgBr_2$, as per Table 4.4.

The addition of one equivalent of $ZnMes_2$ / 2 $MgBr_2$ to **68** results in a silent ^{31}P NMR spectrum (Figure 4.34, *a*), which is to be expected as in the corresponding ^{1}H NMR spectrum (Figure 4.31, *a*) only the iron complexes **68** and **71** are observed, both of which are ^{31}P NMR silent. However, further additions of **64** lead to the observation of two singlet peaks; one at 35 ppm (Figure 4.34, *b* to *f*), and a second, very broad one at δ= -17 ppm (Figure 4.34, *b* to *g*). Due to the formation of ZnBrMes as a result of transmetallation with iron, subsequent coordination of dpbz would lead to ZnBrMes(dpbz), **74**, accounting for the peak at approximately δ= -17 ppm (Figure 4.35). The initial formation of a weak peak, which gradually becomes more prominent, is in agreement with the ^{1}H NMR analysis from the reaction, which demonstrates dissociation of dpbz from iron as more zinc is added to reaction mixtures.

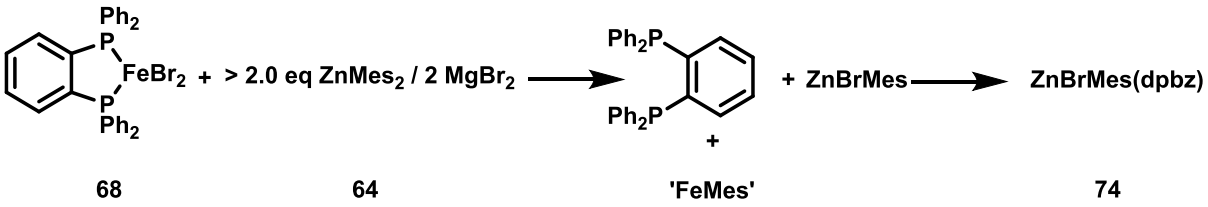

Figure 4.35: Reaction of **68** with **64**, to give the arylzinc-halide dpbz complex **74**, as evidenced *via* ^{31}P NMR spectroscopy.

Less trivial, though perhaps more interesting to explain, is the appearance of the sharp singlet at δ = 35 ppm, which does not correspond to any previously observed or isolated complex. The downfield position of the peak means that it is highly unlikely to belong to a discrete zinc-diphosphine type intermediate,[103] neither can it be assigned as an iron-dpbz complex as the paramagnetic nature of any such product would result in no ^{31}P signal being observed. As such, it is here tentatively ascribed to the formation of a bimetallic intermediate, containing both zinc and iron, with one or both of the phosphine atoms coordinated to zinc (Figure 4.36).

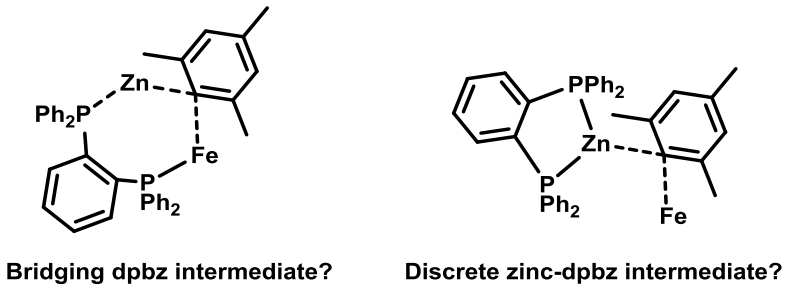

Figure 4.36: Proposed formation of a zinc-dpbz intermediate species, either completely on the zinc centre or containing an iron-phosphorus bond.

Although quantification of the intermediates formed is not possible due to extreme line broadening of already weak signals, qualitative conclusions can be drawn from the above results. Importantly, the presence of dpbz in reaction mixtures can be said to result in an increased propensity towards transmetallation from zinc to iron, with higher-order transmetallation products observed sooner than in the corresponding ligand-free experiments.

4.6 Conclusions and future work

The examination of transmetallation processes between iron and zinc centres has been shown, predominantly *via* NMR analysis, to induce a number of intermediates that are often observed in equilibrium with one another. Upon reaction with a stoichiometric loading of $FeBr_2$

in the absence of any additives, a non-bulky diarylzinc reagent **54** gave rapid transmetallation and reductive elimination, as evidenced by the subsequent formation of iron nanoparticles and the homo-coupled product **57.** Addition of magnesium and zinc salts to stoichiometric reaction mixtures between $FeBr_2$ and **54** retards considerably the rate of transmetallation, yielding isolable bromoferrate complexes **58** and **59**, and neutral bimetallic complexes **60** and **61**, respectively. However, this barrier to transmetallation in the presence of added salts is overcome when a larger – and more catalytically relevant – loading of diarylzinc is added.

Identification of intermediate iron species was made possible by switching to a bulkier diarylzinc compound, **64.** In the absence of any salt additive, incomplete transmetallation was demonstrated, and signals potentially corresponding to a bimetallic zinc-iron species were observed. Upon the addition of magnesium salts, a similar reactivity to the less-bulky diarylzinc analogue was initially noted, most likely giving bromoferrate complexes such as **58.** This observation suggests that although magnesium serves to encourage transmetallation to iron of bulky aryl groups, its primary role in catalysis is not directly linked to transmetallation. Further increasing the ratio of iron to zinc resulted in observation of signals assigned as ferrate species **62** (a homoleptic complex), **65** and **66** (heteroleptic complexes). In contrast to the previously reported homoleptic complex **62**, the heteroleptic complexes appear rather more thermally robust, and a sample of **65** prepared separately proved stable with respect to decomposition for over 24 h at room temperature under an inert atmosphere.

Addition of the diphosphine ligand dpbz to transmetallation mixtures results in a range of iron and zinc diphosphine complexes, which were identified by comparison with isolated samples, prepared separately. Despite the use of the well-defined iron-dpbz complex $FeBr_2$(dpbz), **68**, as the starting complex, evidence of dissociation of dpbz from iron was observed with less than 10 equivalents of **64** added. The hetero- and homoleptic complexes described above were also observed, confirming the complete transmetallation of both iron complexes with 25 equivalents of zinc added. The formation of signals corresponding to zinc-phosphine complexes within the ^{31}P NMR spectra from such mixtures indicates that upon dissociation from iron coordination of dpbz to zinc takes place. Due to the lack of reactivity from dpbz towards **64**, the effect of initial diphosphine coordination to zinc was not possible here. Switching from a mesityl to an o*rtho*-tolyl nucleophile may allow for the synthesis of the $ZnAr_2$(dpbz) complex, whilst also providing enough steric bulk to allow for observation of resultant iron intermediates.

Transmetallation from the iron mesityl complex **62** to $ZnBr_2$ was also demonstrated, further highlighting the complicated and dynamic nature of transmetallation processes between zinc and iron. Quantification of the process was possible in this case, and the reaction was observed to proceed efficiently regardless of ratio of iron and zinc present. Based on the observation of transmetallated zinc product and the chemical shift of the iron-aryl peaks observed, in addition to the same peaks in the ^1H NMR spectra of reactions between other MX_2 salts, the resultant iron intermediates in this case are unlikely to exist as discrete monometallic complexes, and the formation of cluster complexes is possible.

The quantification of the iron-species formed as a result of transmetallation was not possible throughout much of this work, due to the extreme line-broadening observed as a result of the paramagnetic nature of the intermediates formed, in addition to the weak concentrations necessary for dissolution. A qualitative comparison with separately prepared samples allows for a reasonable level of confidence towards the assignment of *in situ* formed intermediates, however this would be greatly increased by the isolation and characterisation of such species, particularly the heteroleptic complexes **65** and **66.**

In conclusion, it would appear that whilst transmetallation from diarylzinc reagents to iron is possible in the absence of a diphosphine ligand, the efficacy of transmetallation is increased in their presence. In contrast, magnesium salts, the presence of which is also necessary in iron-catalysed Negishi cross-coupling reactions, appear to help facilitate transmetallation from bulky diarylzinc reagents, but are not necessary when a catalytically relevant diarylzinc reagent is used. It therefore remains unclear what role these magnesium salts impart upon catalysis, other than to say they are most likely involved in other steps of the catalytic reaction.

Chapter 5 *The role of diphosphine ligands in the iron-catalysed Negishi cross-coupling*

5.1 Introduction

Early work on the iron-catalysed Negishi cross-coupling from within the Bedford group focussed mainly on the organic development of the reaction, using a model system consisting of a benzyl halide and diarylzinc reagent.[130] Upon the realisation of diphosphine ligands as the most effective ligand class for the reaction, work from the theses of Emily Neeve, Joshua Nunn, Paul Cogswell and Dominic Pye, in addition to post-doctoral work from Dr. Peter Brenner, contributed to analysis of the reaction mechanism.[63] More recently, work from Dr. Antonis Messinis has further refined and optimised the reaction (Figure 5.1) to allow for a more thorough investigation towards realisation of the active species and reaction pathways occurring during catalytic turnover.[103]

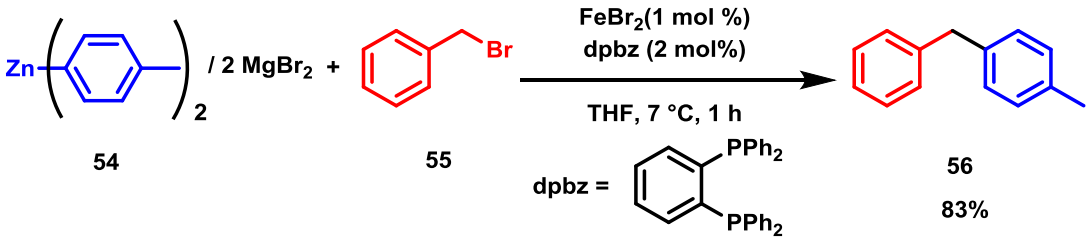

Figure 5.1: Model iron-catalysed Negishi cross-coupling reaction investigated by the Bedford group.

5.1.1 The effect on catalysis of varying the iron pre-catalyst

Investigations on the iron-catalysed Negishi cross-coupling reaction, between a benzyl halide electrophile and a diarylzinc nucleophile, have resulted in an increased understanding of several potential steps within the reaction. Complexes **75** and **4** were isolated from reaction mixtures relevant to catalysis, giving rise to the assertion that reaction of $FeBr_2$ / dpbz solutions with diarylzinc reagents in THF results in the *in situ* formation of iron(I) species (Figure 5.2).[63] Both **75** and **4** were shown to form as a result of transmetallation to iron, followed by reductive elimination. Whilst the use of **75** as a pre-catalyst led to an observed rate of reaction much below that of the model system, leading to the conclusion that it functions as an off-cycle intermediate, the reaction profile obtained when **4** was used a pre-catalyst suggested that it may be present within the active catalytic cycle.[136]

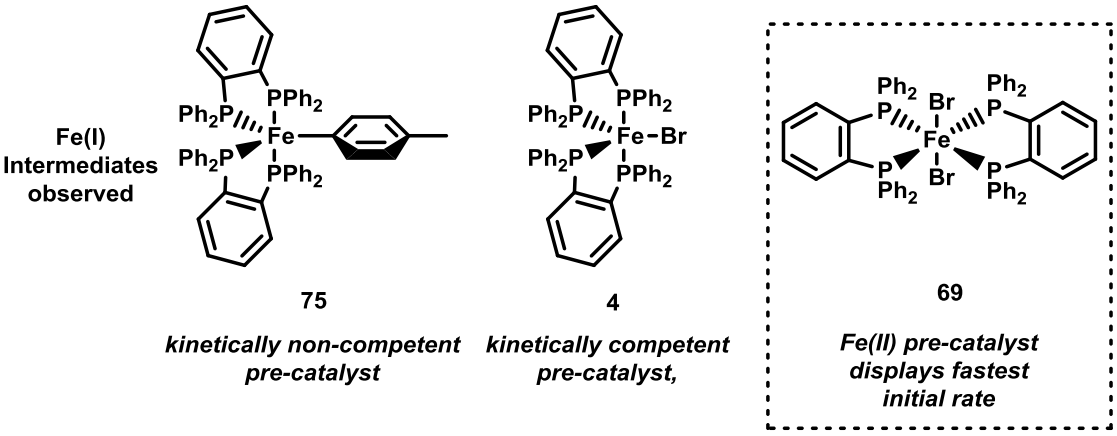

Figure 5.2: Fe(I) complexes **75** and **4**, postulated as intermediates in the iron-catalysed Negishi cross-coupling reaction, in addition to the Fe(II) complex **69**, which functions as the most active pre-catalyst for the reaction.

However, iron(II) pre-catalysts were shown to give the highest initial rate of reaction when used in the cross-coupling between **54** and **55**, as shown in (Figure 5.3, *a*).[103] The reaction profile was the same using the preformed complex **69**, or $FeBr_2$ and 2 equivalents of dpbz. Interestingly, within the first 15 seconds of the reaction using **69** as a pre-catalyst, a 'burst phase' was observed, in which the rate of reaction greatly exceeded that of the rest of catalytic turnover.[103]

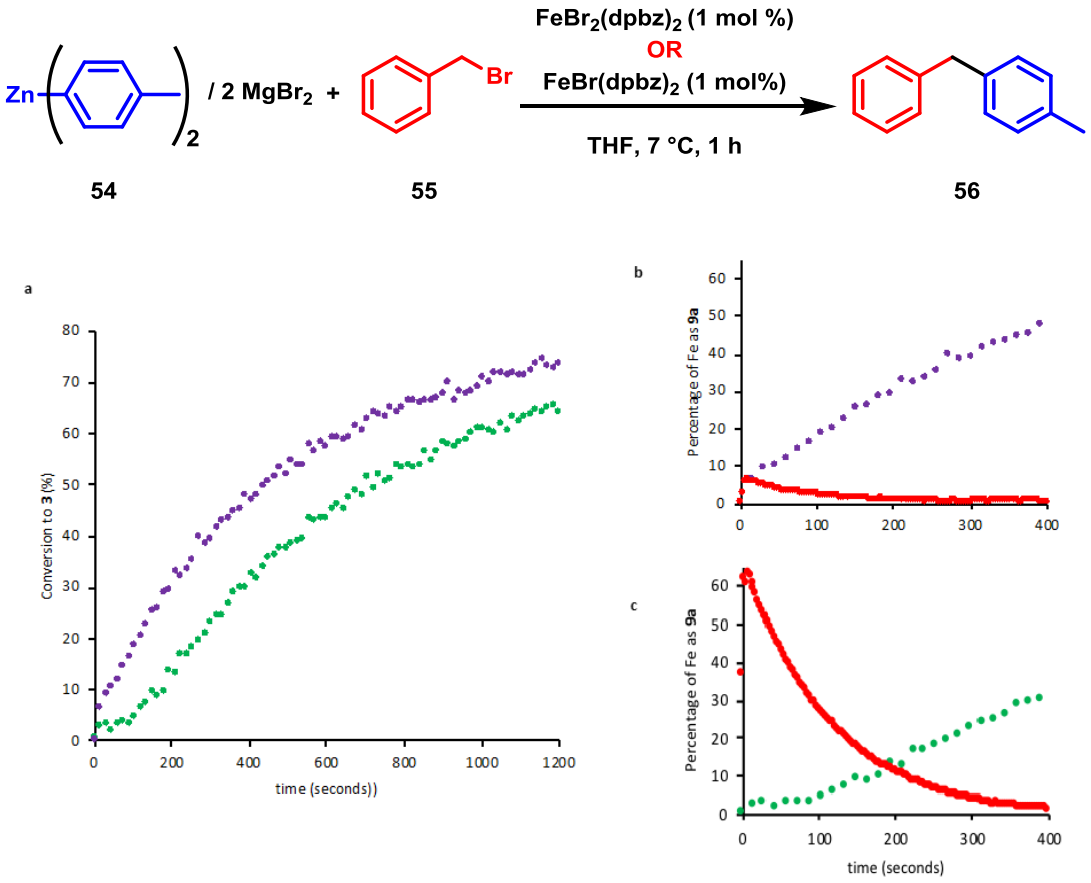

Figure 5.3: *a*: Comparative initial rates in the iron-catalysed Negishi cross-coupling reaction when the Fe(I) complex **4** and Fe(II) complex **69** are used as pre-catalysts. *b* and *c*: *in situ* React-IR data corresponding to the amount of the Fe(I) species **4** formed within catalysis, using **4** (b) and **69** (c) as pre-catalysts. [103]

In situ quantification using UV / Vis spectroscopy (Figure 5.3, *b*) confirmed that whilst the Fe(I) complex **4** is initially formed when the Fe(II) complex **69** is used as a pre-catalyst, its concentration rises to a maximum of only 6% of the total iron concentration at the very start of the burst phase before falling rapidly to concentration levels below the detection limit of the spectrometer.[103] Moreover, when the Fe(I) complex **4** is used to initiate catalysis, a smaller burst phase is apparent, and after an initial period of activity, a period of catalytic dormancy of around 1 minute is instead observed. Quantification of the amount of **4** present in solution (Figure 5.3, *c*) reveals that after initially making up over 60% of the total iron speciation, this proportion drops to <1% after 400 s.[103] Taken together, these data indicate that the Fe(I) complex **4**, whilst a competent pre-catalyst, is not responsible for the product formed during both the burst and post-burst phase manifolds when itself or **69** is used as a pre-catalyst. This was further confirmed by examining the rate of reduction of **69** to **4** by the diarylzinc reagent

54, which was slow with respect to the cross-coupling reaction, and the rate of oxidation of **4** by **55**, which was shown to be faster than the cross-coupling reaction.[103]

The observed burst phase within the reactions using both the Fe(II) and Fe(I) pre-catalysts was attributed to the same short-lived and highly active intermediate, identification of which was not possible through standard analytical techniques.

A kinetic profiling of the reaction was undertaken using both *in situ* FT-IR monitoring with concurrent manual quenching of aliquots for GC analysis. Due to the burst phase lasting for a length of time too short for an accurate kinetic study, the remainder of catalytic turnover was investigated, from which the rate law displayed in Equation 5.1 was deduced:

Equation 5.1: Experimentally derived kinetic rate law of the iron-catalysed Negishi cross-coupling reaction between **54** and **55.**

$$\frac{d[\mathbf{56}]}{dt} = k\,[FeBr_2]^{1.4}[dpbz]^{x}[\mathbf{54}]^{0}[\mathbf{55}]^{0}$$

The greater than first-order dependence in iron indicates that the rate-limiting step of the reaction involves two discrete iron species, while its fractional nature suggests that the mechanism is convoluted, and that complex kinetic processes are taking place within the reaction.[110] The zero order dependence in both the nucleophile **54** and electrophile **55** signifies that the rate-limiting step does not involve participation of either. Significantly, a change in the order with respect to dpbz was observed, with x = 1.4 up to an iron: dpbz ratio of 1: 2, and 0 above that point.

5.1.2 The effect on catalysis of varying the diphosphine ligand

The importance of the ligand used in catalysis was probed by undertaking a screen of twelve sterically and electronically diverse diphosphine ligands. Broadly speaking, the ligands can be split into three classes based on their performance in the reaction, as shown in Figure 5.4.

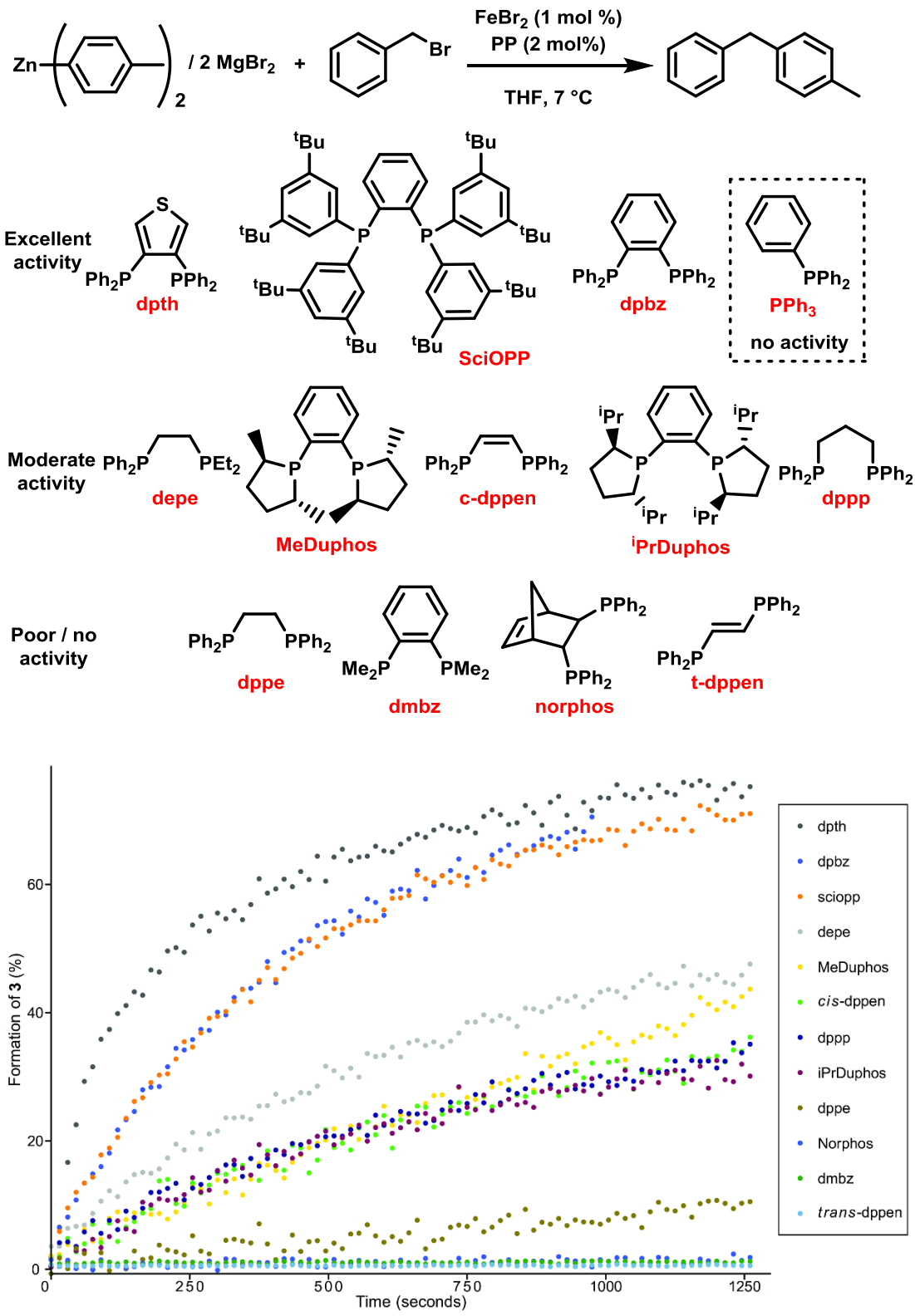

Figure 5.4: Screen of diphosphine ligands used in the iron-catalysed Negishi cross-coupling, grouped according to their performance in catalysis.

An extensive perusal of the properties of each ligand displayed in Figure 5.4, using several models,[137–139] covering both their steric and electronic properties, revealed that aside

from the need for a bidentate ligand (as highlighted by the lack of activity when PPh_3, effectively a monodentate derivative of dpbz, was used) no discernible trend between the performance of the ligands tested and their structural and electronic properties could be observed.

With the exception of dmbz, dppe and t-dppen, all the ligands displayed in Figure 5.4 were able to form complexes of the type $FeBr_2(PP)$ upon reaction with iron(II) bromide in THF. Interestingly, those that failed to yield mono-diphosphine tetrahedral complexes were among those to result in systems with poor catalytic activity, suggesting that an ability to form iron-diphosphine complexes may be crucial to invoking catalytic activity. The ligands dpbz and dppe were shown to be able to form octahedral complexes of the type $FeBr_2(PP)_2$. However, the differing performance of the two ligands indicates that this is not a prerequisite for an efficacious catalytic system. This is highlighted by the failure to form $FeBr_2(PP)_2$ structures by the ligands dpth and SciOPP, both of which give rise to highly active systems. Further, as discussed in Chapter 4, $FeBr_2(dpbz)_2$ **69** was shown in THF solution to exist as $FeBr_2(dpbz)$ **68**, with one free equivalent of dpbz.

Curiously, the ligand dmbz, for which a mono-diphosphine iron complex is not observed (presumably on thermodynamic grounds) and does not furnish an active catalytic system, was shown to form the corresponding bis-complex, $FeBr_2(dmbz)_2$ (even when equimolar amounts of the $FeBr_2$ and the ligand are mixed) which is highly stable with respect to decomposition and solubilisation. The strong diphosphine binding to iron was demonstrated by the short Fe-P bond length of 2.3333(4) Å (*cf.* **69**, Fe-P = 2.546(5) Å). The addition of dmbz to an $FeBr_2$ / dpbz system resulted in an instant loss of activity, poisoning the system, as displayed in Figure 5.5.

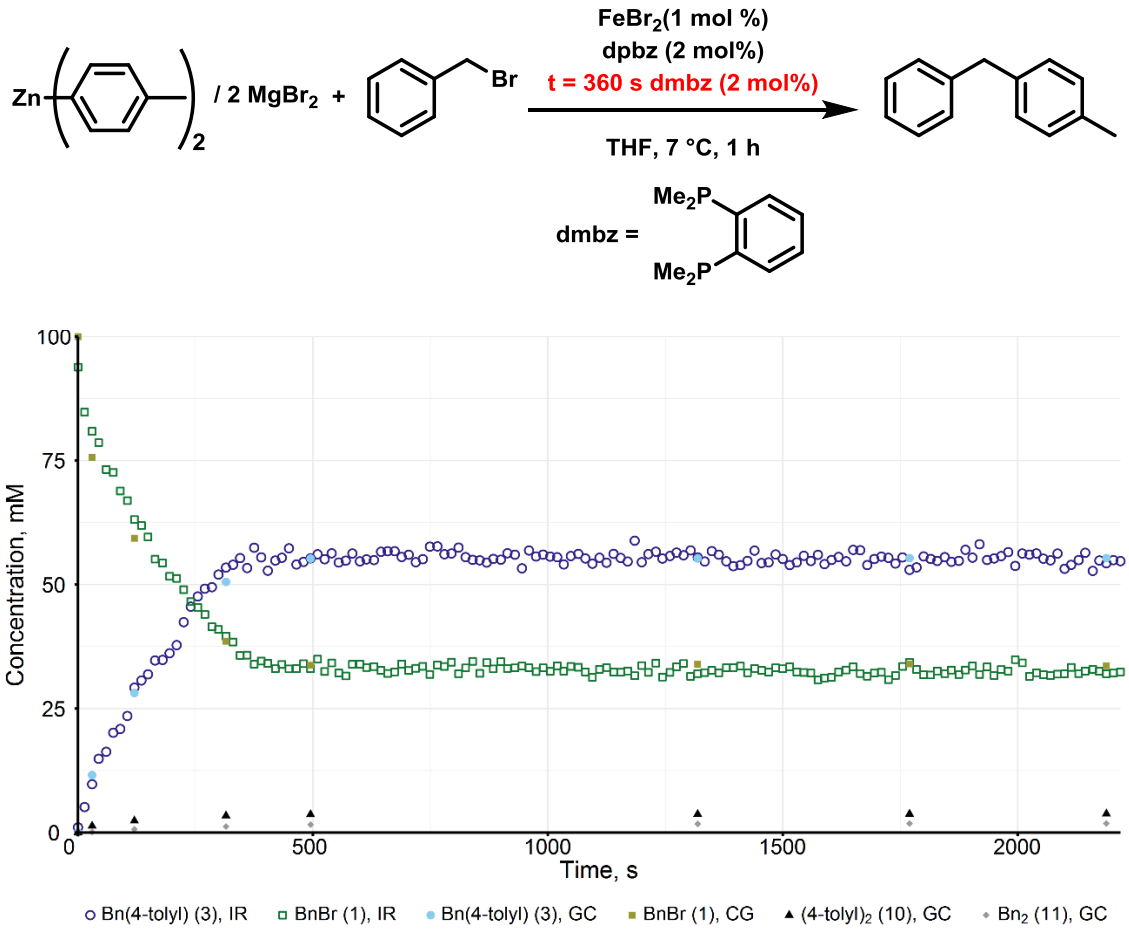

Figure 5.5: Negishi coupling between **54** and **55**, catalysed by $FeBr_2$ and dpbz, with addition of dmbz after 360 s.

Conversely, the addition of dpbz to a reaction mixture utilising the ligand t-dppen (a ligand that displays low activity) resulted in an immediate uptake in reaction rate, giving a system with an activity of that of the reaction in which dpbz alone is used as the ligand. These results suggest that whilst crucial for catalytic activity, the role of the diphosphine ligand may not be as straightforward as simply coordinating to iron.

5.1.3 Time resolved X-ray absorption fine structure (XAFS) spectroscopy

XAFS is a powerful technique, allowing for characterisation of the desired system on a molecular level.[140] Implementation of the method can provide information regarding the coordination geometry about an atom of interest, in addition to its electronic properties and oxidation state, all of which are of interest in homogeneous catalysis. Despite the information that can be obtained, the technique has, until the last decade,[141] found limited successful use with respect to homogeneous systems due to the convoluted data analysis[142] and the relatively high concentration of samples required with such systems.[143] More generally, the need of

synchrotron radiation also precludes widespread use of the technique. Applications of XAFS within iron-catalysed cross-coupling reactions are scarce, and to date have not focused on time-resolved, *in situ* analysis.[144, 145, 146] However, more recently, with the advent of advanced data processing techniques and Quick-EXAFS (QEXAFS), *in situ* monitoring of homogeneous reactions and comment upon the characteristics of the catalyst within them have become possible.[147]

In an XAFS experiment, a sample is irradiated with high-energy X-rays, with an intensity I_0, produced from a synchrotron. After interaction with a sample the intensity of the transmitted radiation, I_t , is given by application of the Beer-Lambert law, where μ(E) is the linear absorption coefficient and *x* is the absorption path length (Equation 5.2).

Equation 5.2: The Beer-Lambert law

$$I_t = I_0 \, e^{-\mu(E)x}$$

If the energy of the X-ray photons is high enough, excitation of a core electron is possible, resulting in ejection of the excited electron from the core-shell and an accompanied large increase in absorption, as described by the photo-electric effect. Importantly, as the absorption energy (E_0) is related to the binding energy of the electron, the technique provides element specificity. When plotted as a function of energy, as displayed in Figure 5.6, analysis of the resulting spectrum is carried out around the absorption energy value, termed the absorption edge, where $E = E_0$. Using a monochromator, the energy applied in an EXAFS experiment can be tuned to excite an electron from a specific core electron orbital, with the resultant absorption defining the edge observed. Accordingly, excitation of a 1s electron (where the principal quantum number, *n*, = 1) occurs at the K-edge; excitation of an electron in an orbital where $n = 2$ (for example, a 2s or 2p electron) occurs at the L edge; and excitation from an orbital where $n = 3$ (a 3s, 3p or 3d orbital) occurs at the M edge. The energy required for each edge therefore follows the ordering K > L > M.[140]

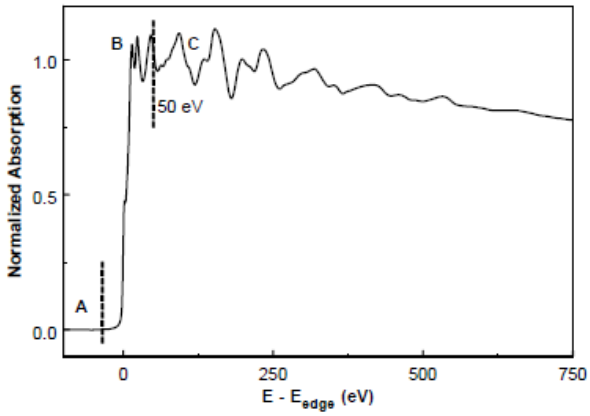

Figure 5.6: X-ray absorption spectrum of Cu foil, where normalised absorbance is plotted against energy. The pre-edge, X-ray absorption near edge (XANES) and extended X-ray absorption fine structure (EXAFS) regions are displayed (A, B and C respectively).[142]

At energies lower than the absorption edge (pre-edge; $E < E_0$), information on the geometry and oxidation state can be obtained (Figure 5.6, A). Around the absorption edge, the so-called XANES (X-ray absorption near-edge spectroscopy) region provides information on the coordination geometry and oxidation state present (Figure 5.6, B). The final area of information is termed the EXAFS (Extended X-ray absorption fine structure, $E > E_0$) region, from which geometrical data can be derived (Figure 5.6, C).

5.1.4 General considerations

In the previous chapter the transmetallation between iron centres and diarylzinc reagents, both in the presence and absence of coordinated dpbz, was shown to form homoleptic complexes with no diphosphine ligand attached to iron, with concomitant formation of zinc-dpbz species observed. The work in the following chapter is concerned with elucidation of the iron, zinc and phosphorus species present throughout turnover in the iron-catalysed Negishi cross-coupling discussed above, both within the initial burst phase and in the bulk of turnover following. This work has been published,[103] and due to the variety of techniques employed, is the result of a large scale collaboration between researchers at the University of Bristol (Dr. Antonis Messinis) and the Diamond Light Source, Harwell (Dr. Peter Wells, Dr. Diego Gianolio and Dr. Emma Gibson). They are acknowledged where appropriate; all other work is that of the author.

5.2 Time resolved XAFS studies: iron speciation during the burst phase

As discussed in the Chapter 1, a large part of the available literature discussing the mechanism of iron-catalysed cross-coupling reactions is undertaken from a physical inorganic standpoint. Whilst clear in their delivery of what is often a wealth of information upon organometallic iron speciation possible during catalytic reactions, without validation alongside thorough kinetic analyses, an often-simplistic view can be obtained. This is highlighted by realisation of the burst phase present in the iron-catalysed Negishi reaction, which without profiling of the reaction with a high density of time points would not have been possible. However, whilst confirmation of the burst phase is possible with accurate reaction profiling, elucidation of the short lived and highly active species responsible for it, is not. In order to provide further information on the iron speciation during catalysis, including the initial burst phase, time-resolved X-ray absorption fine structure spectroscopy (XAFS) was employed. All X-ray absorption spectroscopy (XAS) data was recorded at the Diamond Light Source, Harwell, by Dr. Antonis Messinis, Dr. Peter Wells, Dr. Diego Gianolio and Dr. Emma Gibson.

So as to allow the reaction to be monitored in a time-resolved manner throughout turnover, a custom-made flow cell was used. As opposed to a reaction stirred in a flask, where progress is monitored over time, in a continuous flow regime distance from initial mixing of reagents provides a snapshot of a reaction at a given time.[148] Calculating the residence time and total volume of the cell allows for accurate determination of the reaction profile at any point within the cell to be determined. At 6 seconds, the first point (A) (Figure 5.7) lies within the initial burst phase of the reaction and corresponds to less than 6% conversion of starting material to product. The other points (B, 166 s; C, 482 s; D, 817 s) lie in the post-burst phase part of the reaction, and correspond to approximately 39%, 65% and 76% conversion to product, respectively (these values were determined in a separate, batch experiment carried out by Dr. Antonis Messinis). Each of the four points were followed individually using XAS.

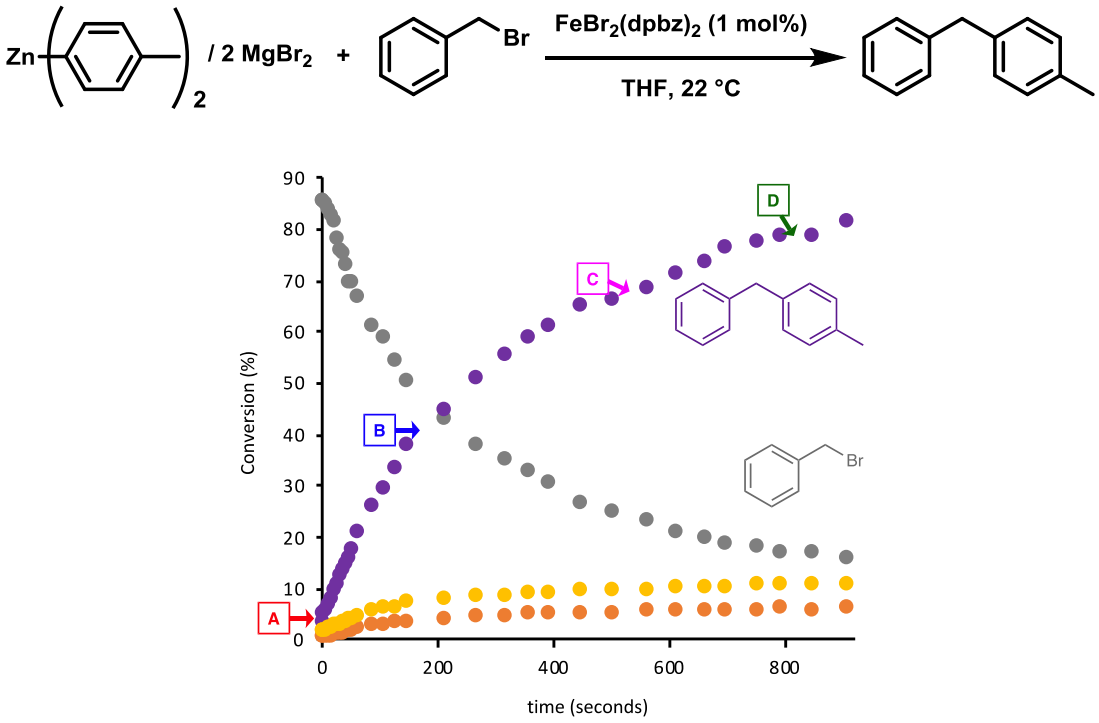

Figure 5.7: Points selected for analysis *via* time-resolved XAFS in the reaction shown above. The reaction was carried out at 22 °C, by Dr. Antonis Messinis.

As displayed in Figure 5.8, *a*, at time point A in the reaction the EXAFS data display a significant shift from the pre-recorded spectrum, corresponding to the pre-catalyst, $FeBr_2$(dpbz). Long range scattering paths, consistent with metallic Fe(0) are observable, in addition to Fe-C/O scattering paths with bond lengths of 1.85 and 2.05 Å. Simulations of the data fit well with the observed result. The XANES data displayed in Figure 5.8, *b* confirm that at time point A in the reaction, metallic iron is present due to the broad nature of the pre-edge peak at 7115 eV, as highlighted by the red squares visible on the Figure.

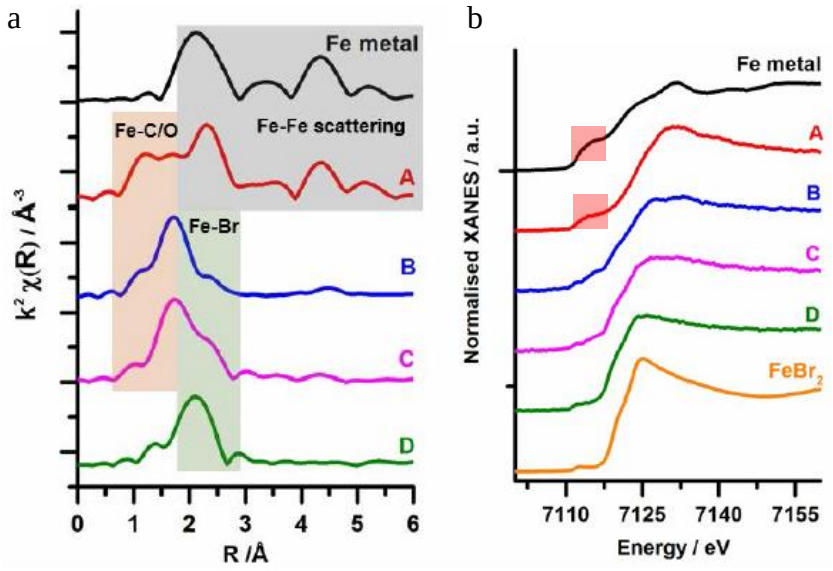

Figure 5.8: *a*) Fourier transform EXAFS data corresponding to Fe foil (top) and the time points A, B, C and D monitored throughout the reaction as described in Figure 5.7. *b*) Normalised XANES spectra corresponding to (from top to bottom) Fe foil, the time points A, B, C and D and $FeBr_2$. Reaction and analysis carried out by Dr. Antonis Messinis and researchers at the Diamond Light Source.

Although differentiation between carbon and oxygen neighbours to iron is not resolvable within the technique (a limitation of XAFS is the inability to differentiate between centres with similar atomic numbers), the bond lengths of 1.85 and 2.05 Å can be compared to literature values of pre-defined iron complexes containing carbon and oxygen bonds. It can be reasonably assumed that the possible carbon centres available for bonding are from the aryl nucleophile and benzyl electrophile, whilst the oxygen bond is almost certainly from THF. The shorter of the two scatterings (1.85 Å) is most likely due to an iron-aryl interaction, as structurally characterised Fe-C(aryl) complexes present Fe-C bonds ranging from 1.93 Å (in Fe(III) complexes)[149] to between 1.96 and 2.08 Å (for Fe(II)[150, 151] and Fe(I)[68] complexes). The longer distance can be assigned to either an iron-benzyl or iron-THF interaction; previously reported Fe-C(benzyl) complexes range from 2.04 to 2.12 Å,[58, 152] whilst Fe-O bond lengths in iron-THF adducts are typically 2.05 to 2.13 Å. [153–156] Taken together, the data suggest that by time point A in the reaction, complete dissociation of dpbz from the pre-catalyst occurs, followed by reduction, to give metallic iron nanoparticles which may be responsible for the high rate of reaction observed within the burst phase (Figure 5.9).

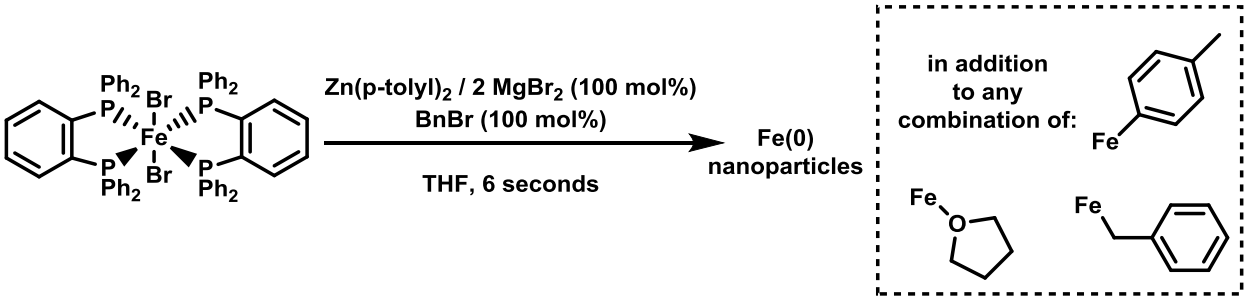

Figure 5.9: Summary of the proposed initial reactivity observed in the iron-catalysed Negishi cross-coupling reaction at time point A.

5.3 Time resolved XAFS studies: iron speciation during the post-burst phase

As the reaction progresses, the Fe-Fe scattering paths in the EXAFS data corresponding to metallic Fe disappear and are completely replaced by the Fe-C/O ones, which are in turn replaced by Fe-Br (Figure 5.8, *a*). The change in structure is confirmed by an expanded stacked XANES plot (Figure 5.10, *a*) in which a shift of the main edge to lower energy is observed as the reaction progresses. The shift is confirmed as being due to the presence of a halide, rather than a redox event regarding iron, by analysis of XANES spectra of $FeBr_3$ and Fe_2O_3, which confirm the previously observed tendency of first-row transition metal halide complexes to give lower edge values than expected.[148] The XANES derivative spectra confirm the bromide neighbour further, with the peak at 7119 eV relating well to an externally measured spectrum of $FeBr_2$ (Figure 5.10, *b*). Simulations of the EXAFS data corresponding to point B in the reaction fit well with scattering paths relating to iron with a bromide neighbour, in addition to two further scattering paths corresponding to either a carbon and / or oxygen, which are assigned as the same species observed at point A of the reaction.

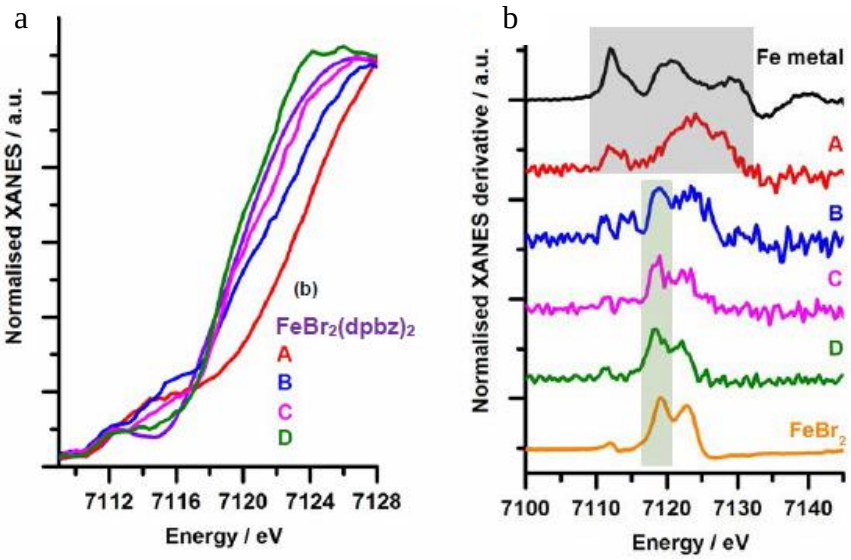

Figure 5.10: a) Expanded normalised XANES data showing the edge position of the pre-catalyst $FeBr_2$(dpbz) and the positions A, B, C and D. b) Expanded normalised XANES spectra corresponding to (from top to bottom) Fe foil, the time points A, B, C and D and $FeBr_2$. Reaction and analysis carried out by Dr. Antonis Messinis and researchers at the Diamond Light Source.

At point C in the reaction, data consistent with those in point B are again observed, but with a greater contribution from the bromide scattering, and a concomitant reduction in the C / O intensity (Figure 5.10, *b*). By point D in the reaction, the data collected correspond almost completely to iron-bromide scatterings, which could be assigned as simply $FeBr_2$; however, the absence of any scatterings consistent with a Fe-O species, indicating that no THF is coordinated to iron at this point, mean an anionic species is more likely to be present. The bromoferrate complex **61**, previously discussed in (Section 4.2.2), is therefore a more likely candidate for the terminal iron species in solution, for which the data fit well.[103] The above is summarised in Figure 5.11.

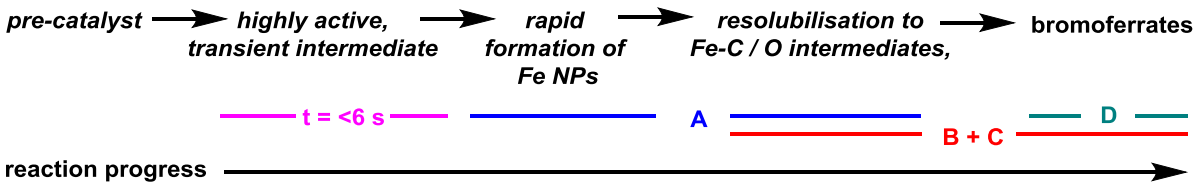

Figure 5.11: Proposed sequence of events regarding iron speciation in the iron-catalysed Negishi cross-coupling reaction, based on XAS data.

The data presented above hold several points of interest. Most strikingly, at no point in the reaction are scatterings consistent with a phosphorus neighbour to iron observed. This is confirmed both visually in Figures 5.8 and 5.10, and also in the simulated data, where

incorporation of phosphorus results in much poorer fits to the data in all cases. At time point A, corresponding to the initial burst phase of the reaction, the observation of metallic iron from a pre-formed and well-defined iron-dpbz complex is initially surprising, as diphosphine ligands are generally assumed to protect metal centres with respect to decomposition by remaining coordinated to them.[157] However, as described in Chapter 4, transmetallation and reductive elimination from iron were observed in the absence of dpbz to give iron-nanoparticles, whilst the reaction of the pre-catalyst **69** with $ZnMes_2$ led to the observation of complete dissociation of dpbz, and formation of the homoleptic complex **62**, *via* the heteroleptic aryl / halide complexes **65** and **66.** It is therefore also possible that, rather than being responsible for the high rate of reaction during the burst phase, the nanoparticles represent the product of decomposition from an even more active, and extremely short lived, homogeneous intermediate(s) that exists when the time of the reaction is < 6 seconds, as has been previously postulated to occur in iron-catalysed Kumada reactions.[58] Such iron speciation may be forming here prior to time point A, with the lack of steric bulk in the 4-tolyl nucleophile responsible for the rapid decomposition observed (Figure 5.12).

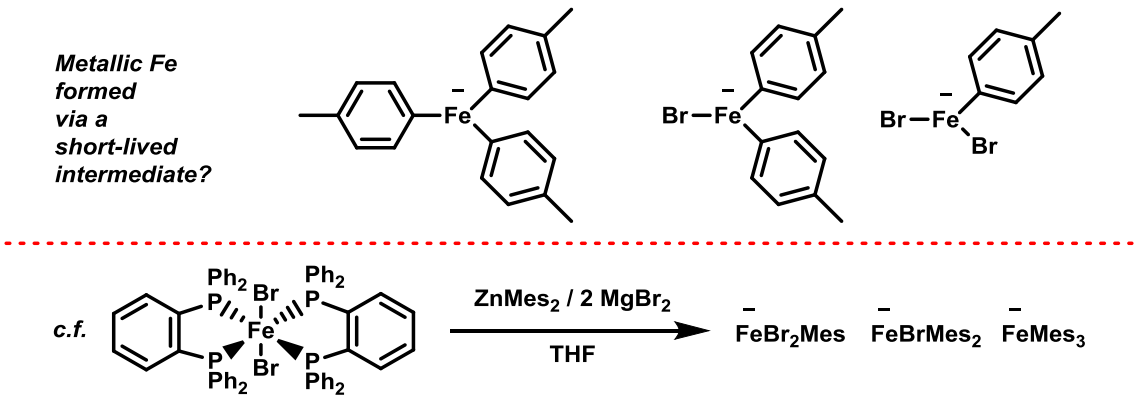

Figure 5.12: Possible short-lived homogeneous intermediates from which metallic iron may form, following decomposition, before time point A in the reaction. Bottom: Previously observed reactivity from Chapter 4 whereby transmetallation of **69** results in loss of dpbz and observation of hetero- and homoleptic iron-mesityl complexes.

Whilst the final structures and oxidation states of the iron intermediates proposed remain unknown aside from the discussed scatterings, the clear absence of any scatterings corresponding to an iron-phosphorus intermediate, at any of the time points measured, indicates that the position of phosphorus is separate from that of iron through the entire reaction. Due to the requirement of dpbz (or other diphosphine ligands; Figure 5.4) to enable catalytic activity, and its non-zero order in the rate-law equation, it is highly unlikely to remain uncoordinated in

solution. Taken together, the data are highly suggestive of dpbz coordination to zinc; in order to elucidate whether this may be the case, whilst simultaneously providing further confirmation that dpbz is not coordinated to iron, the reaction was next investigated *via* NMR spectroscopy.

5.4 The equilibrium between iron and zinc halides with dpbz

The reaction of a 1: 1 ratio of $ZnBr_2$ with dpbz to give $ZnBr_2$(dpbz), **72**, was disclosed in Chapter 4; the same reactivity to give complexes of the type $ZnBr_2$(PP), is observed for each of the disphosphines displayed in Figure 5.4. Mono- and bis-arylated zinc-diphosphine species are also accessible *via* manipulation of the hetero-Schlenk equilibrium, followed by addition of dpbz to yield the mono-arylated complex ZnBr(4-tolyl)(dpbz), **76**, whilst stoichiometric mixing of dpbz and Zn(4-tolyl)$_2$ give Zn(4-tolyl)$_2$(dpbz), **77** (Figure 5.13).

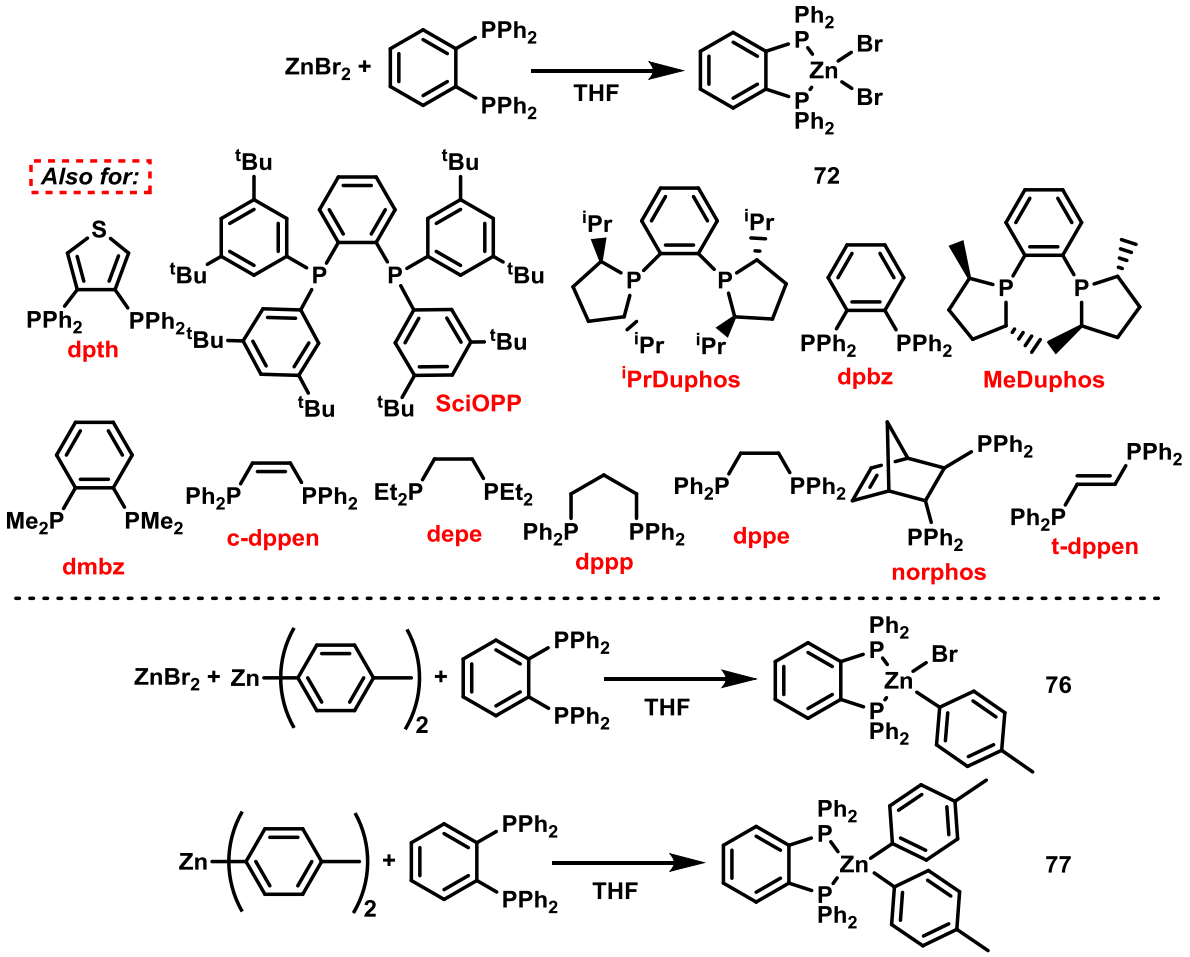

Figure 5.13: Top: Reaction of $ZnBr_2$ with dpbz to give **72**, and with a range of diphosphines to give $ZnBr_2$(PP) complexes. Bottom: Synthesis of mono- and di-aryl zinc dpbz complexes **76** and **77**. All products were characterised by ^{1}H and ^{31}P NMR spectroscopy, in addition to X-ray crystallography by Dr. Antonis Messinis.

Clearly zinc-diphosphine complexes are readily accessible in isolation; however, this alone does not provide sufficient validation for the diphosphine ligand present within catalytic reactions residing on zinc. A more representative perspective can be gained by establishing the position of diphosphine equilibrium when both zinc and iron are present simultaneously. However due to the propensity of such systems to undergo rapid transmetallation, and when non-bulky aryl groups are present within reaction mixtures, decomposition, experiments between the true nucleophile, $Zn(4\text{-tolyl})_2$, **54**, and iron are not directly possible. It was demonstrated computationally that the transfer of dpbz from $FeBr_2$(dpbz) to $ZnPh_2(THF)_2$ is mildly endergonic (ΔG = +1.0 kcal mol^{-1}) between a 1: 1 mixture of the two, demonstrating that the transfer is likely to be feasible when a higher loading of zinc is present, as would be the case in catalysis.

In order to determine experimentally the equilibrium position of dpbz between iron and zinc, the reaction was performed in the absence of aryl groups. Reaction of $FeBr_2$(dpbz), **68**, with increasing equivalents of $ZnBr_2$ was monitored by ^1H and ^{31}P NMR spectroscopy, with the stacked ^1H NMR spectra displayed in Figure 5.14.

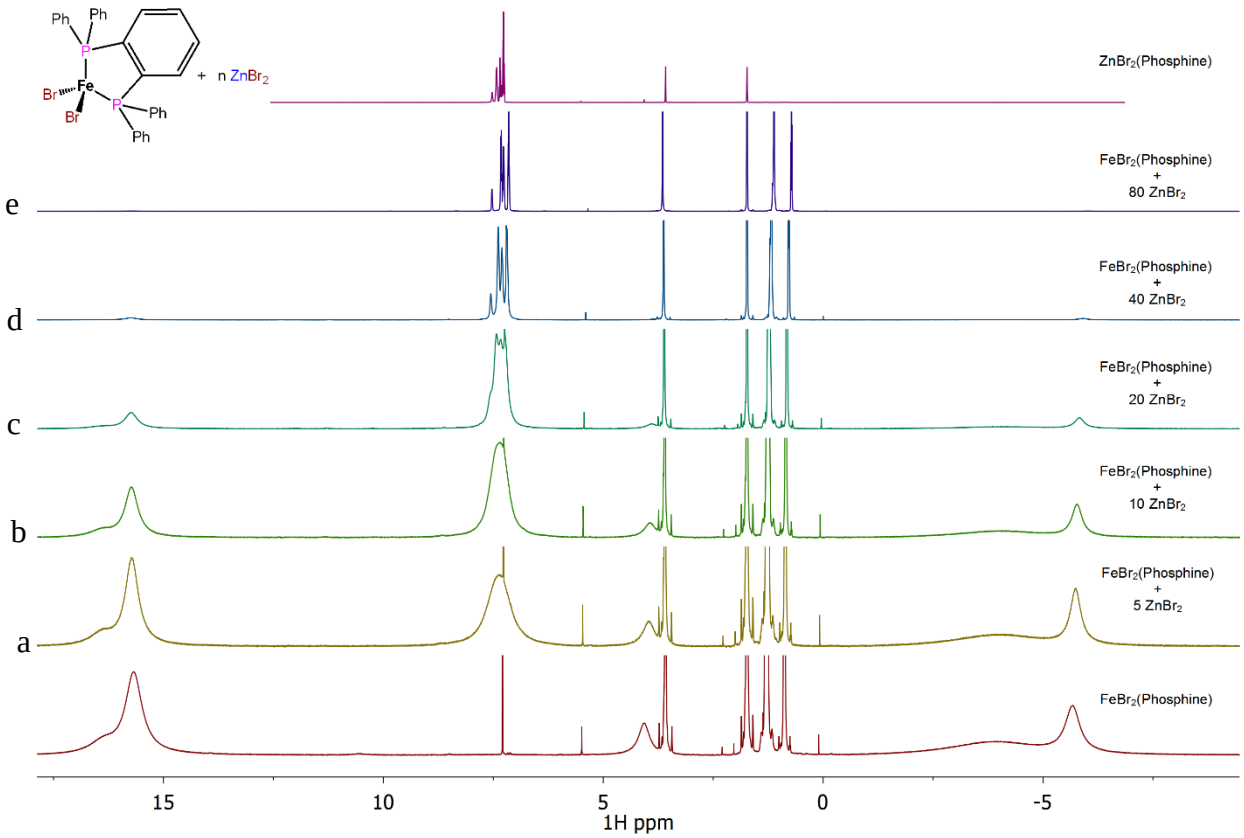

Figure 5.14: Stacked ^{1}H NMR spectra, from -15 to 20 ppm, corresponding to the addition of increasing equivalents of $ZnBr_2$ to $FeBr_2$(dpbz), **68.** All reactions and analysis were carried out by Dr. Antonis Messinis.

As demonstrated in Figure 5.14, increasing the amount of zinc bromide present in reaction mixtures results in the disappearance of peaks corresponding to $FeBr_2$(dpbz), with concomitant appearance and growth of signals corresponding to $ZnBr_2$(dpbz). The presence of a dodecane internal standard allows for quantification of the proportion of dpbz residing on zinc to be calculated, with the results displayed in Table 5.1.

Table 5.1: Equivalents of $ZnBr_2$ added to $FeBr_2$(dpbz) and the resultant proportions of dpbz species present. Reactions performed by Dr. Antonis Messinis.

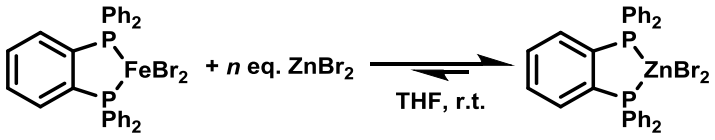

Spectrum	*eq. $ZnBr_2$*	*Fraction of dpbz on Zn*	*K (approxim*ate*)*
a	5	0.25	0.3
b	10	0.37	0.6
c	20	0.56	1.3
d	40	0.79	3.8
e	80	0.90	9

Whilst not entirely representative of a catalytic reaction in which a diarylzinc reagent is used, the results displayed in Table 5.1 clearly demonstrate that the transfer of dpbz from iron to zinc is not only feasible, but also favoured under a catalytic stoichiometry. These results were supported computationally by Prof. Robin Bedford, with calculations on the transfer of dpbz from $FeBr_2$(dpbz) to $ZnBr_2(THF)_2$ giving $\Delta G = +0.5$ kcal mol^{-1} for a 1: 1 mixture of the two, corresponding to an equilibrium value of $K = 0.4$ at 298 K, not dissimilar to the experimentally determined value.

Due to the paramagnetic nature of $FeBr_2$(dpbz), **68**, no peak is initially observed in the ^{31}P NMR spectrum of the reaction displayed in Table 5.1. However, the resultant zinc complex $ZnBr_2$(dpbz), **72**, is not paramagnetic and as such as a single peak at -24 ppm is observed in the ^{31}P NMR spectrum when 80 equivalents of $ZnBr_2$ are added. Whilst observation of dpbz transfer from iron to a diarylzinc species is not observable in isolation (due to competitive transmetallation), the non-paramagnetic nature of the resulting zinc-diphosphine complexes means that, should they form during a catalytic reaction, signals in the ^{31}P NMR should be visible, and assignable as such. Accordingly, the reaction between **54** and **55** in the presence of $FeBr_2$ / 2 dpbz was monitored *via* both ^{1}H and ^{31}P NMR spectroscopy.

5.5 In situ NMR detection of zinc-diphosphine species

The NMR experiments were carried out at 25 °C, with a total reaction time of approximately one hour. As displayed in Figure 5.15, quantification of reaction progression was possible *via* single scan (alleviating the concern of T_1 considerations) ^{1}H NMR

spectroscopy, by monitoring the benzylic protons in both the substrate, **55**, and product **56** (see section 7.5 for further details).

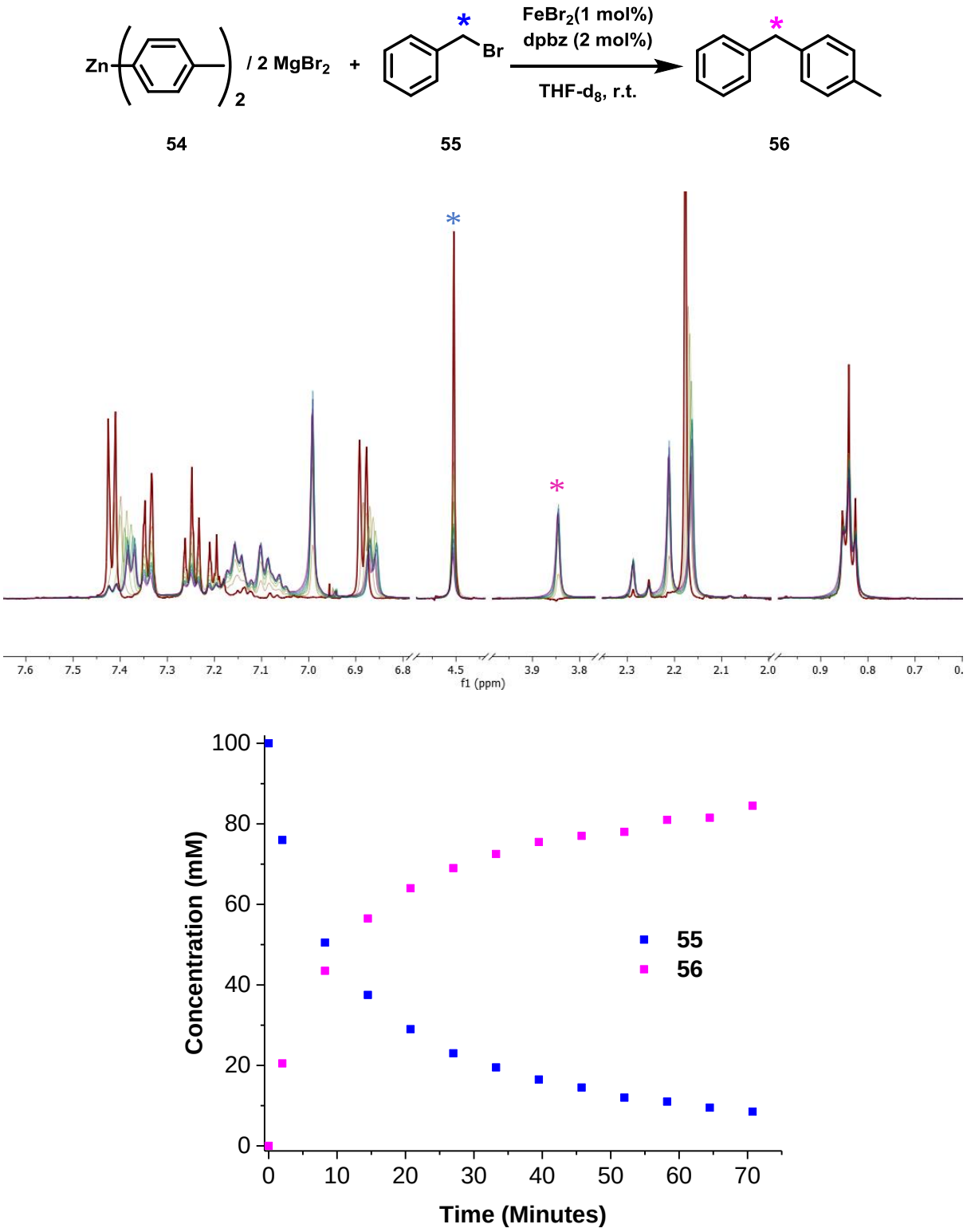

Figure 5.15: Progression of the iron-catalysed Negishi cross-coupling over time, monitored *via* ^{1}H NMR spectroscopy.

In order to comment on the speciation of dpbz throughout catalysis, a high scan rate in the ^{31}P NMR experiment was required. Whilst possible (rapid relaxation delays are observed when transition metals are present in solution[158]) this did not turn out to be practical, due to the low concentration (2 µM) of dpbz present in the reaction, and the broad nature of the resultant signals. Accordingly, the reaction was first performed in a qualitative fashion, whereby phosphorus speciation was monitored over two time-windows (3-8 minutes and 9-14 minutes) during catalytic turnover, corresponding to 25 – 50% and 50 – 63% conversion to **56** respectively (Figure 5.16).

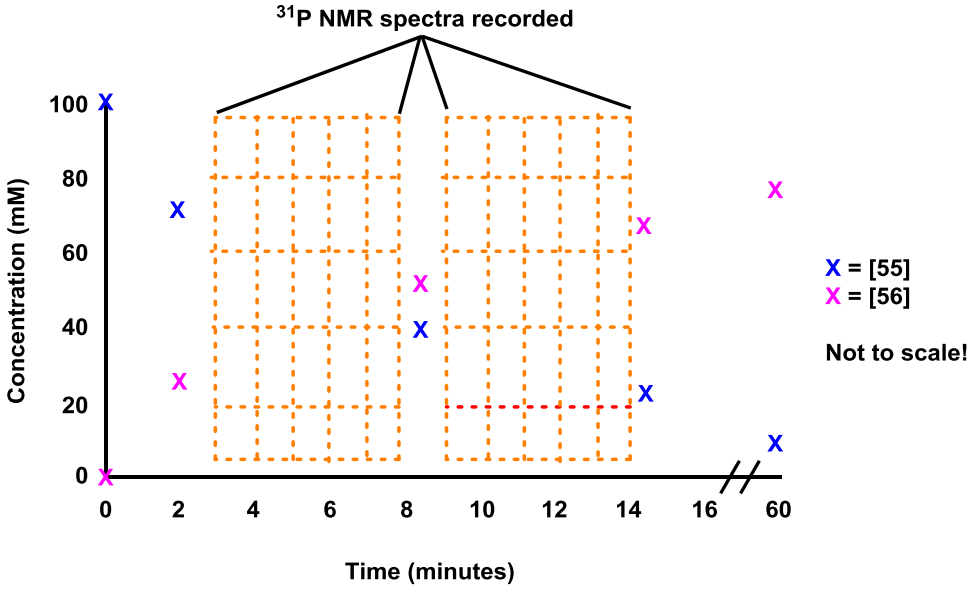

Figure 5.16: Representation of time windows 1 and 2, in which qualitative ^{31}P NMR spectra were recorded.

Importantly, and gratifyingly, a single broad peak at around -17 ppm was observed in both recorded spectra, corresponding to formation of a zinc-diphosphine adduct(s), and providing further confirmation that throughout the bulk of catalytic turnover (the range covered corresponds to nearly half the reaction) the ligand, dpbz, resides on zinc (Figure 5.17)

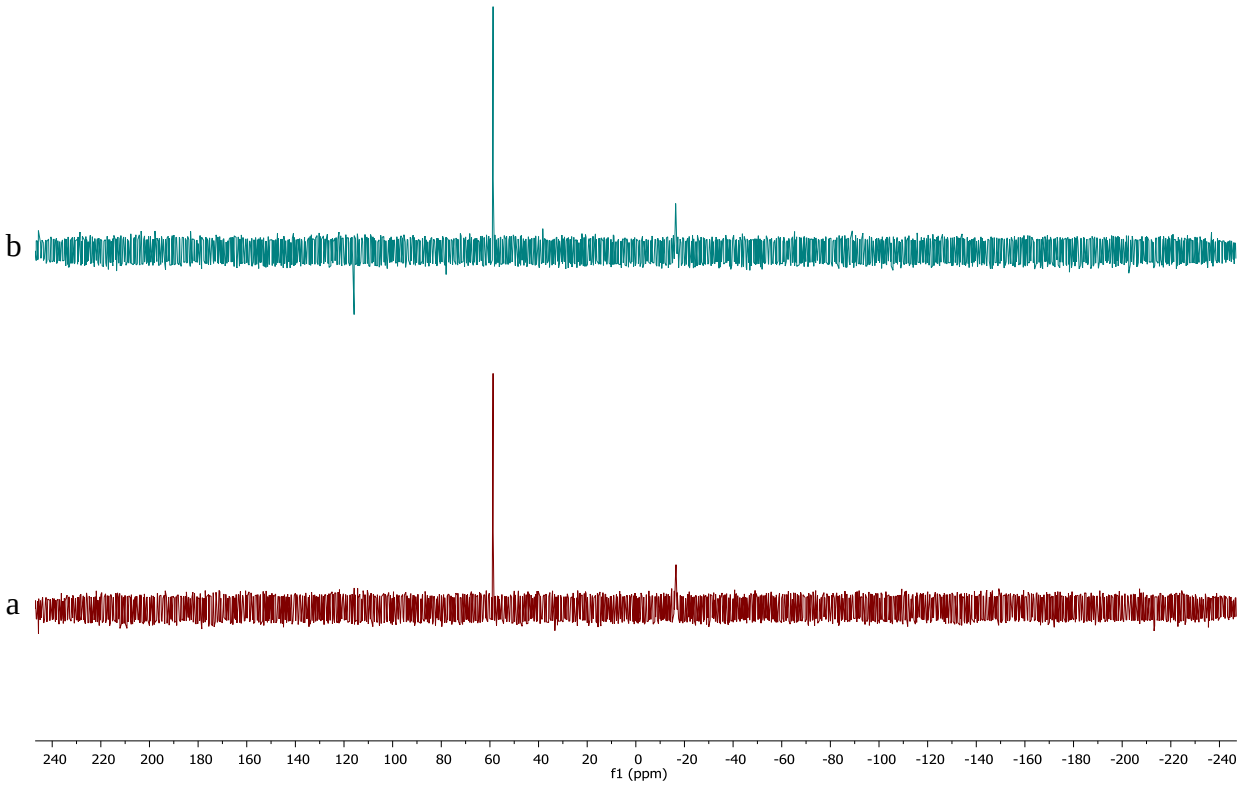

Figure 5.17: Stacked ^{31}P NMR spectra, from -240 to 240 ppm, displaying, in addition to the reference standard at 58 ppm, in both *a* (time window 1) and *b* (time window 2) a single peak at -17 ppm, corresponding to a zinc-diphosphine adduct(s). The peak at around 120 ppm in *b* is anomalous.

In order to provide quantification of the amount of dpbz coordinated to zinc throughout the bulk of catalytic turnover, ^{31}P spectra collected with a greater number of scans were necessary, without monitoring of the organic progression of the reaction. Therefore, following acquisition of a t_0 ^{1}H NMR spectrum, the reaction was initiated and a ^{31}P NMR spectrum recorded over the first 40 minutes of the reaction, as displayed in Figure 5.18.

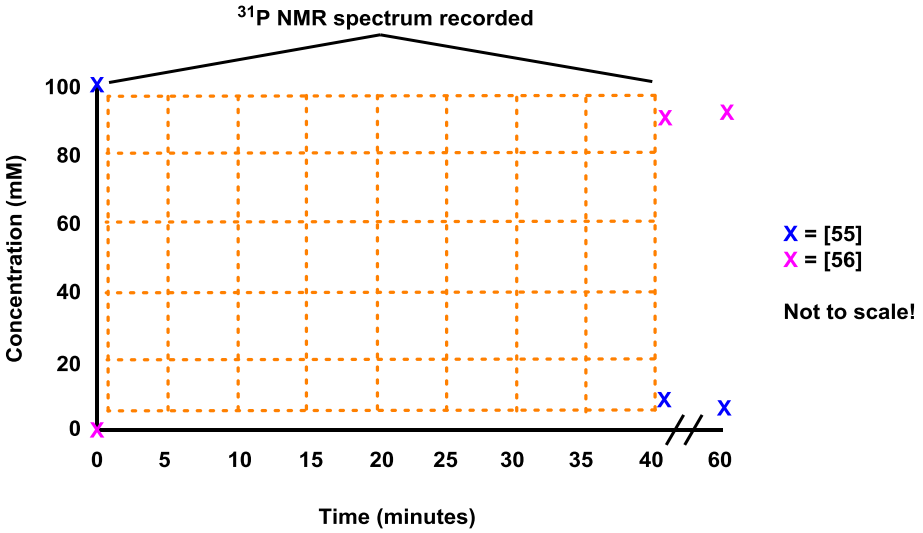

Figure 5.18: Representation of the time window over which quantitation of phosphorus speciation was carried out.

A capillary containing $NiCl_2(dppe)_2$ was used as an external standard for quantification purposes, and following calculation of the T_1 delays for each phosphorus centre, the entire amount of dpbz present in the reaction was confirmed to reside on the zinc centre (See Experimental for full details). Whilst comment upon the exact nature of the species observed is not possible (indeed, there may be several zinc-diphosphine species present at any moment of the reaction) it can be said with near-certainty that no dpbz is coordinated to iron throughout the catalytic reaction, within the detection limits of the technique.

5.6 Mechanistic implications

A summary of the most important findings regarding the iron-catalysed Negishi cross-coupling from this Chapter (and Chapter 4, in which transmetallation is discussed) are presented below.

i) Both time-resolved XAFS and ^{31}P NMR spectroscopic studies demonstrate that, within the resolution of the techniques, during catalytic turnover all of the observable diphosphine ligand resides on zinc, not iron.

ii) Further, the XAFS studies demonstrate that within the first seconds of the reaction no iron-bromide species are present; however, at the end of the reaction, the entire iron speciation is composed of an iron-bromide complex.

iii) The reaction of $ZnMes_2$ reagents with $FeBr_2$ forms organoferrates, even in the presence of dpbz.

iv) The order of reaction is 1.5 in [iron] and 0 for both [electrophile] and [diarylzinc]. For dpbz a reaction order of 1.5 is observed up to an iron: dpbz ratio of 1:2, and thereafter becomes independent. Importantly, this rules out simple coordination of dpbz to zinc as being key to the rate-limiting step, as otherwise the order in dpbz would remain positive at all loadings.

Due to the lack of similarity regarding both the iron speciation and the rate of reaction between the initial burst phase and the rest of turnover, the two should be treated separately; the burst phase will not be discussed further here, other than to say that it remains poorly understood and further investigations into its nature are ongoing within the group. Post burst-phase, it is proposed that the diarylzinc reagent, without dpbz coordinated, reacts with an iron bromide species (not necessarily iron(II) bromide) to form intermediate **78**, in which the bromide ligands on iron act as bridges to zinc, as observed in the isolated complex **61.** Following initial adduct formation, co-ordination of dpbz to zinc gives intermediate **79**, and is proposed to occur rapidly (Figure 5.19).

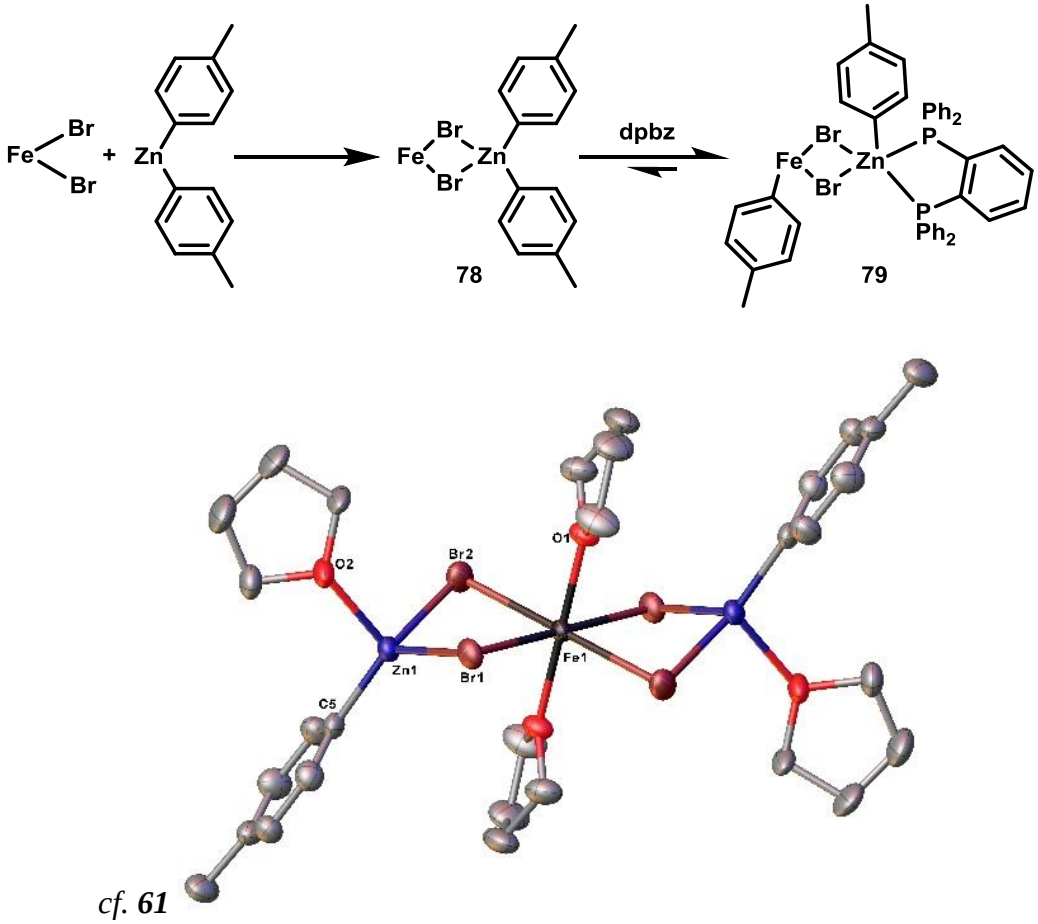

Figure 5.19: Proposed role of dpbz (or other efficacious diphosphine ligand) in the iron-catalysed Negishi cross-coupling reaction. **61** was synthesised and characterised by Dr. Antonis Messinis.

The above steps concur with the observed lack of Fe-P interactions observed in the XAFS data, and the observation of Zn-P signals in the ^{31}P NMR spectra. Whilst dpbz is likely not necessary for transmetallation from zinc to iron (as demonstrated in Chapter 4, where transmetallation is observed readily in the absence of diphosphine ligand) it is likely to be coordinated to zinc whenever this step takes place. It is reasonable to suggest that the intermediate **76** acts as an activated source of iron for further reactions later in the cycle.

Following on from these initial steps are certainly several others, possibly simultaneously and all important to the catalytic reaction, including the rate determining step of the reaction. However, with the data in hand, further comment on the mechanism of the reaction would be premature, other than to say that, based on the order in Fe of 1.4, the necessary activation of the electrophile is likely to occur on a second iron centre, and that the interaction between these two centres is reasoned to be rate-limiting . Due to the demonstrated quantitative formation of zinc diphosphine adducts within the entirety of turnover, the role of dpbz can be treated as discrete from this electrophile activation, unless zinc is in some way involved in that step, which due to the observed 0 order of reaction in zinc, unlike iron, can reasonably be ruled out.

5.7 Conclusions and future work

Time resolved *in situ* XAFS and NMR spectroscopy have been used to demonstrate that the diphosphine ligands necessary for reactivity in iron-catalysed Negishi cross-couplings are not coordinated to iron, but to zinc. At least two distinct manifolds were shown to be present during the reaction: an initial short-lived burst phase, corresponding to the first few seconds of turnover, in which iron nanoparticles are formed; and the remaining time of the reaction, in which homogeneous iron species are present and are responsible for the bulk of catalytic turnover, albeit at a much slower rate than the burst phase. At the end of the reaction all of the iron present has been shown to most likely be in the form of bromoferrates.

In addition to the *in situ* spectroscopies employed, synthetic experiments and DFT calculations also confirmed that, at mixtures representative of catalysis, the equilibrium of the reaction between iron-diphosphine and zinc lies almost completely towards the zinc-diphosphine products. The same preference for zinc coordination was observed for several other diphosphines that function as effective ligands in the reaction; importantly, dmbz, a ligand that results in no activity, was found to coordinate almost completely to iron.

It has previously been demonstrated,[58, 104] albeit with magnesium rather than zinc based nucleophiles, that the resultant nanoparticles formed following the reduction of homogeneous

iron species react rapidly with electrophiles, presumably *via* oxidative processes, to resolubilise and form homogeneous intermediates. No comment was made here on the oxidative part of the reaction; it has been previously suggested that this may occur *via* reaction of an Fe(I) intermediate with the electrophile.[46, 63] However, the kinetic results disclosed here demonstrate that this theory is no longer valid. In recent years, the relevance of multi-nuclear iron cluster species as intermediates in cross-coupling reactions has been reported,[59] and it is possible that such intermediates are forming here within the bulk phase of catalysis, and are responsible for electrophile activation.

Pertinent to this is the oxidation state of iron within the reaction. Following reduction to metallic iron nanoparticles in the burst phase, which have an oxidation state of 0, any re-oxidation event would result in an oxidation state of >0. However, such a process may operate *via* heterogeneous pathways (which are often poorly understood), or in a homogeneous regime (in which either single or two electron pathways may be present). Undertaking of a Hammett-type analysis, with a focus separately on the burst phase and bulk manifolds of the reaction, may further elucidate the mechanism of this step. The exposure of the reaction to physical organic spectroscopies, such as Mössbauer spectroscopy and magnetic circular dichromism (MCD) may also provide information on the oxidation state of iron.

Despite the remaining unknowns of this reaction, it is difficult to overstate the potential importance of the results discussed in this Chapter. It can no longer be assumed for iron-catalysed reactions that the ligands often required to effect homogeneous transformations remain coordinated to the iron centre, even in pre-formed complexes such as **69**. This paradigm of thinking can be further extended from iron to other transition metal catalysed reactions involving zinc reagents, and potentially to every reaction in which competitive ligand binding with a substrate is possible.

Chapter 6 *A continuous wave EPR investigation into the behaviour of a Cr(I) diphosphine complex under UV irradiation*

6.1 Introduction

6.1.1 Chromium complexes as catalysts for the selective oligomerisation of ethylene

Linear alpha olefins (LAOs; 1-alkenes ranging from C_4 to C_{20}) are an important class of petrochemical intermediate, which are produced industrially in a range of large-scale processes.[159, 160] Among the most high-value grades of LAO are 1-hexene and 1-octene, which are particularly valuable due to their use as co-monomers in ethylene polymerisation.[161] Their selective formation over less desirable carbon-number products therefore holds numerous cost advantages, reducing the costs of the purification steps for a product which subsequently has a higher market value. However, the selective formation of C_6 and C_8 products is challenging, and few metals have been reported to selectively carry out this process, with titanium[162] and tantalum[163] among those reported to do so. Computational studies suggesting selective zirconium and hafnium systems can be found. However in practice they often favour polymerisation rather than oligomerisation.[164, 165] The most successfully employed metal to have so far been used for the reaction is chromium,[166] with the first reports detailing the selective formation of 1-hexene appearing nearly 50 years ago.[167] The origin of the selectivity observed in reactions using chromium based catalysts is attributed to a change in the reaction mechanism, from a classic Cossee-Arlman type mechanism often observed in polymerisation reactions, to the metallocene one displayed in Figure 6.1. [168, 169]

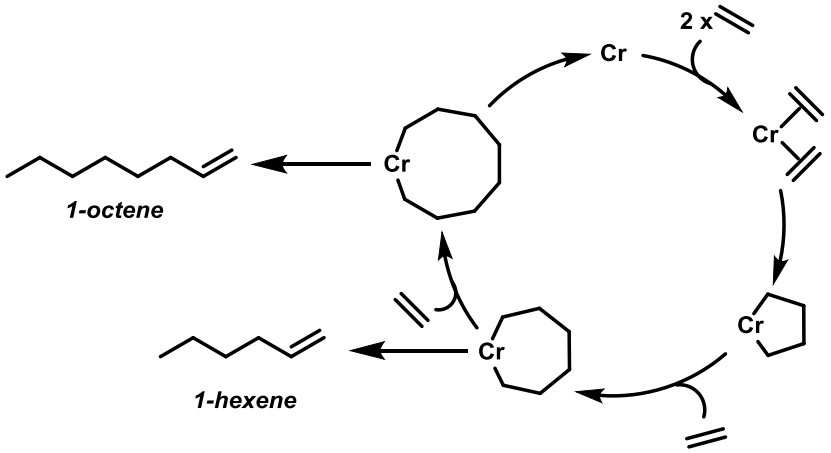

Figure 6.1: Metallocene mechanism for the selective oligomerisation of ethylene, to 1-hexene or 1-octene, using chromium catalysts.

Amongst others, Chevron-Philips utilise a homogeneous chromium system with a pyrrole-based ligand for the production of 1-hexene on an industrial scale.[170] More recently, several classes of extremely active catalysts employing bis(phosphino)amine (PNP) ligands, in

combination with chromium(III) halide salts and aluminium activators, such as triethylaluminium (TEA) or methylaluminoxane (MAO), have been reported for ethylene tri- and tetramerization.[171–173] Facile tuning of the steric and electronic properties of the PNP ligand can affect the activity and selectivity of the reaction, to allow for production of either desired product. As displayed in Figure 6.2, a slight alteration of the PNP ligand used and running the system at higher pressures enable the selective formation of 1-octene[172] rather than the originally reported selectivity towards 1-hexene.[171] The pendant methoxy group was suggested to be capable of coordination to the chromium centre, giving rise to a ligand with variable hapticity[174] and capable of stabilising further unsaturated chromium intermediates, ensuring selectivity to 1-hexene. In the absence of a pendant methoxy group, a further insertion of one ethylene unit is more favourable and allows for selectivity towards 1-octene.

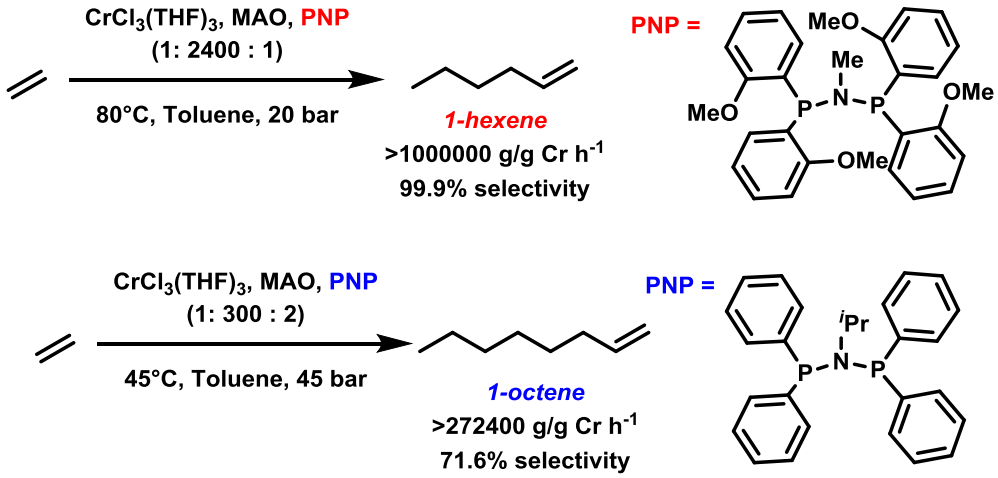

Figure 6.2: Highly active chromium(PNP) systems for the selective production of 1-hexene or 1-octene.

6.1.2: Mechanistic aspects of the chromium catalysed selective oligomerisation of ethylene

The capability of ligands to display variable hapticity has been demonstrated as crucial in determining selectivity in the titanium catalysed oligomerisation of ethylene (Figure 6.3, top).[175] Computational and experimental work suggested that intramolecular coordination, rather than externally from an arene solvent was occurring, due to the resulting weaker coordination from interaction of the ancillary ligand with the metal centre.[176] The potential importance of intramolecular ligand coordination has also been demonstrated for the commercially used Chevron-Philips process (Figure 6.3, bottom). Addition of a second aluminium activator bearing a halide ligand (diethylaluminium chloride, $AlEt_2Cl$) was shown

to improve both the catalyst activity and selectivity towards 1-hexene formation. Computationally this was shown to potentially be due to a resulting greater stabilisation of reactive intermediates, due to the associating capability of the aluminium-based chloride ligand.[177]

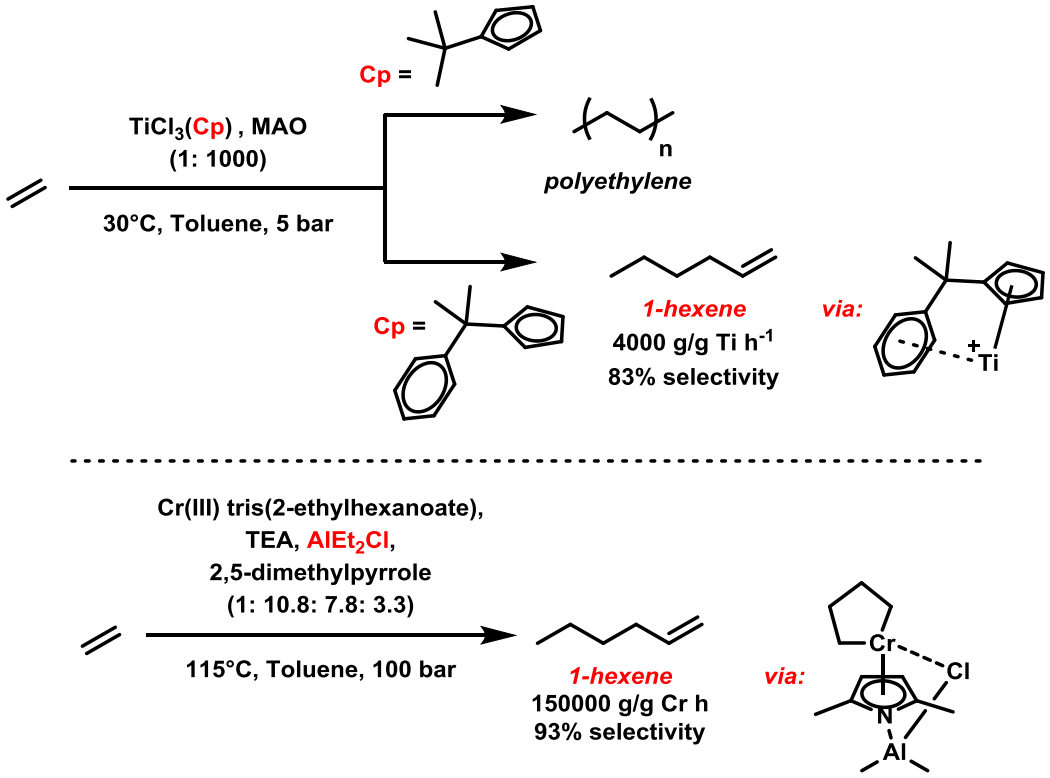

Figure 6.3: Top: The selective trimerisation of ethylene using a titanium-Cp catalyst system, reasoned to occur *via* intramolecular coordination of a pendant phenyl ring. Bottom: Chevron-Phillips ethylene trimerisation system, in which stabilisation of the chromium centre by association of a chloride ligand has been postulated.

Whilst the metallacyclic mechanism by which chromium catalysts produce 1-hexene and 1-octene from ethylene is generally accepted,[168, 169] the oxidation state of the chromium centre is less clear, with reports suggesting various chromium (n/n+2) cycles are involved.[178, 179] However, more recently a growing body of literature has been supportive of a chromium(I/III) system,[180] in which spin crossover at the chromium centre has been implicated as a potentially important consideration, as demonstrated by both NMR[181] and DFT[182] studies.

The majority of studies on such systems have focused on Cr(III) complexes, most likely due to this being the oxidation state of the pre-catalyst in the industrial processes employed, with a comparative scarcity of reports concerning the Cr(I) analogues. However, due to the paramagnetic intermediates often observed in such systems, EPR spectroscopy has been used

to good effect to allow for the characterisation of model Cr(I) systems, with information on the interaction of the ligand with the metal centre readily available.[183] For example, following the addition of TEA to **80**, successive displacement of carbonyl ligands from the chromium(I) centre, with concomitant η-6 coordination of one and then two ligand-based phenyl groups, was observed by EPR, to initially produce the piano stool complex **81**, followed by the sandwich complex, **82** (Figure 6.4).[184,185] **81** and **82** demonstrate the potential hemi-lability of the ancillary ligand at a chromium(I) centre following activation, when using mixtures representative of the catalytic system in question.

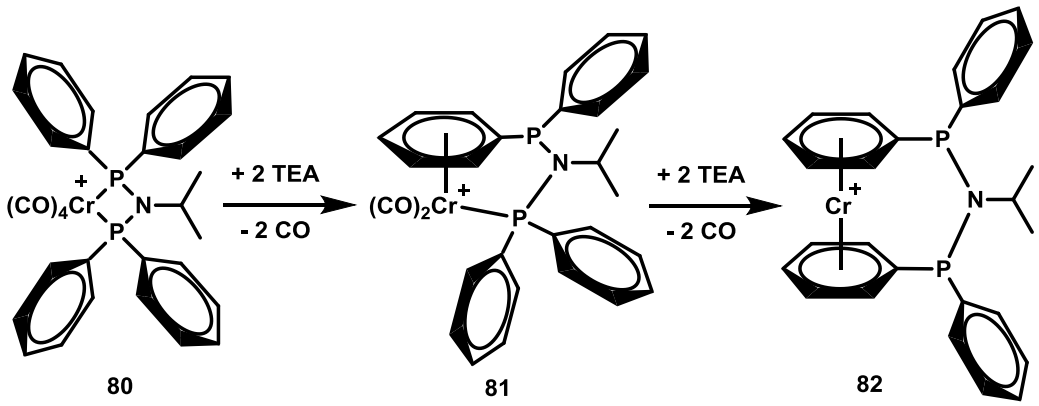

Figure 6.4: The observation, *via* EPR spectroscopy, of Cr(I) piano-stool and sandwich compounds **81** and **82** from the addition of triethylaluminium (TEA) to **80**

6.1.3 The effect of photoirradiation on Cr(I) carbonyl complexes

The activation of chromium pre-catalysts for the selective oligomerisation of ethylene is typically carried out using alkyl aluminium activators, such as MAO and TEA.[178] Despite the highly active systems that are formed following this activation alternative activation modes for the chromium pre-catalysts are desirable, due to the pyrophoric nature of alkyl aluminium reagents. By incorporating carbonyl ligands into the pre-catalyst and exposing the system to UV irradiation, photodecarbonylation, and subsequent activation, may be possible. Previous work on the photodecarbonylation of $Cr(CO)_6$ has shown the process to occur rapidly,[186] but there are contrasting reports in the literature regarding the photochemistry of Cr(I) carbonyl species bearing diphosphine ligands. Wass reported that upon exposure to irradiation, the Cr(I) complex $[Cr(CO)_4(PNP)]^+$, **80**, did not undergo loss of any carbonyl ligands, and did not present an active catalyst; however, the authors did not comment on the source of irradiation used or the length of exposure (Figure 6.5, *i*).[187] In contrast, Hanton (SASOL) reported that when using the same complex, UV irradiation followed by addition of TEA resulted in a

catalytic system with comparable activity to that of the model system, where TEA was used alone. An induction period was also observed, ascribed to the scavenging of free CO produced following irradiation, which is thought to act as a poison. Interestingly, approximately 33% of the chromium present following irradiation was reduced to the corresponding Cr(0) complex $Cr(CO)_4$(PNP), **83**, (Figure 6.5, *ii*).[188] It is important to note that when comparing the results obtained by Wass and Hanton, different anions were used in each study. Indeed, Hanton commented on the inactivity of the Wass system as possibly being due to selection of an anion that is too strongly coordinating.[189]

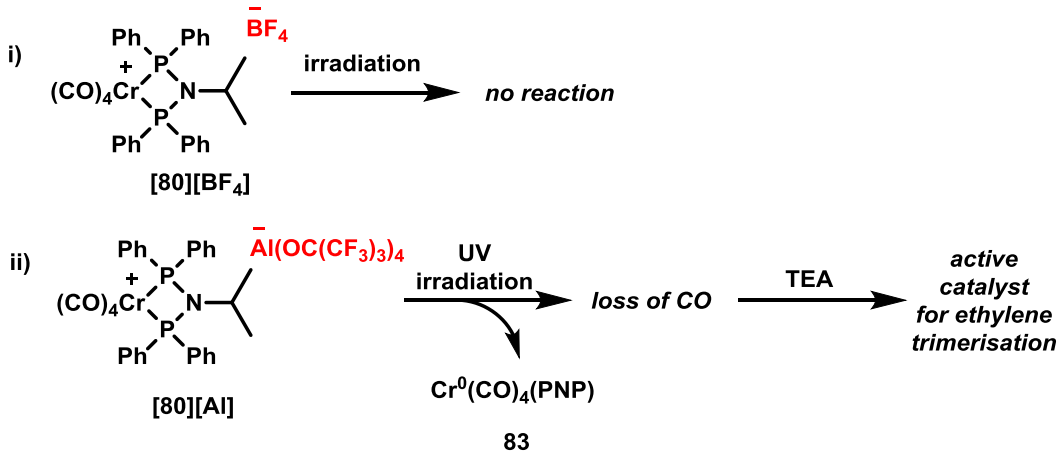

Figure 6.5: Reported change in reactivity of the Cr(I)(PNP) complex **80** under irradiation, depending upon the anion present.

6.1.4 EPR spectroscopy

6.1.4.1 EPR spectra in the liquid phase (isotropic systems)

Electron paramagnetic resonance (EPR) spectroscopy is a non-destructive magnetic resonance technique, used to investigate systems containing one or more unpaired electrons.[190] The technique finds use in many areas of chemistry, and it is particularly useful for the study of transition metal ions, which can often be paramagnetic, and thus contain unpaired electrons.[191] When an external magnetic field is applied to a system containing an unpaired electron (S = ½), the degeneracy of the two possible electron spin states of the electron (m_S, = +½ or -½) is removed, resulting in two non-degenerate quantised states. The resulting splitting in a magnetic field is termed the electron Zeeman effect, and the magnitude of the splitting can be increased by increasing the strength of the applied magnetic field. The two spin states are referred to as the electron Zeeman levels (Figure 6.6).[192] More generally, upon application of a magnetic field 2S+1 states are available. However, for systems with multiple unpaired

electrons (S > ½) zero field splitting contributions dominate the spectrum; such high spin states will not be discussed here.[192]

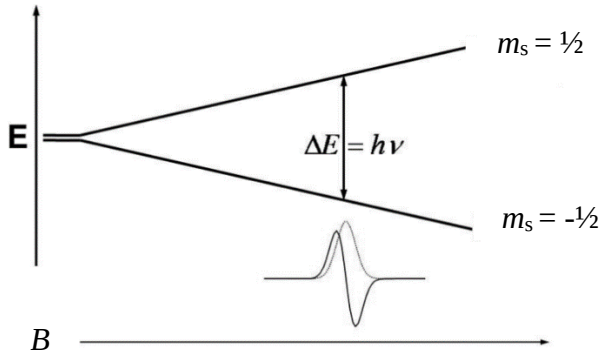

Figure 6.6: Energy levels for an electron spin (S = + ½ or – ½) in an applied magnetic field B.[193] The inset displays the resulting EPR spectrum.

Most commonly, EPR experiments are carried out in continuous wave (CW) mode, in which the sample is irradiated with a fixed microwave frequency, while the external magnetic field is swept.[194] Pulsed experiments are also possible and are becoming more common, but they require more sophisticated and expensive equipment.[195] As with other spectroscopic techniques, when the energy of the applied radiation matches the energy separation between the two states, absorption of energy occurs, and this results in resonance. The electron then undergoes a transition, from low to high energy levels (m_s = -½ to m_s = +½), giving a peak in the resulting EPR spectrum. Conventionally, this is then plotted as a first derivative rather than in absorption mode. Due to the small energy gaps between states, the excitation energy corresponds to the microwave region, with samples typically irradiated with radiation possessing a frequency of around 9.5 GHz, referred to as the X-band region.[192] EPR spectra therefore appear as a plot of microwave absorption as a function of the applied magnetic field (Figure 6.7).

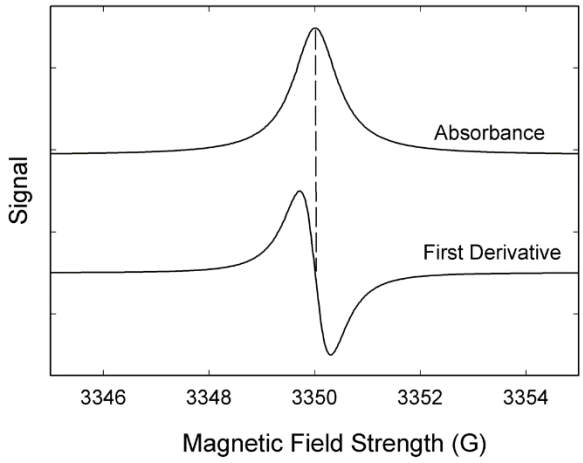

Figure 6.7: Example of an isotropic EPR spectrum (X-band), showing both the absorption and first derivative profiles.[196]

The small energy gap between the two spin states results in a very small population difference between energy levels (less than 1%), so in theory EPR, like NMR, is an intrinsically low sensitive technique. However, this small population difference still allows for good signal to noise ratios in the detection method. Furthermore, the mass of the electron is around 2000 times smaller compared to that of a proton, and thus possesses a larger magnetic moment, as described by the Bohr magneton, μ_B, (Equation 6.1). EPR is therefore the more sensitive of the two magnetic resonance techniques.

Equation 6.1: Definition of the Bohr magneton, μ_B, which is used to express the magnetic moment of the electron. e = elementary charge, $\hbar =$ reduced Plancks's constant, m_e = mass of electron.

$$\mu_B = \frac{e\hbar}{2m_e} = 9.274\ x\ 10^{-24}\ JT^{-1}$$

The Bohr magneton can be used to quantify the energy of the electron Zeeman levels (Equation 6.2).

Equation 6.2: The energy of the electron Zeeman levels resulting from the interaction of an unpaired electron with an applied magnetic field. h = Planck's constant, υ = frequency of applied EM radiation, μ_B = Bohr magneton, g_e = electron g factor (approximately = 2.0023), B = applied magnetic field, m_s = electron spin angular momentum number.

$$E = h\nu = g_e\ \mu_B B m_s$$

The proportionality constant linking $h\nu$ to $\mu_B B_{ms}$ is called g, the electron g factor which is a dimensionless factor that is dependent on the chemical environment of the unpaired

electron. The accurate measurements of the *g* value underpin the technique and are used to identify the radical being investigated. It is analogous to the chemical shift values used in NMR and can be measured experimentally, by either accurate measurement of the resonance field and applied microwave frequency, or through *in situ* use of a reference standard with an associated *g* value.

In the presence of nuclei possessing a magnetic spin ($I \neq 0$), further magnetic interactions with the electron spin and the applied magnetic field are possible, resulting in multi-line spectra possessing more information on the chemical system present.[197] The interaction of the nuclear spin with an applied magnetic field (B) results in the loss of nuclear degeneracy, and a resultant nuclear Zeeman splitting is observed (Equation 6.3).

Equation 6.3: Expression of the nuclear Zeeman levels. g_n = nuclear g factor, μ_N = nuclear magneton, B = applied magnetic field, m_l = magnetic quantum number.

$$E = g_n \mu_N B m_l$$

The magnitude of the nuclear Zeeman is also dependent on the nuclear magneton (Equation 6.4).

Equation 6.4: Definition of the nuclear magneton, μ_N, which is used to define the nuclear Zeeman coupling interaction. *e* = elementary charge, $\hbar$ = reduced Plancks's constant, m_p = proton rest mass.

$$\mu_N = \frac{e\hbar}{2m_P} = 5.051\ x\ 10^{-27}\ JT^{-1}$$

Equations 6.3 and 6.4 consider only the interaction of the unpaired electron or nuclear spin with the applied magnetic field (B). However, the two spin systems (S = ½ and I = ½, for an unpaired electron interacting with a proton) can also interact with each other, resulting in a hyperfine interaction (HFC). This creates further perturbations to the energy level scheme (as displayed in Figure 6.8), with the resulting splitting diagram displayed in Figure 6.6. The difference in energy between the levels is the hyperfine coupling constant, *a* (Equation 6.5).

Equation 6.5: Definition of the hyperfine interaction. *a* = hyperfine splitting constant, m_s = electron spin angular momentum number, m_l = magnetic quantum number. In this case, $a << g\mu_B B$

$$HFC = a m_s m_I$$

Combining the three terms above (the electron and nuclear Zeeman terms plus the hyperfine term) into a single equation for the energy of an unpaired electron in an applied field gives the following (Equation 6.6):

Equation 6.6: Expression of the combined electron Zeeman term (EZT), nuclear Zeeman term (NZT) and the resulting hyperfine interaction between the two (HFC).

$$E = g_e \mu_B B m_s - g_N \mu_N B m_l + a m_s m_l$$

$$= \mathrm{EZT} - \mathrm{NZT} + \mathrm{HFC}$$

Allowed transitions in EPR spectroscopy must result in a change in the electron spin state, with no change in the nuclear spin state, *i.e.* $\Delta m_S = \pm 1$ and $\Delta m_I = 0$. Therefore, for a simple two-spin system (S = ½ and I = ½) there are two allowed transitions (Figure 6.8). The multiplicity of the observed lines in EPR spectroscopy is analogous to the multiplicity term in NMR; therefore, in a system where I= ½, there are $2nI+1$ transitions possible, with an intensity as given by Pascal's triangle. For an I = ½ spin system, the multiplicities are 1:1, 1:2:1 and 1:3:3:1 for the doublet, triplet and quartet hyperfine patterns in the case where there are n = 1, 2 or 3 equivalent protons.

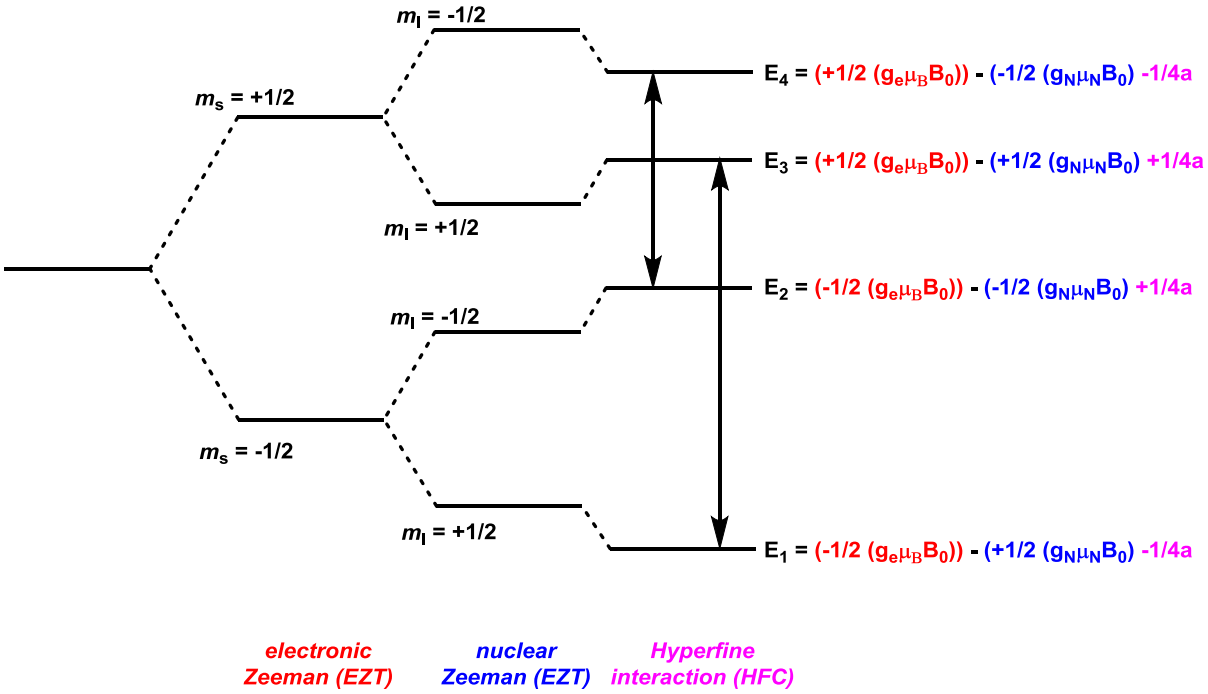

Figure 6.8: Energy level diagram for a two-spin system (S = I = ½), displaying the electronic (EZT) and nuclear (NZT) Zeeman terms and hyperfine interaction (HFC). The arrows displayed correspond to the transitions allowed according to the EPR selection rules, resulting in two observed signals in the EPR spectrum.

6.1.4.2 EPR spectra in frozen solution (anisotropic systems)

If the unpaired electron resides in a non-symmetric *p*, *d* or *f* orbital, rather than a symmetric *s* orbital, the sample is no longer insensitive to direction, and the orientation of the paramagnetic centre within the external field must be considered with respect to the principal *x*, *y* and *z* axes (the same consideration must be made if the EPR experiment is carried out at low temperatures in a frozen solution). Such systems are termed anisotropic. The *g*-value can no longer be regarded as a scalar quantity, instead becoming a vector quantity, designated by the symbol $\boldsymbol{g}$, made up of the components $\boldsymbol{g}_x$, $\boldsymbol{g}_y$ and $\boldsymbol{g}_z$. Whereas in an isotropic system the *x*, *y* and *z* axes are all averaged due to rapid tumbling, resulting in a single averaged *g* value, in an anisotropic system this $\boldsymbol{g}$ factor must be defined for each of the *x*, *y* and *z* directions. The *g*-value for a given orientation now depends on the Cartesian coordinates θ and ϕ, written as $\boldsymbol{g}_x$, $\boldsymbol{g}_y$ and $\boldsymbol{g}_z$, or $\boldsymbol{g}_1$, $\boldsymbol{g}_2$ and $\boldsymbol{g}_3$. **(**Figure 6.9).

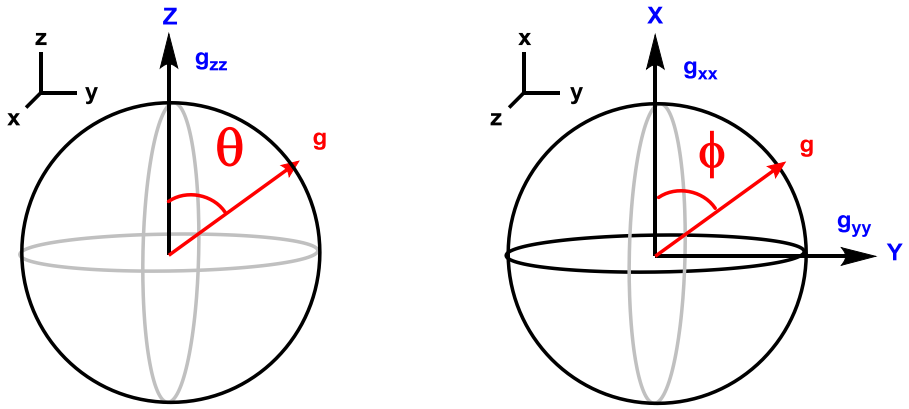

Figure 6.9: Observation of g-anisotropy within the axes *x*, *y* and *z*. The orientation of the magnetic field is defined by the Cartesian coordinates θ and ϕ, which correspond to the angle of *g* with respect to the *z* axis and *xy* plane, respectively. Note: the two objects represent the same image rotated 90° along the y axis.

The averaged value of the *g* tensor components is the isotropic value (Equation 6.7).

Equation 6.7: Calculation of the g factor within an anisotropic system.

$$g_{iso} = \frac{g_{xx} + g_{yy} + g_{zz}}{3}$$

In the powder (or frozen solution) state, three limiting situations occur with respect to the symmetry elements of the paramagnetic system. The first case, which is rare, is when all three axes are equivalent ($\boldsymbol{g}_x = \boldsymbol{g}_y = \boldsymbol{g}_z$) and is known as isotropic. The second case is where one unique axis exists, in which the *x* and *y* planes are equivalent, and the *z* plane is not; this is

referred to as axial. In this case, the applied magnetic field can be aligned either parallel to the unique *z* axis, or perpendicular to it, in the *xy* plane. The parallel and perpendicular cases each provide a separate EPR resonance, meaning that in axial systems two separate EPR resonances are observed. The g_{zz} term can therefore be referred to as $g_{\parallel}$, and the g_{xx} and g_{yy} terms, which are equal, become $g_{\perp}$ (Equation 6.8).

Equation 6.8: Definition of the g factor within axial systems.

$$g_{iso} = \frac{g_{\perp} + g_{\perp} + g_{\parallel}}{3}$$

The final case is one in which all three axes are inequivalent ($\boldsymbol{g}_x \neq \boldsymbol{g}_y \neq \boldsymbol{g}_z$), known as rhombic, which will not be discussed further.

6.1.4.3 EPR spectra of Cr(I) octahedral complexes bearing a diphosphine ligand

Chromium(I) carbonyl complexes bearing a diphosphine ligand exist in a low spin d^5 (S= ½) configuration due to the strong field ligands present.[157] These complexes have been shown to undergo a Jahn-Teller distortion, with an elongation along the *z* axis and contraction along the *x* and *y* axes, resulting in a loss of degeneracy of the triplet ground state and formation of a singly occupied molecular orbital (SOMO) of d_{xy} character (Figure 6.10).[198] Such complexes are therefore characterised by an axial EPR spectrum.[199]

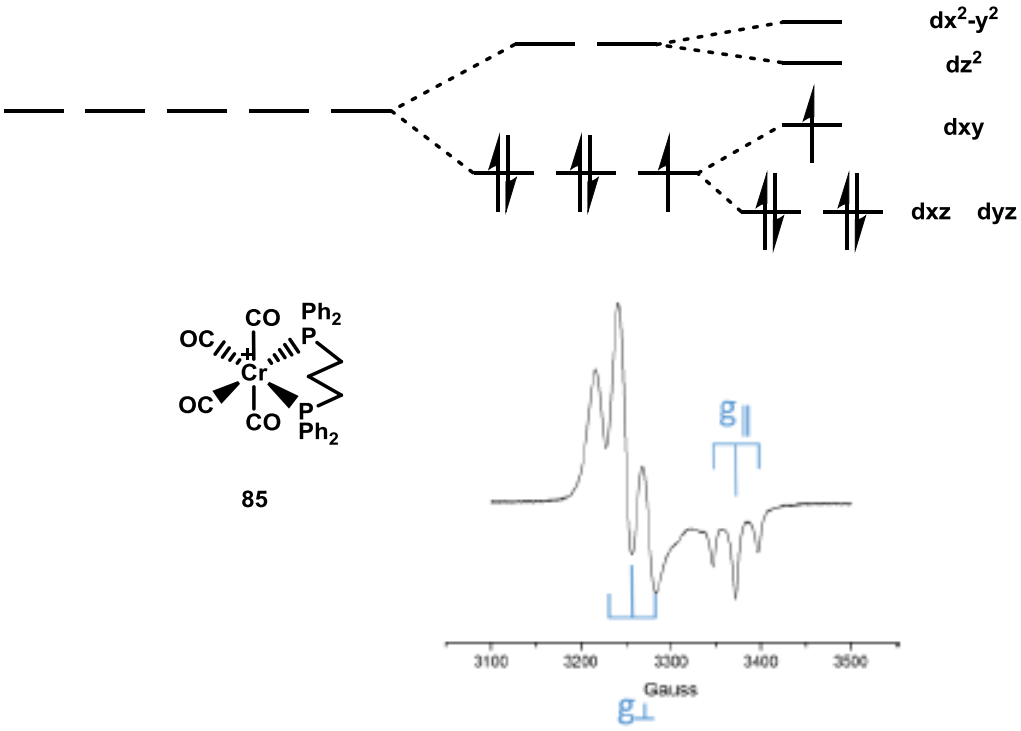

Figure 6.10: Top: Crystal field splitting diagram for octahedral d^5 Cr(I) complexes existing in a high spin configuration, such as **85.** Bottom: Anisotropic axial EPR spectrum of the Cr(I) complex **85**, displaying the perpendicular and parallel transitions.

The Cr(I) complex **85** displays a large hyperfine coupling due to the interaction of the unpaired electron with the two equivalent ^{31}P (I = ½) nuclei. The coupling of the unpaired electron with the chromium I = 3/2 ^{53}Cr centre is barely resolved, owing to the low isotropic abundance (approximately 9.5%). The spin Hamiltonian parameters, obtained by simulation of the experimental spectra, are consistent with a low-spin d^5 Cr(I) centre possessing a SOMO of d_{xy} character.[184]

6.1.5 General considerations

The work in this Chapter is concerned with the effect of UV irradiation upon the chromium(I) diphosphine complex **85**, and with the characterisation of the resulting chromium speciation present following the resulting *in situ* and *ex situ* photochemical transformations. The work was carried out at Cardiff University in combination with Prof. Damien Murphy and the Cardiff EPR group. All simulations were carried out by Dr. Emma Carter and Dr. Andrea Folli.

6.2 Photochemical investigation

*6.2.1 Ambient UV irradiation of $[Cr(CO)_4(dppp)]^+$ **84***

The Cr(I) complex $[Cr(CO)_4(dppp)]^+$ (dppp = 1,3-bis(diphenylphosphino)propane), **84**, was prepared by stoichiometric mixing of the corresponding Cr(0) complex, **85**, with $[Ag][Al(OC(CF_3)_3)_4]$ (from here on referred to as [Al]), according to the literature procedure (Figure 6.11).[188] The resulting dark blue solid was characterised *via* MS and EPR spectroscopy. The spin Hamiltonian parameters are displayed in Table 6.1, Entry 1.

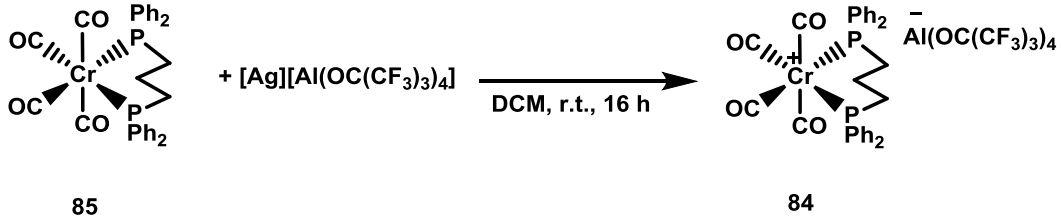

Figure 6.11: Synthesis of $[Cr(CO)_4(dppp)][Al]$, **84.**

The frozen (140 K) EPR spectrum (19.4 mM in DCM) displays an anisotropic axial signal, with hyperfine coupling to the two equivalent ^{31}P nuclei (Figure 6.12, *a*). Following 30 minutes of UV irradiation at 298 K, the colour of the solution was observed to change from dark blue to pale yellow, and the resulting anisotropic EPR spectrum recorded at 140 K is also significantly changed (Figure 6.12, *b*). Whilst still axial in character, the multiplicity is different, and a 5-line quintet (with relative intensities of 1: 4: 6: 4: 1) is now observed. The change in multiplicity is more easily observed in the isotropic EPR spectrum recorded at 298 K and can be assigned to the coupling of the unpaired electron centred on chromium with four equivalent phosphorus nuclei (Figure 6.12, *c*).

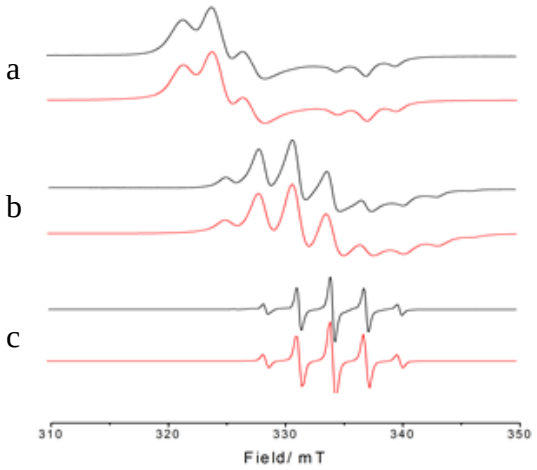

Figure 6.12: X-band CW EPR spectra in DCM of: (*a*): $[Cr(CO)_4(dppp)]^+$, **84**, recorded at 140 K. b and c: $[Cr(CO)_2(dppp)_2]^+$, **86**, recorded at 140 K (*b*) and 298 K (*c*) following exposure of **84** to UV irradiation at 298 K for 30 minutes. Experimental and simulated are shown in black and red lines respectively.

Simulation of the isotropic spectrum yields an isotropic coupling constant a_{iso} = 79.7 MHz, whilst simulation of the anisotropic EPR spectrum corresponding to the species present following irradiation revealed the anisotropic coupling constants as $A_{\perp}$ = 79 MHz and $A_{\parallel}$ = 81 MHz (Table 6.1, entry 2). Weak ^{53}Cr (S = $^3/_2$) satellite features are also observed in the wings of the isotropic spectrum, confirming that the signal arises from a Cr(I) centre. Accordingly, the signals are assigned to a new complex, trans-$[Cr(CO)_2(dppp)_2)]^+$, **86**, which is confirmed by the good agreement observed between the simulated spin Hamiltonian parameters and the DFT derived values (Table 6.1). Cr(I) complexes of the type trans-$[Cr(CO)_2(PP)_2]^+$ have been previously reported, but as a decomposition product *via* oxidation of a Cr(0) precursor; the spin Hamiltonian parameters reported for the complex trans-$[Cr(CO)_2(PP)_2]^+$ (PP = dppm (bis(diphenylphosphino)methane) or dppe (bis-diphenylphosphino)ethane)) are in good agreement with those observed in **86** (Table 6.1, entries 3 and 4).[200]

Table 6.1: Summary of the observed reactivity upon exposure of **84** to UV irradiation at 298 K for 30 minutes, to give **86**, in addition to spin Hamiltonian parameters for **84** and **86** and previously reported complexes of the type trans-$[Cr(CO)_2(PP)_2]^+$.[200] The black and red numbers correspond to experimental and theoretical (DFT derived) values respectively.

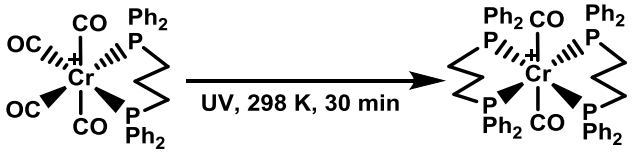

84 **86**

		g				*A* / MHz			
Entry	**Complex**	g_1	g_2	g_3	g_{iso}	A_1	A_2	A_3	a_{iso}
1	$[Cr(CO)_4(\kappa^2\text{-dppp})]^+$ **84**	2.066	2.066	1.988	2.040	±76	±76	±71	±74.3
		2.039	2.029	1.991	2.020	76	68	66	70
2	trans-$[Cr(CO)_2(\kappa^2\text{-dppp})_2]^+$ **86**	2.023	2.023	1.968	2.005	79.0	79.0	81.2	79.7
		2.012	2.009	1.964	1.995	92	81	80	84
3[199]	trans-$[Cr(CO)_2(\kappa^2\text{-dppm})_2]^+$	2.031	2.014	1.973		79.1	74.9	76.4	
4[199]	trans-$[Cr(CO)_2(\kappa^2\text{-dppe})_2]^+$	2.027	2.025	1.980		85.4	80.3	79.4	

86 is kinetically stable with respect to decomposition under ambient conditions, if kept in the dark under an inert atmosphere. In order to probe the stability of **86** further, a sample was prepared, *via* UV irradiation of **84**, and reversibly treated to increasing hydrostatic pressures. By varying the pressure at which the EPR spectrum is recorded, the extraction of parameters provides an indirect insight into the properties of potential transition.[201] At each pressure the EPR spectrum was recorded and as displayed in Figure 6.13, the effect of pressure on **86** is completely and quantifiably reversible up to 2000 bar.

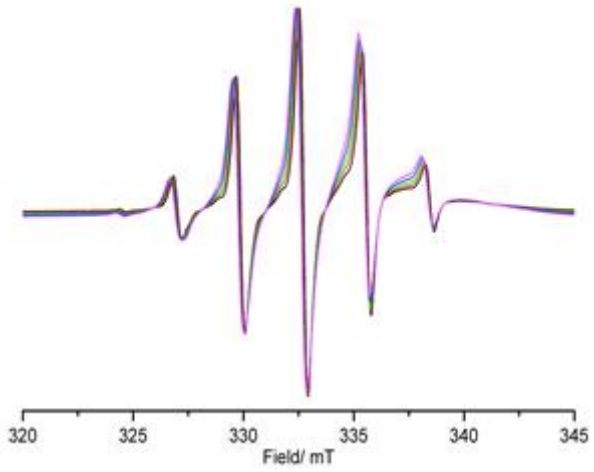

Figure 6.13: X-band CW EPR spectra in DCM of **86** following exposure to increasing pressure. Black = 0 bar, red = 500 bar, green = 1000 bar, blue = 1500 bar, purple = 2000 bar. Experiments performed and analysed by Dr. Andrea Folli.

The isotropic EPR spectra displayed in Figure 6.13 display increased broadening as the pressure is increased, due to a decrease in the rate of tumbling of the Cr(I) centre. Simulation of the data from each variable pressure experiment allows for extraction of the rotation correlation time of the complex (τ_R), which provides information on the interaction of solvent with a solvated complex, as quantified by the molar volume of activation (Equation 6.9).[202]

Equation 6.9: Calculation of the molar volume of activation from the pressure dependence of rotation correlation time (τ). τ_0 = rotational correlation time at atmospheric pressure, $\Delta V^{\ddagger}$ = the volume of activation, R = ideal gas constant, T = temperature (K).

$$ln\frac{\tau}{\tau_0} = \frac{\Delta V \ddagger}{RT}(P)$$

A plot of ln(τ/τ_0) versus pressure is linear, and from the gradient an approximate value of 9.89 mL mol^{-1} is obtained at 298 K (Figure 6.14). This value of $\Delta V^{\ddagger}$ corresponds to the increase in volume of a solvent cage necessary to permit rotation of the Cr(I) centre. It should be noted that this value is approximate, as Equation 6.9 assumes no change in the viscosity of the solvent at higher pressures, which is not the case. Whilst this model has successfully been applied to large biomolecules,[202] the Cr(I) complex investigated here possesses a much smaller molecular weight, and is thus fully exposed to the solvent, meaning the value obtained must be treated approximately. No other changes are observed in the high-pressure spectra, demonstrating the structural stability of **86.**

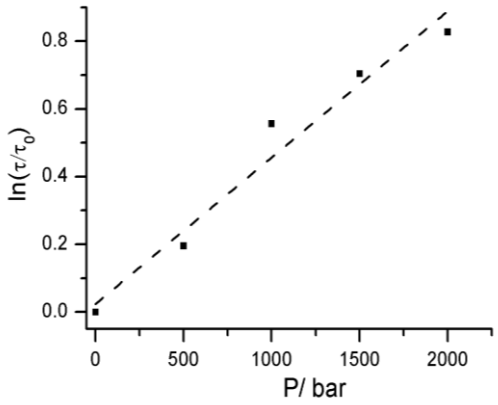

Figure 6.14: Calculation of the molar volume of activation of **86** from a plot of $\ln(\tau/\tau_0)$ against pressure.

Approximate quantification of the amount of **84** that is converted to **86** is possible, and the value obtained of around 50% suggests that the reaction appears to occur quantitatively, as this would account for all of the ligand present within the solution (Cr / dppp = 1 for **84**, and 0.5 for **86**). However, this leaves the remaining 50% of the chromium present in the reaction unaccounted for. Following the loss of dppp from **84**, concomitant formation of $[Cr(CO)_4]^+$, a complex which has been characterised *via* EPR spectroscopy previously,[203] may be possible, however was not observed here.

As discussed in Section 6.1, free Cr(I) species formed in solution following the reaction of **80** with TEA have previously been trapped using coordinating arene solvents, allowing them to be observed *via* EPR spectroscopy.[184] However, attempts to do so here were unsuccessful, suggesting that coordinatively unsaturated Cr(I) species are not being formed following irradiation (or that if they are, their lifetimes are short). On the basis of stoichiometry, the formation of $[Cr(CO)_6]^+$ would appear possible and logical, and the complex has been described as producing a broad peak in the corresponding EPR spectrum.[204] However, all attempts to observe it here were not successful, even at a temperature as low as 5 K. It should be noted that there is literature precedent regarding the elusiveness of this complex within the field of X-band EPR,[205] suggesting that the complex may be present but unobservable.

On the basis of the failure to observe any further Cr(I) species, a change in oxidation state of the chromium centre may be occurring following irradiation, yielding species unobservable *via* EPR spectroscopy. Such an effect has been previously reported, whereby the Cr(I) complex $[Cr(CO)_4(PNP)^{iPr}]^+$ was observed *via* IR spectroscopy to form the corresponding Cr(0) complex in around 33% yield (Figure 6.5).[188] It is therefore possible that oxidative or reductive

processes concerning **84** may occur, and that Cr(0) or Cr(+II) species make up the remaining chromium speciation following irradiation (Figure 6.15).

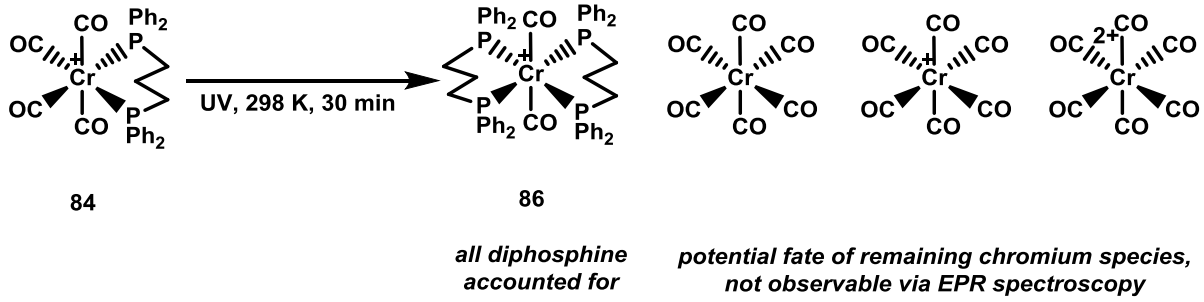

Figure 6.15: Possible chromium species formed following irradiation of **84**.

*6.2.2 Low temperature UV irradiation of Cr(CO)$_4$(dppp) **84***

Whilst the data so far discussed clearly describe the conversion of **84** to **86**, they do not reveal any information on how this photochemical transformation may be occurring. So as to provide an insight into the structure of potential intermediates, the irradiation of **84** was carried out at a lower temperature of 77 K. After two hours of irradiation (19.4 mM in DCM), the sample had changed from dark blue to green, and the resulting anisotropic EPR spectrum is much changed from that of **84** and **86** (Figure 6.16).

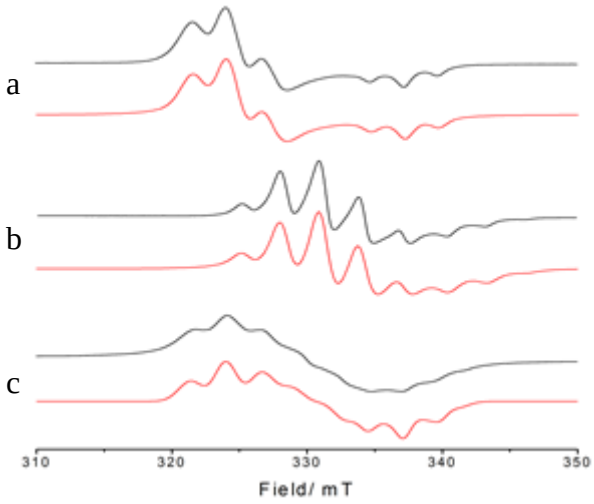

Figure 6.16: X-band CW EPR spectra in DCM, recorded at 140 K, of: *a*: [Cr(CO)$_4$(dppp)]$^+$, **84**, recorded at 140 K. *b*: [Cr(CO)$_2$(dppp)$_2$]$^+$, **86.** *c*: *mer*-[Cr(CO)$_3$(κ^1-dppp)(κ^2- dppp)]$^+$, **87**, observed following irradiation of **84** at 77 K for 2 h. Experimental and simulated data are shown by black and red lines, respectively.

Poor quality data was obtained when attempting to simulate the data according to a single chromium species; however, a satisfactory simulation was obtained corresponding to two separate chromium centres; the first chromium centre can be assigned to residual **84.** The second centre displays signals corresponding to interaction of a Cr(I) centre with two distinct ^{31}P environments; one resulting in a 1:2:1 triplet, corresponding to coupling with two equivalent phosphorus nuclei, and a second displaying a 1:1 doublet, resulting from coupling to a single phosphorus nucleus. The coupling constants for the triplet are $a_{\perp}$ = 60 MHz, $A_{\parallel}$ = 55 MHz, (A_{iso} = 58.3 MHz), whilst for the doublet values of $A_{\perp}$ = 79 MHz, $A_{\parallel}$ = 68 MHz, (a_{iso} = 75.3 MHz) are observed (Table 6.2, entry 2). These data are suggestive of formation of a Cr(I) centre to which two equivalents of the ligand dppp are coordinated; one in a κ^2-bonding mode, and the other in a κ^1-mode, in the form *mer*-$[Cr(CO)_3(\kappa^1\text{-dppp})(\kappa^2\text{- dppp})]^+$, **87.**

Table 6.2: Summary of the observed reactivity upon exposure of **84** to UV irradiation at 77 K for 2 h, to give **87**, in addition to spin Hamiltonian parameters for **84**, **87** and previously reported complexes of the type mer-$[Cr(CO)_3(\kappa^1\text{-PP})(\kappa^2\text{-PP})]^+$. The black and red numbers correspond to experimental and theoretical values respectively.

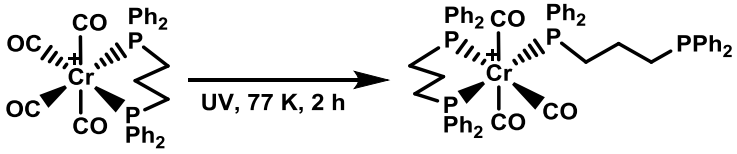

84 **87**

Entry	Complex	*g*				*A* / MHz			
		g_1	g_2	g_3	g_{iso}	A_1	A_2	A_3	a_{iso}
1	$[Cr(CO)_4(\kappa^2\text{-dppp})]^+$ **84**	2.066	2.066	1.988	2.040	±76	±76	±71	±74.3
		2.039	2.029	1.991	2.020	76	68	66	70
2	*mer*-$[Cr(CO)_3(\kappa^1\text{-dppp})(\kappa^2\text{-dppp})]^+$ **87**	2.046	2.046	1.986	2.026	79 60	79 60	68 55	75.3 58.3
		2.024	2.014	1.982	2.007	83 59	70 49	70 44	74 51
3[199]	*mer*-$[Cr(CO)_3(\kappa^1\text{-dppm})(\kappa^2\text{-dppm})]^+$	2.034	2.034	1.982		72	72	63.3	
4[200]	*mer*-$[Cr(CO)_3(\kappa^1\text{-dppe})(\kappa^2\text{-dppe})]^+$	2.055	2.037	1.983		68.7	66	69.6	
5[200]	*mer,mer*-$[\{Cr(CO)_3(\kappa^2\text{-dppe})\}_2(\mu\text{-dppe})]^+$	2.049	2.037	1.989		67.2	69.6	67.5	

Complexes of the type *mer*-$[Cr(CO)_3(\kappa^1\text{-PP})(\kappa^2\text{-PP})]^+$ (PP = dppm and dppe) have been reported and characterised *via* EPR spectroscopy (Table 6.2, entries 3 and 4), but formed *via* oxidation of the corresponding Cr(0) complexes.[199, 200] Interestingly, the dppm and dppe

complexes are reported to display couplings consistent with three equivalent ^{31}P environments, as opposed to the observation here using the ligand dppp, in which two inequivalent ^{31}P environments are recorded. In the case of the ligand dppe, the resulting EPR spectrum was found to be indistinguishable from the bimetallic derivative, *mer,mer*-[{Cr(CO)$_3$(κ^2-dppe)}$_2$(μ-dppe)]$^+$ (Table 6.2, entry 6), in which one diphosphine ligand is coordinated to two chromium centres (one in a (+I) state, the other in a (0) state) in a bridging mode.[200, 206] However, this bimetallic complex was synthesised *via* one-electron oxidation of the preformed bridging [Cr(0), Cr(0)] complex, and on this basis *mer,mer*-[{Cr(CO)$_3$(κ^2-dppp)}$_2$(μ-dppp)]$^+$ is suggested not to form here.

Increasing the time of exposure of **84** to low-temperature UV irradiation results in a decrease in signal intensity, suggestive of a loss of observable Cr(I) species in solution. This indicates that once is formed, **87** requires exposure to irradiation at more ambient temperatures in order for its transformation into **86** to be complete. Further, if a sample is left in the dark for 3 h following low temperature irradiation (to give a mixture of residual **84** and **87**), no signals corresponding to **87** are observed in the subsequently recorded EPR spectrum, with only the starting material **84** present, again at a lower signal intensity. Taken together, these data suggest that the intermediate **87** formed is somewhat more unstable than **84** and **86**, and that formation of **87** from **84** is not reversible, as a loss in signal intensity upon reformation of **84** (the stability of which has been discussed) would not be observed. The failure to observe any of the bis-diphosphine complex **86** when irradiation is carried out at low temperatures demonstrates that, whilst disassociation of one phosphorus centre from **84** is possible, coordination of the resultant free phosphorus centre to a second Cr(I) centre is not, and more ambient temperatures are required to do so (Figure 6.17).

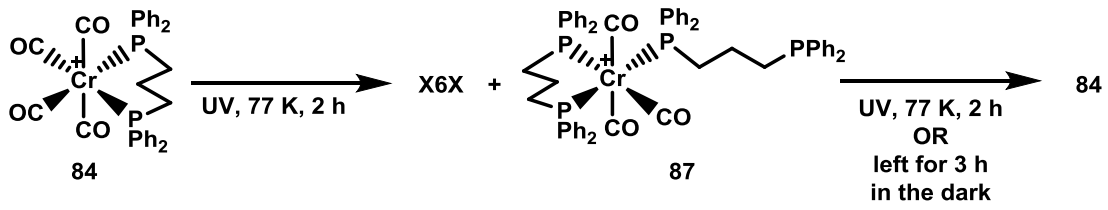

Figure 6.17: Observed instability, and lack of reversibility back to **84**, of **87**.

6.2.3 Mechanistic considerations

From the observation of **87**, which can reasonably be assumed to represent an intermediate in the formation of **86** from **85**, the following mechanism is proposed (Figure

6.18), in which the formation of a diphosphine bridged bimetallic intermediate is postulated. Whilst no such species was experimentally observed here by EPR, the chance of such an intermediate forming is likely to be dependent on the concentration of chromium(I) in solution, and may not form at low chromium concentrations. In order to probe this, the low-temperature irradiation of **84** was repeated at a lower concentration (2.2 mM in DCM). After 2 h, no signals corresponding to either **86** or **87** were observed, suggesting that the photochemical transformations are concentration dependent, and could be occurring *via* a bimetallic complex.

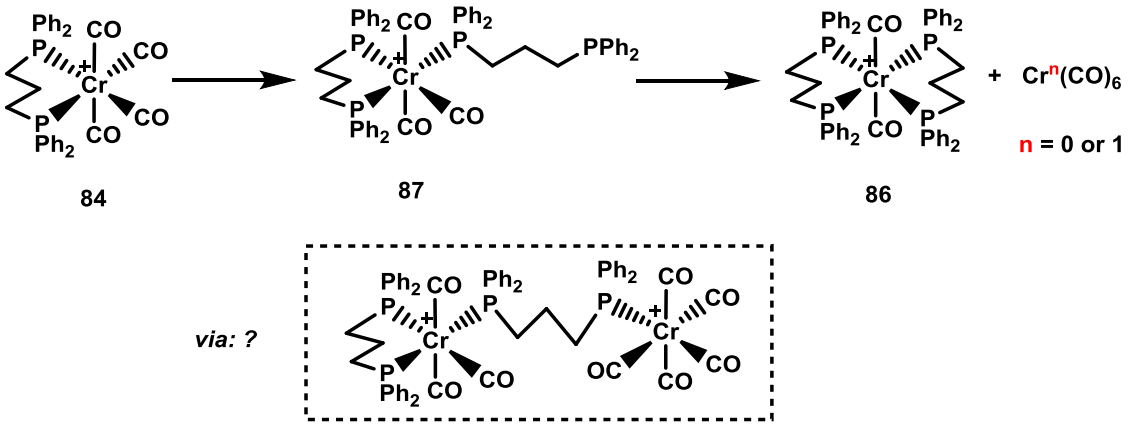

Figure 6.18: Proposed reactivity of **84** when exposed to UV irradiation, to yield **86** *via* **87.**

6.3 Conclusions and future work

The photochemistry resulting from exposure of the chromium (I) diphosphine complex, **84**, by UV irradiation has been investigated *via* EPR spectroscopy. A rearrangement of the mono-diphosphine complex was observed following 30 min of irradiation at room temperature, yielding the corresponding chromium(I) bis-diphosphine complex **86.** The resulting complex is defined by an axial EPR spectrum, with hyperfine coupling between the chromium(I) centre and two equivalent phosphorus nuclei visible in both the perpendicular and parallel components of the spectrum. Approximate quantification suggests that this transformation occurs efficiently and that **86** corresponds to all of the diphosphine ligand present in solution. Elucidation of the remaining chromium speciation was not possible, most likely due to formation of $[Cr(CO)_6]^+$, which is known to be EPR silent, or to a change in oxidation state of chromium to an EPR silent species, as has been observed previously for complexes of this type. The addition of toluene to irradiated solutions had no effect upon the resultant EPR spectrum, suggesting that free chromium(I) species are not present in solution. The bis-diphosphine complex **86** is stable under both ambient conditions and pressures of up to 2000 bar.

Exposure of **84** to UV irradiation at 77 K for 2 h resulted in the observation of the *mer*-species, **87**, in which the diphosphine ligand is coordinated in both an κ^1 and κ^2 fashion. In contrast to **84** and **86**, **87** is not thermally stable, and decomposes if left at ambient conditions, suggesting its formation is not reversible. The transformation of **84** into **87** does not occur quantitatively at low temperatures, and further extending the time of exposure results in a loss of chromium(I) species, suggesting that irradiation at more ambient temperatures is required to complete the transformation into **86.**

In order to comment more fully on the processes occurring following UV irradiation, the use of other spectroscopic techniques is necessary. The use of quantitative UV / visible spectroscopy should allow for comment on the fate of the remaining chromium in solution following irradiation, as was demonstrated in section 6.1. NMR spectroscopy (both ^{1}H and ^{31}P) should allow for observation of any non-paramagnetic chromium species being formed, and would be immediately instructive as to whether or not any photoreduction / oxidation processes are occurring, in addition to more accurate quantification of the intermediates and products. Further information on the nature of the remaining chromium speciation present following irradiation would be obtained using ^{13}C- labelled starting materials. ^{13}C possesses a nuclear spin of $I = ½$, and if it were present would allow for comment on the chromium-carbonyl species formed.

Repeating the irradiation experiments using the appropriate setup would allow for subsequent catalytic testing to be carried out. Whilst the ligand used in this work (dppp) has not been reported to date in an effective catalytic system, switching to a PNP type ligand would allow for a valid catalytic trial to be run. Hanton has previously performed such an experiment without passing comment on the precise nature of the resulting pre-catalyst used.[188] If performed in combination with EPR spectroscopy, a greater insight into the active species present within the reaction may be possible, potentially allowing for an activation method for chromium oligomerisation catalysts that does not use aluminium reagents.

Chapter 7 *Conclusions*

As stated in Chapter 1, there are many reasons for wanting to expand upon the current understanding of iron-catalysed cross-coupling reactions. However, further development of the field will continue to require the use of non-trivial techniques and the analysis of complex data sets, most likely as part of large-scale collaborative efforts. As technological advancements are made and more refined methods of data analysis become available, allowing for more intricate reactions to be designed, this cooperativity is likely to become more important in order to support the findings from a given technique in isolation. It is hoped that the work in this thesis is reflective of these needs; apparently simple systems have been shown to operate *via* complex reaction manifolds (particularly Chapters 2 and 5); and collaborative projects with researchers from different areas of chemistry have been carried out, allowing for access to expert knowledge regarding various spectroscopic techniques (particularly Chapters 5 and 6). No one researcher alone would have been able to elucidate all the insights that have come out of this work, let alone within the timeframe of a Ph.D.

It is somewhat ironic that the model reaction in Chapter 2 was chosen for its apparent simplicity: the coupling of two sterically and electronically similar benzyl reagents using iron(II) chloride, and analysis of the resulting distribution, was originally hoped to be an expedient method of gaining insights upon three simultaneously occurring reactions. However, the kinetic profiles resulting from the investigation demonstrate the complexity with which iron-catalysed reactions (or rather, any reaction employing a catalyst) can operate. This can be extended to results of Chapter 3, in which the dissociation of an NHC ligand from iron was demonstrated. Although this effect was found to be reversible, it serves to highlight that commonly-held assumptions regarding catalyst speciation should not be taken for granted.

This is perhaps no more apparent than in the results from Chapters 4 and 5. Here, one of the tenets of transition metal catalysed reactions, that the ligand is coordinated to the active catalyst centre during turnover, was found not to be occurring, with coordination of the ligand to the zinc coupling partner instead observed. Importantly, within these Chapters several analytical techniques, applied *in situ*, were used in combination, allowing for the surprising results obtained to be reported with clarity and confidence.

To summarise, iron-catalysed reactions provide a challenging, yet hugely rewarding, area of research, the continued development of which will surely lead to many interesting and useful chemical applications being discovered.

Chapter 8 *Experimental*

8.1 General experimental procedures

Unless otherwise stated, all manipulations were carried out under an atmosphere of dry nitrogen using standard Schlenk line techniques, or in an MBraun glovebox. Dry solvents were obtained from a Grubbs solvent purification system or dried over molecular sieves for at least 72 hours. Commercial reagents were used as received without further purification unless otherwise stated. Where necessary, accurate control of reactions was achieved with a Julabo F81-ME cryostat. Solution phase NMR spectra were collected on a Jeol ECS 400, Varian 400-MR or a Varian VNMR S500 spectrometer at ambient probe temperatures (25°C). Chemical shifts (δ) are reported in ppm and were referenced to residual proton impurities in the deuterated solvent. Multiplicities are indicated as: s (singlet), d (doublet), dd (doublet of doublet), t (triplet), dt (doublet of triplet), td (triplet of doublet), q (quartet), quint (quintet), h (heptet), m (multiplet), br s (broad singlet); coupling constants (*J*) are in Hertz (Hz). Elemental analysis (CHN) was performed at the University of Bristol or were obtained by Elemental Microanalysis Ltd, UK. UV-Vis spectra were acquired with an Ocean Optics TP300-series transmission probe or with a 1 cm quartz glass cuvette fitted with a J. Youngs tap coupled to a USB2000+UV-Vis spectrometer with a DT-MINI-2-GS light source. Spectra were collected using Ocean View software and processed using SpectraGryph 1.1. X-ray crystal structure determination was carried out on either a Bruker Microstar or APEX II diffractometer, by Dr. Antonis Messinis, Dr. David Elorriaga or Dr. Hazel Sparkes. Data collections were performed using a CCD area detector from a single crystal mounted on a glass fibre. Intensities were integrated from several series of exposures measuring 0.5° in ω or φ. Absorption corrections were based on equivalent reflections using SADABS. The structures were solved using SHELXS and refined against all Fo2 data with hydrogen atoms riding in calculated positions using SHELXL. Samples for electron microscopy analysis were carried out by Dr Sean Davis and imaged using a JEOL 2100 TEM operating at 200 kV. TEM images were acquired using a Gatan Orius SC1000 digital camera. Energy dispersive X-ray (EDX) analyses and elemental mapping were performed in HAADF-STEM mode with a spot size of 1.5 nm using an Oxford Instruments Aztec X-ray system. EPR experiments were carried out at Cardiff University. X-band EPR spectra (140 K) were recorded on a Bruker EMX spectrometer operating at 100 kHz field modulation, 10 mW microwave power and equipped with a high sensitivity Bruker cavity (ER 4119HS). Spectral simulations were performed by Dr. Emma Carter or Dr. Andrea Folli using the Sim32[176] and EasySpin[177] software packages. UV irradiation was conducted using a Labino Nova Torch UV LED light source, with an output power of 112 mW at the sample.

8.2 Experimental data for Chapter 2

8.2.1 Non-catalysed reaction

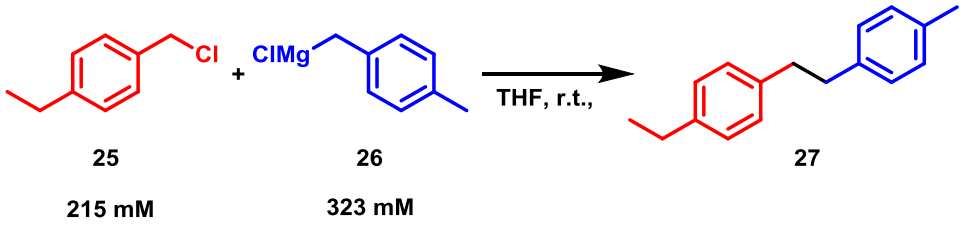

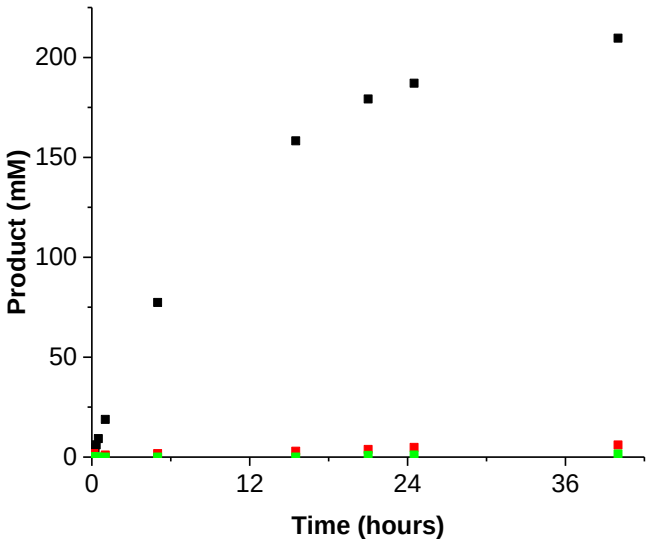

Reaction profile for the catalyst free reaction between **25** and **26**. ■ = **27**, ■ = **28**, ■ = **29**

8.2.2 Kinetic experiments

8.2.2.1 General procedure for the iron-catalysed Kumada cross-coupling reaction

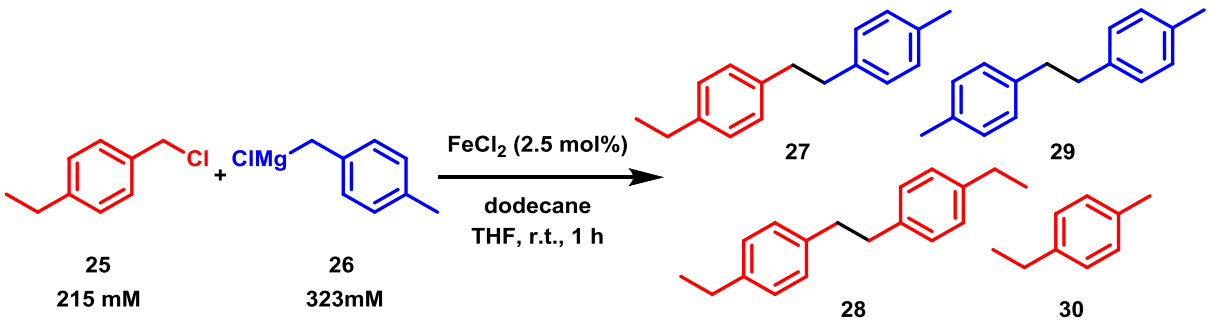

A 25 mL Schlenk tube was equipped with a magnetic stirrer and a fresh rubber septum, then evacuated under heating and backfilled with nitrogen three times. The tube was then placed in a water bath at 23°C, and charged successively with $FeCl_2$ (2.15 mL, 30 mM stock solution in THF, 0.0645 mmol, 5.37 mM) and enough THF so that the total volume following

all additions would be 12.00 mL (in this case = 5.00 mL). **26** (3.90 mL, 1.0 M solution in THF, 3.873 mmol, 323 mM) and dodecane (0.586 mL, 2.582 mmol) were then added, and the solution stirred for 5 minutes. The reaction was initiated by the addition of **25** (0.384 mL, 2.582 mmol, 215 mM) and sampled at accurately recorded intervals by drawing an aliquot (0.05 mL) from the reaction into a 1 mL syringe pre-loaded with NH_4Cl (approximately 0.5 mL). The amounts of **27**, **28**, **29** and **30** were quantified using GC-FID, with the amount of **29** adjusted to account for the amount present within the stock solution of **16.**

8.2.2.2 Determination of reaction orders

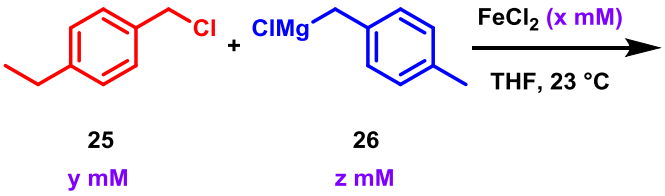

The reactions were performed according to the general procedure described above, however the concentration of each reagent was varied according to the table below, according to the desired reaction.

	Entry	*$FeCl_2$ (mM)*	***25*** *(mM)*	***26*** *(mM)*
Order in Fe	1	2.15	215	323
	2	5.37	215	323
	3	10.76	215	323
	4	16.14	215	323
	5	21.52	215	323
Order in electrophile	6	5.37	71	215
	7	5.37	107	215
	8	5.37	142	215
	9	5.37	215	215
	10	5.37	322	215
	11	5.37	537	215
	12	5.37	645	215
Order .	13	5.37	215	71
	14	5.37	215	107

	15	5.37	215	142
	16	5.37	215	215
	17	5.37	215	268
	18	5.37	215	322
	19	5.37	215	430
	20	5.37	215	537

8.2.2.3 Product inhibition experiment

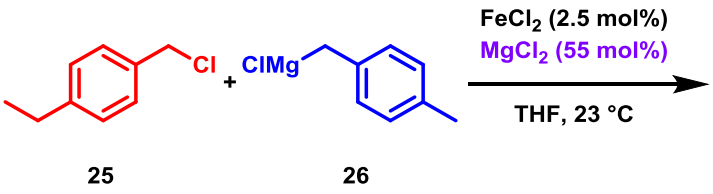

The reaction was performed according to the general procedure described above, with the exception of the addition of a solid portion of anhydrous $MgCl_2$ (162 mg, 1.704 mmol, 55 mol%) to the heated and backfilled Schlenk tube under an atmosphere of argon.

8.2.2.4 Hammett study

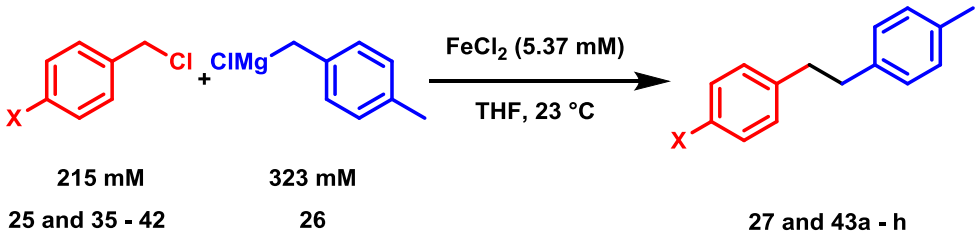

The reactions were performed according to the general procedure above, however the electrophile added was different in each case.

8.2.2.5 Determination of activation parameters

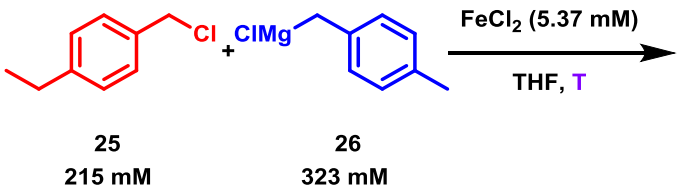

The reactions were performed according to the general procedure above, however in each case a jacketed Schlenk flask was used, which was attached to a Julabo cooling unit. Before the addition of any reagents, the flask was pre-cooled or warmed to the desired temperature and equilibrated for 5 minutes.

*8.2.3 Reactions involving **31***

*8.2.3.1 Preparation of $[Fe(4\text{-}MeBn)_3]^-$, **31***

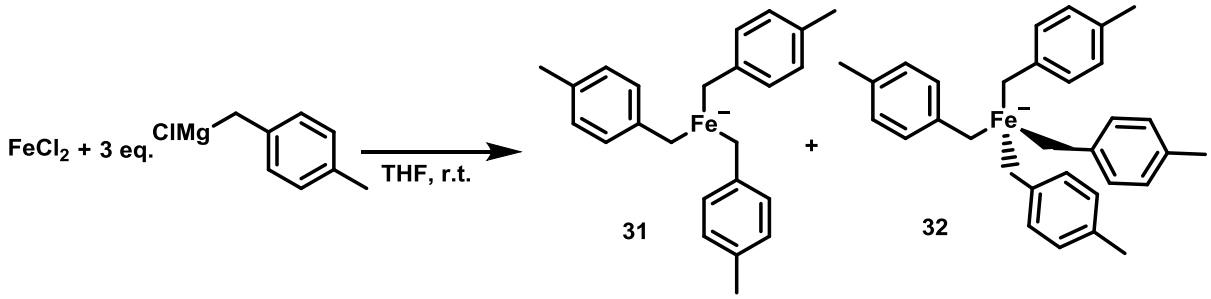

The following literature procedure was used.[58] To a vigorously stirred suspension of $FeCl_2$ (50 mg, 0.4 mmol) in THF (10 mL) was added 4-methylbenzylmagnesium chloride (1.2 mL, 1.0 M solution in THF, 1.2 mmol). After stirring for between 5 and 10 minutes, a deep red solution of **31** was formed, as confirmed *via* ^{1}H NMR spectroscopy. ^{1}H NMR (500 MHz, 25°C, THF) δ 943.92 (s, 6H, benzylic), 80.87 (s, 9H, methyl), 31.47 (s, 6H, meta), -49.38 (s, 6H, ortho). Reducing the volume of the solution to approximately 5 mL and layering with Et_2O, followed by storage at -30 °C for 48 h yielded red crystals suitable for an X-ray crystallographic study, the results of which confirmed the structure as **[31]**[$MgCl(THF)_5$]. Leaving the layered solution for a period of up to one week at -30 °C resulted in second set of crystals growing out of solution, analysis of which revealed the structure to be the four-coordinate iron(III) ferrate complex $[Fe(4\text{-}MeBn)_4]^-$, [**32**][$MgCl(THF)_5$].

*8.2.3.2 Reaction of **31** with DCE*

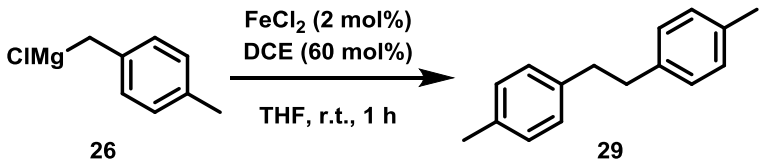

Under an atmosphere of argon, a 7 mL screw top vial was charged with $FeCl_2$ (8.2 mg, 0.06455 mmol), THF (5 mL), dodecane (0.366 mL, 1.93 mmol) and 4-methylbenzylmagnesium chloride, **26**, (3.2 mL, 3.22 mmol, 1.0 M solution in THF). The resultant deep red solution was stirred for 5 minutes, to give **31.** 1,2-dichloroethane (0.152 mL,

1.93 mmol) was then added in one portion, and the resultant solution stirred vigorously. After 1 h, the solution was quenched by the addition of a saturated solution of NH_4Cl (5 mL) under an atmosphere of air, followed by the addition of DCM (5 mL). An aliquot was taken for analysis *via* GC-FID, allowing for quantification of the amount of **29** formed.

*8.2.3.3 Stoichiometric reactions of **31** with **25***

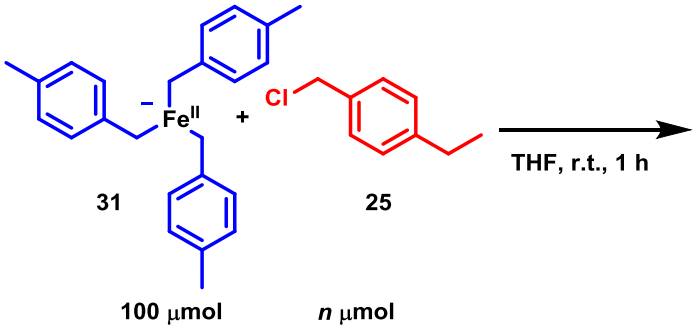

Under an atmosphere of argon, eight separate 7 mL screw top vials were charged with a magnetic stirrer bar in addition to $FeCl_2$ (12.6 mg, 0.1 mmol), THF (3 mL), dodecane (0.113 mL, 0.5 mmol) and 4-methylbenzylmagnesium chloride, **26**, yielding a deep-red solution of **31** in each vial. Each solution was stirred for 5 minutes at room temperature. Subsequently, each vial was loaded with an amount of 4-ethlybenzyl chloride, **25**, according to the table below. Following 1 hour of stirring at room temperature, each vial was quenched *via* the addition of NH_4Cl, extracted with DCM and analysed by GC-FID.

Entry	*n*	*V (μL)*
1	0	0
2	50	7.4
3	100	14.8
4	200	29.7
5	300	44.6
6	400	59.5
7	500	74.3
8	1000	148.7

8.2.4 Preparation of bi-benzyl derivatives

8.2.4.1 General procedure

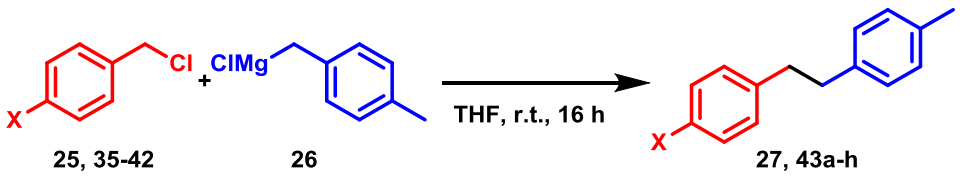

25, 35-42 26 27, 43a-h

A 25 mL Schlenk tube was equipped with a magnetic stirrer and a fresh rubber septum, then evacuated under heating and backfilled with nitrogen three times. The tube was then charged successively with the requisite electrophile (0.5 mmol), THF (10 mL) and 4-methylbenzylmagnesium chloride (0.5 mmol). The reaction was then stirred for 16 h at room temperature, before quenching with NH_4Cl (5 mL) and extraction with DCM (15 mL). After separation, the organic layer was dried ($MgSO_4$) and filtered, before removal of the solvent under reduced pressure, yielding the desired bi-benzyl products **43a-h** as off-white solids. Where necessary, the product was purified by passing through a silica plug (hexanes). Recrystallisation was carried out by storing a concentrated hexanes solution of the product at -30 °C overnight.

1-(4-Methylphenyl)2-(4-ethylphenyl)ethane, ***27***

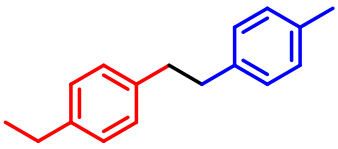

Crystalline white solid. Yield = 96 mg, 86%: **^{1}H NMR** (400 MHz, $CDCl_3$) δ 7.13 (s, 4H), 7.11 (s, 4H), 2.88 (s, 4H), 2.64 (q, *J* = 7.6 Hz, 4H), 2.33 (s, 3H), 1.24 (t, *J* = 7.6 Hz, 3H); **^{13}C NMR** (101 MHz, $CDCl_3$) δ 141.9, 139.3, 139.1, 135.4, 129.2, 128.5, 128.4, 128.0, 37.8, 37.7, 28.6, 21.2, 15.8. **GCMS (EI)** $[M]^+$ 224.1

1,2-Bis(4-ethylphenyl)ethane, ***28***

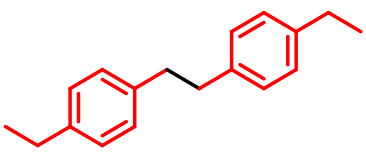

Prepared according to the general procedure described above, using however 4-ethylbenzylmagnesium chloride (1.0 M in THF) as the Grignard reagent. Crystalline white

solid. Yield = 70 mg, 59%: **^{1}H NMR** (400 MHz, $CDCl_3$) δ 7.14 (s, 8H), 2.89 (s, 4H), 2.64 (q, *J* = 7.5 Hz, 4H), 1.25 (t, *J* = 7.7 Hz, 6H); **^{13}C NMR** (101 MHz, $CDCl_3$) δ 141.9, 139.4, 128.5, 128.0, 37.8, 28.6, 15.8. **GCMS (EI)** $[M]^+$ 238.2

1-Methyl-4-phenethylbenzene, ***43a***

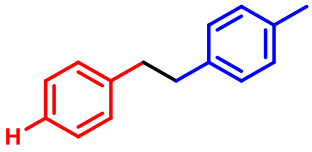

White solid. Yield = 63 mg, 64%: **^{1}H NMR** (400 MHz, $CDCl_3$) δ 7.42 – 7.21 (m, 5H), 7.16 (s, 4H), 2.97 (s, 4H), 2.40 (s, 3H); **^{13}C NMR** (101 MHz, $CDCl_3$) δ 142.1, 138.9, 135.5, 129.2, 128.6, 128.5, 126.0, 38.2, 37.6, 21.2. **GCMS (EI)** $[M]^+$ 196.1. The spectroscopic properties of this compound were consistent with literature data.[207]

1-(4-Methylphenyl)2-(4-fluorophenyl)ethane, ***43b***

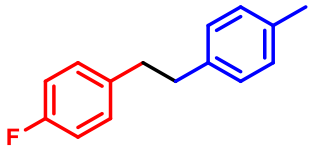

White solid. Yield = 55 mg, 51%: **^{1}H NMR** (400 MHz, $CDCl_3$) δ 7.16 – 7.08 (m, 4H), 7.06 (d, *J* = 8.1 Hz, 2H), 6.96 (t, *J* = 8.7 Hz, 2H), 2.87 (s, 4H), 2.34 (s, 3H); **^{13}C NMR** (101 MHz, $CDCl_3$) δ 161.4 (d, *J* = 243.3 Hz), 138.5, 137.6 (d, *J* = 3.3 Hz), 135.6, 129.9 (d, *J* = 7.8 Hz), 129.2, 128.5, 115.1 (d, *J* = 20.9 Hz), 37.7, 37.3, 21.2. **^{19}F NMR** (377 MHz, $CDCl_3$) δ -117.72. **GCMS (EI)** $[M]^+$ 214.1. The spectroscopic properties of this compound were consistent with literature data.[207]

1-Isopropyl-4-(4-methylphenethyl)benzene, ***43c***

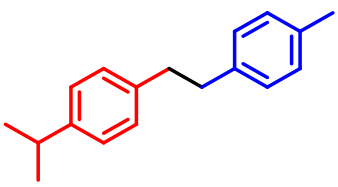

White solid. Yield = 55 mg, 46%: **^{1}H NMR** (400 MHz, $CDCl_3$) δ 7.22 – 7.14 (m, 8H), 3.06 – 2.82 (m, 5H), 2.39 (s, 3H), 1.31 (d, J = 6.9 Hz, 6H).; **^{13}C NMR** (101 MHz, $CDCl_3$) δ 146.6, 139.5, 139.1, 135.4, 129.2, 128.4, 126.5, 37.8, 37.7, 33.9, 24.2, 21.2. **GCMS (EI)** $[M]^+$ 238.2.

1-(4-Methylphenyl)2-(4-trifluoromethylphenyl)ethane, ***43d***

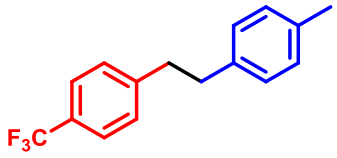

White solid. Yield = 52 mg, 39%: **^{1}H NMR** (400 MHz, $CDCl_3$) δ 7.53 (d, *J* = 8.0 Hz, 2H), 7.28 (d, *J* = 7.8 Hz, 2H), 7.09 (d, *J* = 8.0 Hz, 2H), 7.06 (d, *J* = 8.1 Hz, 2H), 2.99-2.95 (m, 2H), 2.92 – 2.85 (m, 2H), 2.33 (s, 3H); **^{13}C NMR** (101 MHz, $CDCl_3$) δ 146.0, 138.1, 135.8, 129.3, 128.9, 128.4, 125.4 (q, *J* = 3.8 Hz), 37.9, 37.2, 21.2; **^{19}F NMR** (377 MHz, $CDCl_3$) δ -62.29. **GCMS (EI)** $[M]^+$ 264.1. The spectroscopic properties of this compound were consistent with literature data.[207]

Methyl(4-(4-methylphenethyl)phenyl)sulfane, ***43e***

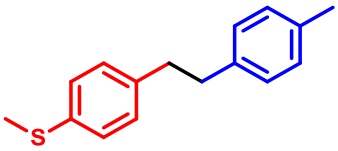

White solid. Yield = 50 mg, 41%: **^{1}H NMR** (400 MHz, $CDCl_3$) δ 7.19 (d, *J* = 8.3 Hz, 2H), 7.13 – 7.04 (m, 6H), 2.86 (s, 4H), 2.47 (s, 3H), 2.32 (s, 3H).; ^{13}C NMR (101 MHz, $CDCl_3$) δ 139.2, 138.7, 135.5, 135.5, 129.2, 128.5, 127.3, 37.6, 37.6, 21.2, 16.5. **GCMS (EI)** $[M]^+$ 242.1. The spectroscopic properties of this compound were consistent with literature data.[208]

1-(4-Methylphenyl)2-(4-methoxyphenyl)ethane, ***43f***

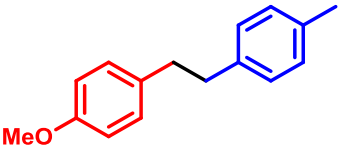

White solid. Yield = 52%: **^{1}H NMR** (400 MHz, $CDCl_3$) δ 7.18 – 7.01 (m, 6H), 6.84 (d, *J* = 8.6 Hz, 2H), 3.80 (s, 3H), 2.86 (s, 4H), 2.34 (s, 3H).; **^{13}C NMR** δ 158.0, 138.9, 135.4, 134.2, 129.5, 129.1, 128.5, 113.9, 55.4, 37.0, 37.3, 21.2. (101 MHz, $CDCl_3$ **GCMS (EI)** $[M]^+$ 226.1. The spectroscopic properties of this compound were consistent with literature data.[207]

*1-(4-Methylphenyl)2-(4-*tert*-butylphenyl)ethane*, ***43g***

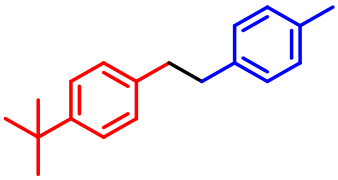

White solid. Yield = 97 mg, 86%: **^{1}H NMR** (400 MHz, $CDCl_3$) δ 7.33 (d, *J* = 8.3 Hz, 4H), 7.17 (d, *J* = 8.3 Hz, 4H), 2.89 (s, 4H), 2.34 (s,3H), 1.33 (s, 9H); **^{13}C NMR** (101 MHz, $CDCl_3$) δ 148.8, 139.1, 139.1, 135.5, 129.2, 128.4, 128.2, 125.4, 37.7, 37.6, 34.5, 31.6, 21.2. **GCMS (EI)** $[M]^+$ 252.2. The spectroscopic properties of this compound were consistent with literature data.[207]

1-(4-Methylphenyl)2-(4-chlorophenyl)ethane, ***43h***

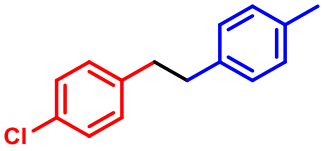

White solid. Yield = 84 mg, 73%: **^{1}H NMR** (400 MHz, $CDCl_3$) δ 7.24 (d, *J* = 8.4 Hz, 2H), 7.10 (d, *J* = 8.1 Hz), 7.06 (d, *J* = 8,1 Hz, 2H) 2.88-2.85 (m, 4H), 2.33 (s, 3H); **^{13}C NMR** (101 MHz, $CDCl_3$) δ 140.2, 138.4, 135.5, 131.7, 130.0, 129.2, 128.5, 128.4, 37.5, 21.2. **GCMS (EI)** $[M]^+$ 230.1. The spectroscopic properties of this compound were consistent with literature data.[207]

8.3 Experimental data for Chapter 3

8.3.1 Synthesis of iron pre-catalysts

8.3.1.1 $FeCl_2(P(C_6H_4OMe)_3)_2$, ***48***

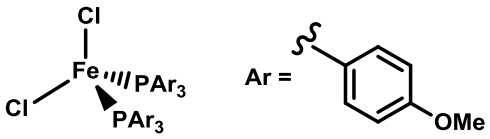

Prepared according to a modified literature procedure.[209] A Schlenk tube was loaded with $FeCl_2$ (125 mg, 0.986 mmol) and tris(4-methoxyphenyl)phosphine (695 mg, 1.972 mmol). The Schlenk was then fitted with a reflux condenser, and benzene (40 mL) was added. The resulting suspension was heated to reflux under nitrogen and stirred for 16 h. Using a cannula, the mixture was then filtered whilst hot, and the solution left to cool to room temperature slowly. After 24 h, white crystals had formed which were separated *via* cannula filtration, washed with cold benzene (3 x 2 mL) and dried to afford the title compound (254 mg, 31%).

8.3.1.2 $FeCl_2(dpbz)_2$, ***49***

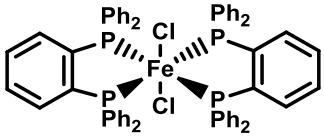

Prepared according to modified literature procedure.[103] A Schlenk tube was loaded with $FeCl_2$ (278.9 mg, 2.20 mmol), dpbz (1.964 g, 4.40 mmol) and THF (25 mL). The mixture was heated at reflux temperature until a solution was obtained, following which the solvent was removed in vacuo. The yellow residue was dissolved in DCM (20 mL), filtered and the solution layered with hexane (20 mL) to give bright yellow crystals of the title compound (1.974 g, 88%).

8.3.1.3 $FeCl_2(dpbz)_2$, ***50·THF***[127]

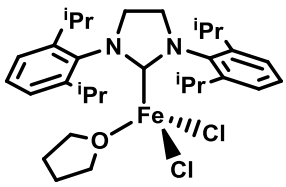

A Schlenk tube was loaded with $FeCl_2(THF)_{1.5}$ (50.0 mg, 0.21 mmol) and SIPr (58.4 mg, 0.15 mmol). THF (30 mL) was added at -78°C and the resulting solution allowed to warm to room temperature slowly over 16 h with stirring. After removal of all volatiles, the beige solid was extracted into Et_2O (10 mL) and filtered again *via* cannula. The solvent was then removed

and the solid re-dissolved in THF (5 mL), before layering with pentane (10 mL). After several days at room temperature, colourless crystals of the title compound were formed (46 mg, 52%). In solution, signals corresponding to $[Fe(SIPr)Cl(\mu\text{-}Cl)]_2$ were observed *via* ^{1}H NMR spectroscopy **^{1}H NMR** (400 MHz, THF) δ 5.80 (12H) 0.80 (4H), -1.33 (4H), -1.80 (12H), -3.55 (4H).

*8.3.1.3 Fe(SIPr)(4-MeBn)$_2$, **51***[127]

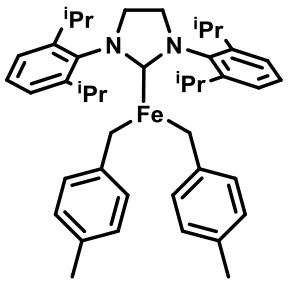

Prepared according to a modified literature procedure.[127] A Schlenk tube was loaded with $FeCl_2(THF)_{1.5}$ (100 mg, 0.42 mmol), $Mg(4\text{-}MeBn)_2(THF)_2$ (194.8 mg, 0.55 mmol) and SIPr (166.8 mg, 0.42 mmol). The flask was then cooled to -78°C and THF (20 mL) and dioxane (2 mL) were added. The resulting solution was allowed to warm to room temperature slowly over 16 h with stirring. The solution was then filtered *via* cannula, and the solvent removed, followed by extraction into Et_2O and removal of all volatiles. The resultant residue was then triturated with pentane (5 x 20 mL) and evaporated to dryness, leaving the title compound as a dark orange solid (182 mg, 65%). Crystals were grown from layering a toluene solution with hexanes. Although a definitive characterisation was not possible, the *para*-methyl signal was unambiguously assigned as the singlet at 75.3 ppm upon comparison with the ^{1}H NMR spectrum arising from the previously reported complex $Fe(SIPr)(Bn)_2$.[127] **^{1}H NMR** (400 MHz, C_6D_6) δ 75.3 (s), 22.2 (s), 20.0 (s), 18.5 (s), -5.2 (s), -16.0 (s), -23.6 (s), -52.4 (s), -82.4 (s).

8.3.2 NMR experiments

*8.3.2.1 Reaction of **50·THF** with **26***

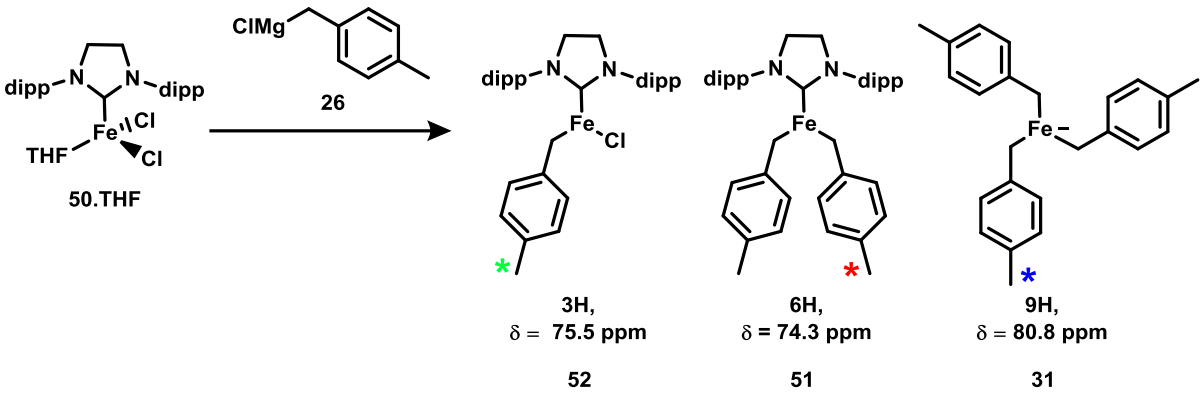

Under an atmosphere of argon, seven screw top vials were each charged with **50·THF** (100 µL, 8.46 µmol, 84.6 µM solution in THF) and THF (enough so that the total volume of each vial after all additions would be 3.00 mL). To each vial was then added the requisite amount of **26** (1.00 M solution in THF). A 0.8 mL aliquot was then taken from each vial and added to a J. Youngs NMR tube, followed by analysis using ^{1}H NMR spectroscopy (no more than 5 minutes passed between addition of **26** and recording of the NMR spectrum for any of the additions). The amounts added in each case are displayed in the table below. The integral corresponding to the *para*-methyl protons of each of the products **52** (3 H), **51** (6 H) and **31** (9 H) was then measured, from which the ratio of each was determined.

Entry	*Grignard: Fe*	***50·THF*** *µL*	***26*** *µL*	*THF mL*
a	0.5	100	4.2	2.895
b	1	100	8.5	2.891
c	2	100	16.9	2.883
d	5	100	42.3	2.857
e	10	100	84.7	2.815
f	15	100	127.0	2.772
g	30	100	254.0	2.645

*8.3.2.2 Reaction of $FeCl_2$ with **26** and SIPr*

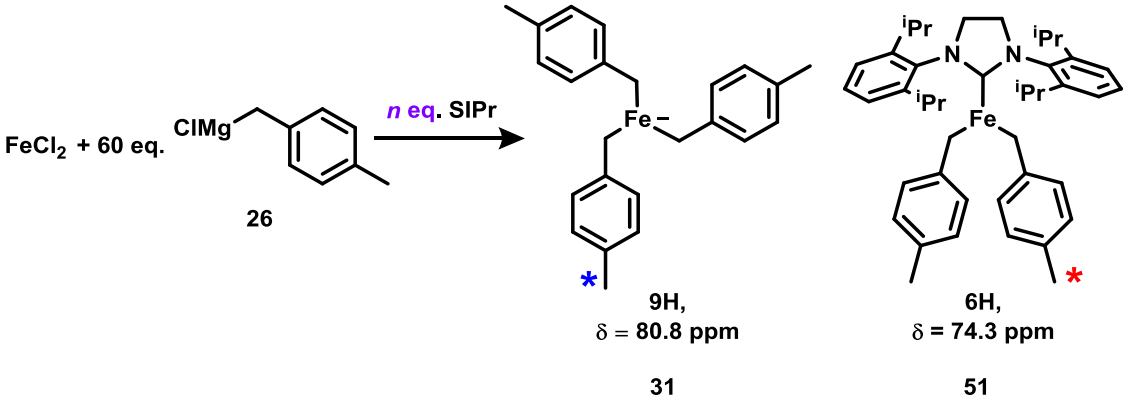

Under an atmosphere of argon, six screw top vials were charged with $FeCl_2$ (5.0 mg, 39.6 µmol) and THF (1.00 mL) and **26** (2.37 mL, 2.37 mmol, 1.0 M solution in THF). To each vial was then added the requisite amount of SIPr, according to the table below. A 0.8 mL aliquot was then taken from each vial and added to a J. Youngs NMR tube, followed by analysis using ^{1}H NMR spectroscopy (no more than 5 minutes passed between addition of SIPr and recording of the NMR spectrum for any of the additions). The amounts added in each case are displayed in the table below. The integral corresponding to the *para*-methyl protons of each of the products **51** (6 H) and **31** (9 H) was then measured, from which the ratio of each was determined.

Entry	*Fe: Grignard: SIPr*	*SIPr µmol*
a	1: 60: 1	39.6
b	1: 60: 2	79.2
c	1: 60: 3	118.9
d	1: 60: 4	158.5
e	1: 60: 5	198.2
f	1: 60: 10	396.4

8.3.3 Kinetic experiments

The reactions were performed according to the general procedure described in 8.2.2, however after the addition of THF, the requisite amount of SIPr (0.396 mM solution in THF) was added, according to the table below, and the resultant solution stirred for 5 minutes before the addition of **26.**

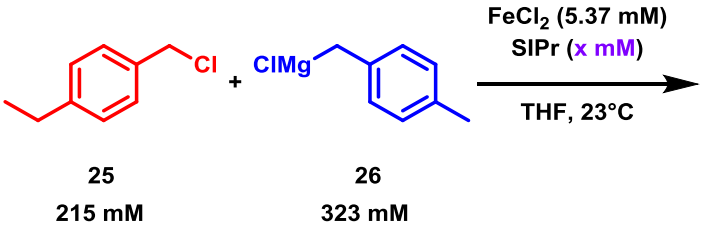

	Entry	$FeCl_2$ (mM)	***25*** (mM)	***26*** (mM)	*SIPr* (mM)
Order in SIPr	1	5.37	215	323	5.37
	2	5.37	215	323	10.74
	3	5.37	215	323	16.11
	4	5.37	215	323	21.48
	5	5.37	215	323	26.85
	6	5.37	215	323	53.7

8.4 Experimental data for Chapter 4

8.4.1 Reactions in the absence of diphosphine ligand

8.4.1.1 Preparation of pure dimesitlyzinc, ***64***

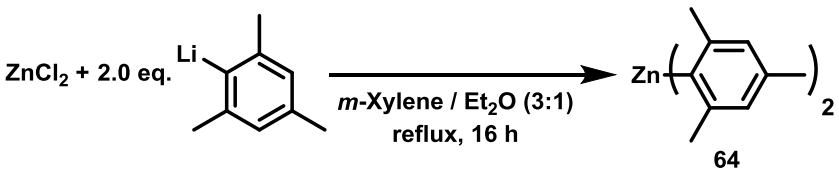

Prepared according to literature procedure.[127] A Schlenk tube was loaded with LiMes (1.000 g, 7.92 mmol), $ZnCl_2$ (540.2 mg, 3.96 mmol) *m*-xylene (15 mL) and Et_2O (4 mL). A reflux condenser was fitted, and the mixture heated to reflux temperature with vigorous stirring for 16 h, during which time a grey precipitate formed. The mixture was then filtered whilst hot and left to cool to room temperature. The title product crystallised as colourless needles (795 mg, 66%). **^{1}H NMR** (400 MHz, THF-$_{d8}$) δ = 6.71 (s, 4H), 2.45 (s, 12H), 2.20 (s, 6H). **^{13}C NMR** (101 MHz, THF-$_{d8}$) δ = 151.95, 145.37, 136.67, 126.48, 27.33, 21.55.

8.4.1 Reactions in the absence of diphosphine ligand

8.4.1.3 Reaction of $FeBr_2$ with pure ***64***

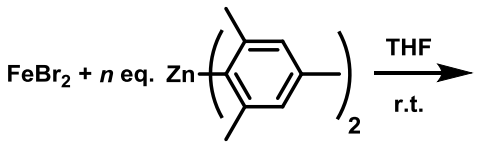

64

Under an atmosphere of argon, seven screw top vials were loaded with $FeBr_2$ (5.0 mg, 23.1 µmol) and the requisite mass of $ZnMes_2$, according to the table below. THF (2.00 mL) was then added, and the vials shaken vigorously. A 0.8 mL aliquot was then taken from each vial and added to a J. Youngs NMR tube, followed by analysis using ^1H NMR spectroscopy.

Entry	*Fe: Zn*	*$ZnMes_2$*	
		µmol	*mg*
a	1: 1	23.1	7.0
b	1: 2	46.3	14.1
c	1: 3	69.6	21.1
d	1: 4	92.8	28.2
e	1: 5	116	35.2
f	1: 6	139	42.3
g	1: 10	231	70.4

*8.4.1.4 Reaction of $FeBr_2$ with **64** / 2 $MgBr_2$*

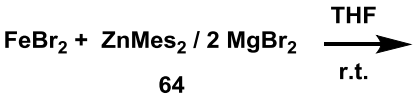

Under an atmosphere of argon, seven screw top vials were charged with $FeBr_2$ (3.2 mg, 15 µmol) and THF (enough so that the total the requisite volume following all additions was 2.00 mL). To each vial was then added the requisite volume of $ZnMes_2$ /2 $MgBr_2$ (91 mM solution in THF), according to the table below. A 0.8 mL aliquot was then taken from each vial and added to a J. Youngs NMR tube, followed by analysis using ^1H NMR spectroscopy.

Entry	*Fe: Zn*	*$ZnMes_2$ / 2 $MgBr_2$*	
		µmol	*µL*
a	1: 1	15	165

b	1: 2	30	330
c	1: 3	45	495
d	1: 4	60	659
e[a]	1: 5	70	769
f[b]	1: 10	70	769
g[c]	1: 25	70	755

a = 3.0 mg $FeBr_2$ added; b = 1.51 mg $FeBr_2$ added; c = 0.6 mg $FeBr_2$ added.

8.4.1.4 Reaction of Fe_2Mes_4 with $[NBu_4][Cl]$

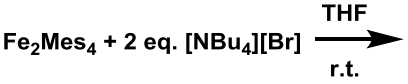

Under an atmosphere of argon, five screw top vials were charged with Fe_2Mes_4 (100 µL, 17.0 µmol of Fe, 85 mM stock solution in THF) and THF (2.00 mL). To each vial was then added the requisite mass of $[NBu_4][Cl]$, according to the table below. A 0.8 mL aliquot was then taken from each vial and filtered through a Millipore filter directly into to a J. Youngs NMR tube, followed by analysis using ^1H NMR spectroscopy.

Entry	*Fe: N*	*$[NBu_4][Cl]$*	
		µmol	*mg*
a	1: 1	17.0	5.5
b	1: 2	34.0	10.9
c	1: 3	67.9	21.9
d	1: 4	85.0	27.4
e	1: 5	170	54.7

*8.4.1.5 Reaction of **62** with $ZnBr_2$*

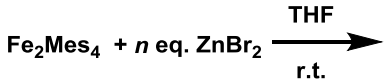

Under an atmosphere of argon, ten screw top vials were loaded with Fe_2Mes_4 (100 µL, 17.0 µmol of Fe, 85 mM stock solution in THF-d_8), dodecane (17.0 µL, 500 mM stock solution in THF-d_8) and THF-d_8 (enough so that the total volume following all additions was equal to 1.00 mL). Each vial was then charged with the requisite volume of $ZnBr_2$ according to the table below (500 mM stock solution in THF-d_8). A 0.8 mL aliquot was then taken from each vial and added to a J. Youngs NMR tube, followed by analysis using ^{1}H NMR spectroscopy.

Entry	*Fe: Zn*	*$ZnBr_2$*	
		µmol	*µL*
a	0.125	2.1	4.2
b	0.250	4.2	8.5
c	0.375	6.3	12.7
d	0.500	8..4	17.0
e	0.625	10.6	21.2
f	1.25	21.2	42.5
g	2.50	42.5	85.0
h	5.00	84.9	170
i	10.00	212	425
j	25.00	424	850

8.4.2 Synthesis of iron diphosphine complexes

8.4.2.1 Synthesis of $FeBr_2$(dpbz), ***68***

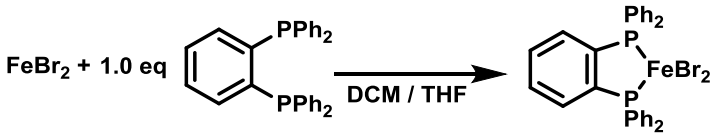

Prepared according to the literature procedure.[127] A Schlenk tube was loaded with $FeBr_2$ (465 mg, 2.20 mmol), dpbz (982 mg, 2.20 mmol), DCM (20 mL) and 10 drops of THF. The mixture was stirred and sonicated until an orange solution was obtained. The solution was then filtered, and the filtrate layered with hexane (30 mL) resulting in the formation of grey crystals of [$FeBr_2$(dpbz)]·CH_2Cl_2. Following filtration and drying, the solid was re-dissolved in THF and layered with hexane, from which crystals of the title compound were formed after 24 h at

room temperature. **^{1}H NMR** (500 MHz, THF-d8) δ = 16.3 (s), 15.7 (s), 4.1 (s), -4.0 (s), -5.7 (s).

*8.4.2.2 Synthesis of $FeBr_2(dpbz)_2$, **69***

Prepared using a modification of a previously reported procedure.[134] A Schlenk tube was loaded with $FeBr_2$ (465 mg, 2.20mmol) followed by addition of THF (5 mL) and dpbz (1.964 g, 4.40 mmol). The mixture was heated at reflux temperature until a solution was obtained and then the solvent was removed *in vacuo*. The yellow residue was dissolved in DCM (20 mL), filtered and the solution layered with hexane (20 mL) to give bright yellow crystals of the **69** suitable for an X-ray crystallographic analysis. The yellow crystals were separated and dried under reduced pressure to form a yellow powder of **69** (1.60 g) while the filtrate was dried, re-dissolved in DCM (10 mL) and layered with hexane (20 mL) to give a second crop of the material which was combined with the first crop (2.14 g, 88%). **^{1}H NMR** (500 MHz, THF-d_8) δ = 15.0 (s), 6.7 (s), -4.3 (s). **^{31}P NMR** (202 MHz, THF-d_8) δ = -13.4. (Note: The observed NMR resonances correspond to **68** in equilibrium with dpbz rather than **69** in solution).

*8.4.2.2 Synthesis of $FeMes_2(dpbz)$, **70***

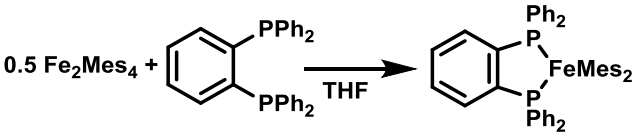

Prepared according to the literature procedure.[127] In an argon filled glovebox, a vial was loaded with Fe_2Mes_4 (5.0 mg, 8.49 µmol, 17.0 µmol of Fe), dpbz (7.58 mg) and THF (2 mL). The resulting dark red solution was filtered through a Millipore filter and layered with hexane (5 mL) resulting in dark red crystals of the title compound after 24 h at room temperature suitable for an X-ray crystallographic study(4.7 mg, 37%). **^{1}H NMR** (500 MHz) δ 86.9 (s), 75.7 (s), 65.7 (s), 12.7 (s), 11.6 (s).

*8.4.2.2 Synthesis of FeBr(Mes)(dpbz), **71***

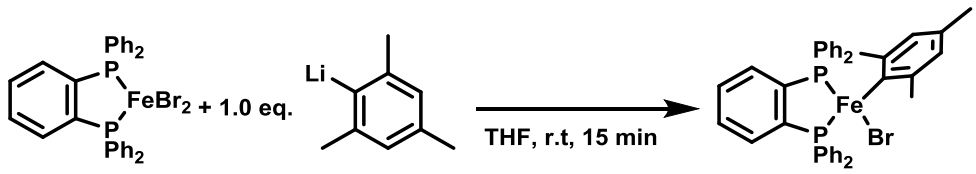

Prepared according to the literature procedure.[127] In an argon filled glovebox, a vial was loaded with [$FeBr_2$(dpbz)], **68**, (5.0 mg, 7.6 µmol), THF (2 mL) and mesitylithium (7.8 µL, 7.6 µmol, 0.97 M solution in THF). The resulting orange solution was filtered through a Millipore filter and layered with hexane (5 mL) resulting in formation of yellow crystals of the title compound (2.3 mg, 43%).**^{1}H NMR** (500 MHz) δ 120.6 (s), 100.9 (s), 86.0 (s), 66.1 (s), 34.7 (s), 27.7 (s), 12.1 (s), 11.7 (s), 9.4 (s), -4.0 (s), -9.2 (s), -11.0 (s).

8.4.3 Synthesis of zinc diphosphine complexes

*8.4.3.1 Synthesis of $ZnBr_2$(dpbz), **72***

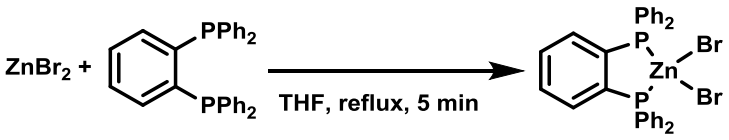

Prepared according to the literature procedure.[127] A Schlenk tube was loaded with $ZnBr_2$ (250 mg, 1.11 mmol), dpbz (495.6 mg, 1.11 mmol) and THF (16 mL) and the mixture was heated with a heat gun until all components dissolved. Upon cooling, colourless crystals were formed which were isolated by decanting the supernatant and washed with THF (3 mL). The crystals were ground, and the resultant powder was left under vacuum for 12 h to give **72.**THF (671 mg, 81%) as a white solid. Crystals of **72** suitable for an X-ray crystallographic analysis were grown by allowing a boiled solution of the compound in THF to slowly cool to room temperature. **^{1}H NMR** (400 MHz, THF-d_8) δ = 7.57-7.49 (m, 2H), 7.48-7.16 (m, 22H). **^{13}C NMR** (101 MHz, THF-d_8) δ = 135.7 (t, *J* =3.7), 135.1 (t, *J* =7.9), 131.9 (s), 131.2 (s), 129.6 (t, *J* =4.7). **^{31}P NMR** (122 MHz, THF-d_8) δ = -22.2 (s). **HRMS** (ESI/Q-TOF) m/z: [M+Na]+ Calcd. for $C_{30}H_{24}Br_2NaP_2Zn$ 690.8909; Found 690.8904.

*8.4.3.2 Synthesis of ZnBr(Mes)(dpbz) / $MgBr_2$, **74***

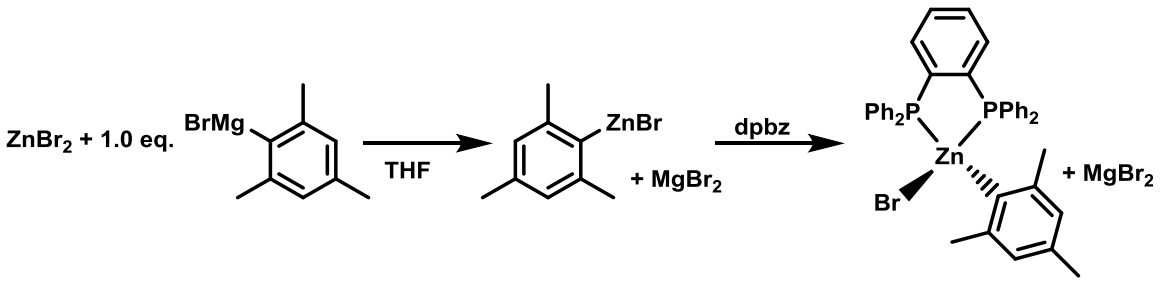

Prepared according to the literature procedure.[127] A Schlenk tube was loaded with $ZnBr_2$ (250 mg, 1.11 mmol), THF (16 mL) and mesitylmagnesium bromide (1.11 mL, 1.11 mmol, 1 M solution in THF). The resulting turbid mixture was stirred vigorously, and dpbz (495.6 mg, 1.11 mmol) was added in one portion, resulting in a colourless solution of **74**. **^{1}H NMR** (500 MHz, THF-d8) δ 7.48 - 6.94 (m, 23H), 6.70 (s, 1H), 6.64 (s, 2H), 2.33 (s, 6H), 2.14 (s, 3H); **^{13}C NMR** (126 MHz, THF-d8) δ 135.26, 135.00, 129.42, 126.52, 26.52, 21.52. **^{31}P NMR** (122 MHz, THF-d8) δ -17.3 (br s, FWHM = 903 Hz).

*8.4.4 Reaction of $FeBr_2$(dpbz) with **68** in the presence of a magnesium salt and dpbz*

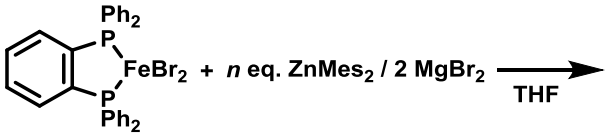

Under an atmosphere of argon, seven screw top vials were charged with $FeBr_2$(dpbz), **68**, (9.9 mg, 15 µmol) and THF (enough so that the total volume following all additions was 2.00 mL). To each vial was then added the requisite volume of $ZnMes_2$ /2 $MgBr_2$ (91 mM solution in THF), according to the table below. A 0.8 mL aliquot was then taken from each vial and added to a J. Youngs NMR tube, followed by analysis using ^{1}H NMR and ^{31}P NMR spectroscopy.

Entry	*Fe: Zn*	*$ZnMes_2$ / 2 $MgBr_2$*	
		µmol	*µL*
a	1: 1	15	165
b	1: 2	30	330
c	1: 3	45	495
d	1: 4	60	659
e[a]	1: 5	70	769

f[b]	1: 10	70	769
g[c]	1: 25	70	755

a = 9.3 mg $FeBr_2$(dpbz) added; b = 4.6 mg $FeBr_2$(dpbz) added; c = 1.9 mg $FeBr_2$(dpbz) added.

8.5 Experimental data for Chapter 5

8.5.1 In situ NMR detection of zinc-diphosphine species: ^{1}H NMR spectroscopy

*8.5.1.1 Calculation of the ^{1}H NMR T_1 spin-lattice relaxation for BnBr, **55**, and Bn(4-tolyl), **56***

In order to determine the ^{1}H T_1 relaxation of BnBr **55** and Bn(4-tolyl) **56** under reaction conditions, an NMR tube was loaded with $FeBr_2$ (40.0 µL, 20.0 mM stock solution in THF-d_8, 0.80 µmol), dodecane (80.0 µL, 500 mM stock solution in THF-d_8, 40.0 µmol), $ZnBr_2$ (400 µL, 200 mM stock solution in THF-d_8, 80.0 µmol), dpbz (20.0 µL, 80.0 mM stock solution in THF-d_8, 1.60 µmol), benzyl bromide (32.0 µL, 2500 mM stock solution in THF-d_8, 80.0 µmol), Bn(4-tolyl) (14.7 µL, neat, 80.0 µmol) and THF-d_8 (213 µL) to give a solution with a total volume of 800 µL. A T_1 experiment was then performed. The calculated T_1 spin-lattice relaxation delays for **55** and **56** were found to be 7.98 ± 0.1063 s and 4.235 ± 0.07352 s respectively. Due to the resulting time required for the sample to fully relax between scans (5 x longest T_1 = 40 s) all ^{1}H NMR spectra were recorded as single scan experiments, performed more than 40 s apart for achieving quantitation.

8.5.1.2 Negishi reaction profile determination by ^{1}H NMR spectroscopic monitoring

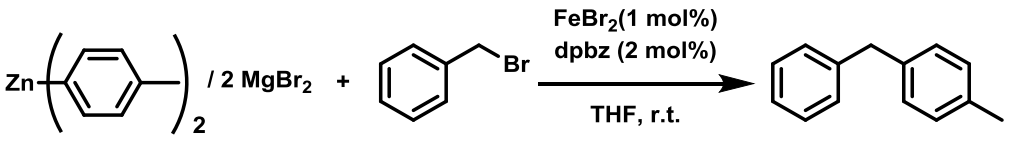

In an argon filled glovebox, $FeBr_2$ (40.0 µL, 20.0 mM stock solution in THF-d_8, 0.80 µmol) was applied to the head of a screw-top NMR tube and left horizontally so as to allow for the solvent to evaporate within the head region of the tube, leaving behind a thin film of $FeBr_2$ located on the top of the NMR tube. Subsequently, the NMR tube was carefully loaded with dpbz (20.0 µL, 80.0 mM stock solution in THF-d_8, 1.60 µmol), benzyl bromide (32.0 µL, 2500

mM stock solution in THF-d_8, 80.0 µmol), dodecane (80.0 µL, 500 mM stock solution in THF-d_8, 40.0 µmol), Zn(4-tolyl)$_2$/2 $MgBr_2$ (400 µL, 200 mM stock solution in THF-d_8, 80.0 µmol) and THF-d_8 (268 µL) to give a solution with a total volume of 800 µL. A capillary containing [$NiCl_2$(dppe)] (50.0 µL, 16.0 mM stock solution in $CDCl_3$, 0.80 µmol) was added and the NMR tube sealed, with the $FeBr_2$ residue remaining undisturbed at the head of the tube. The ^{1}H and ^{31}P NMR spectra at t = 0 s were then recorded, providing the initial concentrations of the starting materials as well as locking and shimming the sample. The tube was then ejected, and the reaction initiated by quickly and carefully shaking the NMR tube so that the $FeBr_2$ residue quickly dissolved. The sample was quickly replaced, and an NMR spectra collection array was initiated whereby the ^{1}H and ^{31}P spectra were recorded over time, with pre-calculated relaxation delays.

8.5.2 In situ NMR detection of zinc-diphosphine species: ^{31}P NMR spectroscopy

8.5.2.1 Calculation of the ^{31}P NMR T_1 spin-lattice relaxation for zinc-diphosphine complexes and the [$NiCl_2$(dppe)] capillary standard

In order to determine a representative ^{31}P T_1 relaxation for the zinc-diphosphine complexes formed during catalysis in the presence of Fe(II), an NMR tube was loaded with $FeBr_2$ (40.0 µL, 20.0 mM stock solution in THF-d_8, 0.80 µmol), dpbz (20.0 µL, 80.0 mM stock solution in THF-d_8, 1.60 µmol), $ZnBr_2$ (400 µL, 200 mM stock solution in THF-d_8, 80.0 µmol) and THF-d_8 (340 µL), to give a solution with a total volume of 800 µL. A capillary containing [$NiCl_2$(dppe)] was added as a reference and standard with a resonance at 58.7 ppm. A T_1 experiment was then run, and the relaxation delay of the peak at -26.6 ppm corresponding to the [$ZnBr_2$(dpbz)] complex in presence of iron was found to be 0.07487 ± 0.01232 s (202 MHz, 298 K, 2 mM in dpbz) while the one for [$NiCl_2$(dppe)] was 0.233 ±0.03011 s (202 MHz, 298 K, 16 mM in $CDCl_3$). Accordingly, the relaxation delay for all quantitative 31P experiments was set to 1.5 s.

8.5.2.2 ^{31}P NMR spectroscopic examination of the phosphorus speciation during the Negishi cross-coupling

The same reaction protocol was used as described in section 8.5.1.1. However, due to the weak ^{31}P NMR signals as a result of the low phosphine concentration during catalysis (2.00

mM) in combination with peak broadening, it was necessary to record the ^{31}P NMR spectrum over the first 40 minutes of the reaction (1024 scans) in order to obtain reasonable signal to noise ratios suitable for reliable integration. According to an ^{1}H NMR that followed after the aforementioned ^{31}P NMR spectrum was recorded, the yield of Bn(p-tolyl) **56** was 87%, signalling the end of the reaction. Subsequently, the same ^{31}P NMR measurement was repeated after the first 40 minutes of reaction providing information on the catalytic reaction's endpoint. Therefore, the observed ^{31}P NMR signal corresponding to the phosphorus species not bound on iron will be the average signal throughout the whole catalysis region. A separate ^{31}P NMR experiment was then performed by filling the same NMR tube in which the aforementioned catalysis took place, equipped with the same [$NiCl_2$(dppe)]-filled capillary with: dpbz (20.0 µL, 80.0 mM stock solution in THF-d_8, 1.60 µmol), dodecane (80.0 µL, 500 mM stock solution in THF-d_8, 40.0 µmol), Zn(4-tolyl)$_2$/ 2 $MgBr_2$ (300 µL, 200 mM stock solution in THF-d_8, 60.0 µmol), Bn(4-tolyl) (7.3 µL, 40.0 µmol), $ZnBr_2$ (40 µL, 500 mM stock solution in THF-d_8, 20.0 µmol), $MgBr_2$ (7.3 mg, 40.0 µmol) and THF-d_8 (353 µL) to give a solution with a total volume of 800 µL. The resultant solution, which mimics the catalytic reaction's composition at 50% conversion but excludes $FeBr_2$, was submitted for a ^{31}P NMR experiment on the same instrument and with the same parameters used for the ^{31}P NMR study of the catalytic reaction under examination. The only difference in this case was the extremely high relaxation delay (60 s) necessary for ensuring that the collected spectrum can be quantified as a result of the absence of paramagnetic $FeBr_2$ in the mixture. In the three spectra collected, two resonances were observed at 58.7 and -16.4 to -15.8 ppm, corresponding to [$NiCl_2$(dppe)] and zinc-diphosphine species respectively.

8.6 Experimental data for Chapter 6

8.6.1 Preparation of Cr(0) and Cr(I) complexes

*8.6.1.1 Preparation of $Cr(CO)_4$(dppp), **85***

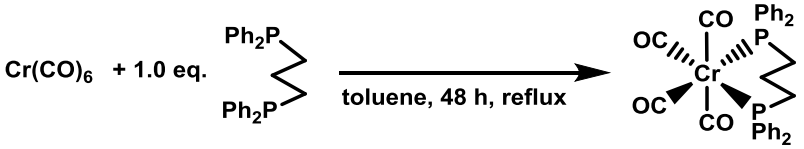

Prepared according to a modified literature procedure.[184] A Schlenk tube was charged with $Cr(CO)_6$ (1.00 g, 4.54 mmol), 1,3-bis(diphenylphosphino)propane (dppp) (1.874 g, 4.54

mmol), and toluene (20 mL). A reflux condenser was fitted, and the mixture was heated at 110 °C for 48 h, after which time the resultant solution was filtered *via* cannula whilst warm and allowed to cool. The solution was concentrated *in vacuo* to a volume of approximately 5 mL, and MeOH (10 mL) was layered. After leaving for 16 h at room temperature, yellow crystals of the desired product had formed, which were separated *via* cannula filtration, washed with cold MeOH (3 x 5 mL) and dried under reduced pressure. **^{1}H NMR** (400 MHz, $CDCl_3$) δ 7.49 – 7.30 (m, 20H), 2.42 (dt, *J* = 9.0, 4.5 Hz, 4H), 1.95 (m, 2H). **^{31}P NMR** (162.0 MHz, $CDCl_3$) δ 42.31 (s). **^{13}C NMR** (122 MHz, $CDCl_3$) δ 19.8, 30.8, 128.4, 129.6, 132.0, 137.9, 221.8, 226.2. The spectroscopic properties of this compound were consistent with literature data.[184]

8.6.1.2 Preparation of [Cr(CO)$_4$(dppp)][Al(OC(CF$_3$)$_3$)$_4$], ***86***

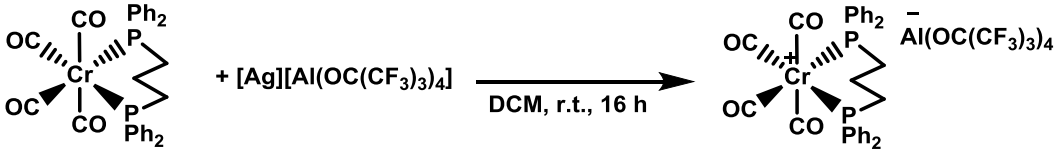

Prepared according to a modified literature procedure.[188] A Schlenk tube (covered with foil to exclude light) was charged with $Cr(CO)_4$(dppp) (200 mg, 0.35 mmol), silver tetrakis(perfluoro-t.-butoxy) aluminate, [Ag][Al(OC(CF_3)$_4$] (436.2 mg, 0.45 mmol) and DCM (20 mL). The resultant mixture was stirred for 16 h in the dark, following filtration *via* cannula and removal of all volatiles *in vacuo*. The resultant blue solid was washed with cold petrol 40:60 (2 x 5 mL) and dried, yielding the title compound (369 mg, 69%). **^{19}F NMR** (377 MHz, CD_2Cl_2) δ -76.9 (s). **ESI$_{pos}$** -MS (DCM): [M+Na] 599.0, [M] 576.0; ESI$_{neg}$ -MS (DCM): [M] 966.9. The spectroscopic properties of this compound were consistent with literature data.[188]

8.6.2 Preparation of EPR samples for UV irradiation

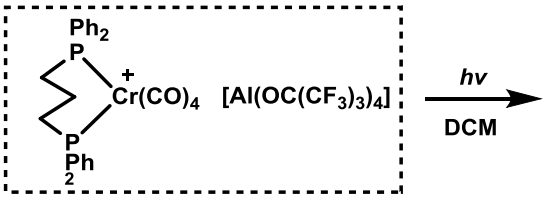

= [Cr(dppp)][Al]

Under an atmosphere of argon, an ampoule was loaded with [Cr][Al], **86**, (30.0 mg, 0.019 mmol) and DCM (1.00 mL) to give a stock solution 19.4 mM in Cr. Samples were prepared by drawing a 200 μL aliquot and sealing under an atmosphere of argon using a suba-seal. Where dilution was necessary, an aliquot was taken from the stock solution inside the glovebox and the requisite amount of DCM added to give a total volume of 200 μL within the EPR tube. The sample was then exposed to UV irradiation for the desired length of time, before the spectrum was recorded.

References

1 A. Behr and P. Neubert, *Applied homogeneous catalysis*, Wiley-VCH, Weinheim, 2012.

2 J. Wang and B. L. Feringa, *Science*, 2011, **331**, 1429–32.

3 A. Biffis, P. Centomo, A. Del Zotto and M. Zecca, *Chem. Rev.*, 2018, **118**, 2249–2295.

4 A. J. Folkes, K. Ahmadi, W. K. Alderton, S. Alix, S. J. Baker, G. Box, I. S. Chuckowree, P. A. Clarke, P. Depledge, S. A. Eccles, L. S. Friedman, A. Hayes, T. C. Hancox, A. Kugendradas, L. Lensun, P. Moore, A. G. Olivero, J. Pang, S. Patel, G. H. Pergl-Wilson, F. I. Raynaud, A. Robson, N. Saghir, L. Salphati, S. Sohal, M. H. Ultsch, M. Valenti, H. J. A. Wallweber, N. C. Wan, C. Wiesmann, P. Workman, A. Zhyvoloup, M. J. Zvelebil and S. J. Shuttleworth, *J. Med. Chem.*, 2008, **51**, 5522–5532.

5 Q. Tian, Z. Cheng, H. M. Yajima, S. J. Savage, K. L. Green, T. Humphries, M. E. Reynolds, S. Babu, F. Gosselin, D. Askin, I. Kurimoto, N. Hirata, M. Iwasaki, Y. Shimasaki and T. Miki, *Org. Process Res. Dev.*, 2013, **17**, 97–107.

6 C. A. Busacca, D. R. Fandrick, J. J. Song and C. H. Senanayake, *Adv. Synth. Catal.*, 2011, **353**, 1825–1864.

7 J. C. Hierso, *Palladium-Catalyzed Coupling Reactions.*, Wiley, Weinheim, 2013.

8 J.W. PCT Int. Appl., WO 2013184702, A1, 2013.

9 M. S. Kharasch and E. K. Fields, *J. Am. Chem. Soc.*, 1941, **63**, 2316–2320.

10 K. Tamao, K. Sumitani and M. Kumada, *J. Am. Chem. Soc.*, 1972, **94**, 4374–4376.

11 R. J. P. Corriu and J. P. Masse, *J. Chem. Soc. Chem. Commun.*, 1972, 144a–144a.

12 S. Baba and E. Negishi, *J. Am. Chem. Soc.*, 1976, **98**, 6729–6731.

13 A. O. King, N. Okukado and E. Negishi, *J. Chem. Soc. Chem. Commun.*, 1977, 683–684.

14 N. Miyaura and A. Suzuki, *J. Chem. Soc. Chem. Commun.*, 1979, 866–867.

15 D. Milstein and J. K. Stille, *J. Am. Chem. Soc.*, 1978, **100**, 3636–3638.

16 J. H. Kirchhoff, M. R. Netherton, I. D. Hills and G. C. Fu, *J. Am. Chem. Soc.*, 2002, **124**, 13662–13663.

17 J. F. Hartwig and F. Paul, *J. Am. Chem. Soc.*, 1995, **117**, 5373–5374.

18 J. M. Brown and N. A. Cooley, *Chem. Rev.*, 1988, **88**, 1031–1046.

19 A. J. J. Lennox and G. C. Lloyd-Jones, *Angew. Chemie - Int. Ed.*, 2013, **52**, 7362–7370.

20 J. del Pozo, G. Salas, R. Álvarez, J. A. Casares and P. Espinet, *Organometallics*, 2016, **35**, 3604–3611.

21 A. A. Yaroshevsky, *Geochemistry Int.*, 2006, **44**, 48–55.

22 5-year cost of palladium, http://www.infomine.com/investment/metal-prices/palladium/5-year/, (accessed 18 March 2019).

23 A. Cowley, *Pgm Market Report*, 2019.

24 P. Nuss and M. J. Eckelman, *PLoS One*, 2014, **9**, e101298.

25 J. D. Hayler, D. K. Leahy and E. M. Simmons, *Organometallics*, 2019, **38**, 36–46.

26 C. Steinlechner, A. F. Roesel, E. Oberem, A. Päpcke, N. Rockstroh, F. Gloaguen, S. Lochbrunner, R. Ludwig, A. Spannenberg, H. Junge, R. Francke and M. Beller, *ACS Catal.*, 2019, **9**, 2091–2100.

27 5-year cost of iron, https://tradingeconomics.com/commodity/iron-ore, (accessed 18 March 2019).

28 D. G. Brown and J. Boström, *J. Med. Chem.*, 2016, **59**, 4443–4458.

29 H. Albright, P. S. Riehl, C. C. McAtee, J. P. Reid, J. R. Ludwig, L. A. Karp, P. M. Zimmerman, M. S.

Sigman and C. S. Schindler, *J. Am. Chem. Soc.*, 2019, **141**, 1690–1700.

30 S. M. Rummelt, H. Zhong, N. G. Léonard, S. P. Semproni and P. J. Chirik, *Organometallics*, 2019, **38**, 1081–1090.

31 M. J. Drance, J. D. Sears, A. M. Mrse, C. E. Moore, A. L. Rheingold, M. L. Neidig and J. S. Figueroa, *Science*, 2019, **363**, 1203–1205.

32 T. Kandemir, M. E. Schuster, A. Senyshyn, M. Behrens and R. Schlögl, *Angew. Chemie Int. Ed.*, 2013, **52**, 12723–12726.

33 M. Tamura and J. Kochi, *J. Organomet. Chem.*, 1971, **31**, 289–309.

34 G. Cahiez and H. Avedissian, *Synthesis (Stuttg).*, 1998, **1998**, 1199–1205.

35 A. Fürstner and A. Leitner, *Angew. Chemie - Int. Ed.*, 2002, **41**, 609–612.

36 M. Nakamura, S. Ito, K. Matsuo and E. Nakamura, *Synlett*, 2005, **2005**, 1794–1798.

37 M. Carril, A. Correa and C. Bolm, *Angew. Chemie - Int. Ed.*, 2008, **47**, 4862–4865.

38 R. B. Bedford, M. A. Hall, G. R. Hodges, M. Huwe and M. C. Wilkinson, *Chem. Commun.*, 2009, 6430–6432.

39 T. Hatakeyama, T. Hashimoto, Y. Kondo, Y. Fujiwara, H. Seike, H. Takaya, Y. Tamada, T. Ono and M. Nakamura, *J. Am. Chem. Soc.*, 2010, **132**, 10674–10676.

40 M. Jin, L. Adak and M. Nakamura, *J. Am. Chem. Soc.*, 2015, **137**, 7128–7134.

41 H. M. O'Brien, M. Manzotti, R. D. Abrams, D. Elorriaga, H. A. Sparkes, S. A. Davis and R. B. Bedford, *Nat. Catal.*, 2018, **1**, 429–437.

42 M. L. Neidig, S. H. Carpenter, D. J. Curran, J. C. Demuth, V. E. Fleischauer, T. E. Iannuzzi, P. G. N. Neate, J. D. Sears and N. J. Wolford, *Acc. Chem. Res.*, 2019, **52**, 140–150.

43 W. Dohle, F. Kopp, G. Cahiez and P. Knochel, *Synlett*, 2001, **3**, 1901–1904.

44 T. Nagano and T. Hayashi, *Org. Lett.*, 2004, **6**, 1297–1299.

45 J. Quintin, X. Franck, R. Hocquemiller and B. Figadère, *Tetrahedron Lett.*, 2002, **43**, 3547–3549.

46 J. Kleimark, A. Hedström, P. F. Larsson, C. Johansson and P. O. Norrby, *ChemCatChem*, 2009, **1**, 152–161.

47 B. Bogdanovi and M. Schwickardi, *Angew. Chemie - Int. Ed.*, 2000, **39**, 4610–4612.

48 A. Fürstner, A. Leitner, M. Méndez and H. Krause, *J. Am. Chem. Soc.*, 2002, **124**, 13856–13863.

49 K. Jonas, L. Schieferstein, C. Krüger and Y.-H. Tsay, *Angew. Chemie Int. Ed. English*, 1979, **18**, 550–551.

50 R. Martin and A. Fürstner, *Angew. Chemie - Int. Ed.*, 2004, **43**, 3955–3957.

51 A. Fürstner, R. Martin, H. Krause, G. Seidel, R. Goddard and C. W. Lehmann, *J. Am. Chem. Soc.*, 2008, **130**, 8773–8787.

52 J. D. Sears, S. B. Muñoz, S. L. Daifuku, A. A. Shaps, S. H. Carpenter, W. W. Brennessel and M. L. Neidig, *Angew. Chemie - Int. Ed.*, 2019, **58**, 2769–2773.

53 A. Casitas, J. A. Rees, R. Goddard, E. Bill, S. DeBeer and A. Fürstner, *Angew. Chemie - Int. Ed.*, 2017, **56**, 10108–10113.

54 M. H. Al-Afyouni, K. L. Fillman, W. W. Brennessel and M. L. Neidig, *J. Am. Chem. Soc.*, 2014, **136**, 15457–15460.

55 S. B. Muñoz, S. L. Daifuku, W. W. Brennessel and M. L. Neidig, *J. Am. Chem. Soc.*, 2016, **138**, 7492–7495.

56 S. B. Muñoz, S. L. Daifuku, J. D. Sears, T. M. Baker, S. H. Carpenter, W. W. Brennessel and M. L. Neidig, *Angew. Chemie - Int. Ed.*, 2018, **57**, 6496–6500.

57 R. B. Bedford, P. B. Brenner, D. Elorriaga, J. N. Harvey and J. Nunn, *Dalt. Trans.*, 2016, **45**, 15811–15817.

58 R. B. Bedford, P. B. Brenner, E. Carter, P. M. Cogswell, M. F. Haddow, J. N. Harvey, D. M. Murphy, J. Nunn and C. H. Woodall, *Angew. Chemie - Int. Ed.*, 2014, **53**, 1804–1808.

59 S. H. Carpenter, T. M. Baker, S. B. Muñoz, W. W. Brennessel and M. L. Neidig, *Chem. Sci.*, 2018, **9**, 7931–7939.

60 F. E. Zhurkin, M. D. Wodrich and X. Hu, *Organometallics*, 2017, **36**, 499–501.

61 R. B. Bedford, *Acc. Chem. Res.*, 2015, **48**, 1485–1493.

62 D. Noda, Y. Sunada, T. Hatakeyama, M. Nakamura and H. Nagashima, *J. Am. Chem. Soc.*, 2009, **131**, 6078–6079.

63 C. J. Adams, R. B. Bedford, E. Carter, N. J. Gower, M. F. Haddow, J. N. Harvey, M. Huwe, M. Á. Cartes, S. M. Mansell, C. Mendoza, D. M. Murphy, E. C. Neeve and J. Nunn, *J. Am. Chem. Soc.*, 2012, **134**, 10333–10336.

64 S. L. Daifuku, J. L. Kneebone, B. E. R. Snyder and M. L. Neidig, *J. Am. Chem. Soc.*, 2015, **137**, 11432–11444.

65 J. L. Kneebone, W. W. Brennessel and M. L. Neidig, *J. Am. Chem. Soc.*, 2017, **139**, 6988–7003.

66 T. Hatakeyama, Y. Okada, Y. Yoshimoto and M. Nakamura, *Angew. Chemie - Int. Ed.*, 2011, **50**, 10973–10976.

67 R. B. Bedford, P. B. Brenner, E. Carter, T. W. Carvell, P. M. Cogswell, T. Gallagher, J. N. Harvey, D. M. Murphy, E. C. Neeve, J. Nunn and D. R. Pye, *Chem. - A Eur. J.*, 2014, **20**, 7935–7938.

68 R. B. Bedford, P. B. Brenner, E. Carter, J. Clifton, P. M. Cogswell, N. J. Gower, M. F. Haddow, J. N. Harvey, J. A. Kehl, D. M. Murphy, E. C. Neeve, M. L. Neidig, J. Nunn, B. E. R. Snyder and J. Taylor, *Organometallics*, 2014, **33**, 5767–5780.

69 R. B. Bedford, P. B. Brenner, E. Carter, T. Gallagher, D. M. Murphy and D. R. Pye, *Organometallics*, 2014, **33**, 5940–5943.

70 R. B. Bedford, M. Betham, D. W. Bruce, A. A. Danopoulos, R. M. Frost and M. Hird, *J. Org. Chem.*, 2006, **71**, 1104–1110.

71 T. Hatakeyama and M. Nakamura, *J. Am. Chem. Soc.*, 2007, **129**, 9844–9845.

72 M. Guisán-Ceinos, F. Tato, E. Buñuel, P. Calle and D. J. Cárdenas, *Chem. Sci.*, 2013, **4**, 1098–1104.

73 R. Agata, T. Iwamoto, N. Nakagawa, K. Isozaki, T. Hatakeyama, H. Takaya and M. Nakamura, *Synth.*, 2015, **47**, 1733–1740.

74 Z. Ouyang, J. Du, L. Wang, J. L. Kneebone, M. L. Neidig and L. Deng, *Inorg. Chem.*, 2015, **54**, 8808–8816.

75 Z. Ouyang, Y. Meng, J. Cheng, J. Xiao, S. Gao and L. Deng, *Organometallics*, 2016, **35**, 1361–1367.

76 Z. Ouyang, J. Cheng, L. Li, X. Bao and L. Deng, *Chem. - A Eur. J.*, 2016, **22**, 14162–14165.

77 V. E. Fleischauer, S. B. Muñoz, P. G. N. Neate, W. W. Brennessel and M. L. Neidig, *Chem. Sci.*, 2018, **9**, 1878–1891.

78 J. A. Przyojski, K. P. Veggeberg, H. D. Arman and Z. J. Tonzetich, *ACS Catal.*, 2015, **5**, 5938–5946.

79 R. Agata, T. Hatakeyama, K. Takeuchi, H. Matsuda, T. Iwamoto, H. Takaya, N. Nakatani and M. Nakamura, *Bull. Chem. Soc. Jpn.*, 2018, **92**, 381–390.

80 T. Hatakeyama, S. Hashimoto, K. Ishizuka and M. Nakamura, *J. Am. Chem. Soc.*, 2009, **131**, 11949–

11963.

81 J. L. Kneebone, V. E. Fleischauer, S. L. Daifuku, A. A. Shaps, J. M. Bailey, T. E. Iannuzzi and M. L. Neidig, *Inorg. Chem.*, 2016, **55**, 272–282.

82 S. B. Muñoz, V. E. Fleischauer, W. W. Brennessel and M. L. Neidig, *Organometallics*, 2018, **37**, 3093–3101.

83 K. L. Fillman, J. A. Przyojski, M. H. Al-Afyouni, Z. J. Tonzetich and M. L. Neidig, *Chem. Sci.*, 2015, **6**, 1178–1188.

84 Q. Teng, W. Wu, H. A. Duong and H. V. Huynh, *Chem. Commun.*, 2018, **54**, 6044–6047.

85 C. Kupper, B. Mondal, J. Serrano-Plana, I. Klawitter, F. Neese, M. Costas, S. Ye and F. Meyer, *J. Am. Chem. Soc.*, 2017, **139**, 8939–8949.

86 T. S. Thakur and G. R. Desiraju, *J. Mol. Struct. Theochem*, 2007, **810**, 143–154.

87 A. M. LaPointe, *Inorganica Chim. Acta*, 2003, **345**, 359–362.

88 J. D. Sears, S. B. Muñoz, M. C. A. Cuenca, W. W. Brennessel and M. L. Neidig, *Polyhedron*, 2019, **158**, 91–96.

89 R. A. Lewis, D. E. Smiles, J. M. Darmon, S. C. E. Stieber, G. Wu and T. W. Hayton, *Inorg. Chem.*, 2013, **52**, 8218–8227.

90 W. Seidel and K.-J. Lattermann, *Zeitschrift für Anorg. und Allg. Chemie*, 1982, **488**, 69–74.

91 Q. Liang, T. Janes, X. Gjergji and D. Song, *Dalt. Trans.*, 2016, **45**, 13872–13880.

92 J. Nunn, Ph.D. thesis, University of Bristol, 2014.

93 T. A. Bagenova, A. K. Shilova, E. Deschamps, M. Gruselle, G. Leny and B. Tchoubar, *J. Organomet. Chem.*, 1981, **222**, C1–C4.

94 M. Clémancey, T. Cantat, G. Blondin, J. M. Latour, P. Dorlet and G. Lefèvre, *Inorg. Chem.*, 2017, **56**, 3834–3848.

95 J. I. Seeman, *J. Chem. Educ.*, 1986, **63**, 42–48.

96 A. Hedström, U. Bollmann, J. Bravidor and P. O. Norrby, *Chem. - A Eur. J.*, 2011, **17**, 11991–11993.

97 A. Hedström, Z. Izakian, I. Vreto, C. J. Wallentin and P. O. Norrby, *Chem. - A Eur. J.*, 2015, **21**, 5946–5953.

98 N. R. Deprez and M. S. Sanford, *J. Am. Chem. Soc.*, 2009, **131**, 11234–11241.

99 C. Hansch, A. Leo and R. W. Taft, *Chem. Rev.*, 1991, **91**, 165–195.

100 T. L. Mako and J. A. Byers, *Inorg. Chem. Front.*, 2016, **3**, 766–790.

101 R. A. Copeland, *Evaluation of Enzyme Inhibitors in Drug Discovery*, John Wiley & Sons, Inc., New Jersey, 2013.

102 R. D. Baxter, D. Sale, K. M. Engle, J. Q. Yu and D. G. Blackmond, *J. Am. Chem. Soc.*, 2012, **134**, 4600–4606.

103 A. M. Messinis, S. L. J. Luckham, P. P. Wells, D. Gianolio, E. K. Gibson, H. M. O'Brien, H. A. Sparkes, S. A. Davis, J. Callison, D. Elorriaga, O. Hernandez-Fajardo and R. B. Bedford, *Nat. Catal.*, 2018, **2**, 123–133.

104 R. B. Bedford, M. Betham, D. W. Bruce, S. A. Davis, R. M. Frost and M. Hird, *Chem. Commun.*, 2006, 1398–1400.

105 N. Nagano and T. Hayashi, *Org. Lett.*, 2005, **7**, 491–493.

106 E. V. Anslyn and D. A. Dougherty, *Modern Physical Organic Chemistry*, *University Science Books*, University Science, Sausalito, 2006.

107 D. G. Blackmond, *Angew. Chemie Int. Ed.*, 2005, **44**, 4302–4320.

108 J. Burés, *Angew. Chemie Int. Ed.*, 2016, **55**, 16084–16087.

109 C. D.-T. Nielsen and J. Burés, *Chem. Sci.*, 2019, **10**, 348–353.

110 J. Burés, *Top. Catal.*, 2017, **60**, 631–633.

111 P. L. Houston, *Chemical Kinetics and Reaction Dynamics*, New York, 2001.

112 J. C. Giddings and H. K. Shin, *J. Chem. Phys.*, 1962, **36**, 640–649.

113 L. P. Hammett, *J. Am. Chem. Soc.*, 1937, **59**, 96–103.

114 C. D. Ritchie and W. F. Sager, in *Progress in Physical Organic Chemistry*, John Wiley & Sons, Ltd, 2007, vol. 2, pp. 323–400.

115 X. Creary, M. E. Mehrsheikh-mohammadi and S. Mcdonald, *J. Org. Chem.*, 1987, **52**, 3254–3263.

116 C. Hansch and H. Gao, *Chem. Rev.*, 1997, **97**, 2995–3060.

117 J. F. Hartwig, *Organotransition Metal Chemistry: From Bonding to Catalysis*, University Science Books, Sausalito, 6th edn., 2010.

118 K. Matyjaszewski, S. Coca, S. G. Gaynor, M. Wei and B. E. Woodworth, *Macromolecules*, 1997, **30**, 7348–7350.

119 W. Tang, Y. Kwak, W. Braunecker, N. V. Tsarevsky, M. L. Coote and K. Matyjaszewski, *J. Am. Chem. Soc.*, 2008, **130**, 10702–10713.

120 J. F. Hartwig, *Acc. Chem. Res.*, 1998, **31**, 852–860.

121 F. Basolo and R. Pearson, *Mechanisms of Inorganic Reactions*, Wiley, New York, 2nd edn., 1968.

122 K. Matyjaszewski, *Macromolecules*, 2012, **45**, 4015–4039.

123 G. Lefèvre and A. Jutand, *Chem. - A Eur. J.*, 2014, **20**, 4796–4805.

124 J. I. Steinfield, J. S. Francisco and W. L. Hase, *Chemical Kinetics and Dynamics*, Prentice-Hall, New Jersey, 1999.

125 R. H. Crabtree, *The Organometallic Chemistry of the Transition Metals: Sixth Edition*, John Wiley & Sons, Inc., Hoboken, N.J., 2014.

126 W. A. Herrmann, *Angew. Chemie Int. Ed.*, 2002, **41**, 1290–1309.

127 A. A. Danopoulos, P. Braunstein, M. Wesolek, K. Y. Monakhov, P. Rabu and V. Robert, *Organometallics*, 2012, **31**, 4102–4105.

128 J. Halpern, *Acc. Chem. Res.*, 1970, **3**, 386–392.

129 P. S. Hanley and J. F. Hartwig, *Angew. Chemie Int. Ed.*, 2013, **52**, 8510–8525.

130 R. B. Bedford, M. Huwe and M. C. Wilkinson, *Chem. Commun.*, 2009, 600–602.

131 S. W. Smith and G. C. Fu, *J. Am. Chem. Soc.*, 2008, **130**, 12645–12647.

132 C. Bolm and J. Rudolph, *J. Am. Chem. Soc.*, 2002, **124**, 14850–14851.

133 L. C. McCann and M. G. Organ, *Angew. Chemie Int. Ed.*, 2014, **53**, 4386–4389.

134 J. E. Barclay, G. J. Leigh, A. Houlton and J. Silver, *J. Chem. Soc., Dalt. Trans.*, 1988, 2865–2870.

135 L. Jin, C. Liu, J. Liu, F. Hu, Y. Lan, A. S. Batsanov, J. A. K. Howard, T. B. Marder and A. Lei, *J. Am. Chem. Soc.*, 2009, **131**, 16656–16657.

136 D. L. McNeil, D. J. Beckford, J. L. Kneebone, S. H. Carpenter, W. W. Brennessel and M. L. Neidig, *Acta Crystallogr. Sect. E Crystallogr. Commun.*, 2018, **74**, 803–807.

137 J. Jover and N. Fey, *Dalt. Trans.*, 2013, **42**, 172–181.

138 C. Flener Lovitt, G. Frenking and G. S. Girolami, *Organometallics*, 2012, **31**, 4122–4132.

139 L. Falivene, R. Credendino, A. Poater, A. Petta, L. Serra, R. Oliva, V. Scarano and L. Cavallo, *Organometallics*, 2016, **35**, 2286–2293.

140 M. Newville, *Rev. Mineral. Geochemistry*, 2014, **78**, 33–74.

141 G. J. Sherborne and B. N. Nguyen, *Chem. Cent. J.*, 2015, **9**, 37.

142 M. Tromp, Ph.D. thesis, University of Amsterdam, 2004.

143 D. C. Koningsberger and R. Prins, *X-ray absorption: Principles, applications, techniques of EXAFS, SEXAFS, and XANES*, Wiley, Hoboken, N.J., 1988.

144 A. Welther, M. Bauer, M. Mayer and A. Jacobi von Wangelin, *ChemCatChem*, 2012, **4**, 1088–1093.

145 H. Takaya, S. Nakajima, N. Nakagawa, K. Isozaki, T. Iwamoto, R. Imayoshi, N. J. Gower, L. Adak, T. Hatakeyama, T. Honma, M. Takagaki, Y. Sunada, H. Nagashima, D. Hashizume, O. Takahashi and M. Nakamura, *Bull. Chem. Soc. Jpn.*, 2015, **88**, 410–418.

146 R. Schoch, W. Desens, T. Werner and M. Bauer, *Chem. - A Eur. J.*, 2013, **19**, 15816–15821.

147 M. Tromp, *Philos. Trans. R. Soc. A Math. Phys. Eng. Sci.*, 2015, 373.

148 I. S. Metcalfe, *Chemical reaction engineering : a first course*, Oxford University Press, Oxford, 1997.

149 V. L. Goedken, S.-M. Peng and Y.-A. Park, *J. Am. Chem. Soc.*, 1974, **96**, 284–285.

150 A. Klose, E. Solari, C. Floriani, A. Chiesi-Villa, C. Rizzoli and N. Re, *J. Am. Chem. Soc.*, 1994, **116**, 9123–9135.

151 S. D. Ittel, A. D. English, C. A. Tolman and J. P. Jesson, *Inorganica Chim. Acta*, 1979, **33**, 101–106.

152 T. J. J. Sciarone, A. Meetsma, B. Hesssen and J. H. Teuben, *Chem. Commun.*, 2002, 1580–1581.

153 J. J. Dunsford, D. J. Evans, T. Pugh, S. N. Shah, N. F. Chilton and M. J. Ingleson, *Organometallics*, 2016, **35**, 1098–1106.

154 M. Taherimehr, S. M. Al-Amsyar, C. J. Whiteoak, A. W. Kleij and P. P. Pescarmona, *Green Chem.*, 2013, **15**, 3083.

155 C. Lichtenberg, M. Adelhardt, M. Wörle, T. Büttner, K. Meyer and H. Grützmacher, *Organometallics*, 2015, **34**, 3079–3089.

156 G. Mund, D. Vidovic, R. J. Batchelor, J. F. Britten, R. D. Sharma, C. H. W. Jones and D. B. Leznoff, *Chem. - A Eur. J.*, 2003, **9**, 4757–4763.

157 Y. Jean and C. J. Marsden, *Molecular orbitals of transition metal complexes*, Oxford University Press, Oxford, 2005.

158 P. S. Jarrett and P. J. Sadler, *Inorg. Chem.*, 1991, **30**, 2098–2104.

159 D. F. Wass, *J. Chem. Soc. Dalt. Trans.*, 2007, 816–819.

160 D. S. McGuinness, *Chem. Rev.*, 2011, **111**, 2321–2341.

161 A. Forestière, H. Olivier-Bourbigou and L. Saussine, *Oil Gas Sci. Technol. - Rev. l'IFP*, 2009, **64**, 649–667.

162 P. J. W. Deckers, B. Hessen and J. H. Teuben, *Organometallics*, 2002, **21**, 5122–5135.

163 C. Andes, S. B. Harkins, S. Murtuza, K. Oyler and A. Sen, *J. Am. Chem. Soc.*, 2001, **123**, 7423–7424.

164 S. Tobisch and T. Ziegler, *J. Am. Chem. Soc.*, 2004, **126**, 9059–9071.

165 Y. Gao, J. Chen, Y. Wang, D. B. Pickens, A. Motta, Q. J. Wang, Y.-W. Chung, T. L. Lohr and T. J. Marks, *Nat. Catal.*, 2019, **2**, 236–242.

166 O. L. Sydora, *Organometallics*, 2019, **38**, 997–1010.

167 R. M. Manyik, W. E. Walker and T. P. Wilson, *J. Catal.*, 1977, **47**, 197–209.

168 T. Agapie, S. J. Schofr, J. A. Labinger and J. E. Bercaw, *J. Am. Chem. Soc.*, 2004, **126**, 1304–1305.

169 A. K. Tomov, J. J. Chirinos, D. J. Jones, R. J. Long and V. C. Gibson, *J. Am. Chem. Soc.*, 2005, **127**, 10166–10167.

170 B. Cornils, W. A. Herrmann, M. Beller and R. Paciello, *Applied Homogeneous Catalysis with Organometallic Compounds*, Wiley, Hoboken, N.J., 2017.

171 A. Carter, S. A. Cohen, N. A. Cooley, A. Murphy, J. Scutt and D. F. Wass, *Chem. Commun.*, 2002, **2**, 858–859.

172 A. Bollmann, K. Blann, J. T. Dixon, F. M. Hess, E. Killian, H. Maumela, D. S. McGuinness, D. H. Morgan, A. Neveling, S. Otto, M. Overett, A. M. Z. Slawin, P. Wasserscheid and S. Kuhlmann, *J. Am. Chem. Soc.*, 2004, **126**, 14712–14713.

173 N. A. Hirscher, D. Perez Sierra and T. Agapie, *J. Am. Chem. Soc.*, 2019, jacs.9b01387.

174 P. R. Elowe, C. McCann, P. G. Pringle, S. K. Spitzmesser and J. E. Bercaw, *Organometallics*, 2006, **25**, 5255–5260.

175 P. J. W. Deckers, B. Hessen and J. H. Teuben, *Angew. Chemie*, 2001, **113**, 2584–2587.

176 A. N. J. Blok, P. H. M. Budzelaar and A. W. Gal, *Organometallics*, 2003, **22**, 2564–2570.

177 Y. Yang, Z. Liu, R. Cheng, X. He and B. Liu, *Organometallics*, 2014, **33**, 2599–2607.

178 J. T. Dixon, M. J. Green, F. M. Hess and D. H. Morgan, *J. Organomet. Chem.*, 2004, **689**, 3641–3668.

179 B. Venderbosch, J. P. H. Oudsen, L. A. Wolzak, D. J. Martin, T. J. Korstanje and M. Tromp, *ACS Catal.*, 2019, **9**, 1197–1210.

180 D. S. McGuinness, B. Chan, G. J. P. Britovsek and B. F. Yates, *Aust. J. Chem.*, 2014, **67**, 1481.

181 R. D. Köhn, *Angew. Chemie - Int. Ed.*, 2008, **47**, 245–247.

182 M. Gong, Z. Liu, Y. Li, Y. Ma, Q. Sun, J. Zhang and B. Liu, *Organometallics*, 2016, **35**, 972–981.

183 A. Brückner, J. K. Jabor, A. E. C. McConnell and P. B. Webb, *Organometallics*, 2008, **27**, 3849–3856.

184 L. McDyre, E. Carter, K. J. Cavell, D. M. Murphy, J. A. Platts, K. Sampford, B. D. Ward, W. F. Gabrielli, M. J. Hanton and D. M. Smith, *Organometallics*, 2011, **30**, 4505–4508.

185 E. Carter, K. J. Cavell, W. F. Gabrielli, M. J. Hanton, A. J. Hallett, L. McDyre, J. A. Platts, D. M. Smith and D. M. Murphy, *Organometallics*, 2013, **32**, 1924–1931.

186 R. G. Compton, R. Barghout, J. C. Eklund, A. C. Fisher, S. G. Davies, M. R. Metzler, A. M. Bond, R. Colton and J. N. Walter, *J. Chem. Soc. Dalt. Trans.*, 1993, 3641–3646.

187 L. E. Bowen, M. F. Haddow, A. G. Orpen and D. F. Wass, *Dalt. Trans.*, 2007, 1160.

188 A. J. Rucklidge, D. S. McGuinness, R. P. Tooze, A. M. Z. Slawin, J. D. A. Pelletier, M. J. Hanton and P. B. Webb, *Organometallics*, 2007, **26**, 2782–2787.

189 A. Reisinger, D. Himmel and I. Krossing, *Angew. Chemie - Int. Ed.*, 2006, **45**, 6997–7000.

190 M. Drescher, G. Jeschke and E. (Enrica) Bordignon, *EPR spectroscopy : applications in chemistry and biology*, Springer, New York, 2012.

191 M. Goswami, A. Chirila, C. Rebreyend and B. de Bruin, *Top. Catal.*, 2015, **58**, 719–750.

192 V. Chechik, E. Carter and D. Murphy, *Electron Paramagnetic Resonance*, Oxford University Press, Oxford, 2016.

193 D. M. Murphy, in *Metal Oxide Catalysis*, Wiley-VCH, Weinheim, Germany, 2009, vol. 1, pp. 1–50.

194 J. A. Weil, *Electron paramagnetic resonance : elementary theory and practical applications*, Wiley-Interscience, Hoboken, N.J., 2nd edn., 2007.

195 A. Schweiger, *Principles of pulse electron paramagnetic resonance / Arthur Schweiger and Gunnar Jeschke.*, Oxford University Press, Oxford, 2001.

196 D. Goldfarb and S. Stoll, *EPR spectroscopy : fundamentals and methods*, Wiley, Weinheim, 2018.

197 M. L. Munzarova, P. Kubacek and M. Kaupp, *J. Am. Chem. Soc.*, 2000, **122**, 11900–11913.

198 P. H. Rieger, *Coord. Chem. Rev.*, 1994, **135**–**136**, 203–286.

199 D. A. Cummings, J. McMaster, A. L. Rieger and P. H. Rieger, *Organometallics*, 1997, **16**, 4362–4368.

200 A. L. Rieger and P. H. Rieger, *Organometallics*, 2002, **21**, 5868–5873.

201 C. A. Eckert, *Annu. Rev. Phys. Chem.*, 1972, **23**, 239–264.

202 J. McCoy and W. L. Hubbell, *Proc. Natl. Acad. Sci. U. S. A.*, 2011, **108**, 1331–6.

203 A. Fairhurst, J. R. Morton and K. F. Preston, *Chem. Phys. Lett.*, 1984, **104**, 112–114.

204 R. N. Bagchi, R. Colton, A. M. Bond, D. L. Luscombe and J. E. Moir, *J. Am. Chem. Soc.*, 1986, **108**, 3352–3358.

205 A. M. Bond, B. R. McGarvey, A. L. Rieger and P. H. Rieger, *Inorg. Chem.*, 2000, **39**, 3428–3429.

206 A. M. Bond, R. Colton, J. B. Cooper, K. McGregor, J. N. Walter and D. M. Way, *Organometallics*, 1995, **14**, 49–56.

207 L. Jin, J. Qian, N. Sun, B. Hu, Z. Shen and X. Hu, *Chem. Commun.*, 2018, **54**, 5752–5755.

208 P. Basnet, S. Thapa, D. A. Dickie and R. Giri, *Chem. Commun.*, 2016, **52**, 11072–11075.

209 T. Ando, M. Kamigaito and M. Sawamoto, *Macromolecules*, 1997, **30**, 4507–4510.

210 K. S. Egorova and V. P. Ananikov, *Angew. Chemie Int. Ed.*, 2016, **55**, 12150–12162.

211 K. S. Egorova and V. P. Ananikov, *Organometallics*, 2017, **36**, 4071–4090.

Chapter 9 *Appendix*

9.1 Crystallographic data

Table 9.1: Crystallographic parameters for **31**, **32** and **48**

Compound	**[Fe(4-MeBn)$_3$][MgCl(THF)$_5$] 31**	**[Fe(4-MeBn)$_4$][MgCl(THF)$_5$] 32**	**FeCl$_2$(P(C$_6$H$_4$OMe)$_3$)$_2$ 48**
Empirical formula	$C_{44}H_{67}ClFeMgO_5$	$C_{52}H_{76}ClFeMgO_5$	$C_{42}H_{42}Cl_2FeO_6P_2$
Formula weight	791.58	896.78	831.44
Temperature/K	100	100	100
Crystal system	orthorhombic	monoclinic	monoclinic
Space group	P 21 21 21	P 1 21/c 1	C 1 2/c 1
a/Å	12.8370(2)	14.042(2)	23.2694(11)
b/Å	14.3639(2)	30.241(5)	8.1699(3)
c/Å	23.2927(3)	13.313(2)	24.1462(16)
α/°	90	90	90
β/°	90	117.774(2)	117.917(2)
γ/°	90	90	90
Volume/Å^3	4294.93(11)	5001.9(14)	4056.2(4)
Z	4	4	4
ρ_{calc}g/cm^3	1.224	1.1908	1.362
μ/mm^{-1}	0.470	0.411	0.628
F(000)	1704	1934.9805	1728
Crystal size/mm^3	0.785 x 0.452 x 0.263	0.636 x 0.468 x 0.339	0.653 0.407 x 0.380
Radiation	Mo Kα (λ = 0.71073)	Mo Kα (λ = 0.71073)	Mo Kα (λ = 0.71073)
2θ range for data collection/°	1.749 to 27.913	0.0512 to 28.02	0.997 to 27.914
Index ranges	-16 ≤ h ≤ 16, -18 ≤ k ≤ 18, -2 ≤ l ≤ 30	-18 ≤ h ≤ 18, -15 ≤ k ≤ 19, -14 ≤ l ≤ 17	-30 ≤ h ≤ 30, -10 ≤ k ≤ 10, -31 ≤ l ≤ 31
Reflections collected	39681	44941	26531
R_{int} / R_{sigma}	0.0378/0.0409	0.0528/0.0512	0.0193/0.0140
Data/restraints/parameters	10265/317/481	12062/0/544	4850/0/243
Goodness-of-fit on F^2	1.030	1.0633	1.033
Final R indexes [I>=2σ (I)]	R_1 = 0.0399, wR_2 = 0.0962	R_1 = 0.0505, wR_2 = 0.1388	R_1 = 0.0505, wR_2 = 0.1388
Final R indexes [all data]	R_1 = 0.0399, wR_2 = 0.0991	R_1 = 0.0505, wR_2 = 0.1607	R_1 =0.0267, wR_2 = 0.0705
Largest diff. peak/hole / e Å^{-3}	0.55/-0.31	0.99/-0.62	0.41/-0.30

Table 9.2: Crystallographic parameters for **50·THF**, **51** and **68**

Compound	**$FeCl_2(THF)(SIPr)$ 50·THF**	**$FeSIPr(4\text{-}MeBn)_2$ 51**	**$FeBr_2(dpbz)$ 68**
Empirical formula	$C_{31}H_{46}Cl_2FeN_2O$	$C_{43}H_{56}FeN_2$	$C_{34}H_{32}Br_2FeOP_2$
Formula weight	588.23	656.74	734.20
Temperature/K	100	100	100(2)
Crystal system	orthorhombic	triclinic	triclinic
Space group	Pbca	P -1	*P*-1
a/Å	15.2989(8)	13.2631(5)	9.3634(2)
b/Å	18.3512(10)	15.4645(6)	10.1562(2)
c/Å	21.9772(11)	20.512(8)	18.5426(3)
α/°	90	87.006(2)	100.0110(10)
β/°	90	88.861(2)	96.9930(10)
γ/°	90	79.794(2)	110.7150(10)
Volume/Å^3	6170.2(6)	4153.0(3)	1591.76(5)
Z	12	4	2
ρ_{calc}g/cm^3	1.268	1.05	1.532
μ/mm^{-1}	0.688	0.391	3.110
F(000)	2513.9	1416	740.0
Crystal size/mm^3	0.916 x 0.659 x 0.318	0.747 x 0.666 x 0.598	0.39 × 0.132 × 0.072
Radiation	Mo Kα (λ = 0.71073)	Mo Kα (λ = 0.71073)	MoKα (λ = 0.71073)
2θ range for data collection/°	3.7 to 55.8	0.990 to 27.575	4.41 to 55.148
Index ranges	$-17 \le h \le 20$, $-24 \le k \le 24$, $-28 \le l \le 28$	$-17 \le h \le 17$, $-20 \le k \le 20$, $-26 \le l \le 26$	$-12 \le h \le 12$, $-13 \le k \le 13$, $-24 \le l \le 24$
Reflections collected	83881	68089	28343
R_{int} / R_{sigma}	0.0317/0.0195	0.0507/0.0497	0.0238 / 0.0226
Data/restraints/parameters	7379/0/359	19025/24/870	7354/79/380
Goodness-of-fit on F^2	2.413	1.065	1.033
Final R indexes [I>=2σ (I)]	R_1 = 0.1021, wR_2 = 0.4774	R_1 = 0.0538, wR_2 = 0.1280	R_1 = 0.0262, wR_2 = 0.0623
Final R indexes [all data]	R_1 = 0.1064, wR_2 = 0.4800	R_1 = 0.0538, wR_2 = 0.1389	R_1 = 0.0326, wR_2 = 0.0649
Largest diff. peak/hole / e Å^{-3}	0.84/-3.36	0.75/-0.54	0.63/-0.54

Table 9.3: Crystallographic parameters for **69**, **70** and **72**

Compound	**$FeBr_2(dpbz)_2$ 69**	**$FeMes_2(dpbz)$ 70**	**$ZnBr_2(dpbz)$ 72**
Empirical formula	$C_{60}H_{48}Br_2FeP_4$	$C_{48}H_{46}FeP_2$	$C_{33.5}H_{28}Br_2P_2Zn$
Formula weight	1108.53	740.64	671.69
Temperature/K	240(2)	100(2)	100(2)
Crystal system	monoclinic	triclinic	triclinic
Space group	$P2_1/n$	P-1	P-1
a/Å	11.0317(2)	10.9171(2)	9.3305(3)
b/Å	12.7696(3)	11.1389(2)	10.0923(3)
c/Å	18.0365(5)	16.8884(4)	17.3404(6)
α/°	90	91.3980(10)	83.930(2)
β/°	92.7928(17)	101.9070(10)	83.701(2)
γ/°	90	106.1100(10)	69.116(2)
Volume/Å^3	2537.79(10)	1923.31(7)	1512.49(9)
Z	2	2	1
ρ_{calc}g/cm^3	1.451	1.279	1.576
μ/mm^{-1}	2.037	0.509	3.581
F(000)	1128.0	780.0	718.0
Crystal size/mm^3	0.407 × 0.192 × 0.156	0.362 × 0.251 × 0.194	0.543 × 0.262 × 0.194
Radiation	MoKα (λ = 0.71073)	MoKα (λ = 0.71073)	MoKα (λ = 0.71073)
2θ range for data collection/°	3.91 to 55.938	2.474 to 56.022	4.33 to 56.116
Index ranges	$-12 \le h \le 14$, $-16 \le k \le 15$, $-20 \le l \le 23$	$-13 \le h \le 14$, $-14 \le k \le 14$, $-22 \le l \le 22$	$-12 \le h \le 12$, $-13 \le k \le 13$, $-22 \le l \le 22$
Reflections collected	22913	35907	28215
R_{int} / R_{sigma}	0.0503 / 0.0514	0.0367 / 0.0336	0.0238 / 0.0225
Data/restraints/parameters	6088/0/304	9268/0/466	7297/0/379
Goodness-of-fit on F^2	1.016	1.022	1.039
Final R indexes [I>=2σ (I)]	R_1 = 0.0377, wR_2 = 0.0707	R_1 = 0.0343, wR_2 = 0.0811	R_1 = 0.0244, wR_2 = 0.0603
Final R indexes [all data]	R_1 = 0.0629, wR_2 = 0.0784	R_1 = 0.0453, wR_2 = 0.0863	R_1 = 0.0312, wR_2 = 0.0629
Largest diff. peak/hole / e Å^{-3}	0.39/-0.52	0.44/-0.37	0.91/-0.77

9.2 VTNA plots

VTNA can be a useful method of kinetic analysis, allowing for the simple overlaying of concentration time plots for elucidation of an order of reaction with respect to a reagent. This can be particularly useful in the case of sigmoidal reaction profiles, which are observed within Chapter 2. However, when applied, VTNA generally gave poor overlaps of data at all reaction order values. This is due to the fact that three reactions are occurring simultaneously at any point within the reaction, something that VTNA cannot account for (for references see section 2.4). Therefore, as displayed in the plots below (for determination of the reaction orders with respect to iron and **25**) a poor overlay is observed (it is not possible to use VTNA for determination of reaction orders with respect to **26** as the concentration of Grignard reagent is unknown). Slightly better fits are observed in the case of **27** and **29** than for **28** as more of these products are formed in any given reaction, although in all cases as the reaction progresses there is less overlap (demonstrating less reliable results) observed. Therefore, whilst VTNA should in theory give reliable order data, for the purpose of consistency, the method of initial rates was primarily used instead. All of the following plots were produced by Dr. Antonis Messinis; in all cases the *y* axis is concentration (mM).

*9.2.2 Determination of reaction orders for the formation of **27***

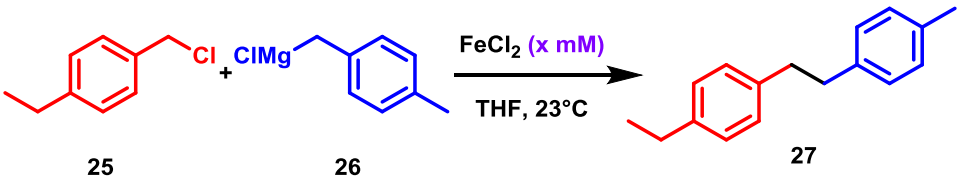

25 **26** **27**

215 mM **323 mM**

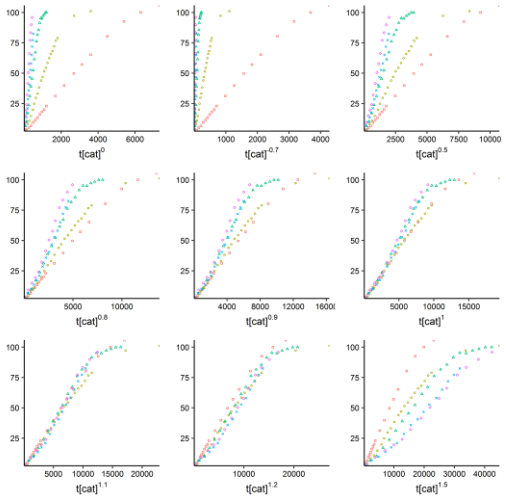

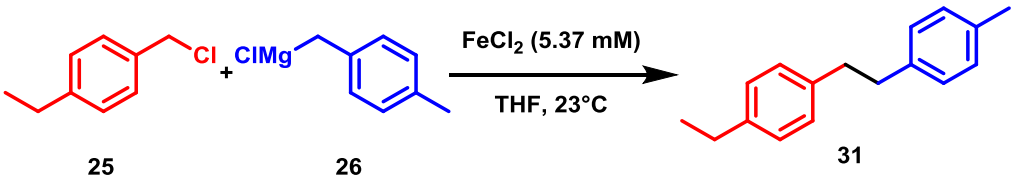

25 **26** **31**

x mM **323 mM**

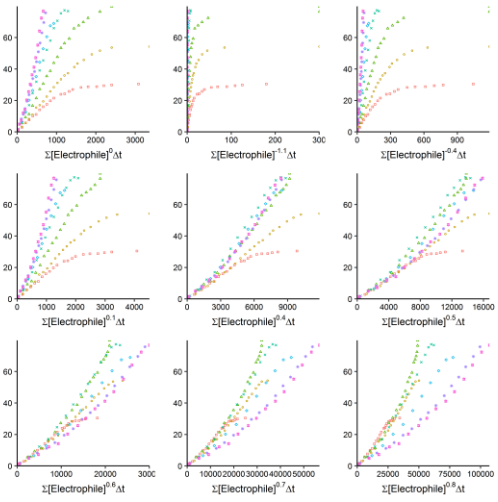

*9.2.3 Determination of reaction orders for the formation of **28***

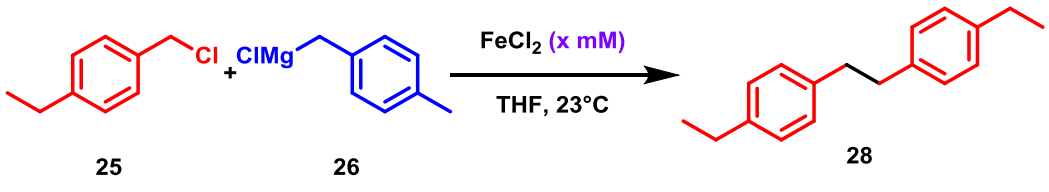

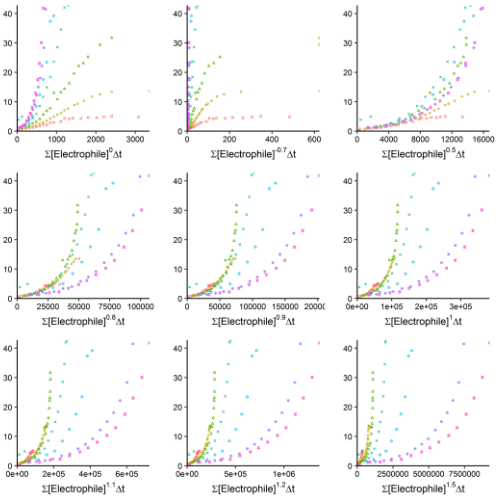

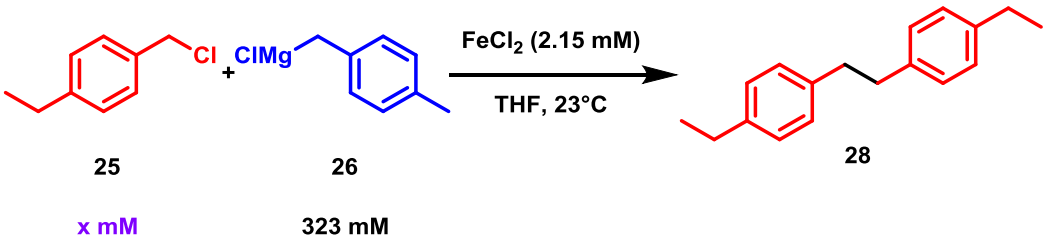

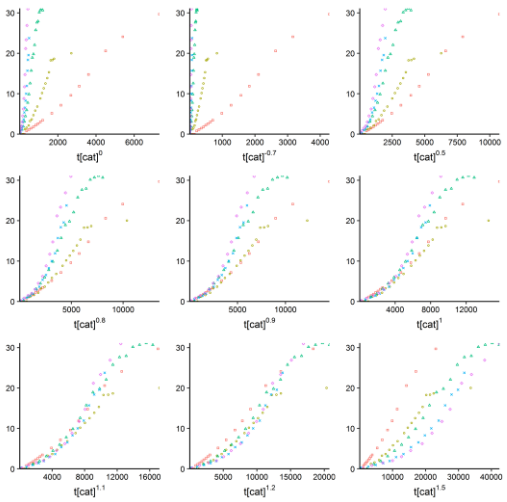

*9.2.4 Determination of reaction orders for the formation of **29***

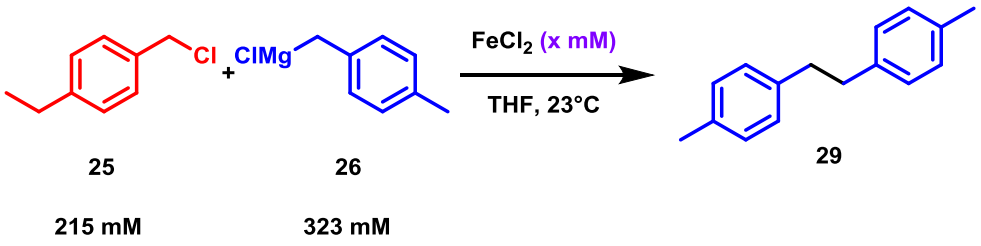

25 **26**

215 mM **323 mM**

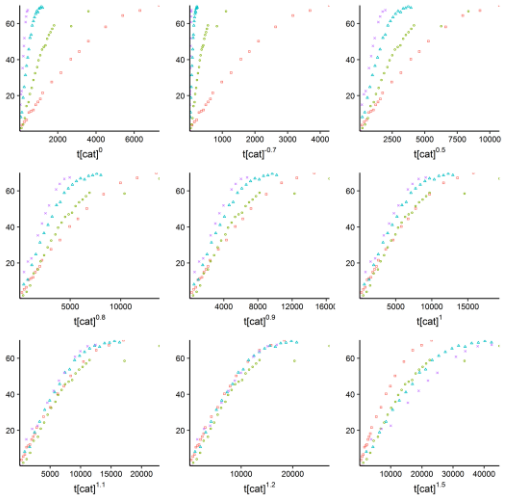

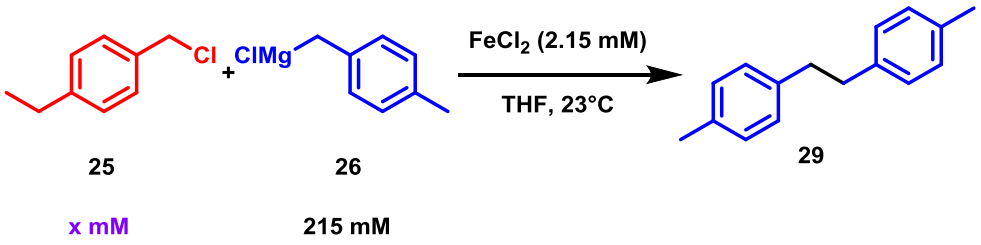

25 **26**

x mM **215 mM**